Transactions of the ASME, Journal of Heat Transfer (ISSN 0022-1481) is published monthly by The American Society of Mechanical Engineers, Three Park Avenue, New York, NY 10016. Periodicals postage paid at New York, NY and additional mailing offices. POSTMASTER: Send address changes to Transactions of the ASME, Journal of Heat Transfer, c/o THE AMERICAN SOCIETY OF MECHANICAL ENGINEERS, 22 Law Drive, Box 2300, Fairfield, NJ 07007-2300. **CHANGES OF ADDRESS** must be received at Society headquarters seven weeks before they are to be effective. Please send old label and new address. **STATEMENT from By-Laws.** The Society shall not be responsible for statements or opinions advanced in papers or ... printed in its publications (B7.1, Para. 3).

Journal of Heat Transfer

Published Monthly by ASME

VOLUME 127 • NUMBER 9 • SEPTEMBER 2005

RESEARCH PAPERS

TECHNICAL BRIEFS

(Contents continued on inside back cover)

This journal is printed on acid-free paper, which exceeds the ANSI Z39.48-1992 specification for permanence of paper and library materials. ♾™
♻ 85% recycled content, including 10% post-consumer fibers.

Journal of Heat Transfer **Volume 127, Number 9** **SEPTEMBER 2005**

The ASME Journal of Heat Transfer is abstracted and indexed in the following:

Applied Science and Technology Index, Chemical Abstracts, Chemical Engineering and Biotechnology Abstracts (Electronic equivalent of Process and Chemical Engineering), Civil Engineering Abstracts, Compendex (The electronic equivalent of Engineering Index), Corrosion Abstracts, Current Contents, E & P Health, Safety, and Environment, Ei EncompassLit, Engineered Materials Abstracts, Engineering Index, Enviroline (The electronic equivalent of Environment Abstracts), Environment Abstracts, Environmental Engineering Abstracts, Environmental Science and Pollution Management, Fluidex, Fuel and Energy Abstracts, Index to Scientific Reviews, INSPEC, International Building Services Abstracts, Mechanical & Transportation Engineering Abstracts, Mechanical Engineering Abstracts, METADEX (The electronic equivalent of Metals Abstracts and Alloys Index), Petroleum Abstracts, Process and Chemical Engineering, Referativnyi Zhurnal, Science Citation Index, SciSearch (The electronic equivalent of Science Citation Index), Theoretical Chemical Engineering

Nitin Goel

D. Yogi Goswami
e-mail: goswami@ufl.edu

Solar Energy and Energy Conversion Laboratory, Mechanical and Aerospace Engineering Department, University of Florida, P.O. Box 116300 Gainesville, FL 32611-6300

A Compact Falling Film Absorber

The paper presents a new design of a falling film absorber that could considerably reduce the absorber size without penalizing the vapor and coolant side pressure drops. The proposed design is based on the fundamental characteristics of an efficient absorber design: large liquid-vapor interfacial area and good wetting characteristics. A finite difference scheme is developed to numerically investigate the performance of the design. The results indicate that the proposed design is more compact and efficient than the horizontal tube-type falling film absorber. [DOI: 10.1115/1.1929781]

Keywords: Absorber, Condenser, Absorption, Falling Film

Introduction

Heat-driven absorption cycles provide refrigeration/air-conditioning with environmentally friendly refrigerants, such as ammonia. The absorber is one of the critical components of such systems in terms of size, efficiency, and cost [1]. The key features of an efficient design are high heat and mass transfer coefficients, and a large surface contact area. Other criteria of a good design are low pressure drops in the liquid, vapor, and coolant regimes. The vapor flow mechanism divides absorbers into two broad categories, namely, those operating in falling film absorption mode and those in bubble absorption mode. The falling film mode over horizontal coolant tubes has been widely utilized in commercial absorption systems. The design accomplishes a low pressure drop on the vapor-side, but it has a low surface contact area and unstable liquid distribution. Numerous heat and mass transfer enhancement techniques like surface profiling/modification, miniaturization, extended fins, and use of surfactants have been extensively analyzed and studied by researchers.

Techniques such as sand blasting, surface patterning, scratching, and surface oxidation have been used to improve the wetting characteristics of liquid films. The effect of a porous surface on the enhancement of surface wettability was studied by Yang and Jou [2]. Benzeguir et al. [3] profiled the solution-side heat transfer surface by employing grooved and wire-wound tubes to generate large mixing waves. Miller and Perez-Blanco [4] studied the effect of a solution-side tubular surface with pin fins, grooves, and twisted fins on the enhancement of mixing and uniformity of the falling film. Similar to the above concept of profiling the solution-side surface, Schwarzer et al. [5] used spiral steps on the inner periphery of the tubes. In addition to the increase in fluid mixing, fins also act as obstructions in the vapor path that consequently induce turbulence in the flow. Constant curvature surfaces (CCS) were studied by Isshiki et al. [6] for the purpose of forming a uniformly thick falling film. Surfactants are also utilized to enhance the mass transfer coefficient and wetting characteristics. The presence of surfactants causes a local variation in the surface tension, which in turn induces turbulence at the liquid-vapor interface. Much research has been devoted to quantifying and understanding the effect of the surfactants [7–10].

Another enhancement technique is the miniaturization of coolant sections. It has already shown promising improvements in heat exchanger technology. Very high heat transfer coefficients can be achieved for microchannels, even in the laminar flow regime. In addition, the surface-to-volume ratio increases with the miniaturization of coolant sections. Garimella [11] proposed the application of small-diameter coolant tubes in the falling film absorber. The experiments conducted by his group also confirmed that a very high absorption heat duty (16 kW) could be accomplished in a compact absorber of a size $0.178 \times 0.178 \times 0.508$ m^3 [12].

Recently, Islam et al. [13] proposed a unique concept of periodically inverting the falling film while the liquid solution flows over the cooling surface. The liquid surface that was previously in contact with the cooled surface is directly exposed to the vapor by inverting the film. This design not only increases the mass flux, but also induces mixing due to shear forces. However, the effective liquid-coolant surface area was drastically reduced.

In the current work, a new design of a falling film absorber is proposed that could considerably reduce the absorber size. The proposed design is based on the fundamental characteristics of an efficient absorber design: large liquid-vapor interfacial area and good wetting characteristics. The design utilizes the unused vertical spacing between the coolant tubes to form the falling film, which consequently leads to an increase in the mass transfer area. The proposed design was numerically compared with a microchannel-based falling film absorber. As horizontal tube-type absorbers with small diameter coolant tubes are very compact, this analysis will help in comparing the proposed design with the current state-of-the-art absorber design.

Proposed Absorber Configuration

It is a well-known fact that the mass transfer process is the dominating factor in the simultaneous heat and mass transfer processes in absorption. An increase in liquid-vapor contact area and induction of turbulence at the liquid-vapor interface are two of the techniques that can increase mass transfer rates. Bubble absorbers are about 50% more compact in comparison to the traditional falling film absorbers [14]. Their compact size results from the generation of an extremely large liquid-vapor interface by bubbling vapor into the bulk liquid. In the case of conventional falling film absorption mode, the interfacial area between the liquid and vapor phases is limited to the surface area of the coolant tubes and liquid droplets falling in between the coolant tubes. However, the surface area of the droplets will be much smaller than that of the coolant tubes. Figure 1 provides a schematic representation of the horizontal tube-type falling film absorber. Several enhancement techniques have been examined and analyzed to improve the performance of a falling film absorber, but the utilization of vertical space between the adjacent coolant tubes has not yet been reported. A falling film can be formed between the adjacent tubes to increase the liquid-vapor surface area. Operating the falling film in sheet mode is one way to form a liquid film between the horizontal tubes. However, it requires comparably higher solution flow rates, which itself reduces the effective liquid-coolant surface area. Another method, confined to lower solution flow rates, would be to have a medium between the horizontal tubes over which a liquid film can be easily formed: Alternatively wrapping a mesh/fabric between the left and right sides of the adjacent tubes, as shown in Fig. 2, can be utilized to form a liquid film between the horizontal tubes. The mesh/fabric can be made up of a com-

Contributed by the Heat Transfer Division for publication in the JOURNAL OF HEAT TRANSFER. Manuscript received August 23, 2004; final manuscript received April 3, 2005. Review conducted by: Suresh V. Garimella.

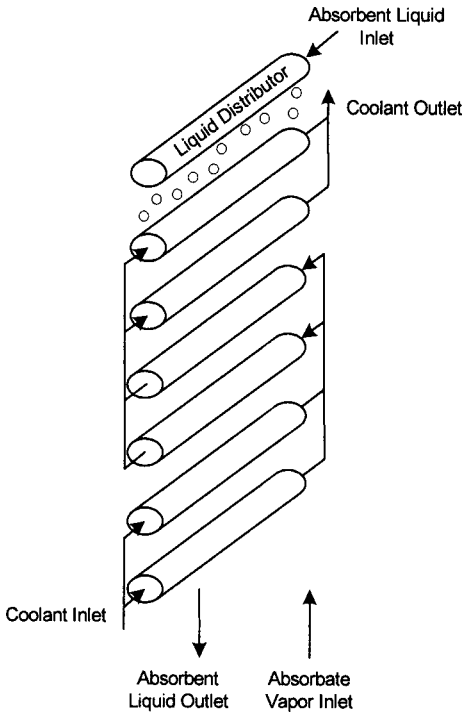

Fig. 1 Conventional horizontal tube-type falling film absorber

patible materials such as aluminum, steel, stainless steel, glass fiber, and nylon [15,16]. The material should also be flexible, and it should conform to the shape of the coolant tube. In addition, the requirement of forming a uniform falling film on the mesh restricts the use of materials that have good wetting characteristics. It should be noted that a smaller angle between the mesh and vertical plane is desirable. The liquid surface tension will not be able to hold the liquid along the mesh for larger angles, and the liquid will drip in the form of droplets. However, this effect can be reduced by changing the size of the mesh openings. The openings of the mesh should be sparse enough to just allow the formation of falling film over the mesh. A sparser and thinner mesh will reduce the effect of the mesh on liquid flow over the coolant tubes. The preliminary experiments conducted found that a fabric/mesh with 16×16 meshes per square inch of the fabric area was quite suitable for this purpose. The concept is so simple that it can also be incorporated in the existing horizontal tube-type falling film absorbers.

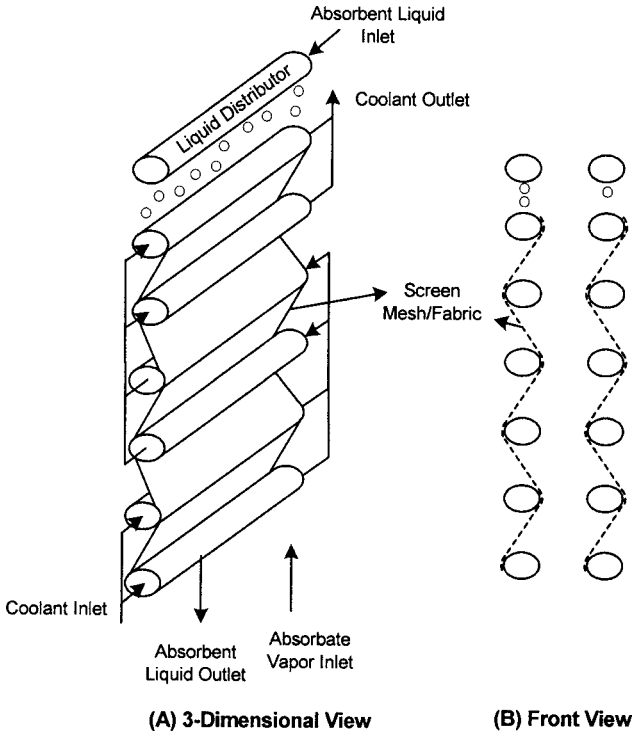

Fig. 2 Proposed falling film absorber (with screen mesh/fabric)

Availability of a larger liquid-vapor contact area might lead to an extra amount of absorption. The resulting increase in the absorption heat will increase the solution temperature. Hence, a larger temperature gradient between the coolant and liquid solution will in turn increase the rate of heat transferred to the coolant. In addition to an increase in surface area, the concept also enhances falling film stability by preventing the coalescence of droplets on horizontal tubes. Fabrics have a natural tendency to soak up liquid by capillary action, and this mechanism also helps in redistributing the liquid solution on the coolant tubes. Furthermore, the liquid flow over an irregular surface of the mesh may induce vortices. It may thus promote mixing of the liquid film while it flows alternatively over the mesh/fabric and coolant tubes. Fujita et al. [17] showed an increase in heat and mass transfer coefficients by 1.5 to 1.8 times on a vertical wetted wall by introducing wire roughness. The falling film mixing replenishes the liquid boundary layer by removing ammonia to the liquid bulk, and thus enhances the absorption rate. The combined effect of increased mass transfer area, liquid film mixing, and film stability will improve the absorption flux. Some other phenomena associated with the proposed design are the increase in liquid hold-up, prevention of satellite droplets, and fin effect of the metallic mesh. These effects may also enhance the performance of the proposed design.

The use of a large number of smaller diameter cooling tubes can considerably increase the cooling surface area per unit volume as compared to a small number of larger diameter tubes. Very high heat transfer coefficients can also be achieved in small diameter tubes. A parallel-series arrangement of the coolant tubes is usually used to reduce the effect of increase in the pressure drop and restrict the flow rate to the appropriate limits. The coupling of miniaturization of the coolant section and film formation between the horizontal tubes can consequently enhance the absorption flux, and thus lead to an efficient absorber design.

Mathematical Model

A numerical model is developed to compare the performance of the proposed absorber with the horizontal tube-type absorber design. The model is based on the application of continuity and energy balance at each differential segment of the absorber. It takes into account the mass transfer resistances in both the liquid and vapor phases, and uses empirical correlations to predict the heat and mass transfer coefficients. The model also considers the coupled nature of heat and mass transfer processes accompanying the falling film absorption. The falling film absorber considered here consists of an array of horizontal coolant tubes over which a weak solution is distributed. The weak solution then flows over the coolant tubes and mesh/fabric under the influence of gravity. The absorbate vapor enters from the bottom of the absorber and flows through the narrow channels formed by an assemblage of coolant tubes. The vapor is absorbed by the weak solution flowing countercurrent to it. The heat of absorption thus released is rejected to the coolant that flows through the coolant tubes. The model considered here is a two-dimensional model that neglects the temperature and concentration variation along the axis of the horizontal tubes. However, the coolant flow is in a cross-counterdirection to the solution while the coolant enters at the bottom and leaves at the top of the absorber. The flow of coolant

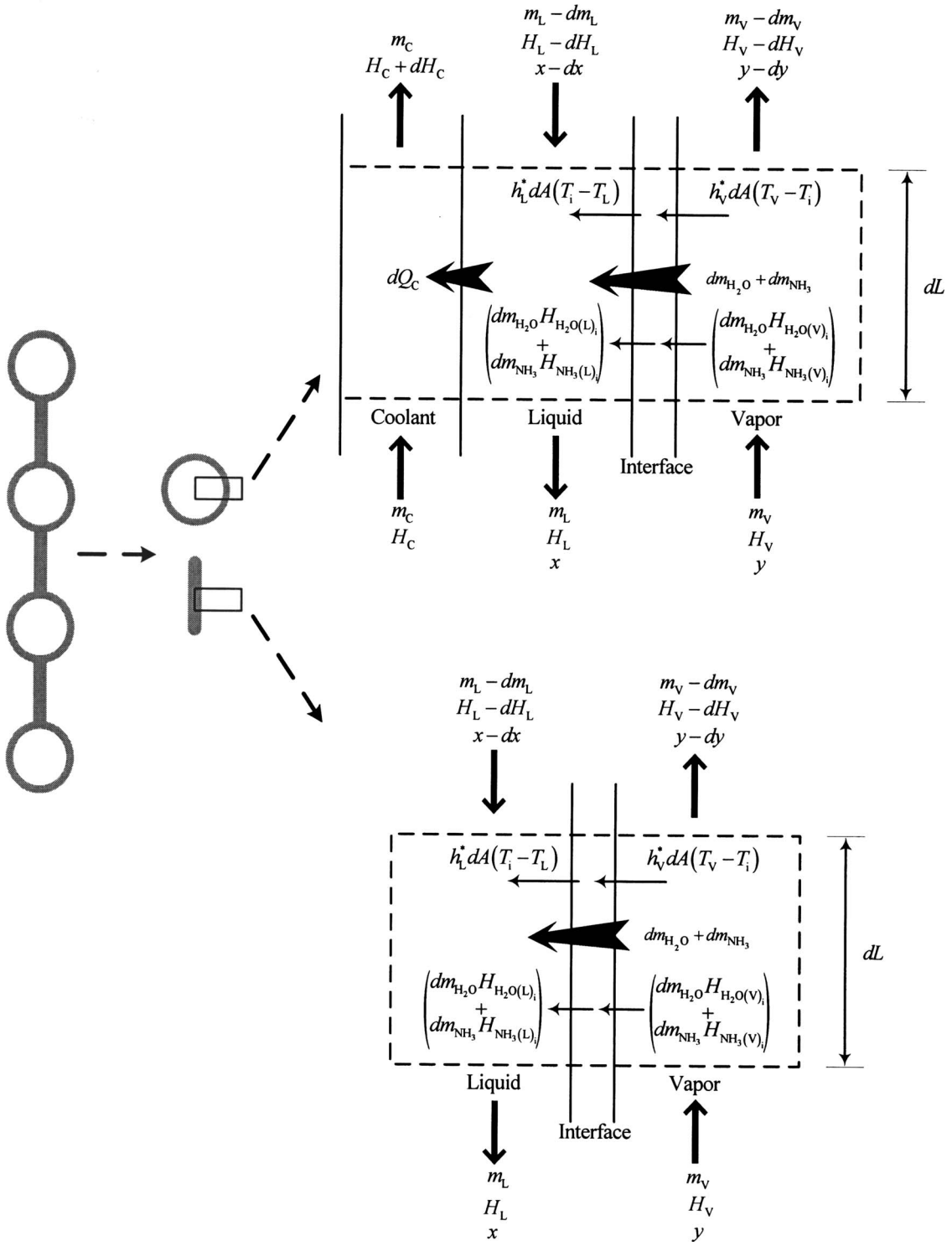

Fig. 3 Schematic of the differential control volume of the proposed design

in the individual tubes being cross-flow to the weak solution leads to a variation in coolant temperature along the tubes. In order to improve the model, the coolant temperature in an individual tube is assumed to be equal to the mean of the inlet and outlet temperatures of the tube. As shown in Fig. 1 and 2, a parallel-series arrangement of the coolant tubes is used to decrease the coolant-side pressure loss to acceptable limits. The presence of mesh/fabric in the proposed design is the only difference between the proposed and horizontal tube-type falling film absorber designs, which are considered for the numerical analysis. Continuity and energy balance equations are applied at each differential control volume of the proposed design, as shown in Fig. 3. Due to the presence of falling film in between the horizontal tubes, the associated heat and mass transfer processes in that region also need to be considered. Hence, the model for the proposed design consists of two types of differential control volumes: the control volume in the cooling region and the control volume in mesh/fabric region. Similarly, the model for the horizontal tube-type absorber design only consists of control volumes present in the cooling region.

The following assumptions were made in building the model:

1. The absorption process is assumed to be in steady state.
2. System pressure is constant.
3. Thermodynamic equilibrium exists at the liquid-vapor interface.
4. The heat transfer surface under the conditions is completely wet (i.e., there is no direct heat transfer between the vapor and the coolant surface).
5. Heat losses to the environment are negligible.
6. Adiabatic absorption in droplets is neglected.
7. No flooding occurs between the two adjacent horizontal tubes.
8. Mass transfer due to thermal and pressure difference is negligible (mass transfer occurs only because of the concentration gradient).
9. Effect of nonabsorbable gases is ignored.
10. The coolant temperature along the radial coordinates of the tubes is assumed to be constant.
11. Conduction heat transfer between the mesh/fabric and coolant tubes is negligible.
12. The flow of absorbate along the periphery of coolant tubes is unaffected by the presence of mesh/fabric.

The mass transfer between the liquid and vapor phases is due to the combined effect of bulk transport and molecular diffusion of NH_3 and H_2O across the liquid-vapor interface. For steady state, the mass flux of the vapor absorbed by the weak solution is given by [18]

$$\frac{dm_{\mathrm{NH_3}}}{M_{\mathrm{NH_3}}} + \frac{dm_{\mathrm{H_2O}}}{M_{\mathrm{H_2O}}} = dA_i K_V \ln\left(\frac{z-\tilde{y}_i}{z-\tilde{y}}\right) \tag{1}$$

$$\frac{dm_{\mathrm{NH_3}}}{M_{\mathrm{NH_3}}} + \frac{dm_{\mathrm{H_2O}}}{M_{\mathrm{H_2O}}} = dA_i K_L \ln\left(\frac{z-\tilde{x}}{z-\tilde{x}_i}\right) \tag{2}$$

Subscripts L, V, and i denote the liquid, vapor, and liquid-vapor interface, respectively. The positive value of mass flux, namely, $dm_{\mathrm{NH_3}}$ and dm_{H2O}, signify the mass transfer from vapor to liquid phase. As both ammonia and water are being absorbed/desorbed, the absorption mass flux consists of both constituents. The mole fraction of ammonia in the absorbing/desorbing vapor is defined as z and can be expressed by Eq. (3). For the working pair, the value of z is normally expected to be between zero and one. However, its value can also be just greater but close to one for some design conditions.

$$z = \left(\frac{\dfrac{dm_{\mathrm{NH_3}}}{M_{\mathrm{NH_3}}}}{\dfrac{dm_{\mathrm{H_2O}}}{M_{\mathrm{H_2O}}} + \dfrac{dm_{\mathrm{NH_3}}}{M_{\mathrm{NH_3}}}}\right) \tag{3}$$

The similarity between heat and mass transfer processes can be utilized to deduce the analogous heat and mass transfer coefficients [19]. The heat and mass transfer analogy is particularly useful when either one of the heat and mass transfer coefficients is difficult to obtain. So, in this case, liquid heat transfer coefficient h_L and vapor mass transfer coefficient K_V are obtained by the use of the following equation for the liquid and vapor phases separately:

$$\frac{h}{M} = C_P K \left(\frac{\mathrm{Sc}}{\mathrm{Pr}}\right)^{2/3} \tag{4}$$

Yih and Chen [20] developed liquid-side mass transfer correlations for laminar, wavy, and turbulent falling films in a wetted-wall column. The correlations were based on the motion of eddies near the liquid-vapor interface, and the value of the constants were obtained by fitting to their own experimental results and the work of ten other researchers. Their correlations are applicable to fully developed conditions only. Even though the wetted-wall columns formed by wrapping mesh between the coolant tubes is not similar to the wetted-wall columns on which the mass transfer relations were established, the application of correlations in the current geometry is a reasonable approximation. However, it must be noted that the extent of potential error due to this assumption has not been established. The correlation for the laminar flow regime was established in the range of $49 < \mathrm{Re}_{\mathrm{film1}} < 300$ and $8.5\,^{\circ}\mathrm{C} < T < 50\,^{\circ}\mathrm{C}$, and can be expressed as

$$K_L = (0.01099\mathrm{Re}_{\mathrm{film}\ 1}^{0.3955}\mathrm{Sc}_L^{0.5})\left[\frac{D_{aw(L)}\rho_L}{M_L}\left(\frac{g}{\nu_L^2}\right)^{1/3}\right] \tag{5}$$

The liquid solution flows alternatively on the mesh and coolant tubes. The convective heat transfer between the vapor and falling film on horizontal tubes $h_{V\mathrm{tube}}$ is modeled as gas flow over a circular cylinder. The equation is valid for $40 < \mathrm{Re}_D < 4000$, and the evaluation of fluid properties is required at a mean boundary layer temperature [21]

$$h_{V\ \mathrm{tube}} = \left(\frac{k_V}{D_O}\right) \times 0.683\mathrm{Re}_{D_O}^{0.466}\mathrm{Pr}_V^{1/3} \tag{6}$$

The convective heat transfer coefficient for the vapor and falling film on the mesh $h_{V\mathrm{mesh}}$ is based on the flow inside a parallel-plate channel under laminar conditions. The correlation assumes uniform surface temperature, and neglects the edge effect due to the finite width of parallel-plate channels. Though the correlation is not exactly applicable to finite rectangular ducts formed by a screen mesh across the tubes, it can be considered as a reasonable approximation for large aspect ratios. The relation is also restricted to fully developed profiles of velocity and temperature, and is given by [22]

$$h_{V\ \mathrm{mesh}} = 7.541\left(\frac{k_V}{D_h}\right) \tag{7}$$

where the hydraulic diameter D_h is defined as

$$D_h = \frac{4(\text{Cross-sectional Area of the Duct})}{(\text{Wetted Perimeter})} \tag{8}$$

The heat transfer between the liquid and vapor phases occurs due to the combined contribution of convective heat transfer and sensible heat load of the mass transferred across the interface. The ordinary convective heat transfer is due to the temperature gradient between the fluid in motion and the bounding surface. If the convective heat transfer is also accompanied by mass transfer across the bounding surface, an extra amount of heat will transfer due to the heat capacity of the mass being transferred. This sensible heat transfer is primarily due to the temperature gradient between the liquid and vapor phases, and consequently between the liquid, liquid-vapor interface, and vapor regimes. The convective heat transfer coefficient can be modified to account for the effect of mass transfer. The modified heat transfer coefficient h^* for simultaneous heat and mass transfer is given by [18]

$$h^* = h\frac{c}{1-e^{-c}} \tag{9}$$

where

$$c = \frac{\dfrac{dm_{\mathrm{NH_3}}}{M_{\mathrm{NH_3}}}C_{p\mathrm{NH_3}} + \dfrac{dm_{\mathrm{H_2O}}}{M_{\mathrm{H_2O}}}C_{p\mathrm{H_2O}}}{h} \tag{10}$$

The mass and concentration balance between the liquid and vapor phases are given by

$$dm_L = dm_V \tag{11}$$

$$m_V y + (m_L - dm_L)(x - dx) = (m_V - dm_V)(y - dy) + m_L x \tag{12}$$

The energy balance equation for the control volume of liquid phase will depend on the location of the falling film on the coolant tubes or the screen mesh as indicated below.

Control volume of liquid phase in the coolant region

$$m_L H_L + dQ_C = (m_L - dm_L)(H_L - dH_L) + h_L^* \times dA(T_i - T_L) + dm_{H_2O} H_{H_2O(L)_i} + dm_{NH_3} H_{NH_3(L)_i} \quad (13)$$

Control volume of liquid phase in the mesh region

$$m_L H_L = (m_L - dm_L)(H_L - dH_L) + h_L^* \times dA(T_i - T_L) + dm_{H_2O} H_{H_2O(L)_i} + dm_{NH_3} H_{NH_3(L)_i} \quad (14)$$

The energy balance equation for the control volume of vapor phase is given by

$$m_V H_V = (m_V - dm_V)(H_V - dH_V) + h_V^* \times dA(T_V - T_i) + dm_{H_2O} H_{H_2O(V)_i} + dm_{NH_3} H_{NH_3(V)_i} \quad (15)$$

The liquid-vapor interface is assumed to be at thermodynamic equilibrium. Concentration, temperature, and pressure of the binary mixture are coupled to each other at the saturation state. In particular, only two of these properties are sufficient to determine the thermodynamic state of a binary mixture. Concentration of ammonia in the vapor and liquid at the interface can then be expressed as

$$y_i = f(T_i, P) \quad (16)$$

$$x_i = f(T_i, P) \quad (17)$$

An energy balance at the liquid-vapor interface gives

$$h_L^* dA(T_i - T_L) + dm_{H_2O} H_{H_2O(L)_i} + dm_{NH_3} H_{NH_3(L)_i} = h_V^* dA(T_V - T_i) + dm_{H_2O} H_{H_2O(V)_i} + dm_{NH_3} H_{NH_3(V)_i} \quad (18)$$

The heat absorbed by the coolant can be found by an energy balance over the coolant, coolant-liquid interface, and global control volumes

$$dQ_C = U dA_C (T_L - T_C) \quad (19)$$

$$dQ_C = m_C dH_C \quad (20)$$

$$dQ_C = (m_L - dm_L)(H_L - dH_L) + m_V H_V - m_L H_L - (m_V - dm_V)(H_V - dH_V) \quad (21)$$

where the overall heat transfer coefficient U combines the various thermal resistances in the path of the heat flow between the weak solution and coolant, and can be expressed as

$$\frac{1}{U} = \frac{1}{h_C} + R_{wall} + \frac{1}{h_{film}} \quad (22)$$

The coolant-side heat transfer coefficient h_C is based on the fully developed laminar flow conditions in the coolant tube. The correlation based on uniform surface heat flux is of the form

$$h_C = 4.364\left(\frac{k_C}{D_I}\right) \quad (23)$$

The correlation developed by Wilke [23] is used to calculate the falling film heat transfer coefficient for the laminar flow regime. The Wilke correlation was established for $Re_{film} < 2460\ Pr^{-0.646}$

$$h_{film} = 1.88\left(\frac{k_L}{\delta}\right) \quad (24)$$

where the average film thickness δ for the laminar flow is given by Nusselt's theory [23]

$$\delta = 0.91 Re_{film}^{1/3}\left(\frac{\nu_L^2}{g}\right)^{1/3} \quad (25)$$

Numerical Technique

A finite difference method is used to solve the system of nonlinear ordinary differential equations. The simulation technique is based on the algorithm employed by Goel et al. [24] to analyze countercurrent falling film absorbers. The absorber is divided into differential segments of an incremental length dL. Each incremental segment is further divided into liquid, vapor, and coolant differential segments. The model is primarily based on two routines. Routine 1 solves the liquid differential segments by marching in the downward direction, whereas Routine 2 marches upward to solve the vapor and coolant differential segments. Due to the interlinking of the liquid, vapor, and coolant control volumes, the vapor and coolant conditions are initially required to solve the liquid region. An initial guess for the conditions of all the vapor and coolant differential segments is taken to be equal to the inlet vapor and coolant conditions. The model iteratively loops over these two routines to achieve better approximations of an unknown solution. This is repeated until all unknown variables converge to stable values. The solution method can be summarized as follows:

1. Assume a length of the absorber and divide the absorber, i.e., coolant tubes and screen mesh, into differential segments of incremental length dL.
2. Equate the vapor and coolant conditions of all incremental steps to the inlet vapor and coolant conditions.
3. Solve the liquid control volume for each segment by marching downward. The values of vapor and coolant conditions at each node are obtained by step (2) in case of first iteration or by Routine 2 in case of later subsequent iterations. The following steps describe Routine 1:
   - i. Guess the liquid-vapor interface temperature T_i.
   - ii. Calculate the liquid- and vapor-side mass fraction of ammonia, x_i and y_i, at the interface using Eqs. (16) and (17).
   - iii. Guess z.
   - iv. Calculate a new value of z by using Eqs. (1) and (2).
   - v. If the difference between the old and new values of z is less than the assumed convergence criterion, go to step vi, otherwise go to step iii.
   - vi. Calculate the mass flux of ammonia and water using Eqs. (1)–(3).
   - vii. Calculate a new value of T_i from an energy balance of interface control volume using Eq. (18).
   - viii. If the difference between the old and new values of T_i is less than the assumed convergence criterion, go to step ix, otherwise go to step i.
   - ix. Calculate the mass flow rate and concentration of the liquid phase for the next segment using Eqs. (11) and (12).
   - x. Calculate the enthalpy of the liquid phase for the next segment from an energy balance of liquid control volume using Eq. (13) or (14). The use of Eq. (13) or (14) depends on the location of the falling film in the coolant or mesh region.
4. Solve the vapor and coolant differential segments by marching upward. The values of the liquid conditions at each node are obtained by Routine 1. The following steps describe Routine 2:
   - i. If the differential segment contains the coolant tube, follow the following steps:
     - a. Guess the average coolant temperature T_C of the coolant tube.
     - b. Guess the liquid-vapor interface temperature T_i.

c. Calculate the liquid- and vapor-side mass fractions of the ammonia, x_i and y_i, at the interface using Eqs. (16) and (17).
d. Guess z.
e. Calculate a new value of z by using Eqs. (1) and (2).
f. If the difference between the old and new values of z is less than the assumed convergence criterion, go to step g, otherwise go to step d.
g. Calculate the mass flux of ammonia and water using Eqs. (1)–(3).
h. Calculate a new value of T_i from the energy balance of the interface control volume using Eq. (18).
i. If the difference between the old and new values of T_i is less than the assumed convergence criterion, go to step j, otherwise go to step b.
j. Calculate the mass flow rate and concentration of the vapor phase for the next segment using Eqs. (11) and (12).
k. Calculate the heat absorbed by the coolant in the differential coolant segment dQ_C using Eq. (19).
l. Calculate the enthalpy of the vapor phase for the next segment from an energy balance for the vapor control volume using Eq. (15).
m. If the next differential element contains mesh, go to step n, otherwise go to step b to calculate the conditions of the next differential element.
n. Calculate the total amount of heat absorbed by the coolant tube by adding all dQ_C of the differential segments pertaining to that coolant tube.
o. Calculate the outlet coolant temperature of the tube using Eq. (20).
p. Calculate a new value of T_C by taking the average of the inlet and outlet coolant temperatures of the tube.
q. If the difference between the old and new values of T_C is less than the assumed convergence criterion, go to step r, otherwise go to step a.
r. If the next coolant tube is not in parallel connection with the current tube, equate the inlet coolant temperature of the next parallel tube assembly to the mean of the outlet coolant temperatures of the current parallel tube assembly.

ii. If the differential segment contain the mesh, follow the following steps:

a. Guess the liquid-vapor interface temperature T_i.
b. Calculate the liquid- and vapor-side mass fractions of the ammonia, x_i and y_i, at the interface using Eqs. (16) and (17).
c. Guess z.
d. Calculate a new value of z by using Eqs. (1) and (2).
e. If the difference between the old and new values of z is less than the assumed convergence criterion, go to step f, otherwise go to step c.
f. Calculate the mass flux of the ammonia and water using Eq. (1)–(3).
g. Calculate a new value of T_i from an energy balance of the interface control volume using Eq. (18).
h. If the difference between the old and new values of T_i is less than the assumed convergence criterion, go to step i, otherwise go to step a.
i. Calculate the mass flow rate and concentration of the vapor phase for the next segment using Eqs. (11) and (12).
j. Calculate the enthalpy of the vapor phase for the next segment of the incremental steps from an energy balance of the vapor control volume using Eq. (15).

Table 1 Operating conditions of the proposed and horizontal tube-type falling film absorber designs

System Pressure, bar	3
Coolant medium	Water
	Inlet Conditions
Coolant mass flow rate, kg/s	0.05
Reynolds number for coolant flow, Re_{D_i}	563
Coolant bulk temperature, K	302.6
Solution mass flow rate, kg/s	0.01
Reynolds number for falling film, Re_{film}	59
Solution bulk temperature, K	323
Solution mass fraction	0.25
Vapor mass flow rate, kg/s	0.0015
Reynolds number for vapor flow, Re_{D_o}	72
Vapor bulk temperature, K	300
Vapor mass fraction	0.997

5. Repeat steps 3 and 4 until the rate of change of any variable between two successive iterations is $<10^{-10}$.
6. Check the mass flow rate of the vapor at the outlet of the absorber. If it is a negative value, decrease the length of the absorber and go to step 2; if it is a positive value and is greater than 1% of the inlet vapor flow rate, increase the length of the absorber and go to step 2; if the value lies between zero and 1% of inlet vapor flow rate, assume the convergence.

Results and Discussion

The mathematical model was used to analyze the performance of the proposed falling film absorber with the horizontal tube-type falling film absorber. The analysis of both the designs is based on the geometric dimensions and operating conditions listed in Tables 1 and 2. The operating conditions considered here are typical conditions encountered in single-stage ammonia/water absorption systems [25]. The design conditions were selected such that a uniform distribution of the weak solution on the horizontal tubes is practically feasible, and thus the numerical results are based on a realistic situation. The finite difference scheme is modeled to calculate the minimum number of tubular rows required to accomplish the given amount of vapor absorption in both designs.

The computational results are summarized in Table 3. As depicted in the table, an absorber with the falling film guidance mechanism in between the coolant tubes will require a lesser number of tubes as compared to a similar horizontal tube type falling film absorber design. This accounts for a size reduction of about 25%. In order to thoroughly analyze the proposed design with respect to the horizontal tube-type absorber design, the temperature, concentration, and mass flow profiles of the different fluid regions were obtained as a function of the coolant tube rows.

Figures 4 and 5 show the variation in bulk mean temperature of the coolant, solution, and vapor along the absorber length for the

Table 2 Geometric dimensions of the proposed and horizontal tube-type falling film absorber designs

Tube outer diameter, mm	3.2
Tube inner diameter, mm	2.3
Tube material	316 Stainless Steel
Tube length, cm	10
Number of tubes per row	4
Number of tube rows per pass	15
Tube vertical pitch, mm	8
Tube traverse pitch, mm	16

proposed and horizontal tube-type falling film absorber designs, respectively. For both designs, the solution temperature increases

Table 3 Computational results of the proposed and horizontal tube-type falling film absorber designs

	Proposed Design	Horizontal Tube-Type Absorber Design
Required length of the coolant tube assembly (L), cm	35	46
Required minimum number of tube rows	46	61
Absorber heat duty, kW	2.68	2.83
Liquid-vapor interface area, m^2	0.266	0.245
Coolant surface area, m^2	0.185	0.245
	Outlet Conditions	
Solution mass flow rate, kg/s	0.0115	0.0115
Solution bulk temperature, K	317.5	314.2
Solution mass fraction	0.347	0.347
Vapor mass flow rate, kg/s	1.2×10^{-5}	1.8×10^{-5}
Vapor bulk temperature, K	327.2	325.8

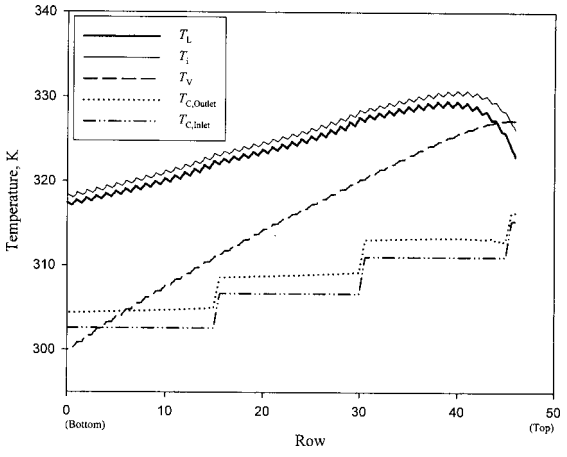

Fig. 4 Variation of temperature for the proposed falling film absorber

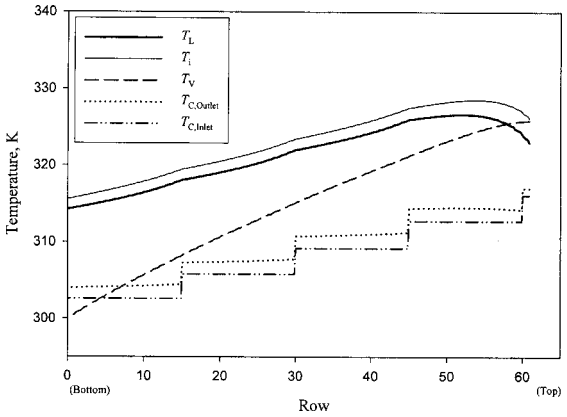

Fig. 5 Variation of temperature for the horizontal tube-type falling film absorber

for a while as the liquid flows down the cooling surface. At the top section of the absorber, heat transfer from the liquid to coolant region is less than the heat transferred to the liquid phase by the heat of absorption. This is due to the fact that subcooling has a combined contribution on the heat transfer from liquid to coolant region, and the mass transfer from vapor to liquid region. The solution temperature reaches a maximum value, and thereafter it decreases as the solution flows down in both designs. Due to the rejection of heat to the coolant, the coolant temperature increases while flowing through the coolant tubes. Also note that the interfacial temperature is always greater than the solution temperature. This is due to the generation of absorption heat at the liquid-vapor interface. For both designs considered, the vapor temperature initially increases quite rapidly as it flows in the upward direction, and then it gradually approaches the interface temperature. The coolant mean temperature sharply increases after every 15 rows of the coolant tubes. It represents the entry of coolant in the next parallel assembly of the coolant tubes. Thus, the periodic surge in the coolant temperature is in agreement with the parallel-series arrangement of the coolant tubes. The difference between the vapor, liquid, liquid-vapor interface, and coolant temperatures can lead to the conclusion that the liquid-side heat transfer resistance is negligible in comparison to the other constituents of heat transfer resistance. However, the vapor phase heat transfer resistance also becomes comparable to the liquid phase heat transfer resistance at the upper section of both absorbers. It is the coolant-side heat transfer resistance that dominates the overall heat transfer resistance at the absorbers' upper section. The noticeable trend for the proposed design is the liquid temperature profile, which decreases and increases alternatively as the solution flows over the coolant tube and mesh, respectively. The flow of solution on the coolant tubes decreases the solution temperature and makes the solution more subcooled. As the solution flows on the screen mesh, it absorbs vapor and the unavailability of a heat rejection mechanism on the screen mesh causes the solution to reach closer-to-saturation conditions. However, the effect of the coolant tubes to decrease the solution temperature is more significant than the effect of the screen mesh to increase the solution temperature, and the net result is a decrease in the solution temperature from the top to the bottom of the absorbers.

Figures 6 and 7 illustrate the mass flow rate of the liquid and vapor phases at various axial positions of both absorbers. The flow rate of the vapor decreases as it flows upward in the absorber, eventually becoming zero at the top section of both cases. This is consistent with the design criterion of complete absorption of the vapor phase. The absorption of vapor results in an increase of the solution flow rate.

The profiles of the composition of absorbing flux, and the concentration of the liquid and vapor phases are shown in Figs. 8 and

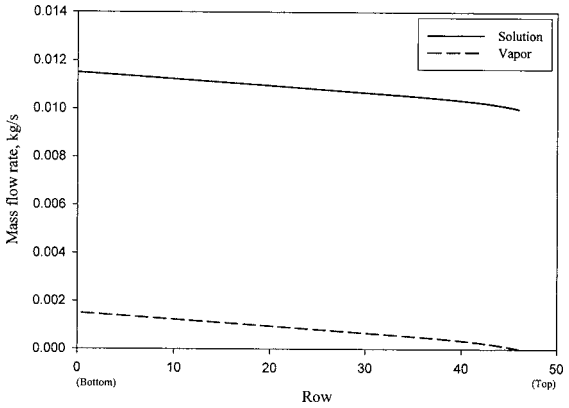

Fig. 6 Variation of mass flow rate for the proposed falling film absorber

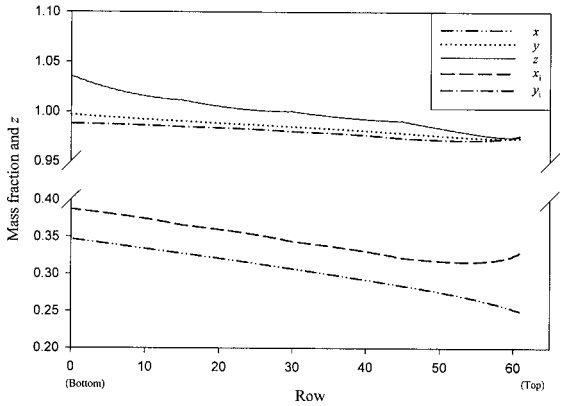

Fig. 9 Variation of concentration for the horizontal tube-type falling film absorber

9. It was found that the concentration of ammonia in the absorbing mass flux z is more than 1 near the inlet vapor region, and thereafter its value decreases to less than 1 for both designs. It implies that a small amount of water vapor is being evaporated in the bottom section of the absorbers. The inlet concentration of vapor considered in the current operating conditions is 0.997. A very low concentration of water in the vapor phase leads to the transfer of water from the liquid to vapor phase by a diffusion mechanism. The results by Kang et al. [14] and Herbine and Perez-Blanco [26] also confirm that desorption of water can occur near the entrance location of the vapor phase. However, in their case, they considered the absorption process in a cocurrent ammonia-water bubble absorber. The alternative decrease and increase in the value of z for the proposed design is due to the flow of liquid alternatively over the coolant tubes and mesh. The value of z also remains higher than the vapor concentration for both designs. However, the difference between the value of z and the vapor mass fraction is quite small. The higher concentration of ammonia in the absorbing flux as compared to that in the vapor phase leads to the decrease in vapor the mass fraction from the bottom to the top of the absorbers. Similar reasoning stands behind the increase in concentration of the solution as it flows in the downward direction. It was also found that the concentration difference between the vapor and liquid-vapor interface is lower than the difference between the liquid and liquid-vapor interface. It implies that for the operating conditions considered, a major fraction of the overall mass transfer resistance lies in the falling film. Perez-Blanco [27] and Kim [28] also considered both the liquid- and vapor-side mass transfer resistances in their numerical model, and found the liquid-side mass transfer resistance to be dominant.

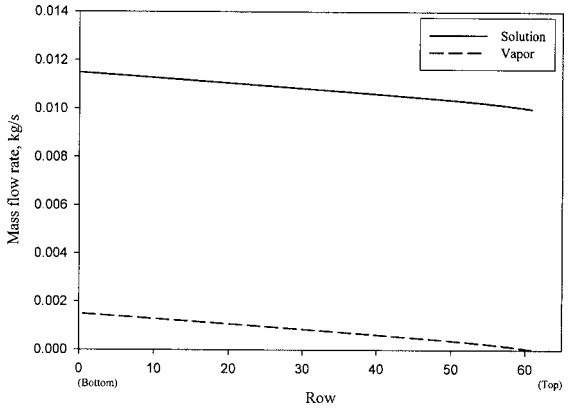

Fig. 7 Variation of mass flow rate for the horizontal tube-type falling film absorber

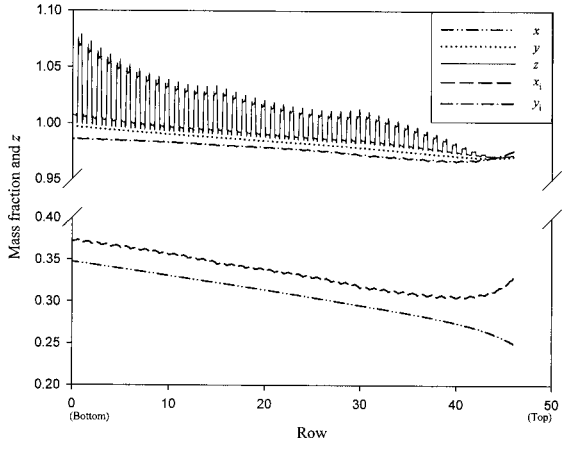

Fig. 8 Variation of concentration for the proposed falling film absorber

Conclusion

A new concept of forming a falling film in between the horizontal coolant tubes by a flow guidance medium like a mesh is presented. The new design is numerically analyzed and compared to the horizontal tube-type falling film absorber. The advantage of increasing the mass transfer area by forming the falling film between the nonutilized vertical spacing is evident from the numerical results. The proposed design is more compact and efficient than the falling film absorber based on small diameter coolant tubes. A size reduction of about 25% is possible for the operating conditions considered. The new design will induce thorough mixing of the liquid film while it flows alternatively over the mesh and coolant tubes. Also, the simplicity of the concept makes it viable to incorporate it in existing falling film absorbers.

However, this is a preliminary attempt to analyze the proposed design with the currently available numerical models. There is no consensus among researchers regarding the existence of a dominant resistance to mass transfer in either the liquid or vapor phase. The mass transfer resistance is quite often neglected in either phase to simplify the numerical models. In this model, we have attempted to avoid the above mentioned controversy by considering the heat and mass resistances in both the liquid and vapor phases. However, several flow mechanisms associated with the flow over the horizontal tubes and fabric/mesh are not considered in order to realize a numerical model. For example, the effect of the fabric/mesh on the larger residence time of the falling film, lack of adiabatic adsorption in the droplets, fin effect of the metallic mesh, wettability enhancement, prevention of the satellite

droplets, etc. are neglected in the current analysis. A complete analysis of the complex heat and mass transfer processes coupled with a flow analysis of falling film is not available in the literature. In addition, the current literature also lacks numerical and experimental flow analysis of a falling film over an irregular mesh. An experimental study is currently being conducted by the authors to compare the performance of the proposed and horizontal tube-type falling film absorber designs. It will help in considering the complex phenomena that were unaccounted for in this numerical scheme.

Nomenclature

A = area, m^2
B = length of the coolant tube, m
C_P = specific heat, kJ/kg K
D_{aw} = volumetric diffusivity, m^2/s
D = diameter of the coolant tube, m
D_h = hydraulic diameter, m
dm = mass flux transferred, kg/s
g = acceleration due to gravity, m/s^2
H = enthalpy, kJ/kg
h = heat transfer coefficient, $kW/m^2 K$
K = mass transfer coefficient, $kmol/m^2 s$
k = thermal conductivity, W/m K
L = length of the coolant tube assembly, m
M = molecular weight, kg/kmole
m = mass flow rate, kg/s
P = total absolute pressure, Pa
Pr = Prandtl number, $\mu C_p/k$
Q = heat transfer, kW
$\mathrm{Re}_{\mathrm{film}}$ = Reynolds number for falling film, $4\Gamma/\mu$
$\mathrm{Re}_{\mathrm{film1}}$ = Reynolds number for falling film, $400V/B\ \nu$
Re_{D_O} = Reynolds number for flow over the coolant tube, $\rho u D_O/\mu$
Sc = Schmidt number, $\mu/\rho D_{aw}$
T = absolute temperature, K
U = overall heat transfer coefficient, $kW/m^2 K$
V = volumetric flow rate, l/min
u = velocity, m/s
x = mass fraction of ammonia in the liquid phase
y = mass fraction of ammonia in the vapor phase
$\tilde{x}$ = mole fraction of ammonia in the liquid phase
$\tilde{y}$ = mole fraction of ammonia in the vapor phase
z = mole fraction of ammonia in the absorbing/desorbing vapor flux

Greek Symbols

δ = falling film thickness, m
μ = dynamic viscosity, kg/m s, $N\,s/m^2$
ν = kinematic viscosity, m^2/s
ρ = density, kg/m^3
Γ = mass flow rate of falling film per unit periphery, kg/m s

Subscripts

C = coolant
film = falling film
film1 = falling film
H_2O = water
i = interface
L = liquid phase
mesh = mesh
NH_3 = ammonia
O = outside
tube = coolant tube
V = vapor phase

Superscripts

* = modified

References

[1] Killion, J. D., and Garimella, S., 2001, "A Critical Review of Models of Coupled Heat and Mass Transfer in Falling-Film Absorption," Int. J. Refrig., **24**, pp. 755–797.
[2] Yang, R., and Jou, D., 1995, "Heat and Mass Transfer of Absorption Process for the Falling Film Flow Inside a Porous Medium," Int. J. Heat Mass Transfer, **38**, pp. 1121–1126.
[3] Benzeguir, B., Setterwall, F., and Uddholm, H., 1991, "Use of a Wave Model to Evaluate Falling Film Absorber Efficiency," Int. J. Refrig., **14**, pp. 292–296.
[4] Miller, W. A., and Perez-Blanco, H., 1993, "Vertical-Tube Aqueous LiBr Falling Film Absorption Using Advanced Surfaces," *ASME Transaction of International Absorption Heat Pump Conference*, ASME, New York, Vol. 31, pp. 185–202.
[5] Schwarzer, B., Rahbar, M. S., and LeGoff, P., 1993, "A Novel Type of Falling Film Heat and Mass Exchanger," *ASME Proc. of International Absorption Heat Pump Conference*, ASME, New York, Vol. 31, pp. 179–183.
[6] Isshiki, N., Ogaka, K., and Sasaki, K., 1988, "Studies on Mechanism and Enhancement of Absorption Heat and Mass Transfer," *Absorption Heat Pumps*, Proc. of Workshop by Commission of the European Communities, Luxembourg: Commission of the European Communities, London, pp. 399–408.
[7] Kashiwagi, T., 1985, "The Activity of Surfactant in High-Performance Absorber and Absorption Enhancement," Refrigeration, **60**, pp. 72–79.
[8] Hozawa, M., Inoue, M., Sato, J., and Tsukada, T., 1991, "Marangoni Convection During Steam Absorption into Aqueous LiBr Solution With Surfactant," J. Chem. Eng. Jpn., **24**, pp. 209–214.
[9] Kim, K. J., Berman, N. S., and Wood, B. D., 1996, "The Interfacial Turbulence in Falling Film Absorption: Effects of Additives," Int. J. Refrig., **19**, pp. 322–330.
[10] Kulankara, S., and Herold, K. E., 2000, "Theory of Heat/Mass Transfer Additives in Absorption Chillers," HVAC&R Res., **6**, pp. 369–380.
[11] Garimella, S., 2000, "Microchannel Components for Absorption Space-Conditioning Systems," ASHRAE Trans., **106**, pp. 453–462.
[12] Meacham, J. M., and Garimella, S., 2003, "Modeling of local Measured Heat and Mass Transfer Variations in a Microchannel Ammonia-Water Absorber," ASHRAE Trans., **109**, pp. 412–422.
[13] Islam, R., Md., Wijeysundera, N. E., and Ho, J. C., 2003, "Performance Study of a Falling-Film Absorber With a Film-Inverting Configuration," Int. J. Refrig., **26**, pp. 909–917.
[14] Kang, Y. T., Akisawa, A., and Kashiwagi, T., 2000, "Analytical Investigation of Two Different Absorption Modes: Falling Film and Bubble Types," Int. J. Refrig., **22**, pp. 640–649.
[15] Schweitzer, P. A., 2000, *Mechanical and Corrosion-Resistant Properties of Plastics and Elastomers—Corrosion Technology*, Marcel Dekker, New York.
[16] Schweitzer, P. A., 1998, *Encyclopedia of Corrosion Technology*, Marcel Dekker, New York.
[17] Fujita, H., Takahama, H., Yabashi, H., and Takagi, K., 1980, "Effects of Wall Roughnesses on Heat and Mass Transfer in Countercurrent Flow of Air and Water Film," Heat Transfer-Jpn. Res., **9**, pp. 42–53.
[18] Treybal, R. E., 1980, *Mass Transfer Operations*, McGraw-Hill, New York.
[19] Chilton, T. H., and Colburn, A. P., 1934, "Mass Transfer (Absorption) Coefficients," Ind. Eng. Chem., **26**, pp. 1183–1187.
[20] Yih, S. M., and Chen, K. Y., 1982, "Gas Absorption into Wavy and Turbulent Falling Liquid Films in a Wetted-Wall Column," Chem. Eng. Commun., **17**, pp. 123–136.
[21] Incropera, F. P., and DeWitt, D. P., 2002, *Fundamentals of Heat and Mass Transfer*, 5th Edition, Wiley, New York.
[22] Shah, R. K., and London, A. L., 1978, *Laminar Flow Forced Convection in Ducts*, Academic Press, New York.
[23] Yih, S. M., 1986, "Modeling Heat and Mass Transport in Falling Liquid Films," *Handbook of Heat and Mass Transfer: Mass Transfer and Reactor Design*, N. P. Cheremisinoff, eds., Gulf Publishing Company, Houston, pp. 111–120.
[24] Goel, N., Goswami, D. Y., 2005, "Analysis of a Counter-Current Vapor Flow Absorber," Int. J. Heat Mass Transfer, **48**, 1283–1292.
[25] Herold, K. E., Radermacher, R., and Klein, S. A., 1996, *Absorption Chillers and Heat Pumps*, CRC Press, Boca Raton.
[26] Herbine, G. S., and Perez-Blanco, H., 1995, "Model of an Ammonia-Water Bubble Absorber," ASHRAE Trans., **101**, pp. 1324–1332.
[27] Perez-Blanco, H., 1988, "A Model of an Ammonia-Water Falling Film Absorber," ASHRAE Trans., **94**, pp. 467–483.
[28] Kim, B., 1998, "Heat and Mass Transfer in a Falling Film Absorber of Ammonia-Water Absorption Systems," Heat Transfer Eng., **19**, pp. 53–63.

Heat Transfer and Pressure Drop Characteristics of Laminar Flow in Rectangular and Square Plain Ducts and Ducts With Twisted-Tape Inserts

S. K. Saha[1]
Mechanical Engineering Department, Bengal Engineering and Science University, Shibpur Howrah 711 103, West Bengal, India
e-mail: sujoy_k_saha@hotmail.com

D. N. Mallick
Applied Mechanics and Drawing Department, Bengal Engineering and Science University, Shibpur Howrah 711 103, West Bengal, India
e-mail: dnmbec@mailcity.com

The present paper reports the results of an experimental investigation of the heat transfer and pressure drop characteristics of laminar flow of viscous oil through horizontal rectangular and square plain ducts and ducts inserted with full-length twisted tapes, short-length twisted tapes, and regularly spaced twisted-tape elements. Isothermal pressure drop measurements were taken in acrylic ducts. Heat transfer measurements were taken in electrically heated stainless-steel ducts imposing uniform wall heat flux boundary conditions. The duct aspect ratios AR were 1, 0.5, and 0.333. The twist ratios of the twisted tapes were y=2.692, 5.385, 2.597, 5.193, 2.308, and 4.615. Short-length tapes were 0.9, 0.7, and 0.5 times the duct length. The space ratios were s=2.692, 5.385, 2.597, 5.193, 2.308, and 4.615. Both friction factor and Nusselt number increase with decreasing y and AR for AR≤1 and increasing Re, Sw, and Pr. As the tape-length decreases, both friction factor and Nusselt number decrease. Friction factor increases as s decreases, and Nusselt number increases as s increases. Isothermal friction factor correlation and comprehensive Nusselt number correlation have been developed to predict data reasonably well in the entire range of parameters. Performance evaluation says that short-length twisted tapes are worse and regularly spaced twisted-tape elements are better than the full-length twisted tapes. [DOI: 10.1115/1.2010493]

Keywords: Convection, Laminar Flow, Twisted-Tape, Heat Transfer Augmentation, Swirl Flow, Uniform Wall Heat Flux

Introduction

Full-length twisted tapes as shown in Fig. 1(*a*) are used for laminar flow heat transfer augmentation. Date and Singham [1], Date [2], and Hong and Bergles [3] investigated heat transfer enhancement in laminar viscous liquid flows in tubes with uniform wall heat flux (UWHF). Additional data for UWHF condition have been reported for laminar flows of air [4] and oil [5]. Manglik and Bergles [6] analyzed, numerically, the laminar flow heat transfer in a semicircular tube with uniform wall temperature (UWT) defining the lower bound of heat transfer augmentation in circular tubes with twisted-strip inserts. Carlson et al. [7] observed the favorable effect of the twisted-tape inserts for augmenting the heat transfer rate in liquid metal reactor steam generators. Sukhatme et al. [8] reported as high as 44% of total heat transfer due to the tape-fin effect for laminar flow of a high Pr (~700) fluid. Saha et al. [9] have considered regularly spaced twisted-tape elements connected by thin circular rods as shown in Fig. 1(*b*). Date and Saha [10] numerically solved the Navier-Stokes and energy equations in their three-dimensional parabolic form and predicted the friction and heat transfer characteristics for laminar flow in a circular tube fitted with regularly spaced twisted-tape elements, which are connected by thin circular rods. Patil [11] studied the friction and heat transfer characteristics of laminar swirl flow of a pseudoplastic-type power-law fluid in a circular tube using varying width full-length twisted tapes under a uniform wall temperature condition. Saha et al. [12] have experimentally studied the friction and heat transfer characteristics of laminar swirl flow through a circular tube fitted with regularly spaced twisted-tape elements. Saha and Dutta [13] have made an experimental study of laminar swirl flow through a circular tube fitted with twisted tapes. Manglik et al. [14] have worked in the scaling and correlation of low Reynolds number swirl flows and friction factors in circular tubes with twisted-tape inserts. Manglik and Bergles [15] developed comprehensive correlations for friction factor and Nusselt number for laminar flow with twisted-tape inserts in isothermal tubes.

In all the above-cited literature, the investigation was carried out for flow through a circular tube with twisted-tape inserts. In this paper experimental results of pressure drop and heat transfer measurements of laminar flow in rectangular and square plain ducts and ducts with twisted tapes, along with the correlations for friction factor and Nusselt number, are reported. Duct aspect ratio, tape twist ratio, space ratio, Reynolds number, swirl parameter, Prandtl number and Grashoff number govern the heat transfer and pressure drop characteristics, which are quantitatively represented by Nusselt number and friction factor.

Experimental Setup, Operating Procedure and Data Reduction

A schematic diagram of the experimental setup is shown in Fig. 2. The setup consists of (i) a storage tank in which the working fluid is stored, (ii) a working fluid circulating loop, (iii) the test section, (iv) the calming section, (v) an accumulator, and (vi) a cooling water supply system. The working fluid was circulated through the loop by a gear pump driven by a 2 kW electric motor.

[1]Corresponding author.

Contributed by the Heat Transfer Division for publication in the JOURNAL OF HEAT TRANSFER. Manuscript received: June 11, 2004; Final manuscript received November 21, 2004. Review conducted by: John H. Lienhard V.

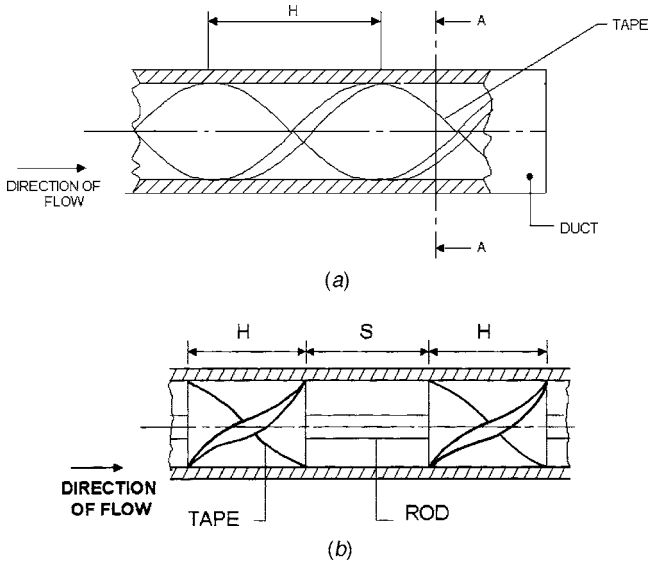

Fig. 1 (*a*) Full-length twisted-tape insert inside a duct and (*b*) regularly spaced twisted-tape elements

The working fluid was stored in a storage tank of 70 l capacity. The storage tank was a rectangular box made of mild steel. Its length, breadth, and height were 0.9, 0.395, and 0.5 m, respectively. The level of the fluid in the storage tank was indicated by a glass level indicator. The working fluid was heated by a 2 kW heater in the storage tank. The heater wires were connected through autotransformers so that the heating rate could be adjusted and the fluid could be heated to the desired temperature level. The working fluid passed through one of the two calibrated rotameters, the calming section to allow the velocity profile to develop fully at the entry to the test section where the heat addition took place, a mixing chamber for thorough mixing of the fluid, a heat exchanger coil for removal of heat, and a weighing platform before the fluid returned to the reservoir. An accumulator in the circulating loop limited fluctuation of the pressure. A pressure gage indicated the delivery pressure of the pump. Isothermal pressure drop measurements were taken in 3.05 m long acrylic ducts. The heat transfer test section is shown in Fig. 3. It was a

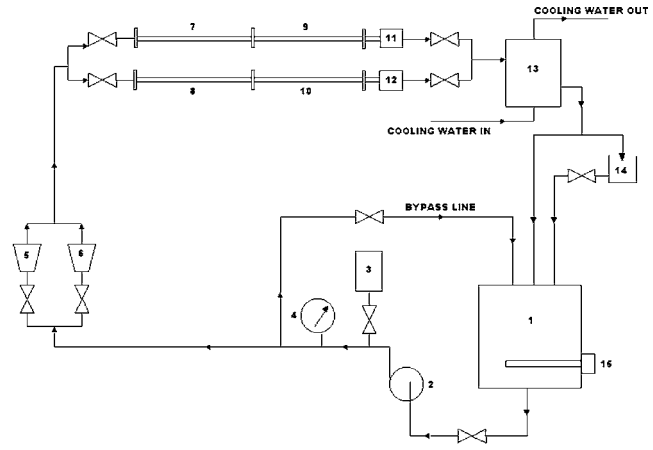

Fig. 2 Schematic diagram of the experimental setup

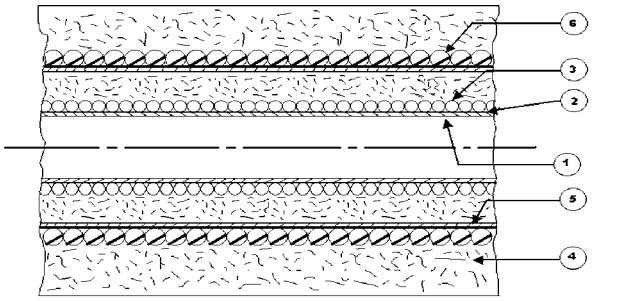

Fig. 3 Heat transfer test section

smooth 18/8 stainless-steel duct. The test section was 2 m long. The test section was heated electrically by wrapping uniformly two nichrome heater wires (20 gage and 1.65 Ω/m) of identical length in parallel. The resistance of each wire was 30.385 Ω. The geometry information and range of parameters are given in Table 1. Porcelain beads on the heater wires ensured that the heater wires were electrically insulated from the test sections. The inlet and outlet bulk-mean temperatures of the fluid were measured by thermocouples (placed in wells 5 cm upstream from the inlet and 20 cm downstream from the outlet of the test section). The mixing chamber at the exit of the test section was meant for thorough mixing of the circulating fluid. The mixing chamber consisted of a rectangular box of mild steel with rectangular plates arranged inside in such a fashion that the working fluid moved in a tortuous path to give a uniform temperature along the cross section. In addition, five mixing baffles made out of brass sheet were mounted on a thin rod at fixed intervals and these were inserted

Table 1 Geometry information and range of parameters

Width of Duct : 13 mm (for all ducts)
Depth of Duct :
square duct – 13 mm (AR = 1)
rectangular duct --- 26 mm (AR = 0.5), 39 mm (AR=0.333)
Length of Duct :
Pressure Drop Tests : 3.05 m
Heat Transfer Tests : 2 m
Data have been generated for :
Hydraulic diameter, D_h = 13 mm, 17.33 mm, 19.50 mm
Aspect ratio, AR = 1, 0.5, 0.333
Twist ratio, y = 2.692, 5.385, 2.597, 5.193, 2.308, 4.615
Space ratio, s = 2.692, 5.385, 2.597, 5.193, 2.308, 4.615
Twisted-Tape length, l = 1, 0.9, 0.7, 0.5
Mass flow rate, $\dot{m}$ -- 1.185 – 42.050 kg / min
Reynolds number, Re --- 30 < Re < 1100
Prandtl number, Pr --- 80 < Pr < 500
Heat flux, q" -- 1105 – 29461 W / m^2
$\Delta T_b = T_{bo} - T_{bi}$ --- 2 – 20°C
$\Delta T = T_{wi} - T_b$ --- 1.5 – 25°C

into the pipe just before the inlet of the mixing chamber. Each brass sector occupied $\sim\frac{3}{4}$ of the cross-sectional area of the duct. A three-junction thermopile was used to accurately record the temperature rise of the working fluid in the test section. A copper duct having the same hydraulic diameter as that of the test section and of length 2.25 m was used as the calming section.

In order to reduce axial conduction of heat at the ends of the test section, Teflon® spacer disks of thickness 3 cm each were used on either side of the test section. The spacers were bored and finished to match the test-section dimensions. Teflon bushes fixed at pitch circle holes of the mild steel flanges eliminated metal-to-metal contact and minimized heat loss by conduction. Thus the test section was thermally insulated from the rest of the piping.

The heat transfer test section had 28 thermocouples brazed at seven axial positions (each axial position had four thermocouples, one each at the middle of four edges of the cross section) on the outer surface of the duct wall to measure its temperature. The thermocouples were of 34 gage copper-constantan wire. They were fabricated from a single roll, and the wire was calibrated at the ice and steam points. The performance of the thermocouples was checked. The axial positions of the thermocouples from the onset of heating along the downstream direction were 0.05, 0.5, 1.0, 1.25, 1.5, 1.75, and 1.95 m, respectively.

It may be noted that more thermocouples were located in the second half of the duct where the temperature profile was likely to be fully developed. Axial grooves 6 mm long, 1.5 mm wide, and 0.6 mm deep were cut at each circumferential position on the outer surface of the duct to facilitate brazing of the thermocouples. The thermocouple wires were covered with a plastic sleeve except for the first 12 cm near the duct wall where there were fine porcelain beads to withstand the high temperature of the wall. All the thermocouple wires at each axial position were bunched together and those were taken out radially to be connected to a 36 point selector switch box, which, in turn, was connected to a digital multimeter and a single cold junction at 0 °C. The test-section duct was first wrapped with glass fiber tape over which the heater wires with porcelain beads on them were wound. It was then covered with a layer of asbestos rope, which, in turn, was insulated with glass wool of thickness 120 mm to minimize heat loss in the radial direction.

The circulating fluid was cooled by water in a coil-in-shell heat exchanger. The shell was a cylindrical drum, 0.34 m dia and 0.4 m long, made of mild steel sheet. It had two openings, one at the bottom for coolant inlet and the other at the top for coolant outlet. The working fluid passed through a copper tube 10 mm i.d., 12 mm o.d., and 18 mm long, made into coaxial coils having 0.34 and 0.25 m pitch circle diameters. To augment the heat transfer coefficient between the coolant and the outer surface of the duct, the velocity of the coolant past the duct coils was increased by putting a closed empty cylinder drum (30 cm long and 22 cm dia) coaxially. Thus the copper duct coils were effectively placed in the annular space between the inner cylinder drum and the outer shell. The base of the inner drum was welded to three small pieces of rods, which, in turn, were welded to the bottom of the shell. The gaps between the shell and the inner drum at the top and bottom were equal, and these allowed coolant to flow without much pressure drop.

The cooling water supply system consisted of a reservoir, centrifugal pump, overhead tank, rotameter, bypass line, and a line from the overhead tank to the heat exchanger. Water from the reservoir was continuously pumped into the overhead tank at a rate slightly higher than the supply rate to the heat exchanger by regulating a bypass valve. The overflow line maintained the level of water in the overhead tank constant. The cooling water flow rate to the heat exchanger passed through a rotameter, and it was regulated by a valve.

The working fluid circulating loop had two rotameters to cover a wide range of flow rates. These rotameters gave a measure of the flow rate, and, accordingly, valves were adjusted to get the approximate desired flow rate. However, the actual flow rate was measured by collecting the working fluid in a container placed on the platform of a weighing machine. The time of collection was recorded by a stop watch. The whole pipeline through which the working fluid passed was covered with glass wool, and special care was taken in insulating the calming and test sections. To ensure that the test section ran full at low flow rates, the pipeline after the mixing chamber rose vertically for ~200 mm above the level of the test section.

On the delivery side of the pump, an accumulator was fixed to the pipeline through a gate valve to minimize the pressure fluctuation. This ensured a uniform flow rate of the working fluid. The accumulator was cylindrical in shape and made of mild steel sheet. It was 0.35 m long and 0.2 m dia. A pressure gage fitted to the pipeline next to the accumulator showed the delivery pressure of the pump. The bypass valve in the working fluid loop was adjusted so that the delivery pressure of the pump did not exceed the design working pressure of the pump.

There were ten pressure taps made of small pieces of acrylic tubes. The twisted tapes were made in the laboratory from a 0.5 mm thick stainless-steel strip. The two ends of a strip were held on a lathe, one at the headstock end and the other at the tail-stock end by special devices made in the laboratory. The strip was then subjected to twist by turning the chuck manually. The twisted-tape was made red hot to relieve stress and again subjected to twist. By alternately heating and subjecting it to a certain amount of twist, the desired twist ratios were obtained. During the process of making twisted tapes, failure due to buckling and distortion had occasionally occurred. The short-length tape extended up to a non-dimensional length l as given in Table 1. The space length s in regularly spaced twisted-tape elements is also given in Table 1. Successive tapes along the duct in regularly spaced twisted-tape elements were aligned with respect to each other. The tape-fin effect was eliminated by covering the twisted tapes with insulating tapes before these were inserted into the test section.

After the experimental setup was assembled, the storage tank was filled with the working fluid so that both the heaters were immersed in oil. The loop was then checked for leaks. Preliminary experiments were carried out to check the reliability of the thermocouples. Heaters in the oil reservoir were switched on, and oil was pumped through the test section without any heat input to it. The cooling water was circulated through the heat exchanger. When the steady state was reached after a few hours, all the thermocouple readings were taken and these were found to match with each other within a few microvolts. In an experimental run, the pump was switched on and the heat input to the storage tank was set to the desired level to bring the oil to a predetermined temperature. The oil flow rate was controlled to the desired value by adjusting the valves, and the approximate flow rate was obtained from the rotameter. The heaters to the test section were then switched on, and the required heat input was supplied by adjusting the variable autotransformers. During the experiments, only some predetermined heat inputs were supplied in order to get some particular values of heat fluxes. The cooling water pump was switched on and the valve controlling the flow of water to the heat exchanger was operated to give a desired flow rate. The bypass valve was also adjusted so that water trickled down the overflow line continuously, and the water level in the overhead tank remained constant. The oil temperature at the inlet to the test sections was controlled by adjusting the heat input to the reservoir and the cooling water flow rate to the heat exchanger.

A steady state was usually obtained after 5–6 h. In this state, all the thermocouple readings were noted. The mass flow rate was measured by collecting the fluid in a container placed on the platform of a weighing machine for 1 min. The power input to the test section was obtained from calibrated wattmeters.

The fluid thermodynamic and transport properties were evaluated by the interpolating polynomials developed from the properties at discrete points given by the oil supplier, Indian Oil Corpo-

ration. The friction factors were calculated from the pressure drop measured by manometer. The net heat input to the fluid was determined by correcting the electrical heat input for losses in the leads and for heat losses through the insulation. The enthalpy rise of the fluid was calculated. The set of data taken in a run was accepted only if the difference between the net heat input and the enthalpy rise was $<5\%$. In such a case the actual heat input to the test section was taken as the average of the two. The bulk temperature of the fluid at any axial position at a distance from the inlet was computed by assuming a linear temperature variation along the length. The inner wall temperatures were determined from the measured values of the outer wall temperatures by applying the one-dimensional heat conduction equation. The peripherally averaged inner wall temperature at any axial position was taken as the arithmetic mean of the inner wall temperatures at that axial position. The heat transfer coefficient at any axial position was determined from the heat flux based on the inner surface area, the average inner wall temperature, and the calculated bulk temperature at that axial position. The local Nusselt numbers were axially averaged by Simpson's rule of numerical integration. The properties of the fluid were evaluated at the bulk mean temperature. Uncertainty analysis as shown in the Appendix was carried out as suggested by Kline and McClintock [16], and the uncertainty involved in the estimation of friction factor and Nusselt number were within ±5% and ±8%, respectively.

Results and Discussion

Initially it was suggested that the swirl flow effects can be captured by the parameter (Re/y) as it is done by Dean number in plain duct flow. However, the Dean number represents a balance of centrifugal, convective inertia, and viscous forces, whereas (Re/y) represents the centrifugal-viscous force ratio. In twisted-tape flows, the centrifugal force due to helically swirling flow and the convective inertia of the bulk axial flow are balanced by the viscous force and, consequently, Sw (the swirl parameter) is defined as shown below, the reference velocity being the actual swirl flow velocity at the duct wall, which directly influences the shear stress. On the basis of the solid-body rotation, the swirl velocity V_s is represented by its axial and tangential velocity components. This is in concurrence with the forced-vortex flow considerations. These velocities are related to the mass flow rate and the tape geometry.

The present experimental program has been carried out in four parts. Data have been generated for the following cases:

1. Short-length twisted-tape friction factor. Full-length twisted tapes have also been considered.
2. Short-length twisted-tape Nusselt number. Full-length twisted tapes have also been considered.
3. Regularly spaced twisted-tape elements friction factor.
4. Regularly spaced twisted-tape elements Nusselt number.

Confirmatory tests have been carried out for the experimental setup with plain circular duct, circular duct with full-length straight tape ($y=\infty$), and full-length twisted-tape with finite tape twist ($y<\infty$). The experimental setup was validated by the satisfactory data. Figure 4 shows a comparison of the present experimental data for a plain circular duct with the correlation of Bandyopadhyay et al. [5] in the measured ranges of parameters. The maximum percentage deviation is ±12.8% whereas 85% of the data lie within ±6% of the prediction. It should be noted that in Fig. 4 the contribution of the forced convection has been neglected as it was very small compared to that of free convection in the range of validity of the correlation.

It has been observed both experimentally and theoretically [9,10] that twisted tapes with twist ratios of >5.0 do not generate sufficient swirl intensity and, therefore, twist ratios of >5.0 have not been considered in the present investigation. Twist ratios of <2.5 cause buckling of twisted tapes quite frequently while

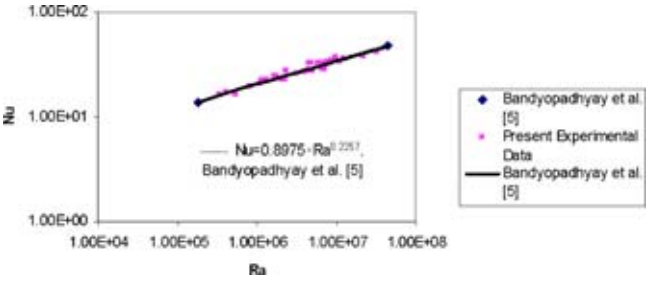

Fig. 4 Comparison of present experimental plain circular duct data with Bandyopadhyay et al. [5]

manufacturing and, therefore, twist ratios of <2.5 have not been considered. Full-length twisted tapes have been considered for all the cases of aspect ratios and twist ratios as a benchmark and as a comparison of full-length twisted tapes vis-à-vis short-length twisted tapes. In the case of short-length twisted-tape-generated swirl flow, the swirl gradually developed from zero intensity at the duct entrance to its full intensity as the flow progressed in the downstream direction. Thereafter, the swirl decayed as the fluid came out of the twisted-tape zone and the straight flow tended to gradually set in.

In all the cases, for $\mathrm{Sw}<100$, $(f\mathrm{Re})_{sw}$ showed an asymptotic trend and this increased only after $\mathrm{Sw}>100$. This shows, for $\mathrm{Sw}<100$, the swirl intensity is not very high and the flow behaves like a laminar flow in a smooth plain duct. The pressure drop measurements clearly showed the existence of decaying swirl flow in the case of short-length twisted-tape and periodically fully developed swirl flow in the case of regularly spaced twisted-tape elements after a few cycles of tape-rod assembly. There was only 3–5% of maximum wall temperature variation in peripheral outside wall temperatures measured at four locations in an axial station. The measured temperature variation thermally confirmed fully developed periodic swirl flow after a few cycles of tape-rod assembly in the case of regularly spaced twisted-tape elements.

Short-Length Twisted-Tape Friction Factor Results.

Effect of Twist Ratio. Figures 5 and 6 show the effects of twist ratio y on friction factor. Friction factor increases as the twist ratio decreases, i.e., the tape-twist increases for a given twisted-tape length and the aspect ratio since the swirl intensity increases and the friction surface area increases. However, the increase in friction factor is not very large since $y=5.0$ does not make a very large difference in swirl intensity from that in the case with $y=2.5$, and the velocity profile does not get much flatter in case of $y=5.0$ than that in the case of $y=2.5$.

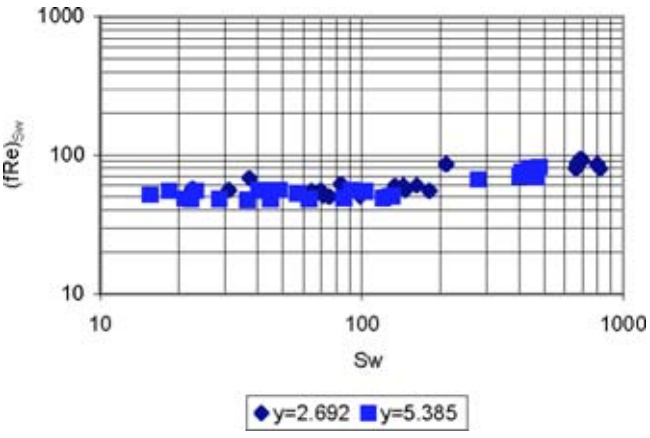

Fig. 5 $(f\mathrm{Re})_{sw}$ versus Sw—l=1, AR=1

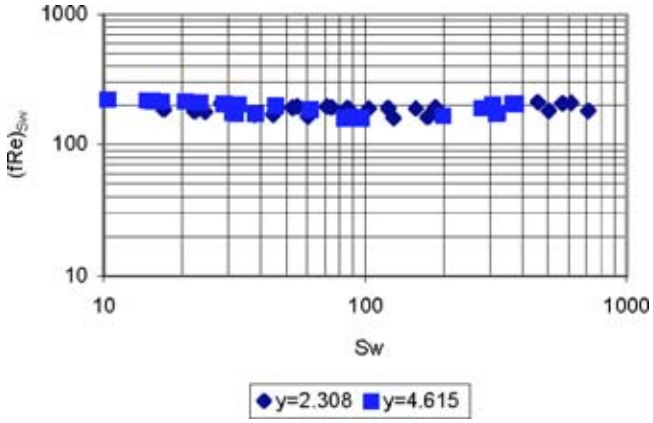

Fig. 6 $(fRe)_{sw}$ versus Sw—l=0.5, AR=0.333

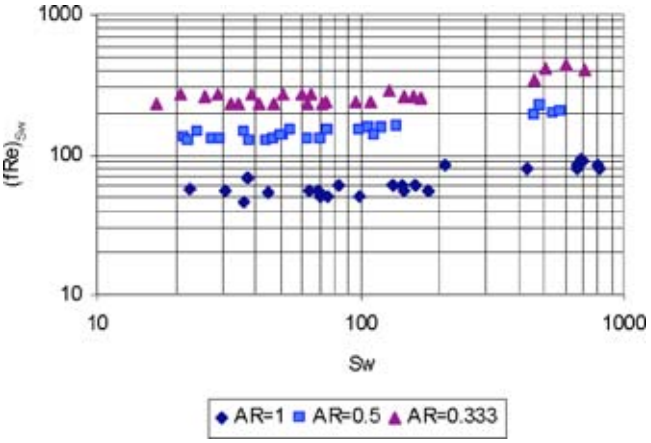

Fig. 9 $(fRe)_{sw}$ versus Sw—y=2.532, l=1

Effect of Twisted-Tape Length. Figures 7 and 8 show the effects of twisted-tape length l on friction factor. Friction factor decreases as the twisted-tape length decreases for a given twist ratio and aspect ratio, since the friction surface area decreases and the swirl decays early and perhaps straight flow sets in. It is also observed that the larger the tape length, the more prominent the effect of tape length, and as the twisted-tape becomes shorter beyond a certain point, the effect of tape length is not very palpable because the effect of swirl developed to its full intensity is more important than the frictional surface area. Figures 7 and 8 also show that the tighter the tape is twisted the more prominent the effect of twisted-tape length since the swirl persists further downstream of the twisted-tape, and the setting-in of straight flow is delayed.

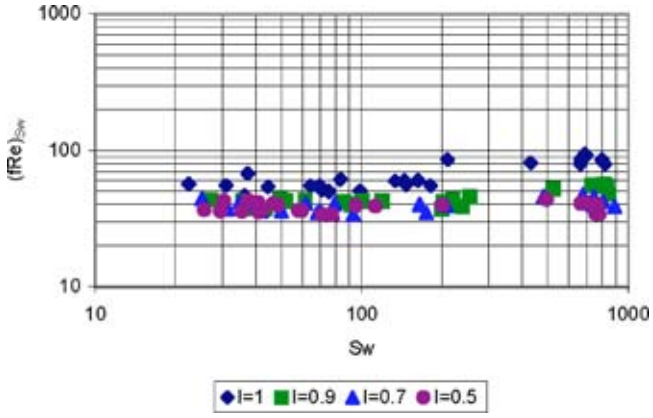

Fig. 7 $(fRe)_{sw}$ versus Sw—AR=1, y=2.692

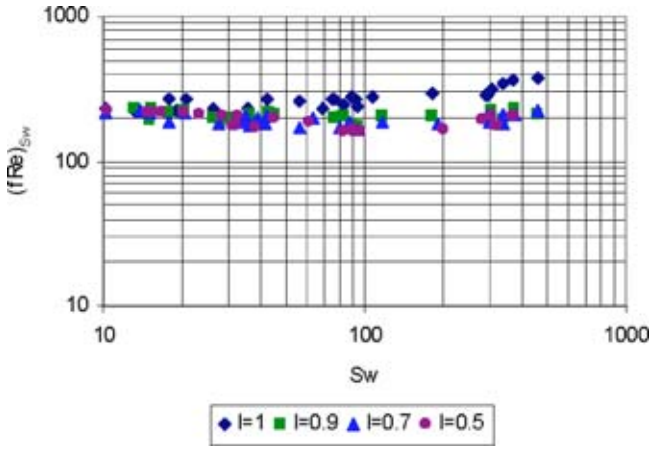

Fig. 8 $(fRe)_{sw}$ versus Sw—AR=0.333, y=4.615

Effect of Duct Aspect Ratio. Figures 9 and 10 show the effect of aspect ratio of the duct on friction factor. It is observed that the effect of aspect ratio is, by far, the most prominent and is extremely palpable. As the aspect ratio ($\leqslant$1) decreases, the friction factor increases for a given twist ratio and twisted-tape length; and this effect is evenly palpable irrespective of the values of twist ratio and tape length. This can be appreciated since the lower the aspect ratio, the more the mixing of the more asymmetric velocity profiles and the secondary motion and associated momentum loss.

Nusselt Number Results. The heat transfer experiments were conducted for all the cases as it was done for pressure drop measurements. Figures 11–16 show the effects of twist ratio, twisted-tape length, and duct aspect ratio on Nusselt number. All observations for heat transfer measurements are generally true in a similar way as those were for pressure drop measurements. However, it is observed that the effect of duct aspect ratio is not as conspicuous as it was in the case of pressure drop measurements. This is because in the moderate Prandtl number range, as in the present investigation, the thermal boundary layer is very thin and the duct aspect ratio does not have significant effect on thermal boundary layer thickness and the consequent convective thermal resistance.

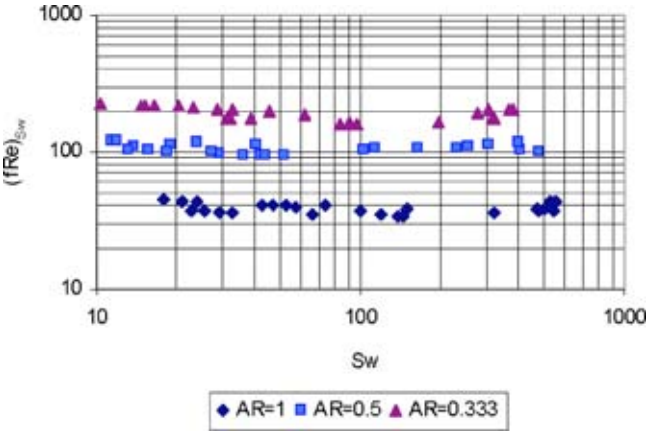

Fig. 10 $(fRe)_{sw}$ versus Sw—y=5.064, l=0.5

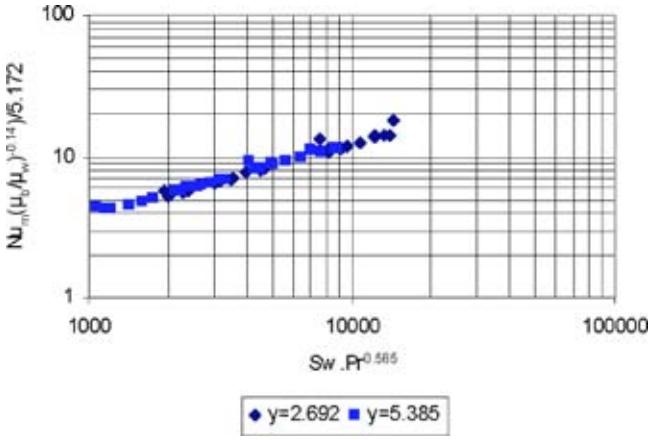

Fig. 11 $Nu_m[(\mu_b/\mu_w)^{-0.14}]/5.172$ **versus** $(Sw.Pr)^{0.565}$, $l=1$, AR $=1$

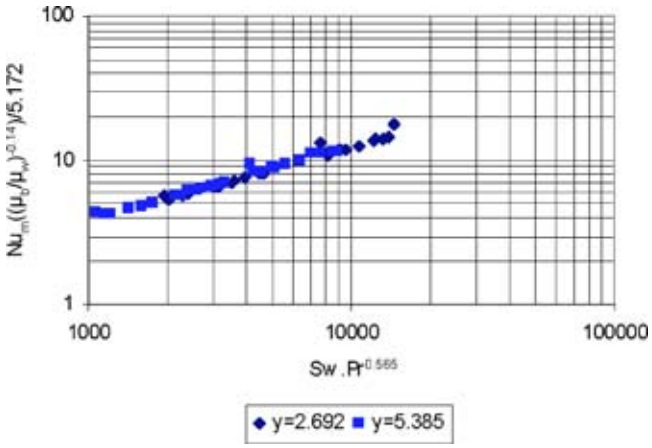

Fig. 12 $Nu_m[(\mu_b/\mu_w)^{-0.14}]/5.172$ **versus** $(Sw.Pr)^{0.565}$, $l=0.5$, AR $=0.333$

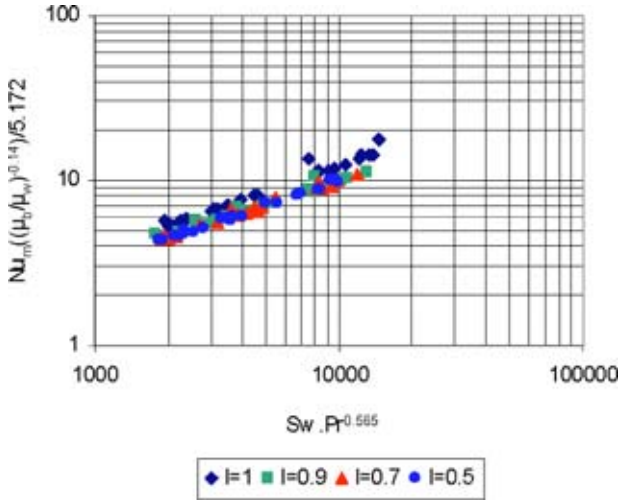

Fig. 13 $Nu_m[(\mu_b/\mu_w)^{-0.14}]/5.172$ **versus** $(Sw.Pr)^{0.565}$, AR$=1$, y $=2.692$

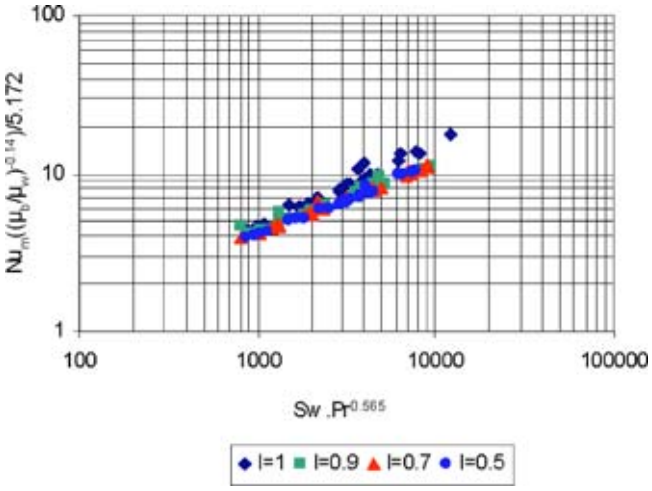

Fig. 14 $Nu_m[(\mu_b/\mu_w)^{-0.14}]/5.172$ **versus** $(Sw.Pr)^{0.565}$), AR $=0.333$, $y=4.615$

Regularly Spaced Twisted-Tape Element Friction Factor Results. It has been established [9,10] that $s>5.0$ does not give any better result for regularly spaced twisted-tape elements, and, consequently, $s>5.0$ has not been considered.

Effect of Duct Aspect Ratio. Figure 17 shows the effect of duct aspect ratio on friction factor, and it is observed that, for a given y and s, the friction factor increases with the decrease of the duct aspect ratio (<1). Friction factor sharply increases when aspect ratio decreases from unity to 0.5. However, friction factor does not increase as much when aspect ratio decreases from 0.5 to 0.333. This observation is true for all y and s. This is because as the aspect ratio decreases from unity up to a certain value, the secondary flow causes vigorous mixing and a consequent increase in pressure drop; this effect is not very conspicuous when the duct aspect ratio continues to decrease beyond that.

Effect of Twist Ratio. Figure 18 shows the effect of twist ratio on friction factor. For given aspect and space ratios, the friction factor increases with decreasing twist ratio; although the increase is not very sharp. This is quite palpable and precludes any further explanation.

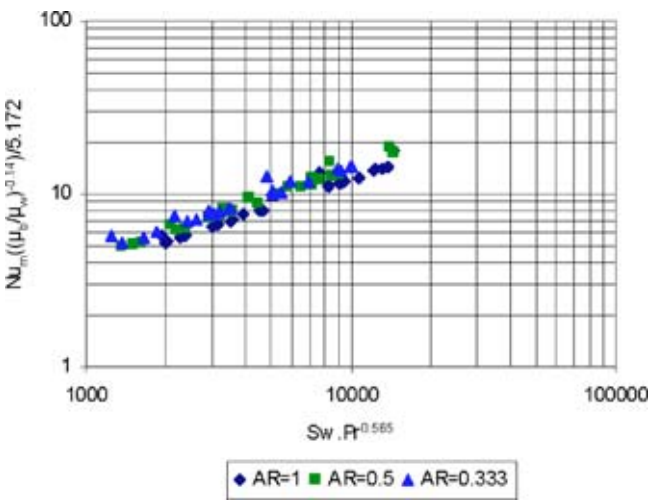

Fig. 15 $Nu_m[(\mu_b/\mu_w)^{-0.14}]/5.172$ **versus** $(Sw.Pr)^{0.565}$, $y=2.532$, $l=1$

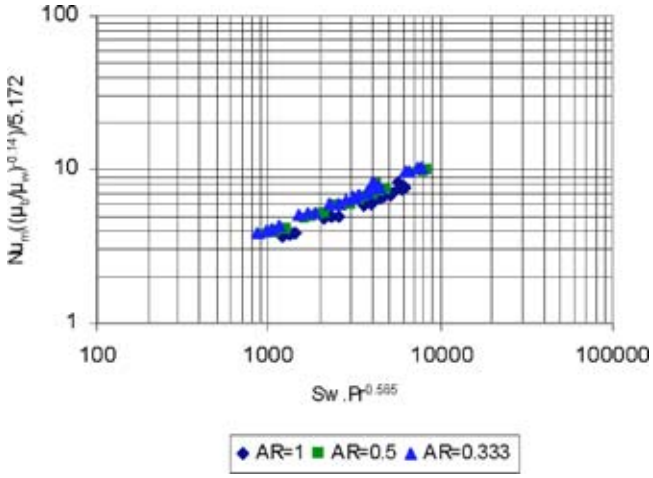

Fig. 16 $Nu_m[(\mu_b/\mu_w)^{-0.14}]/5.172$ **versus** $(Sw.Pr)^{0.565}$, $y=5.064$, $l=0.5$

Effect of Space Ratio. Figure 19 shows the effect of space ratio on friction factor. For a given twist ratio and aspect ratio, friction factor increases as s decreases because of more frequent mixing and associated momentum loss. Also, small s means a greater number of twisted-tape elements and friction surface and pressure loss.

Nusselt Number Results. Figures 20–22 show the effects of duct aspect ratio, twist ratio, and space ratio on Nusselt number,

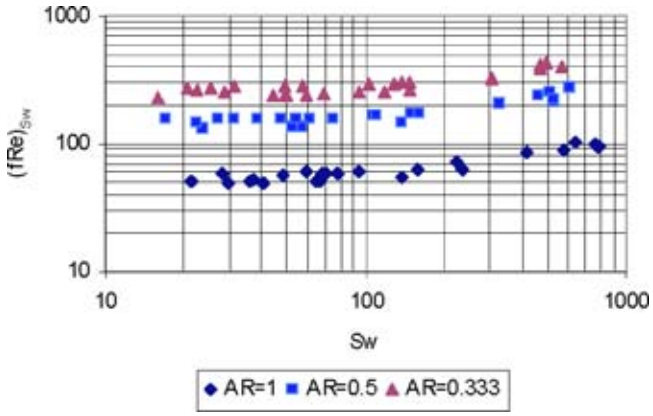

Fig. 17 $(fRe)_{sw}$ **versus Sw—**$y=2.532$, $s=2.532$

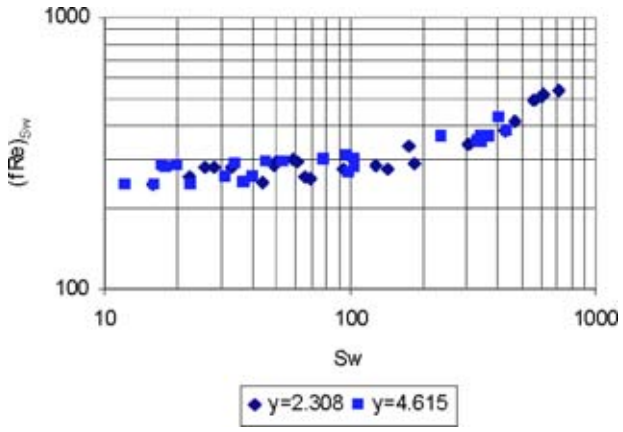

Fig. 18 $(fRe)_{sw}$ **versus Sw—**$s=4.615$, AR=0.333

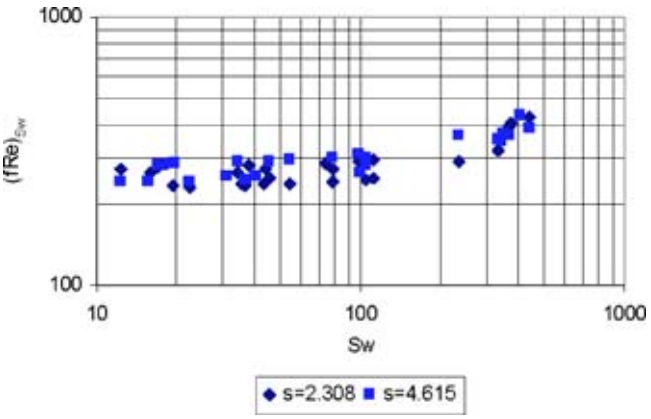

Fig. 19 $(fRe)_{sw}$ **versus Sw—**$y=4.615$, AR=0.333

respectively. All observations for heat transfer measurements are generally true in a similar way as those were for pressure drop measurements. However, it is observed that the effect of space ratio is reverse and more prominent than that was in the case of pressure drop measurements. Here, the Nusselt number increases with an increase in s for given aspect and twist ratios. This is

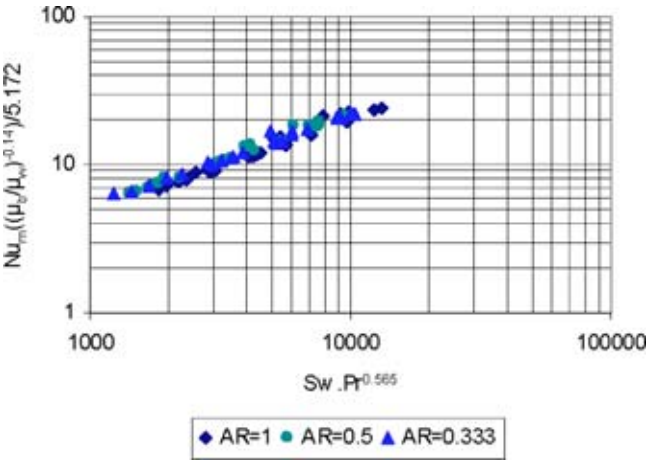

Fig. 20 $Nu_m[(\mu_b/\mu_w)^{-0.14}]/5.172$ **versus** $(Sw.Pr)^{0.565}$, $y=2.532$, $s=2.532$

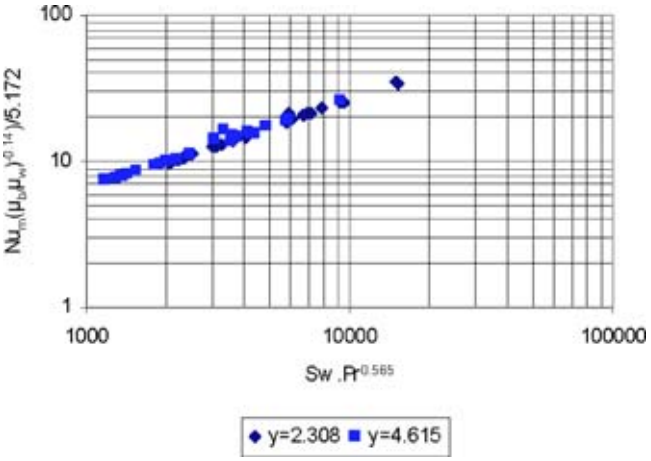

Fig. 21 $Nu_m[(\mu_b/\mu_w)^{-0.14}]/5.172$ **versus** $(Sw.Pr)^{0.565}$, $s=4.615$, AR=0.333

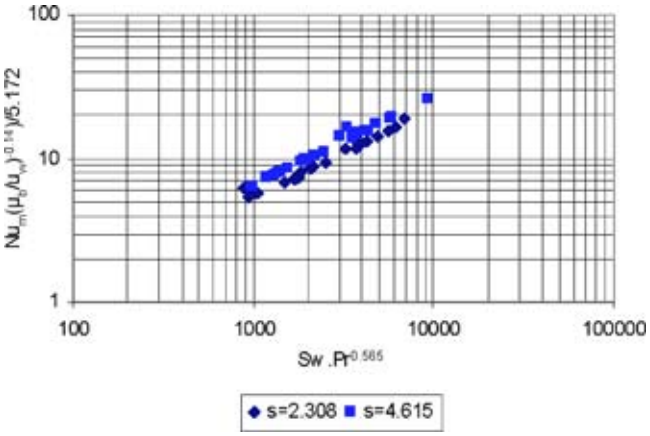

Fig. 22 $\mathrm{Nu}_m[(\mu_b/\mu_w)^{-0.14}]/5.172$ **versus** $(\mathrm{Sw}.\mathrm{Pr})^{0.565}$, $y=4.615$, $\mathrm{AR}=0.333$

because, for viscous flow as in the present case, the buoyancy force in the annular space region becomes more important than the decaying swirl flow.

Correlations

It has been discussed, in detail, by Manglik and Bergles [15] that the friction factor and the Nusselt number can be correlated by the swirl parameter Sw. For flows with high Gr or Ra and weak swirl flow effects, buoyancy-driven free convection appears. The secondary motions due to centrifugal and buoyancy forces are not complementary, and they tend to negate each other. Consequently, the relative magnitude of the force balance, i.e., the parameter $\mathrm{Gr}/\mathrm{Sw}^2$, determines the dominant flow phenomenon. For $\mathrm{Gr} \ll \mathrm{Sw}^2$, free convection effects dominate, and for $\mathrm{Gr} \gg \mathrm{Sw}^2$, pure swirl flow exists; this is analogous to the familiar $\mathrm{Gr} \gg \mathrm{Re}^2$ scale for forced and free convection in smooth plain duct flows. For a given flow rate, the swirl intensity is determined by the tape-twist pitch H (i.e., with small H) the centrifugal force dominates and the resulting swirl motion suppresses free convective circulation, and as $H \to \infty$, swirl motion diminishes and free convective effects dominate.

An asymptotic condition is approached when $\mathrm{Sw} \to 0$, which is identified by the limit $H \to \infty$ (i.e., a straight-tape insert) and is represented by hydrodynamically fully developed laminar flow in circular-segment duct. The correlations in the present investigation have been developed by log linear regression fit. The correlations are applicable in the measured ranges of parameters.

For square ducts as well as rectangular ducts of aspect ratio AR, the correlation has been found to be

$$(f\,\mathrm{Re})_{sw} = 17.355\left(\frac{\pi + 2 - 2\delta/D_h}{\pi - 4\delta/D_h}\right)^2 (1 + 10^{-6}\,\mathrm{Sw}^{2.67})^{1/7} R^{-1.46} \tag{1}$$

where $R=\mathrm{AR}$ for $\mathrm{AR} \leqslant 1$ and $R=1/\mathrm{AR}$ for $\mathrm{AR} > 1$. Equation (1) gives the correlation for isothermal fully developed friction factor for square and rectangular ducts having full-length twisted-tape inserts.

For short-length twisted-tape inserts inside square and rectangular ducts, the fully developed isothermal friction factor is correlated by log-linear regression fit as

$$(f\,\mathrm{Re})_{sw} = 17.355\left(\frac{\pi + 2 - 2\delta/D_h}{\pi - 4\delta/D_h}\right)^2 (1 + 10^{-6}\,\mathrm{Sw}^{2.67})^{1/7} \times [R^{-1.46}(1 + aX + bX^2 + cX^3)] \tag{2}$$

where $R=\mathrm{AR}$, for $\mathrm{AR} \leqslant 1$ and $R=1/\mathrm{AR}$ for $\mathrm{AR} > 1$ and

$$a = -8.51 \times 10^{-2} \quad b = 7.16 \times 10^{-3} \quad c = -2.81 \times 10^{-4}$$

and

$$X = (1 - l)^{0.2}\mathrm{Sw}^{0.425}$$

For regularly spaced twisted-tape element inserts inside square and rectangular ducts, the fully developed isothermal friction factor is correlated by log-linear regression fit as

$$(f\,\mathrm{Re})_{sw} = 17.355\left(\frac{\pi + 2 - 2\delta/D_h}{\pi - 4\delta/D_h}\right)^2 (1 + 10^{-6}\mathrm{Sw}^{2.67})^{1/7} \times [R^{-1.46}(1 + aX + bX^2 + cX^3)] \tag{3}$$

where $R=\mathrm{AR}$ for $\mathrm{AR} \leqslant 1$ and $R=1/\mathrm{AR}$ for $\mathrm{AR} > 1$ and

$$a = 2.86 \times 10^{-3} \quad b = -1.23 \times 10^{-5} \quad c = 1.45 \times 10^{-8}$$

and

$$X = \mathrm{Sw}^{0.425} s \exp(ds)$$

For constant wall heat flux applied to square and rectangular ducts fitted with full-length twisted tapes, the length-averaged Nusselt number correlation has been found by log-linear regression fit

$$\mathrm{Nu} = 5.172\{[(1 + 0.08932\mathrm{Gz}^{0.9125})^{2.5} + 8.2273 \times 10^{-6}(\mathrm{Sw}\,.\,\mathrm{Pr}^{0.565})^{2.655}]^{2.0} + 1.5638 \times 10^{-15}(\mathrm{Re}_{ax}\,.\,\mathrm{Ra})^{2.18}\}^{0.1}\left(\frac{\mu_b}{\mu_w}\right)^{0.14}(R + 0.1)^{0.15} \tag{4}$$

where $R=\mathrm{AR}$ for $\mathrm{AR} \geqslant 1$ and $R=1/\mathrm{AR}$ for $\mathrm{AR} < 1$.

For short-length twisted-tape inserts in square and rectangular ducts under constant wall heat flux, the length-averaged Nusselt number is correlated as

$$\mathrm{Nu} = 5.172\{[(1 + 0.08932\mathrm{Gz}^{0.9125})^{2.5} + 8.2273 \times 10^{-6}(\mathrm{Sw}\,.\,\mathrm{Pr}^{0.565})^{2.655}]^{2.0} + 1.5638 \times 10^{-15}(\mathrm{Re}_{ax}\,.\,\mathrm{Ra})^{2.18}\}^{0.1}\left(\frac{\mu_b}{\mu_w}\right)^{0.14} \times (R + 0.1)^{0.15} \times (1 + aX + bX^2 + cX^3) \tag{5}$$

where $R=\mathrm{AR}$ for $\mathrm{AR} \geqslant 1$ and $R=1/\mathrm{AR}$ for $\mathrm{AR} < 1$ and

$$a = -6.18 \times 10^{-3} \quad b = 4.15 \times 10^{-5} \quad c = -5.96 \times 10^{-8}$$

and

$$X = (1 - l)^{0.2}\mathrm{Sw}^{0.531}\mathrm{Pr}^{0.3}$$

For regularly spaced twisted-tape element inserts in square and rectangular ducts under constant wall heat flux, the length-averaged Nusselt number is correlated as

$$\mathrm{Nu} = 5.172\{[(1 + 0.08932\mathrm{Gz}^{0.9125})^{2.5} + 8.2273 \times 10^{-6}(\mathrm{Sw}\,.\,\mathrm{Pr}^{0.565})^{2.655}]^{2.0} + 1.5638 \times 10^{-15}(\mathrm{Re}_{ax}\,.\,\mathrm{Ra})^{2.18}\}^{0.1}\left(\frac{\mu_b}{\mu_w}\right)^{0.14} \times (R + 0.1)^{0.15} \times (1 + aX + bX^2 + cX^3) \tag{6}$$

where $R=\mathrm{AR}$ for $\mathrm{AR} \geqslant 1$ and $R=1/\mathrm{AR}$ for $\mathrm{AR} < 1$ and

$$a = 1.48 \times 10^{-3} \quad b = -8.16 \times 10^{-7} \quad c = 1.32 \times 10^{-10}$$

and

$$X = \mathrm{Sw}^{0.531}\mathrm{Pr}^{0.3} s \exp(ds)$$

All correlations have been found to predict the experimental data within ±20%. Figures 23–26 show the scatter of the data around the correlation.

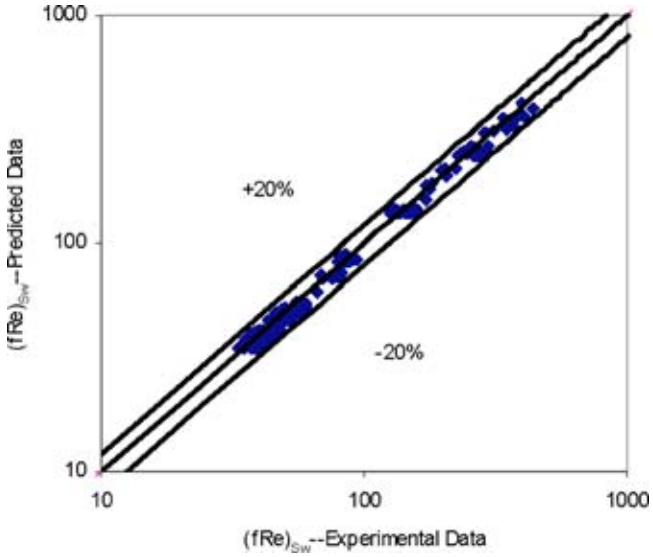

Fig. 23 Comparison of present experimental data with the predictions of Eq. (2) for short-length twisted tape

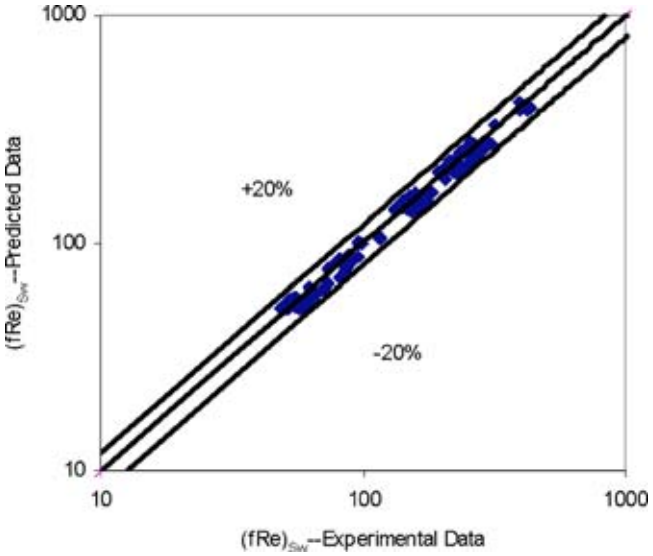

Fig. 25 Comparison of present experimental data with the predictions of Eq. (3) for regularly spaced twisted-tape elements

Performance Evaluation

The performance of the present geometry has been evaluated on the basis of the following two important criteria:

- Criterion 1. Basic geometry fixed, pumping power fixed; increase heat transfer; performance ratio R_1
- Criterion 2. Basic geometry fixed, heat duty fixed; reduce pumping power; performance ratio R_2

$$R_1 = \frac{\mathrm{Nu}_{\mathrm{slt,rst}}}{\mathrm{Nu}_{\mathrm{flt}}}$$

$\mathrm{Nu}_{\mathrm{slt,rst}}$ at a given Re, $\mathrm{Re}_{\mathrm{slt,rst}}$ is obtained from the correlation for short-length twisted tape or regularly spaced twisted tape elements. $\mathrm{Nu}_{\mathrm{flt}}$ for full-length twisted tape is taken at the $\mathrm{Re}, \mathrm{Re}_{\mathrm{flt}}$, where $\mathrm{Re}_{\mathrm{flt}}$ is calculated from the constant pumping power consideration as

$$\mathrm{Re}_{\mathrm{flt}} = \left[\left(\frac{f_{sw,\mathrm{slt,rst}}}{f_{sw,\mathrm{flt}}} \right) \left(\frac{A_{c,\mathrm{slt,rst}}}{A_{c,\mathrm{flt}}} \right) \mathrm{Re}^3_{sw,\mathrm{slt,rstt}} \right]^{1/3}$$

where $A_{c,\mathrm{slt}} = l(\pi D_h^2 - 4\delta D_h) + (1-l)\pi D_h^2$

$$A_{c,\mathrm{rst}} = [(\pi D_h^2 - 4\delta D_h)y + \pi(D_h^2 - d^2)s]/(y+s)$$

$$A_{c,\mathrm{flt}} = \left(\frac{\pi}{4} \right) D_h^2 - \delta D_h$$

$$R_2 = \frac{(f_{sw}\mathrm{Re}^3_{sw}A_c)_{\mathrm{slt,rst}}}{(f_{sw}\mathrm{Re}^3_{sw}A_c)_{\mathrm{flt}}}$$

For a given $\mathrm{Re}, \mathrm{Re}_{\mathrm{slt,rst}}$, the $\mathrm{Nu}_{\mathrm{slt,rst}}$ is obtained from the correlation. $\mathrm{Re}_{\mathrm{flt}}$ corresponding to $\mathrm{Nu}_{\mathrm{slt,rst}}$ is obtained from the correlation for full-length twisted-tape.

The performance ratios R_1 and R_2 for short-length twisted tapes are given in Table 2. From the performance ratio it is clearly observed that short-length twisted tapes perform worse than their

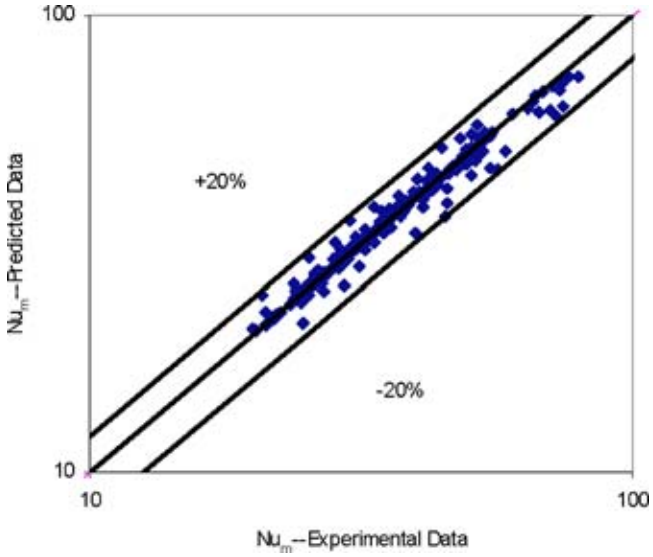

Fig. 24 Comparison of present experimental data with the predictions of Eq. (5) for short-length twisted tape

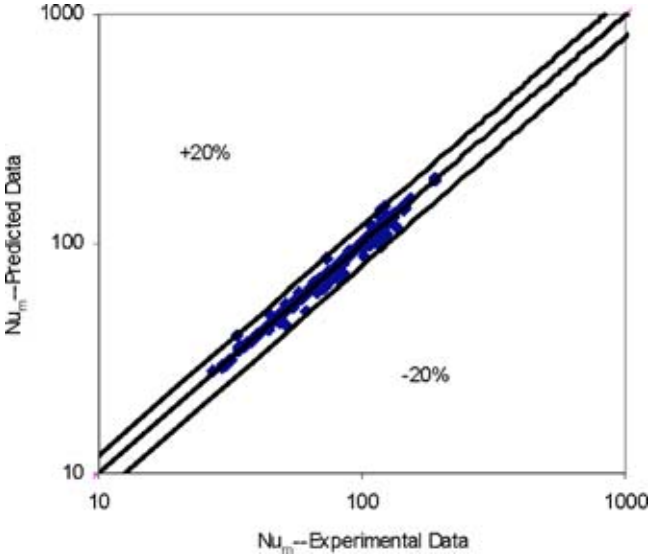

Fig. 26 Comparison of present experimental data with the predictions of Eq. (6) for regularly spaced twisted-tape elements

Table 2 Performance ratio, short-length twisted tape, $y_1=2.5$, $y_2=5.0$

AR		l=0.9		l=0.7		l=0.5	
		y_1	y_2	y_1	y_2	y_1	y_2
1	R_1	0.80-0.86	0.80-0.90	0.81-0.85	0.80-0.87	0.80-0.85	0.80-0.86
	R_2	2.41-3.72	2.00-3.76	2.68-3.78	2.42-4.04	2.74-3.81	2.76-4.26
0.5	R_1	0.80-0.88	0.82-0.91	0.80-0.88	0.80-0.89	0.80-0.92	0.80-0.87
	R_2	2.09-3.72	1.91-4.00	2.05-3.79	2.37-4.86	1.63-4.15	2.61-5.43
0.333	R_1	0.81-0.89	0.81-0.91	0.80-0.88	0.79-0.88	0.80-0.90	0.80-0.88
	R_2	2.08-3.72	1.87-4.01	2.07-3.80	2.38-5.76	1.79-8.56	2.81-5.82

full-length counterparts and, therefore, these are not recommended. The performance ratios R_1 and R_2 for regularly spaced twisted-tape elements are given in Table 3. From the performance ratio it is clearly observed that the regularly spaced twisted-tape elements perform significantly better than their full-length counterparts and these are recommended.

Conclusions

Heat transfer and pressure drop characteristics of laminar flow in rectangular and square plain ducts and ducts with twisted-tape inserts have been experimentally investigated. The heat transfer test section was under uniform wall heat flux condition.

Axially local pressure drop measurements as well as the axial variation of duct wall temperature indicated that the flow was periodically fully developed after some distance from the upstream end in the case of regularly spaced twisted-tape elements. The development length depends on the values of y, s, Re, and Pr. The higher, the Re, y, s, and Pr the higher the development length. In the case of short-length twisted tapes, the swirl decayed downstream of the twisted tape and the straight flow set in; the distance after which the straight flow set in depended on the twist ratio and the length of the twisted-tape.

The buoyancy effect due to the changes in density driven by temperature differences of the fluid has been observed in the plain duct portion in the case of short-length twisted tape and in the annular space region in case of regularly spaced twisted-tape elements. The swirl flow inertia forces were prevalent in the twisted-tape region.

Friction factor and Nusselt number correlations have been developed. The present experimental data and the performance evaluation show that the short-length twisted tape in square and rectangular ducts, through which laminar flow occurs under uniform wall heat flux boundary condition, performs worse than the full-length twisted tape. However, regularly spaced twisted-tape elements perform significantly better than the full-length twisted tapes.

Nomenclature

A = heat transfer area, m^2

Table 3 Performance ratio, regularly spaced twisted-tape elements, $y_1=2.5$, $y_2=5.0$, $s_1=2.5$, and $s_2=5.0$

AR		s_1		s_2	
		y_1	y_2	y_1	y_2
1	R_1	1.25-1.56	1.16-1.39	1.52-1.77	1.29-1.60
	R_2	0.08-0.26	0.14-0.37	0.04-0.08	0.06-0.19
0.5	R_1	1.20-1.42	1.15-1.44	1.42-1.75	1.36-1.72
	R_2	0.11-0.31	0.11-0.29	0.04-0.11	0.04-0.12
0.333	R_1	1.16-1.42	1.14-1.34	1.44-1.76	1.31-1.69
	R_2	0.13-0.37	0.16-0.35	0.04-0.12	0.05-0.14

A_c = axial flow cross-sectional area, $=(\pi D_h^2/4) - \delta D_h, m^2$

A_o = plain duct flow cross-sectional area, $=WD, m^2$

AR = aspect ratio=W/D, dimensionless

C_p = constant pressure specific heat, J/kg K

D = depth of the duct cross-section, diameter, m

D_h = hydraulic diameter of the test duct, $=4A_c/P, m$

d = non-dimensional diameter of the rod connecting two successive tape elements

d^* = actual diameter of the rod=dD_h, m

f = fully developed Fanning friction factor $=(\frac{1}{2})[\Delta P/(\rho V_0^2)](D_h/z)$, dimensionless

f_{sw} = swirl flow friction factor, $=\Delta P D_h/(2\rho V_s^2 L_s) = f(L/L_s)(V_0/V_s)^2$, dimensionless

$(f\mathrm{Re})_{sw}$ = $(f\mathrm{Re})_{sw}=(f\mathrm{Re})\{[\pi-(4\delta/D_h)]/\pi\} \times[1+(\pi/2y)^2]^{-1}$, dimensionless

g = gravitational acceleration, m/s^2

Gr = Grashof number=$g\beta\rho^2 D_h^3 \Delta T_w/\mu^2$, dimensionless

Gz = Graetz number=$\dot{m}C_p/kL$, dimensionless

H = pitch for 180 deg rotation of twisted tape, m

h_z = axially local heat transfer coefficient, $W/(m^2\,K)$

k = fluid thermal conductivity, W/(mK)

L = axial length, length of the duct, m

L_s = maximum helical flow length=$L[1+(\pi/2y)^2]^{1/2}$, m

L_T = length of twisted tape, m

l = nondimensional twisted-tape length=L_T/L, dimensionless

$\dot{m}$ = mass flow rate, kg/min

Nu_m = axially averaged Nusselt number=$(1/L)\int_0^L (h_z D_h dz/k)$, dimensionless

ΔP = pressure drop, N/m^2

P = wetted perimeter in the particular cross-section of the duct, m

Pr = fluid Prandtl number=$\mu C_p/k$, dimensionless

R_1, R_2 = performance ratios

Ra = Rayleigh number=GrPr

Re_{ax} = Reynolds number based on axial velocity $=(\rho V_a D_h)/\mu$, dimensionless

Re_{sw} = Reynolds number based on swirl velocity $=(\rho V_s D_h)/\mu$, dimensionless

Re = Reynolds number based on plain duct diameter $=(\rho V_0 D_h)/\mu$, dimensionless

S = space between two successive tape elements, m

s = space ratio=S/D_h, dimensionless

S_w = swirl parameter $=\mathrm{Re}_{sw}/\sqrt{y}=(\mathrm{Re}/\sqrt{y}) \times\{\pi/[\pi-(4\delta/D_h)]\} \times[1+(\pi/2y)^2]^{0.5}$, dimensionless

ΔT_w = wall to fluid bulk temperature difference, K

V_a = mean axial velocity=$\dot{m}/\rho A_c$, m/s

V_o = mean velocity based on plain duct diameter $=\dot{m}/\rho A_0$, m/s

V_s = actual swirl velocity at duct wall $=V_a[1+(\pi/2y)^2]^{0.5}$, m/s

y = twist ratio=H/D_h, dimensionless

z = axial length, the distance between the measuring pressure taps, m

Greek Symbols

β = coefficient of isobaric thermal expansion, K^{-1}

δ = tape thickness, m

μ = fluid dynamic viscosity, kg/ms
ρ = density of the fluid, kg/m^3

Subscripts

ax = at axial flow condition
b = at bulk fluid temperature
flt = full-length twisted tape
h = hydraulic diameter
rst = regularly spaced twisted-tape elements
slt = short-length twisted tape
sw = at swirl flow condition
w = at duct wall temperature

Appendix: Uncertainty Analysis

All the quantities that are measured to estimate the Nusselt number and the friction factor are subject to certain uncertainties because of errors in the measurement. These individual uncertainties as well as the combined effect of these are presented here. The analysis is carried out on the basis of the suggestion made by Kline and McClintock [16]. It is to be noted that the present uncertainty analysis is concerned with the errors pertinent to the measurements made during the investigation. The possible errors in the properties are not included since the physical and transport properties of the working fluid are well documented.

Analysis. First, the analysis for the friction factor is presented. The analysis for the Nusselt number is presented after that.

Friction Factor.

$$f = \frac{1}{2}\left\{\frac{\Delta P}{L_p}\right\}\left\{\frac{\rho D^3}{\mathrm{Re}^2\,\mu^2}\right\} \tag{A1}$$

$$\frac{\Delta f}{f} = \frac{1}{f}\left[\left\{\frac{\partial f}{\partial(\Delta P)}\Delta(\Delta P)\right\}^2 + \left\{\frac{\partial f}{\partial L_p}\Delta L_p\right\}^2 + \left\{\frac{\partial f}{\partial D}\Delta D\right\}^2 + \left\{\frac{\partial f}{\partial(\mathrm{Re})}\Delta\,\mathrm{Re}\right\}^2\right]^{0.5} \tag{A2}$$

or

$$\frac{\Delta f}{f} = \left[\left\{\frac{\Delta(\Delta P)}{\Delta P}\right\}^2 + \left\{\frac{\Delta L_p}{L_p}\right\}^2 + \left\{\frac{3\Delta D}{D}\right\}^2 + \left\{\frac{2\Delta\,\mathrm{Re}}{\mathrm{Re}}\right\}^2\right]^{0.5} \tag{A3}$$

$$\Delta P \propto h \tag{A4}$$

$$\therefore\ \frac{\Delta(\Delta P)}{\Delta P} = \frac{\Delta h}{h} \tag{A5}$$

$$\mathrm{Re} = \frac{4\dot{m}}{\pi D\mu} \tag{A6}$$

$$\frac{\Delta\,\mathrm{Re}}{\mathrm{Re}} = \left[\left(\frac{\Delta\dot{m}}{\dot{m}}\right)^2 + \left(\frac{\Delta D}{D}\right)^2\right]^{0.5} \tag{A7}$$

The uncertainty in friction factor has been calculated from the above equations.

Nusselt Number.

$$\mathrm{Nu} = \frac{hD}{k} \tag{A8}$$

$$\frac{\Delta\mathrm{Nu}}{\mathrm{Nu}} = \frac{1}{\mathrm{Nu}}\left[\left\{\frac{\partial}{\partial h}(\mathrm{Nu})\Delta h\right\}^2 + \left\{\frac{\partial}{\partial D}(\mathrm{Nu})\Delta D\right\}^2 + \left\{\frac{\partial}{\partial k}(\mathrm{Nu})\Delta k\right\}^2\right]^{0.5}$$

or

$$\frac{\Delta\mathrm{Nu}}{\mathrm{Nu}} = \left\{\left(\frac{\Delta h}{h}\right)^2 + \left(\frac{\Delta D}{D}\right)^2\right\}^{0.5} \tag{A9}$$

$$h = \frac{q''}{T_{wi} - T_b} \tag{A10}$$

$$\frac{\Delta h}{h} = \frac{1}{h}\left[\left\{\frac{\partial h}{\partial q''}\Delta q''\right\}^2 + \left\{\frac{\partial h}{\partial T_{wi}}\Delta T_{wi}\right\}^2 + \left\{\frac{\partial h}{\partial T_b}\Delta T_b\right\}^2\right]^{0.5}$$

$$\frac{\Delta h}{h} = \left[\left\{\frac{\Delta q''}{q''}\right\}^2 + \left\{\frac{\Delta T_{wi}}{T_{wi} - T_b}\right\}^2 + \left\{\frac{\Delta T_b}{T_{wi} - T_b}\right\}^2\right]^{0.5} \tag{A11}$$

$$q'' = \frac{0.5}{\pi D L_h}[(V^2/R) + \dot{m}C_p(T_{bo} - T_{bi})] \tag{A12}$$

$$\frac{\Delta q''}{q''} = \frac{1}{q''}\left[\left\{\frac{\partial}{\partial R}(q'')\Delta R\right\}^2 + \left\{\frac{\partial}{\partial V}(q'')\Delta V\right\}^2 + \left\{\frac{\partial}{\partial \dot{m}}(q'')\Delta\dot{m}\right\}^2 + \left\{\frac{\partial}{\partial T_{bo}}(q'')\Delta T_{bo}\right\}^2 + \left\{\frac{\partial}{\partial T_{bi}}(q'')\Delta T_{bi}\right\}^2 + \left\{\frac{\partial}{\partial D}(q'')\Delta D\right\}^2 + \left\{\frac{\partial}{\partial L_h}(q'')\Delta L_h\right\}^2\right]^{0.5}$$

$$\frac{\Delta q''}{q''} = \left[\frac{1}{(1 + \dot{m}C_pR\Delta T_b/V^2)^2}\left(\frac{\Delta R}{R}\right)^2 + \frac{4}{(1 + \dot{m}C_pR\Delta T_b/V^2)^2}\left(\frac{\Delta V}{V}\right)^2 + \frac{1}{\left(1 + \dfrac{V^2}{R\dot{m}C_p\Delta T_b}\right)^2}\left(\frac{\Delta\dot{m}}{\dot{m}}\right)^2 + \frac{1}{\left(1 + \dfrac{V^2}{R\dot{m}C_p\Delta T_b}\right)^2}\left(\frac{\Delta T_{bo}}{\Delta T_b}\right)^2 + \frac{1}{\left(1 + \dfrac{V^2}{R\dot{m}C_p\Delta T_b}\right)^2}\left(\frac{\Delta T_{bi}}{\Delta T_b}\right)^2 + \left(\frac{\Delta D}{D}\right)^2 + \left(\frac{\Delta L_h}{L_h}\right)^2\right]^{0.5} \tag{A13}$$

where $\Delta T_b = T_{bo} - T_{bi}$.

The uncertainty in Nusselt number has been calculated from Eqs. (A8)–(A13). The accuracies of the measured quantities are given below in the tabular form:

Quantity	Accuracy	Quantity	Accuracy
ΔD_h	0.00002 m	ΔL	0.001 m
$\Delta\dot{m}$	1.667E-5 kg/s	Δh	0.001 m
ΔT	0.025°C	ΔV	0.1 V
R	0.00002 Ω		

References

[1] Date, A. W., and Singham, J. R., 1972, "Numerical Prediction of Friction Factor and Heat Transfer Characteristics of Fully Developed Laminar Flow in Tubes Containing Twisted Tapes," ASME Paper No. 72 IIT-17.
[2] Date, A. W., 1974, "Prediction of Fully-Developed Flow in a Tube Containing a Twisted-Tape," Int. J. Heat Mass Transfer, **17**(8), pp. 845–859.
[3] Hong, S. W., and Bergles, A. E., 1976, "Augmentation of Laminar Flow Heat Transfer in Tubes by Means of Twisted-Tape Inserts," ASME J. Heat Transfer, **98**(2), pp. 251–256.
[4] Watanabe, K., Taira, T., and Mori, Y., 1983, "Heat Transfer Augmentation in Tubular Flow by Twisted Tapes at High Temperatures and Optimum Performance," Heat Transfer-Jpn. Res., **12**(3), pp. 1–31.
[5] Bandyopadhyay, P. S., Gaitonde, U. N., and Sukhatme, S. P., 1991, "Influence of Free Convection on Heat Transfer During Laminar Flow in Tubes With Twisted Tapes," Exp. Therm. Fluid Sci., **4**(5), pp. 577–586.
[6] Manglik, R. M., and Bergles, A. E., 1988, "Laminar Flow Heat Transfer in a Semi-Circular Tube With Uniform Wall Temperature," Int. J. Heat Mass Transfer, **31**(3), pp. 625–636.
[7] Carlson, R. D., France, D. M., Gabler, M. J., Kim, K., and Veljovich, W., 1986, "Heat Transfer Augmentation in Liquid Metal Reactor Steam Generators," *Proc. ASME/ANS Joint Nuclear Power Conf.*, ASME, New York, pp. 211–217.
[8] Sukhatme, S. P., Gaitonde, U. N., Shidore, C. S., and Kuncolienkar, R. S., 1987, "Forced Convection Heat Transfer to a Viscous Liquid in Laminar Flow in a Tube With A Twisted-Tape," Proc. of 9th National Heat and Mass Transfer Conf., IISc, Bangalore, Paper No. HMT-87, Part B, pp. 1–3.

[9] Saha, S. K., Gaitonde, U. N., Date, A. W., 1989, "Heat Transfer and Pressure Drop Characteristics of Laminar Flow in a Circular Tube Fitted With Regularly Spaced Twisted-Tape Elements," Exp. Therm. Fluid Sci., **2**(3), pp. 310–322.
[10] Date, A. W., and Saha, S. K., 1990, "Numerical Prediction of Laminar Flow and Heat Transfer Characteristics in a Tube Fitted With Regularly Spaced Twisted-Tape Elements," Int. J. Heat Fluid Flow, **11**(4), pp. 346–354.
[11] Patil, A. G., 2000, "Laminar Flow Heat Transfer and Pressure Drop Characteristics of Power-Law Fluids Inside Tubes With Varying Width Twisted Tape Inserts," ASME J. Heat Transfer, **122**(1), pp. 143–149.
[12] Saha, S. K., Dutta, A., and Dhal, S. K., 2001, "Friction and Heat Transfer Characteristics of Laminar Swirl Flow Through a Circular Tube Fitted With Regularly Spaced Twisted: Tape Elements," Int. J. Heat Mass Transfer, **44**, pp. 4211–4223.
[13] Saha, S. K., and Dutta, A., 2001, "Thermohydraulic Study of Laminar Swirl Flow Through a Circular Tube Fitted With Twisted Tapes," ASME J. Heat Transfer, **123**, pp. 417–427.
[14] Manglik, R. M., Maramraju, S., and Bergles, A. E., 2001, "The Scaling and Correlation of Low Reynolds Number Swirl Flows and Friction Factors in Circular Tubes With Twisted-Tape Inserts," J. Enhanced Heat Transfer, **8**, pp. 383–395.
[15] Manglik, R. M., and Bergles, A. E., 1993, "Heat Transfer and Pressure Drop Characteristics for Twisted-Tape Inserts in Isothermal Tubes: Part I—Laminar Flows," ASME J. Heat Transfer, **115**, pp. 881–889.
[16] Kline, S. J., and McClintock, F. A., 1953, "Describing Uncertainties in Single Sample Experiments," Mech. Eng. (Am. Soc. Mech. Eng.), **75**(1), pp. 3–8.

Modeling and Experiments of Laser Cladding With Droplet Injection

J. Choi
e-mail: jchoi@umr.edu

L. Han

Y. Hua

Department of Mechanical and Aerospace Engineering,
University of Missouri-Rolla,
1870 Miner Circle,
Rolla, MO 65409, USA

Laser aided Directed Material Deposition (DMD) is an additive manufacturing process based on laser cladding. A full understanding of laser cladding is essential in order to achieve a steady state and robust DMD process. A two dimensional mathematical model of laser cladding with droplet injection was developed to understand the influence of fluid flow on the mixing, dilution depth, and deposition dimension, while incorporating melting, solidification, and evaporation phenomena. The fluid flow in the melt pool that is driven by thermal capillary convection and an energy balance at the liquid–vapor and the solid–liquid interface was investigated and the impact of the droplets on the melt pool shape and ripple was also studied. Dynamic motion, development of melt pool and the formation of cladding layer were simulated. The simulated results for average surface roughness were compared with the experimental data and showed a comparable trend. [DOI: 10.1115/1.2005273]

Keywords: Laser Cladding, Direct Metal/Material Deposition, Droplet Injection, Fluid Flow, Dilution Depth, Surface Roughness, Volume-of-Fluid Algorithm

Introduction

Laser technology has been used in various manufacturing processes to replace convectional manufacturing technologies such as welding, cutting, drilling, cladding, etc. [1]. Laser-aided manufacturing can be faster, more precise, and cause a smaller heat-affected than conventional methods. As a promising manufacturing technology, the laser-aided direct metal deposition (DMD) process offers the ability to make a metal component directly from 3D CAD dimensions [2–4]. Repeating the laser-cladding pass layer by layer, a 3D object can be formed with the help of CAD data. A great technical challenge to make the DMD process viable and effective is how to control the deposition dimension, microstructure, and mechanical properties. Control of these properties implies control over the melt pool size and solidification time, thereby the cooling rate, to get the desired deposition dimension and mechanical properties and minimize the postprocess cost and time. This requires quantitative understanding of the relationship among independent process variables such as laser power, beam diameter, traverse speed, and powder feeding rate, etc. In addition, understanding the transport phenomena and properties of the melt pool is very important to control the product quality.

The injection of powder into the melt pool distinguishes the cladding process from other laser processes, such as laser surface hardening or laser remelting. The average powder size, distribution, and injection velocity make a big difference on the shape and ripple of the melt pool. Only a limited number of models for the cladding process have been reported [5–10], and all of the existing models assume that the shape of the melt pool is known *a priori*. Weerasinghe and Steen [5] developed a finite difference model of laser cladding by powder injection. They included the effect of preheating the powder with the laser beam and also the effect of the powder in shadowing part of the laser energy from the surface. Kar and Mazumder [6] described a one-dimensional diffusion model including the dissolution of the powder and mixing. Rappaz et al. [7,8] also established a two-dimensional finite element model to compute the shape of the melt pool. Their model took into account the interactions between the powder particles and the laser beam and the change of absorption with the shape of the melt pool. Quantitative investigations into the effects of convection and powder particle injection have not been included in the above modeling works.

In this study, a two-dimensional model for laser cladding is presented, which includes solidification, melting, and evaporation phenomena. A continuum model was employed to solve Navier–Stokes equations for both solid and liquid phases. A volume-of-fluid (VOF) algorithm was incorporated to obtain the solution of the free surface. As the main driving force, surface tension and thermocapillary force were combined into the model as body forces. Also, the velocity field affected by the impact of the droplet injection was calculated. The current model is a transient model with the laser beam moving in the X direction. The experimental verification was carried out following a single-pass laser cladding process. Figure 1 shows a schematic sketch for the laser cladding process.

Mathematical Model

Convection is the single most important factor influencing the geometry of the laser melt pool. Convection influences pool shape, aspect ratio, and surface ripples, which can result in defects such as variable penetration, porosity, and lack of fusion during laser processing. In surface melting processes such as the laser cladding process, where the power density level is on the order of 10^5 and 10^7 W/cm^2, momentum transfer or convection can be significant. The features of the model, the governing equations and associated boundary conditions are presented in the following section and the basic assumptions of this model are as follows:

(1) A laser beam having a defined power distribution strikes the surface of an opaque material of finite depth, and length.
(2) Only part of the energy is absorbed by the workpiece and powder. Studies show that the amount of laser energy absorbed by the different materials is 37%–60% [21,22].
(3) The absorbed energy induces surface tension driven flow due to the high-temperature gradient.

Contributed by the Heat Transfer Division for publication in the JOURNAL OF HEAT TRANSFER. Manuscript receieved: September 4, 2004. Final manuscript received: March 22, 2005. Review conducted by: Ranga Pitchumani.

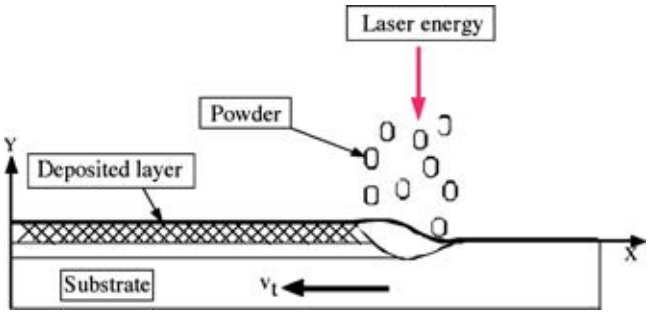

Fig. 1 Schematic sketch of laser cladding process

(4) The liquid metal is Newtonian, so the Navier–Stokes equation is applicable.
(5) All properties of the liquid and solid metal are constant, independent of temperature. (This allows simplifications of the model; however, variable properties can be treated with slight modifications.)

Governing Equations. The continuity equation, momentum equation, and energy equations based on continuum formulation are modified and used in the present study. They are given below: continuity equation:

$$\frac{\partial}{\partial t}(\rho) + \nabla \cdot (\rho \boldsymbol{V}) = 0, \tag{1}$$

momentum equation:

$$\frac{\partial}{\partial t}(\rho u) + \nabla \cdot (\rho \boldsymbol{V} u) = \nabla \cdot \left(\mu_l \frac{\rho}{\rho_l} \nabla u \right) - \frac{\partial p}{\partial x} - \frac{\mu_l}{K} \frac{\rho}{\rho_l} (u - u_s), \tag{2}$$

$$\frac{\partial}{\partial t}(\rho v) + \nabla \cdot (\rho \boldsymbol{V} v) = \nabla \cdot \left(\mu_l \frac{\rho}{\rho_l} \nabla v \right) - \frac{\partial p}{\partial y} - \frac{\mu_l}{K} \frac{\rho}{\rho_l} (v - v_s) + \rho \cdot g, \tag{3}$$

energy equation:

$$\frac{\partial(\rho h)}{\partial t} + \nabla \cdot (\rho \boldsymbol{V} h) = \nabla \cdot (k \nabla T) - \nabla \cdot [\rho (h_l - h)(V - V_s)], \tag{4}$$

evolution of free surface:

$$\frac{\partial F}{\partial t} + (\boldsymbol{V} \cdot \nabla) F = 0. \tag{5}$$

Note that the momentum and energy equations contain the phase interaction terms. In Eqs. (1)–(4), the density (ρ), specific heat (c), thermal conductivity (k), solid mass fraction (f_s), liquid mass fraction (f_l), solid volume fraction (g_s), liquid volume fraction (g_l), velocity (V) and the enthalpy (h) are defined as below:

$$\rho = \rho_s g_s + \rho_l g_l, \quad c = f_s c_s + f_l c_l, \quad k = g_s k_s + g_l k_l,$$

$$h = f_s h_s + f_s h_l, \quad f_s = \frac{g_s \rho_s}{\rho}, \quad f_l = \frac{g_l \rho_l}{\rho},$$

$$\boldsymbol{V} = f_s \boldsymbol{V}_s + f_l \boldsymbol{V}_l, \quad f_s + f_l = 1, \quad g_s + g_l = 1. \tag{6}$$

In Eq. (5), F expresses the fractional volume occupied by fluid in that computational cell. F takes a value of unity at a cell in space occupied by fluid and a value of zero if fluid does not occupy that cell, and cells with F value between zero and unity are partially filled with fluid and identified as surface cells. The liquid–vapor interface is located at the $F=0.5$ contour [18].

For implementation purposes, we assume the phase specific heats are constants, thus the phase enthalpy for the solid and the liquid can be expressed as:

$$h_s = \int_0^T c_s dT = c_s T, \tag{7}$$

$$h_l = \int_0^{T_s} c_s dT + L_m + \int_{T_s}^T c_l dT = c_l T + (c_s - c_l) T_s + L_m. \tag{8}$$

During the melting and solidification, the mass fraction of the phase depends on factors such as mixture concentration and the evolution of microstructures. In the present research, thermodynamic relations are used as described in the equation below and phase concentrations are obtained assuming local thermodynamic equilibrium:

$$f_s = 1 - \frac{1}{1 - k_p} \frac{T - T_l}{T - T_m} \tag{9}$$

where k_p is the equilibrium partitioning ratio.

In Eqs. (2) and (3), K is the permeability of the two-phase mushy region which is modeled as a porous media. Following the approach suggested by Bennon and Incropera [11], the present study employs the Kozeny–Carman equation for the permeability [15,16]:

$$K = \frac{K_0 g_l^3}{(1 - g_l)^2}, \tag{10}$$

where K_0 is the permeability coefficient.

Substituting the above equations into the energy equation, Eq. (4) can be transformed into following form:

$$\frac{\partial(\rho C_l T)}{\partial t} + \boldsymbol{V} \cdot \nabla (\rho \cdot C_l T) = \nabla \cdot (k \nabla T) - \frac{\partial(\rho f_l L_m)}{\partial t} + \frac{\partial(\rho f_s \Delta C_p T)}{\partial t} + \nabla \cdot [\rho f_s (L_m + \Delta C_p T)] \boldsymbol{V}_s \tag{11}$$

Boundary Conditions

Liquid-Vapor Free Surface. A free surface cell with one or more empty neighbors is subject to normal and tangential boundary conditions:
shear stress balance:

$$\mu \left(\frac{\partial u_s}{\partial n} + \frac{\partial v_n}{\partial s} \right) = \frac{\partial \gamma}{\partial T} \cdot \frac{\partial T}{\partial s}. \tag{12}$$

normal stress balance:

$$p = p_v + \gamma \cdot \kappa, \tag{13}$$

where u_s and v_s are the tangential and normal velocity component at the free surface. p_v is the vapor pressure in the gas region. γ and κ represent surface tension coefficient and curvature, respectively. In the present study, γ is assumed not to vary with temperature, and κ can be solved using the following equation given in [12]:

$$\kappa = -\left[\nabla \cdot \left(\frac{n}{|n|} \right) \right] = \frac{1}{|n|} \left[\left(\frac{n}{|n|} \cdot \nabla \right) |n| - (\nabla \cdot n) \right], \tag{14}$$

where n is a normal vector of local free surface, which is a gradient of VOF function:

$$n = \nabla F. \tag{15}$$

In this model, surface tensions in tangential and normal directions are decomposed in X and Y components, which are included in X and Y momentum equations, respectively. Detail derivations

refer to [12].

An energy balance at the free surface satisfies the following equation:

$$k\frac{\partial T}{\partial n}=\frac{\lambda\cdot P_{\text{laser}}}{\pi\cdot R^2}\exp\left(-\frac{r^2}{R^2}\right)-h_c(T-T_\infty)-\varepsilon\cdot\sigma(T^4-T_\infty^4)-\dot{m}_{ev}L_v, \tag{16}$$

where P_{laser} is the power of laser beam, λ is the absorption coefficient, and R is the radius of laser beam. The Gaussian energy distribution is assumed, and heat loss from convection, radiation and evaporation are included. According to a recent experimental study [22], the clad zone reflects approximately half of the laser power, because the onset of melting is associated with a rise in material reflectivity, and a molten pool surface in an inert atmosphere is smooth and oxide free. The remaining half of the laser power is redistributed approximately as follows: (a) 10% is reflected off the powder cloud, (b) 30% is used to heat the substrate, and (c) 10% is used to melt the clad layer. Therefore, about 40% of laser power is absorbed at the clad zone. In this study, the bounding values of 30% and 50% of laser absorptivity were utilized for the calculations.

In the evaporation term, $\dot{m}_{ev}$ is the evaporation mass rate and L_v is the latent heat for liquid-vapor phase change. The equation given by Dushman [23]:

$$\log(\dot{m}_{ev})=A_v+\log(p_{\text{atm}})-0.5\log(T), \tag{17}$$

was adapted to calculate the evaporation rate. For a metal such as 304L stainless steel, p_{atm} can be used as [24]

$$\log(p_{\text{atm}})=6.1210-\frac{18\,836}{T}. \tag{18}$$

For the heat loss due to convection and radiation, the convective heat transfer and the radiation transfer at the free surface were considered. However, it was estimated that the heat loss by convection is relatively small ($\sim$0.1% of laser power) although the temperature at the cladding zone reaches beyond the melting point and the melt pool is exposed to a stream of Ar flow, which carries powder to the clad zone (forced convection). Assuming a heat transfer coefficient of 100 $\text{W/m}^2\,\text{K}$, the area of the clad zone 3.14 mm^2, and the temperature difference 2000 K, respectively, the heat loss due to convection is about 0.628 W. Meanwhile, the heat loss due to radiation was reported to be about 1% of laser power [22].

Bottom Surface and Side Surface. The boundary conditions at the left, bottom and right wall, shown in Fig. 1, satisfy the equations below:

$$-k\frac{\partial T}{\partial n}=h_c(T-T_\infty)+\varepsilon\cdot\sigma(T^4-T_\infty^4), \tag{19}$$

$$u=0,\quad v=0. \tag{20}$$

It is also estimated that the heat loss due to radiation at the surface–surrounding interface, except the clad zone, is quite small ($\sim$0.1% of laser power) and can be neglected since the temperature difference with respect to T_∞ at the left, bottom, and right walls is not large in Eq. (19). The neglecting of the radiation term in Eq. (19) leads to simplification of the numerical calculation procedure.

Mass Balance on Top Surface. The injection of powder particles onto the top surface can be classified into three types: (i) Powder particles that were not melted during the flight and hit the solid part of the substrate. Experiments show that these powder particles deflect and scatter around the melt pool. (ii) Powder particles that have been melted before they arrive on the substrate and hit the solid part of substrate. They will stick to the substrate and are treated as droplets. (iii) Powder particles or droplets that fall into the melt pool. They will be absorbed and join the convection of the melt pool. In this study, the powder particles belonging to the last two cases will be utilized. The mass ratio of utilized powder to total powder can be obtained by experiment. The experimental data show that this ratio is about 20%–40%. In order to simplify the model, the first situation is not included in the model, and also an assumption was made for the last two cases that those utilized powder particles have been melted before they touch the top surface and are treated as droplets.

Temperature of the Powder. Powder particles are heated by the laser beam during their flight. For a self-consistent model of the cladding process, it is necessary to take into account the temperature of the incoming powder particles on the top free surface. Strict calculation of the powder temperature is very complicated. A simplified model proposed by Jouvard, et al. [9] has a good agreement with the experimental results in calculating the powder temperature. By following the model, the temperatures of the powder particles can be obtained, and it was found that about 80% of the powder particles reach a temperature close to the melting temperature. It is reasonable to assume that the powder particles are at the melting temperature when they touch the top free surface.

Numerical Method

Because Eqs. (2) and (3) are applicable for solid phase and liquid phase, the solid–liquid interface has been included into the equation. A semi-implicit SOLA-VOF [13] based algorithm was used for the solution of continuity and momentum Eqs. (1)–(3). The thermal energy transport Eq. (4) was solved using an explicit finite volume approximation.

A fixed-grid system of 200×100 uniform grid points was utilized for the cladding domain of 4 mm$\times$2 mm. A finer grid system was also tried by reducing the grid spacing to half (i.e., 400×200) to check the accuracy of the calculated results. Little improvement was obtained with the finer grid, though it took about 4 times the central processing unit (CPU) time, as compared to the original grid system. The selected grid system can be considered to be a compromise between computational cost and accuracy.

A. Steps of iteration procedure:

(1) Initialize the velocities, pressure, temperature, and VOF function.
(2) Solve the momentum equations utilizing a two-step projection method [19]. Surface tensions are solved and included into momentum equations as body forces. In this step, new velocities and pressure are solved. Details for the two-step projection are as follows.
(3) Advance VOF function in time domain using donor–acceptor flux approximation method [14] to update new free surface.
(4) Solve the energy equation using new velocities obtained in step 2.
(5) Update old velocities, pressure, temperature, and VOF function using new values, and back to step 2 for the next iteration until the time to finish is reached.

In the two-step projection method, momentum equations can be approximated as follows:

$$\frac{\boldsymbol{V}^*-\boldsymbol{V}^n}{\Delta t}=-\nabla\cdot(\boldsymbol{VV})^n+\frac{1}{\rho^n}\nabla\cdot\tau^n+\frac{1}{\rho^n}S_\phi^n, \tag{21}$$

$$\frac{\boldsymbol{V}^{n+1}-\boldsymbol{V}^*}{\Delta t}=\frac{1}{\rho^n}\nabla p^{n+1}. \tag{22}$$

In Eq. (21), S_ϕ is a source term including surface tension and the phase change term. V^* can be solved based on the information at step n. Using the fact from the continuity equation that the velocity field is divergence-free, that is, $\nabla\cdot V_t=0$, Eq. (22) can be written as:

$$\nabla \cdot \left[\frac{1}{\rho^n} \nabla p^{n+1} \right] = \frac{\nabla \cdot \mathbf{V}^*}{\Delta t}. \quad (23)$$

Equation (23) is the pressure Poisson equation and it can be solved by successive-over-relaxation method or conjugate-gradient method [17].

In the calculation domain, the flow field was discretized into a finite volume and a staggered grid was used on which velocities were defined at the cell face, and pressure, temperature, and VOF function are located at the cell center.

Numerical stability. The numerical difference equations are subject to linear numerical stability conditions that are detailed in Hirt and Nichols [20]. Material cannot move more than one cell in one time step yielding the Courant condition:

$$\Delta t < \min\left(\frac{\Delta x_i}{|u_{i,j}|}, \frac{\Delta y_j}{|v_{i,j}|} \right). \quad (24)$$

Second, momentum must not diffuse more than about one cell in one time step:

$$\frac{\mu_l \Delta t}{\rho_l} < \frac{1}{2} \frac{(\Delta x_i \Delta y_j)^2}{(\Delta x_i)^2 + (\Delta y_j)^2} \quad (25)$$

Third, when surface tension is included there must be a limit to prevent capillary waves from traveling more than one cell width in one time step [20]:

$$\frac{\sigma . \Delta t^2}{\rho \min(\Delta x_i^2, \Delta y_j^2)} < 0.25. \quad (26)$$

Finally, with Δt chosen, a stability condition on α is needed:

$$1 \geqslant \alpha > \max\left\{ \left| \frac{u_{i,j} \Delta t}{\Delta x_i} \right|, \left| \frac{v_{i,j} \Delta t}{\Delta y_j} \right| \right\} \quad (27)$$

An α approximately 1.2–1.5 times larger than the right-hand member of the last inequality is a good choice [20]. If α is too large, an unnecessary amount of numerical smoothing (diffusion-like truncation error) may be introduced.

Simulation Results

In order to consider the influence of powder injection on the shape of the melt pool, a case without powder injection has been taken into account. Also, the influence of droplet injection and surface quality of cladding layer is discussed.

Simulations of the following three cases are based on the material properties and process parameters, as shown in Table 1, just listed for the main properties and parameters.

Case A: melt pool without powder injection

Figures 2(*a*)–2(*c*) present the temperature distribution, the flow field, and the melt pool shape, respectively, for the case without powder injection. Processing parameters are as follows; velocity of laser beam, 12.7 mm/s, power of laser beam, 600 W, diameter of laser beam, 0.7 mm, and absorption coefficient, 0.5. The numbers labeled on the figure are the cell index, and each cell has a size of 20 μm in both the X and Y direction. In the figure, the laser beam starts at 0.8 mm ($X=40$), and these results are obtained at the time, $t=160$ ms.

Since the laser beam is a moving, transient problem, the melt pool is not symmetric. The highest temperature is located under the laser beam, but it was observed that there is a little bit of lag since convection phenomena in the melt pool may make a partial contribution to the temperature distribution since the thermal capillary force is the main force driving the flow. However, it has been also shown that the lag may not be just due to the convection in the melt pool, but it may exist due to the fact that the surface immediately beneath the beam continues to be heated as the tail of the beam passes over it. Due to the high temperature gradient, surface tensions also have a very large gradient, which produces the ripple effect in the melt pool, since the surface tension force

Table 1 Material properties and process parameters used for this model

Property	Symbol	Value
Evaporation constant	A_v	2.52
Specific Heat of Liquid	c_l	800 $(Jkg^{-1}K^{-1})$
Specific Heat of Solid	c_s	700 $(Jkg^{-1}K^{-1})$
Convection Heat Transfer Coefficient	h_c	10 $((Wm^{-2}K^{-1})$
Conductivity of Liquid	k_l	21 $(Wm^{-1}K^{-1})$
Conductivity of Solid	k_s	21 $(Wm^{-1}K^{-1})$
Latent Heat of Melt	L_m	2.5×10^5 (Jkg^{-1})
Latent Heat of Evaporation	L_v	6.34×10^6 (Jkg^{-1})
Power of Laser Beam	P_{laser}	500~1000 (W)
Radius of Laser Beam	R	0.7 (mm)
Liquidus Temperature	T_l	1700 (K)
Solidus Temperature	T_s	1650 (K)
Velocity of Laser Beam	V_{laser}	12.7 $(mm\ s^{-1})$
Powder Absorptivity	α	0.3~0.4
Absorption coefficient of Laser power	λ	0.3~0.5
Dynamic Viscosity	μ_l	6×10^{-3} $(kgm^{-1}s^{-1})$
Density of Liquid	ρ_l	6900 (kgm^{-3})
Density of Solid	ρ_s	7800 (kgm^{-3})

(thermal-capillary force) is the main driving force included in the momentum equation. Other forces such as buoyancy force or electromagnetic force were not included in the model, considering the relatively shallow melt pool, the disturbance from incoming droplets, and very weak presence of electromagnetic force during laser–material interaction. In the case that the velocity of the laser beam is not fast enough, the surface of the melt pool near the solidification interface can become flat before it is solidified. In Fig. 2(*a*), it shows that as the laser-beam moved away, the top surface was solidified to be almost flat. Figure 2(*b*) shows that a ripple appeared at the left part of the laser beam which was located at $X=141.6$ ($X=2.832$ mm). The highest velocity obtained was about 0.05 m/s, which was found at the cell location, $X=128$ ($X=2.56$ mm), and $Y=35$ ($Y=0.7$ mm). Figure 2(*c*) shows the melt pool size. The depth of the melt pool was calculated as ~0.2 mm and the length of the melt pool was calculated as ~1.4 mm.

Case B: melt pool with droplet injection

Figures 3(*a*)–3(*f*) shows the influence of droplet injection on the melt pool. For this case, the following simulation parameters were used; diameter of droplet, 100 μm, velocity of droplet, −0.2 m/s, time interval of each picture, 1 ms, laser beam power, 1000 W, absorptivity, 0.3, and other parameters are kept the same as those in case A. Figure 3(*a*) shows the melt pool shape at the simulation time=82 ms, and every 1 ms until 87 ms, as shown in Figs. 3(*b*)–3(*f*). It is observed that the deeper the droplet is approaching into the melt pool and pushing the fluid away, the higher the speed of the flow is at the top surface. At $t=85$ ms, as shown in Fig. 3(*d*), the next droplet already touches the top surface, and Figs. 3(*e*) and 3(*f*) show its influence and impact on the melt pool.

Case C:

Figure 4 represents the surface quality of the cladding layer, which was obtained with a powder mass flow rate of 5 g/min and an absorption coefficient 0.3, and other parameters are kept the same as those in the case B. Figure 4(*a*) shows the surface roughness profile after $t=160$ ms of the deposited layer and shape of melt pool during the process (area enlarged, and average deposition height= ~0.16 mm). The average surface

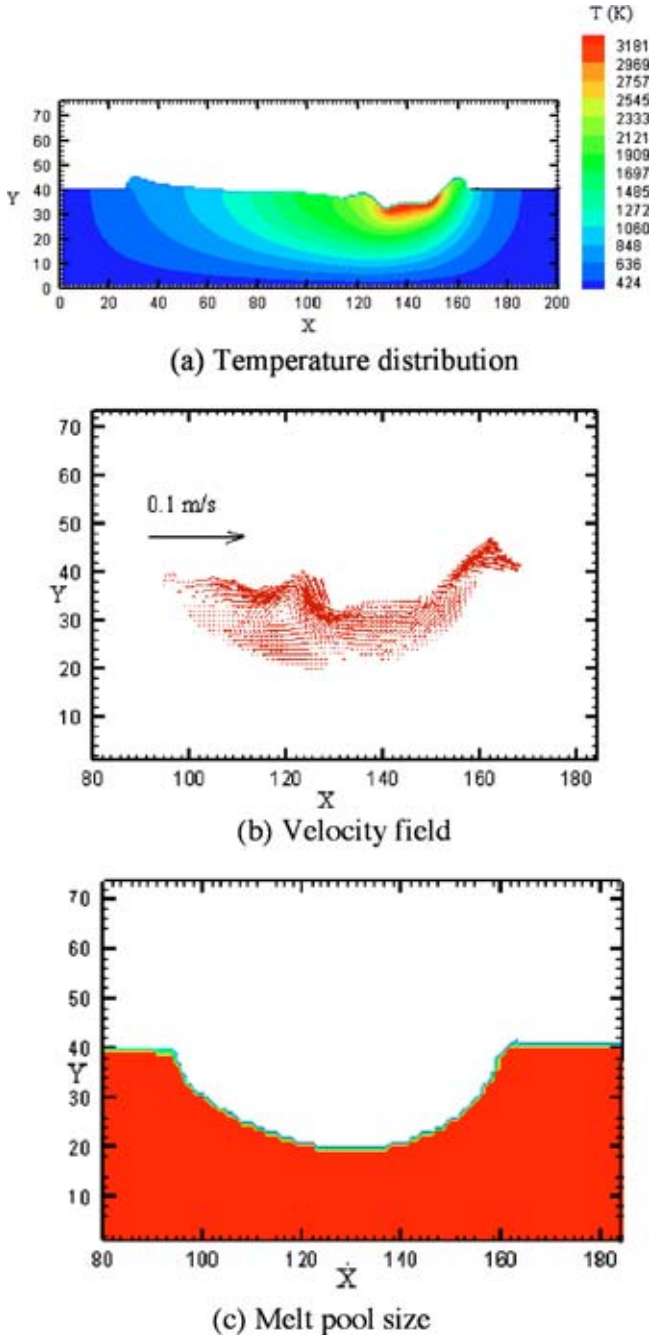

Fig. 2 Moving laser beam without droplet injection (moving velocity of laser beam, 12.7 mm/s, laser power, 600 W, beam diameter, 0.7 mm, and absorption coefficient, 0.5); (a) temperature distribution; (b) velocity field; and (c) melt pool size

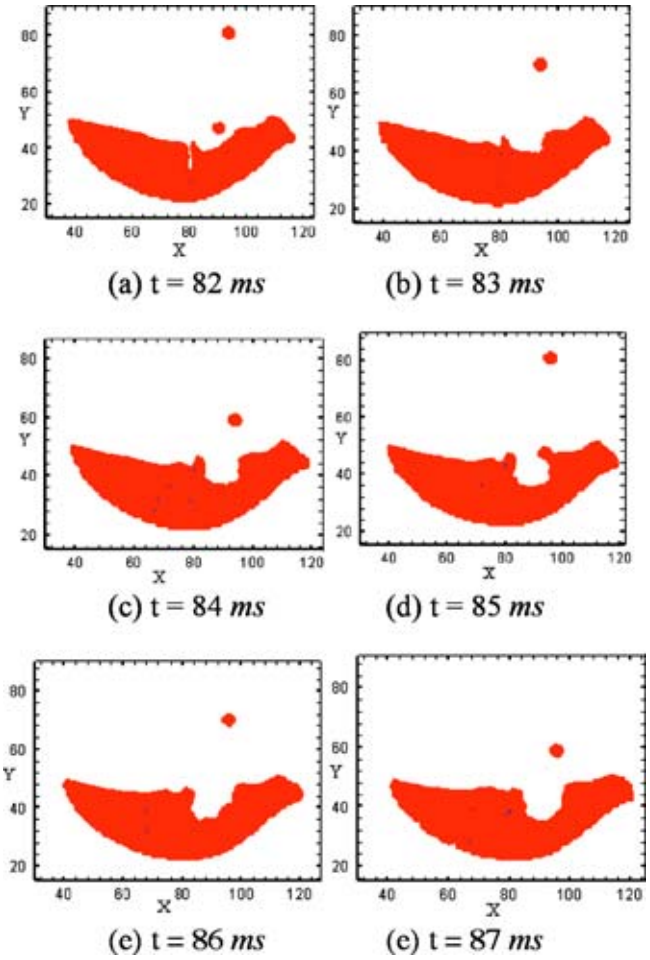

Fig. 3 Influences of droplet injection on melt pool (diameter of droplet, 100 μm, velocity of droplet −0.2 m/s, interval between droplets, 3 ms, laser beam power, 1000 W, and absorption coefficient, 0.3), (a) t=82 ms, (b) t=83 ms, (c) t=84 ms, (d) t=85 ms, (e) t=86 ms, and (e) t=87 ms

roughness obtained was about 20 μm, as shown in Fig. 4(*b*). It should be noted that the volume of the solid is not just affected by the addition of material due to droplet impingement, but also by the loss of material due to evaporation as the model considers the evaporation term in Eq. (16).

Experimental Verfication and Discussion

Experimental Setup. For the experimental verification, a 1.7 kW CO_2 laser with fundamental (Gaussian) beam mode was used. The laser is operated in cw mode, and the laser spot diameter is 0.7 mm. H13 tool steel powder (DELCROME® 6552 from Stellite® coatings) is delivered through a concentric nozzle with argon gas [volume flow rate=10.0 SCFH (16.9884 m^3/min)]. The nozzle assembly is a part of laser beam delivery head and is mounted on the *Z* axis, while the workpiece travels with the *X* and *Y* axis. The worktable travels at 12.7 mm/s during the process. To avoid the motion-acceleration effect and keep the workpiece velocity steady, the laser beam is triggered after the workpiece travels to 38.1 mm from the starting point. The molten pool is shielded by argon gas with gas flow rate, 20.0 SCFH (33.9768 m^3/min). A mild steel plate is used as a substrate and the standoff distance between the bottom of the nozzle and workpiece is maintained at 8 mm. To avoid potential time lag between

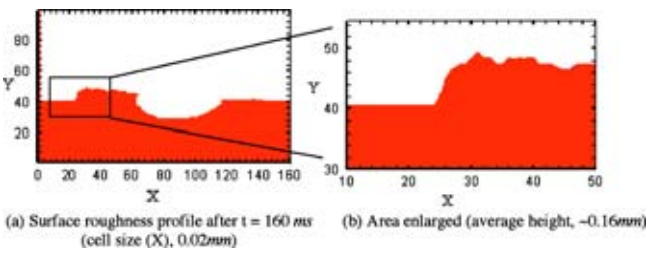

Fig. 4 Surface roughness of cladding layer, (a) surface roughness profile after t=160 ms (cell size (X), 0.02 mm), (b) area enlarged (average height, ~0.16 mm)

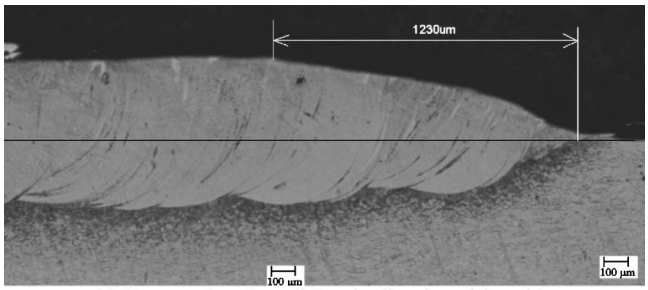

(a) Cross-sectioned parallel to the direction of deposition

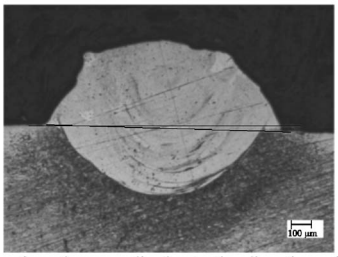

(b) Cross-sectioned perpendicular to the direction of deposition

Fig. 5 Typical single-pass laser clad (nominal laser power, 600 W; Gaussian mode; powder mass flow rate, 8 g/min), (a) cross-sectioned parallel to the direction of deposition, (b) cross-sectioned perpendicular to the direction of deposition

powder hopper and the molten pool, when changing powder flow, the powder feeder is turned on 5 s before the laser deposition begins. The term dilution depth, defined as the thickness of the substrate that was melted during the cladding process, was employed, though dilution, the ratio of thickness of substrate that was melted during the cladding process to the sum of thickness of the melted substrate and thickness of clad, is widely used. In this study, of interest is the fact that dilution increases with increasing laser power but decreases with increasing powder mass flow rate. For the laser cladding process, minimal dilution is desirable. To investigate the effects of laser power and powder mass flow rate on dilution depth and clad surface roughness, two sets of samples are made. One set is obtained varying the laser power from 228 to 600 W, while keeping powder mass flow rate constant (6 g/min). The other set is obtained, varying the powder mass flow rate between 5 and 10 g/min while keeping the laser power (600 W) constant. The samples are sectioned parallel to the deposition direction near the center line and then polished at the center line of the clad sample. The samples are etched with 2% nital solution and the dilution depth and surface roughness were measured using an optical microscopy (Nikon EPIPHOT 200).

Figure 5 shows a typical single-pass laser clad sample, which is a cross-sectioned parallel and perpendicular to the direction of deposition. As shown in Fig. 5, the deposition height increases from 0 to 337 μm as it moves to 1230 μm position. The deposition heights and dilution depths were measured at every 40 μm interval with Scion® Image software equipped with the optical microscopy, and data were taken from clad length of either 3.12 or 4.68 mm away from the start point of each specimen, where the clad shape reaches steady state. Surface roughness (R_a), average clad height, and dilution depth are measured from the optical micrograph, as shown in Figs. 6–8. These figures show the measured surface roughness (R_a), average clad height, and dilution depth as varying with laser power and powder mass flow rate, respectively. The data were curve fitted and plotted, as shown in Figs. 6(a) and 6(b) (second order polynomial fit), Figs. 7(b) and 8(a) (exponential fit), and Figs. 7(a) and 8(b) (third order polynomial fit.). For the experimental data, possible measurement errors are shown using assumed uncertainty limits of ±10% error bars.

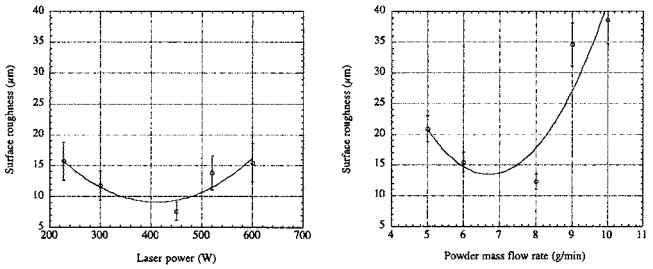

(a) (b)

Fig. 6 Measured surface roughness (a) as a function of effective laser power assuming 40% absorption; (b) as a function of powder mass flow rate

Experimental Results and Discussion. From Figs. 6(a) and 6(b), it was observed that either high or low laser power as well as powder mass flow rate resulted in higher surface roughness. It implies that there are optimal process parameters for laser power and powder mass flow rate to get minimal surface roughness. The deposition may go unsteady at some points at low laser power level due to either lack of power or unsteady heat dissipation through the substrate due to transient heat diffusion, thereby resulting in higher surface roughness. Likewise, the surface roughness level may become higher at high power level due to either high recoil pressure arising from solid/liquid interface or high evaporation pressure at the liquid/vapor interface. Similar phenomena were observed, varying powder mass flow rate and laser power. As shown in the figures, good surface roughness well below 10 μm can be generated with effective laser power (measured, assuming 40% absorption) between 350 and 450 W and powder mass flow at 6 g/min. It was also observed that varying powder mass flow rate results in a higher influence on surface roughness than that of laser power. Since the control of powder

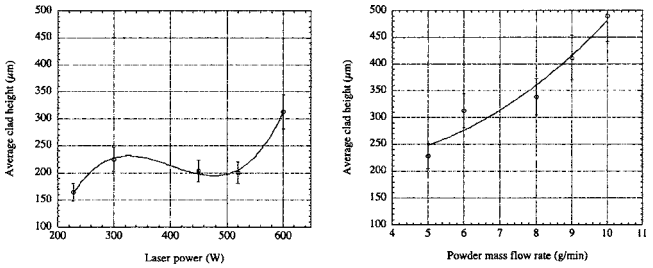

(a) (b)

Fig. 7 Measured average clad height (μm) (a) as a function of effective laser power assuming 40% absorption, (b) as a function of powder mass flow rate

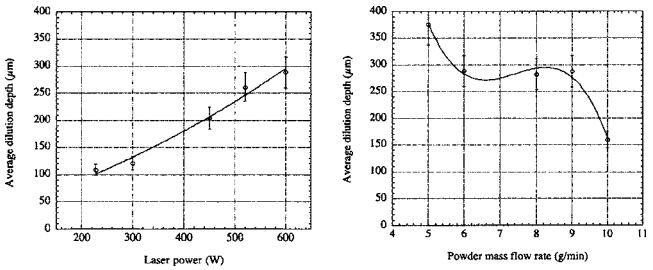

(a) (b)

Fig. 8 Measured average dilution depth (μm) (a) as a function of effective laser power assuming 40% absorption; (b) as a function of powder mass flow rate

Table 2 Three simulation cases for $\dot{m}_{del}/\dot{m}_{eff}$ (assuming the deposition shape, half-ellipse with a=0.5 mm, b=0.254 mm, traverse speed, v=762.0 mm/min, nominal powder mass flow rate, m=6 g/min, and powder encatchment ratio, ~20%)

	d, Average powder diameter (μm)	Δt, Time-interval between droplets (ms)	V_{del}, Powder volume flow rate at melt pool (mm^3/min)	$\dot{m}_{del}$, Powder mass flow rate at melt pool (g/min)	V_{eff} Effective deposition volume rate (mm^3/min)	$\dot{m}_{eff}$, Effective deposition mass rate (g/min)	$\dot{m}_{del}/\dot{m}_{eff}$, Mass rate ratio
1	100.00	0.20	157.08	1.23	152.01	1.19	1.03
2	150.00	0.70	151.47	1.18	152.01	1.19	1.00
3	170.00	1.00	154.35	1.20	152.01	1.19	1.02

mass flow rate is much more difficult than that of laser power and the powder distribution on the melt pool is fairly random, the influence on surface roughness level is higher.

Figures 7(*a*) and 7(*b*) show the average clad height changes, with increasing laser power and powder mass flow rate. As expected, the clad height increases as laser power increases to about 300 W, as shown in Fig. 7(*a*). Then, the height remains steady between 300 and 500 W, and the deposition height increases as the laser power increases to 600 W. Meanwhile, keeping laser power constant and increasing powder mass flow rate, it was observed that the clad height increases exponentially as shown in Fig. 7(*b*). With the increase of the powder mass flow rate the clad width also increases, but much more slowly, meanwhile the clad height increases almost linearly. Therefore, it is believed that, in order to control the clad height effectively, varying the powder mass flow rate can be easier than varying the laser power.

As shown in Fig. 8(*a*), the average dilution depth generally increases as laser power increases. For laser power in the range of 300–500 W, the level of dilution depth shows a practically linear relationship with laser power. Though the influence of laser power on clad width as well as clad height is quite small in this power range, as observed in Fig. 7(*a*), higher specific energy due to the increase of laser power may result in higher dilution depth. However, to keep the dilution depth uniform and/or minimal, it is suggested that the specific energy should be kept constant with uniform powder flow. In Fig. 8(*b*), it was also observed that the dilution is high when the powder mass flow rate is low, as the clad width was much smaller than those of higher powder mass flow. It is evident that the heat dissipated to the substrate is higher due to low powder mass flow rate, thereby higher dilution level. However, the dilution level is almost unchanged in the range of 6–9 g/min. With the measurement of the clad height and width in this range, it was found that the clad height increases but the clad width changes just a little bit. It is apparent that as the clad height and clad width increase the dilution level for higher powder mass flow rate decreases rapidly.

In order to compare the experimental results with simulation cases, the possible simulation cases closely matching with experiments are identified, as shown in Table 2. The comparison between simulated results by the two-dimensional model and the real experimental results, which involve three-dimensional phenomena, may not be so convincing. However, it is believed that the comparison can still provide valuable information about what the effects of laser beam motion on dilution depth and clad height are, and the impact of droplet injection on surface roughness using the model.

The net amount of delivered powder mass flow rate, $\dot{m}_{\mathrm{del}}$, based on the number of droplets delivered into the melt pool, can be estimated using the following formula;

$$\dot{m}_{\mathrm{del}} = \frac{\pi \rho d^3}{6\Delta t_{\mathrm{ave}}} \tag{28}$$

where ρ is the density of powder, Δt_{ave}, the average time interval between individual droplets, and d, the average diameter. It should be noted that the droplet was assumed to be cylindrical with the depth of $(2/3)d$, taking into account for the limitation by the two-dimensional model.

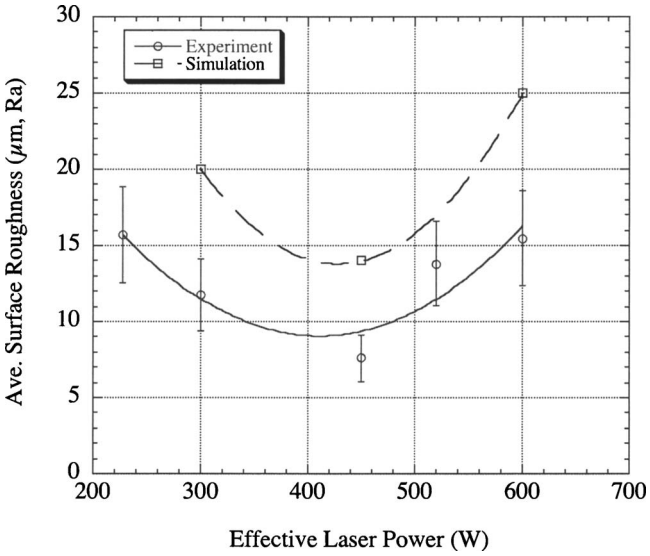

Fig. 9 Comparison between experimental and simulated results of average surface roughness (nominal powder mass feed rate ($\dot{m}_n$)=6.0 g/min)

Similarly, effective deposition rate (mass), $\dot{m}_{\mathrm{eff}}$, can be estimated with nominal powder mass flow rate, $\dot{m}_n$, measured from the hopper, and the powder encatchment ratio, η, using the following formula:

$$\eta \cdot \dot{m}_n = \dot{m}_{eff} = \rho \frac{\pi ab}{2} v_t, \tag{29}$$

where a and b are the averaged semimajor and semiminor segment for the unspecified half-ellipse deposition, ρ, the density of powder, and v_t, the traverse speed. With Eqs. (28) and (29), average time interval between individual powders, can be obtained as following:

$$\Delta t_{\mathrm{ave}} = \frac{d^3}{3abv_t}. \tag{30}$$

Three cases with different laser powers, 300, 450, and 600 W, respectively, were simulated and the average surface roughness was obtained to compare with the experimental results, as shown in Fig. 9, for the nominal powder mass feed rate ($\dot{m}_n$) =6.0 g/min. Considering low deposition rates and powder utilization efficiencies for a coaxial nozzle, it has been reported that the powder encatchment ratio ranges from 20% to 40% [25–27]. Assuming the lower end (20%) of powder encatchment ratio, η, the simulated data show a similar trend to those of the experiments, though the simulated results are not matched very well with the experimental results. It is explained that the difference between experimental and simulation results was largely caused by the higher speed of fluid flow at the free surface, resulting in higher surface roughness, since the two-dimensional model does not conduct heat faster than a three-dimensional model. It is expected that a fully developed three-dimensional laser cladding model can reduce the difference.

Concluding Remarks

A mathematical model has been developed to simulate the laser cladding processing. In this model, the effect of laser beam motion and the impact of droplet injection were investigated. VOF technique was used to track the free surface, and a continuum model was introduced to solve the melting and solidification process. Surface tension and thermal-capillary force were handled as

body forces. From the calculation, it shows that the melt pool shape and size become smaller when considering the powder injection, since a large part of energy is absorbed by the powder particle. It was observed that the melt pool shape also depends on the size and velocity of the droplet and the mass flow rate. In order to verify the model, experiments were conducted. The simulated results showed similar trends to those of the experiments.

Acknowledgments

This work was partially supported by the fund from Science and Engineering Service/US Army AMC (Grant No. DAH001-02-S-0003/TYPE). The laser based manufacturing laboratory at the University of Missouri–Rolla provided the experimental facility, thanks to the help from Dr. H. L. Tsai.

Nomenclature

A_v = evaporation constant
a = averaged semimajor segment for the unspecified half-ellipse deposition
b = averaged semiminor segment for the unspecified half-ellipse deposition
C_l = specific heat of liquid
C_s = specific heat of solid
d = average diameter of the powder
F = volume of fluid function
$\tilde{F}$ = divergence part of VOF function
F_{sv} = surface force
f_l = liquid mass fraction
f_s = solid mass fraction
g_l = liquid volume fraction
g_s = solid volume fraction
h = enthalpy
h_c = convective heat transfer coefficient
h_l = liquid enthalpy
h_s = solid enthalpy
k = thermal conductivity
L_m = latent heat of fusion of material
L_v = latent heat for liquid-vapor phase change
$\dot{m}_{ev}$ = evaporation mass rate
$\dot{m}_{\mathrm{del}}$ = delivered powder mass flow rate
$\dot{m}_{\mathrm{eff}}$ = effective deposition rate (mass)
$\dot{m}_n$ = nominal powder mass flow rate
R = radius of the laser beam
T = temperature
T_l = liquidus temperature
T_s = solidus temperature
T_∞ = ambient temperature
p, p_{atm} = pressure
P_{laser} = power of laser beam
P_v = vapor pressure in the gas region
K = permeability
K_0 = permeability coefficient
S_ϕ = source term
t = random variant or time
Δt = time step
Δt_{ave} = average time interval between individual powders
u = velocity in X direction
v = velocity in Y direction
u_s = tangential velocity at free surface
v_s = normal velocity at free surface
v_t = traverse speed of sample
$\boldsymbol{V}$ = velocity vector
$\tilde{V}$ = calculated temporary velocity vector
Δx = mesh spacing along X axis
Δy = mesh spacing along Y axis

Subscript

i = ith cell
j = jth cell
l = liquid phase
s = solid phase

Superscript

n = time step n

Greek symbols

γ = surface tension coefficient
ε = radiation emissivity
κ = free surface curvature
μ_l = dynamic viscosity of liquid metal
η = powder encatchment ratio
λ = dummy variable or absorption coefficient
σ = Stefan-Boltzmann constant
ρ = density
ρ_l = density of liquid
ρ_s = density of solid
τ = viscous stress tensor

References

[1] Mazumder, J., 1991, "Overview of Melt Dynamics in Laser Processing," Opt. Eng., **30**, pp. 1208–1219.
[2] Mazumder, J., Choi, J., Nagarathnam, K., Koch, J., and Hetzner, D., 1997, "The Direct Metal Deposition of H13 Tool Steel for 3D Components," JOM, **49**, pp. 55–60.
[3] Choi, J., 2002, "Process and Properties Control In Laser Aided Direct Metal/Materials Deposition Process," 2002 ASME IMECE, IMECE2002-MED-33568, New Orleans, LA, Nov. 11–15.
[4] Hua, Y., and Choi, J., "Feedback Control Effects on Dimensions and Defects of H13 Tool Steel by DMD Process," Paper No. 1308, Proceedings of ICALEO 2003, Jacksonville, FL, October 13–16, 2003.
[5] Weerasinghe, V. M., and Steen, W. M., 1983, "Computer Simulation Model for Laser Cladding," Transport phenomena in materials processing, PED 10/HTD 29, ASME, New York, NY, pp. 15–23.
[6] Kar, A., and Mazumder, J., 1987, "One-dimensional Diffusion Model for Extended Solid Solution in Laser Cladding," J. Appl. Phys., **61**, 2645–2655.
[7] Hoadley, A. F. A., and Rappaz, M., 1992, "A Thermal Model of Laser Cladding by Powder Injection," Metall. Trans. B **23B**, pp. 631–642.
[8] Picasso, M., and Rappaz, M., 1994, "Laser-Powder-Material Interactions in the Laser Cladding Process," J. Phys. IV, **C4**, pp. 27–33.
[9] Jouvard, J-.M., Grevey, D. F., Lemoine, F., and Vannes, A. B., 1997, "Continuous Wave Nd:YAG Laser Cladding Modeling: A Physical Study of Track Creation during Low Power Processing," J. Laser Appl., **9**, pp. 43–50.
[10] Toyserkani, E., Khajepour, A., and Corbin, S., 2003, "Three-Dimensional Finite Element Modeling of Laser Cladding by Powder Injection: Effects of Powder Feedrate and Travel Speed on the Process," J. Laser Appl., **15**, pp. 153–160.
[11] Bennon, W., and Incropera, F., 1987, "A Continuum Model for Momentum, Heat and Species Transport in Binary Solid-Liquid Phase Change Systems - I. Model Formulation," Int. J. Heat Mass Transfer, **30**, pp. 2161–2170.
[12] Prankash, C., and Voller, V., 1989, "On the Numerical Solution of Continuum Mixture Model Equations Describing Binary Solid-Liquid Phase Change," Numer. Heat Transfer, Part B, **15**, pp. 171–189.
[13] Nichols, B. D., Hirt, C. W., and Hotchkiss, R. S., 1980, "SOLA-VOF: A Solution Algorithm for Transient Fluid Flow with Multiple Free Boundaries," LA-8355, Los Alamos National Laboratory.
[14] Kothe, D. B., Mjolsness, R. C., and Torrey, M. D., 1991, "Ripple: A Computer Program for Incompressible Flows with Free Surfaces," LA-12007-MS, Los Alamos National Laboratory.
[15] Carman, P. C., 1937, "Fluid Flow through Granular Beds," Trans. Inst. Chem. Eng., **15**, pp. 150–166.
[16] Wang, Y., and Tsai, H. L., 2001, "Impingement of Filler Droplets and Weld Pool Dynamics during Gas Metal Arc Welding Process," Int. J. Heat Mass Transfer, **44**, pp. 2067–2080.
[17] Patankar, S. V., 1980, Numerical Heat Transfer and Fluid Flow, Hemisphere, New York.
[18] Sasmal, G. P., and Hochstein, J. I., 1994, "Marangoni Convection with a Curved and Deforming Free Surface in a Cavity," J. Fluids Eng., **116**, pp. 577–582.
[19] Bell, J. B., Colella, P., and Glas, H. M., 1989, "A Second-Order Projection Method for the Incompressible Navier-Stokes Equations," J. Comput. Phys., **85**, pp. 257–283.

[20] Hirt, C. W., and Nichols, B. D., 1981, "Volume of Fluid (VOF) Method for the Dynamics of Free Boundaries," J. Comput. Phys., **39**, pp. 201–225.
[21] Li, L. J., and Mazumder, J., 1985, in *Proceedings of Laser Processing of Materials*, edited by K. Mukherjee, and J. Mazumder (Metallurgical Society of American Institute of Metallurgical Engineers, Warrendale, PA, 1985), pp. 35–50.
[22] Gedda, E., Powel, J., Wahlstöm, G., Li, W.-B., Engström, H, and Magnusson, C., 2002, "Energy Redistribution during CO_2 Laser Cladding," J. Laser Appl., **14**, pp. 78–82.
[23] Dushman, S, 1962, *Scientific Foundation of Vacuum Technology* (John Wiley, New York.
[24] Kim, C. S., 1975, "Thermophysical Properties of Stainless Steels," Argonne National Laboratory, Argonne, IL, Report No. ANL-75-55.
[25] Lin, J., and Steen, W., 1998, "Design Characteristics and Development of a Nozzle for Coaxial Laser Cladding," J. Laser Appl., **10**, pp. 55–63.
[26] Lin, J., 2000, "Laser Attenuation of the Focused Powder Streams in Coaxial Laser Cladding," J. Laser Appl., **12**, pp. 28–33.
[27] Mazumder, J., Schifferer, A., and Choi, J., 1999, "Direct Materials Deposition: Designed Macro and Microstructure," Mater. Res. Innovations, **3**, pp. 118–131.

Effects of Plasma Parameters on the Temperature Field in a Workpiece Experiencing Solid-Liquid Phase Transition

F. B. Yeh[1]
Department of Marine Mechanical Engineering,
Chinese Naval Academy,
P. O. Box 90175, Tsoying, Kaohsiung, Taiwan, ROC
e-mail: fbyeh@mail.cna.edu.tw

P. S. Wei
Fellow ASME
Department of Mechanical and Electro-Mechanical Engineering,
National Sun Yat-Sen University,
Kaohsiung, Taiwan, ROC

The heat transfer characteristics of a workpiece subject to plasma heating and melting are theoretically and systematically studied. Plasma etching, spray deposition, sputtering, cutting and surface treatment, etc., are usually controlled by energy transfer from plasma to workpieces. In this work, the one-dimensional unsteady conduction equation accounting for solid-liquid phase transition with distinct thermal properties in a workpiece is solved. The plasma is composed of a collisionless presheath and sheath on an electrically floating workpiece that partially reflects or secondarily emits ions and electrons. The energy transport from plasma to the surface is kinetically, analytically and exactly calculated from self-consistent velocity distributions of the ions and electrons. The results show that the predicted surface temperature and energy transmission factor agree well with experimental data. The effects of plasma characteristics and thermal parameters of the workpiece on unsteady temperature profiles and thickness of the molten layer in the workpiece are quantitatively provided in this work. Energy released from recombination of the ions and electrons on the surface is found to play the most important role on heating the workpiece. The deviation of surface temperature contributed by recombination energy can be 1000 K. [DOI: 10.1115/1.1999653]

Keywords: Plasma Energy Flux, Phase Change, Sheath, Presheath, Energy Transmission Factor

Introduction

Plasma etching, spray deposition, sputtering, cutting, surface treatment, and nuclear fusion devices, etc., are usually controlled by energy transfer from the plasma to surfaces. Energy transfer between plasma and a surface is quite different from the ordinary situations encountered in air, inert gases and vacuum. In view of high thermal speed associated with rapid losses of the electrons to the wall, the plasma exhibits a net positive charge. A thin layer called the sheath or space-charge region in a thickness of around several Debye lengths ($\sim 10^{-6}$ m) thus exists on the wall [1]. The potential barrier adjusts itself, so that the flux of electrons that have enough energy to go over the barrier to the wall is equal to the flux of ions reaching an electrically floating wall. The presheath ($\sim 10^{-4}$ m), which lies between the bulk plasma and sheath, is an ionization region to supply the ions lost to the wall. Regardless of the Debye shielding, small electrostatic potential in the presheath still accelerates the ions up to and beyond sonic speed before entering the sheath, as first explicitly pointed out by Bohm [2].

Heat transport in the workpiece is evidently determined by the plasma energy transfer, which is controlled by the sheath voltage in front of the surface. The sheath voltage depends on plasma parameters such as the charge number, mass and temperature ratios of the ions and electrons generated in the presheath, and properties of the wall, etc. Over the past decades there has been intensive research to study energy transport encountered in the cathode or the near wall region of electric arc discharges, lamps, fusion devices, edge plasmas, ion implantation, deposition, etching, etc. [3–8]. For example, Schmitz and Riemann [7] analyzed transport processes in an atmospheric pressure arc discharge. Considering ion equilibrium of the plasma column and balances of energy and currents in the presheath and on the cathode surface, the electrical variables and cathode surface temperature were self-consistently and iteratively determined with given total pressure and current density, heavy particle and electron temperatures in the plasma column. Their study did not discuss and present in detail the influence of parameters of plasma and materials on the temperature distribution in the metallic cathode body. Predicting the total energy flux or the energy transmission factor [3], however, has been based on incomplete and approximate intuition to include different components of energy fluxes. A self-consistent and exact determination of the total energy from a kinetic analysis can be referred to Emmert et al. [9], and Wei and Yeh [10] and Yeh and Wei [11]. The former treated the wall completely absorbing the electrons and ions, while the latter allowed the wall to be partially reflecting (or secondarily emitting) ions and electrons.

Simulations of temperature distributions in a workpiece in contact with plasma as functions of parameters controlling the plasma characteristics and thermal properties of the workpiece are still incomplete [8,12–19]. Hussla et al. [8] and Visser [12] solved an unsteady, lumped heat conduction equation in a wafer during plasma etching. Ignoring detailed analysis of plasma, heat transfer from plasma to the wafer was estimated from surface temperature measurements via fluoroptic thermometry. Zhou et al. [13] proposed a detailed theoretical model to study the influence of the plasma arc conditions and cathode material on cathode erosion. It was shown that temperature of the cathode surface and mass loss rates increase with total currents and plasma temperature. The thermionic electrons emitted from the surface were found to be important for surface temperatures greater than 3500 K and current densities about 10^7–10^8 A/m^2. Ye et al. [14] conducted experiments and numerical analysis to investigate heat flux from

[1]Corresponding author.

Contributed by the Heat Transfer Division for publication in the JOURNAL OF HEAT TRANSFER. Manuscript received by the Heat Transfer Division January 22, 2004; revision received April 27, 2005. Review conducted by: B. Farouk.

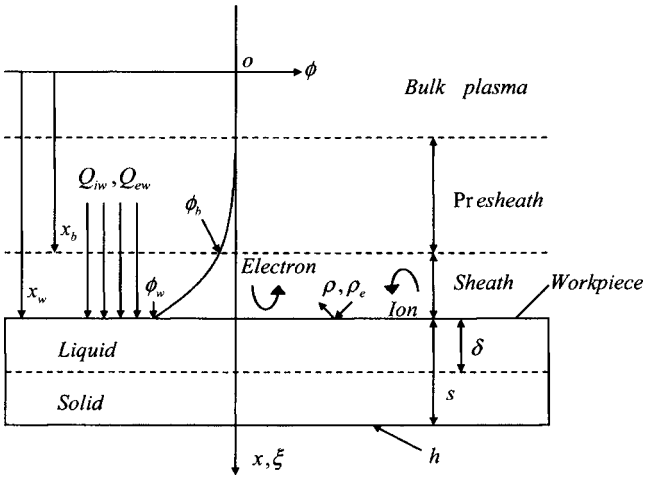

Fig. 1 System sketch for the physical model and coordinates

plasma to an electron-emissive material surface. Heat flux was estimated from energy balance equation of the electrons in plasma. Solving a time-dependent energy equation for the plate subject to heat transport from the plasma, it was found that the sheath voltage, surface temperature, and electron temperature exhibited *S* curves of bifurcation against plasma heat transfer rate. The effects of ion reflection on the energy transmission factor were also studied by Takamura et al. [15].

Raffray and Federici [16] developed a code to solve heat conduction in plasma facing components under various surface heat transfer processes, including evaporation, melting, and radiation and their interactions with components and the coolant. The properties of plasmas, however, were not accounted for. Takaki et al. [17] obtained a one-dimensional temperature profile in a workpiece by experimentally evaluating the plasma heat transfer on the surface. The effects of surface temperature, magnetic field and different materials on the effective emission coefficient were studied by Tsvetkov and Tanabe [18]. They obtained a one-dimensional numerical solution for temperature in a workpiece by using a simple model to evaluate heat input from the plasma. Kersten et al. [19] provided a general survey for energy balances on substrate surfaces during plasma processing. The effects of plasma parameters and workpiece properties on temperature in workpieces, however, were not included.

In this study, an unsteady heat conduction model is proposed to systematically predict unsteady temperature distributions in a workpiece in contact with plasma. The workpiece experiences heating and solid-liquid transition is induced by energy flux coming from the bulk plasma through the presheath and sheath to the surface. The effects of the parameters governing the characteristics of the plasma and properties of workpieces on the heating process are quantitatively and rigorously presented. The results thus give insight into controlling temperature and thickness of the molten layer evolution in the workpiece by choosing appropriate process parameters.

System Model

In this study, a workpiece with thickness *s* at initial temperature T_0 is subject to energy transport from plasma, as illustrated in Fig. 1. In view of high energy, including the total energies of the ions and electrons, temperature in the workpiece increases and readily results in solid-liquid transition. The plasma comprised of the bulk plasma, a presheath, and a sheath is in contact with an electrically floating workpiece partially reflecting or secondarily emitting ions and electrons. For the sake of charge neutrality, electrostatic potential is zero in the bulk plasma. Electrostatic potential decreases and gives rise to acceleration of the ions in the positive *x* direction toward the surface. On the other hand, the electrons in the forward direction need to overcome the potential. The major assumptions made are as follows [10,11]:

1. The model is one-dimensional due to thin thickness of the region considered. The plasma is in a quasi-steady state, while heat transfer in the workpiece is unsteady.
2. Transport processes in the plasma in contact with the workpiece surface can be modeled as those in a plasma between two parallel plates.
3. The presheath and sheath are imposed by a negligible magnetic field or a magnetic field in a direction parallel to the ion flow. As a result, the one-dimensional ion flow can be assured.
4. The workpiece surface is electrically floating. However, it can be readily extended to a biased surface.
5. The ionization rate is determined from the model by Emmert et al. [9]. This model is based on the fact that the ions would be a Maxwell–Boltzmann distribution in the absence of an electrostatic field far from the wall. This proposition has been confirmed by measurements of the ion distribution functions from Bachet et al. [20], and a successful comparison between the measured ion density and velocity from Goeckner et al. [21] and theoretical prediction by Yeh and Wei [11]. Collisionality in the presheath, unfortunately, is often marginal. That is, the mean-free paths between ions and electrons can be of the same magnitude as the thickness of the presheath. Modeling different kinds of atomic or molecular collisions is complicated and inaccurate. A further study is essentially required.
6. Thermionic and field emissions of ions and electrons are ignored.
7. The effects of neutral particles are ignored.
8. Ion and electron reflectivities are constant. The secondary emissions of ions and electrons can be included into the reflectivities [22].
9. Distinct thermal conductivities of the liquid and solid phases in the workpiece are allowed. Joule heat in the workpiece is neglected.

Plasma Energy Transport to Workpiece Surface. The dimensionless plasma energy flux transport to the surface is given by [11]

$$Q^*_{\text{totw}} = Q^*_{iw} + Q^*_{ew} + Q^*_{\text{rec}} + Q^*_{\text{ab}} = j^*_{iw}\left(\Omega + \chi_w - \chi_b + \frac{E^*_i}{Z_i} - \varphi^*\right) + j^*_{ew}(2 + \varphi^*) \tag{1}$$

where dimensionless energy fluxes for the ions, electrons, energies for recombination and absorption of the electrons coming from plasma to the workpiece surface are, respectively,

$$Q^*_{iw} = j^*_{iw}(\Omega + \chi_w - \chi_b) \tag{2}$$

$$Q^*_{ew} = 2j^*_{ew} \tag{3}$$

$$Q^*_{\text{rec}} = j^*_{iw}\left(\frac{E^*_i}{Z_i} - \varphi^*\right) \tag{4}$$

$$Q^*_{ab} = j^*_{ew}\varphi^* \tag{5}$$

Function Ω in Eqs. (1) and (2) is defined as

$$\Omega \equiv \frac{2}{Z_i\kappa} - 1 + \frac{\sqrt{\chi_b}}{D(\sqrt{\chi_b})} \tag{6}$$

Dimensionless energies E^*_i in Eqs. (1) and (4) and φ^* in Eqs. (1), (4), and (5) are, respectively, referred to ionization energy and work function. Dawson function in Eq. (6) is defined in previous studies [10,11]. The sheath edge potential in Eqs. (1), (2), and (6) is satisfied by [9–11]

$$\frac{2}{\sqrt{\pi Z_i \kappa}} D(\sqrt{\chi_b}) = e^{Z_i \kappa \chi_b} \mathrm{erfc}(\sqrt{Z_i \kappa \chi_b}) \tag{7}$$

where function erfc(x) is the complementary error function. The ion and electron current densities at the wall in Eq. (1) are, respectively

$$j_{iw}^* = j_{ib}^* = \Omega_{1b} e^{-\chi_b}, \quad j_{ew}^* = (1-\rho_e)\sqrt{\frac{M}{2\pi}} e^{-\chi_w} \tag{8}$$

where function

$$\Omega_{1b} \equiv \frac{2(1-\rho)}{1+\rho}\sqrt{\frac{2}{Z_i}}\frac{1+Z_i\kappa}{\pi\kappa} e^{\chi_b} D(\sqrt{\chi_b}) \tag{9}$$

Since ion and electron current densities are equal on the floating wall, the dimensionless total plasma energy flux transport to the surface from Eq. (1) becomes

$$Q_{\mathrm{totw}}^* = j_{iw}^* \left[\Omega + \chi_w - \chi_b + \frac{E_i^*}{Z_i} + 2 \right] \tag{10}$$

The dimensionless wall potential yields [10,11]

$$\chi_w = \chi_b + \ln\left(\frac{1-\rho_e}{\Omega_{1b}} \sqrt{\frac{M}{2\pi}} \right) \tag{11}$$

Equations (1) and (10) show that the total energy flux transport to the workpiece depends on ion and electron fluxes, the difference in potentials between the surface and sheath edge, and recombination energies of the ions and electrons.

Dimensionless Energy Equation in Workpiece. Dimensionless heat conduction equation of the workpiece is given by [23,24]

$$\frac{\partial \lambda}{\partial \tau} + \frac{1}{Ste}\frac{\partial f}{\partial \tau} = \frac{\partial}{\partial \xi}\left(K^* \frac{\partial \lambda}{\partial \xi} \right) \tag{12}$$

where the second term on the left-hand side represents evolution of latent heat. Dimensionless Stefan boundary condition yields

$$K_\ell^* \left.\frac{\partial \lambda}{\partial \xi}\right|_\ell + \frac{1}{\mathrm{Ste}}\frac{d\delta^*}{d\tau} = \left.\frac{\partial \lambda}{\partial \xi}\right|_s \tag{13}$$

where the first and second terms on the left-hand side represent heat conduction from liquid to the solidification front and latent heat due to solid-liquid transition, respectively, while the term on the right-hand side is heat conduction from the solidification front to the solid. Energy flux transport from plasma to the surface is balanced by heat conduction into the workpiece

$$-K^* \frac{\partial \lambda}{\partial \xi} = \Theta Q_{\mathrm{totw}}^* \tag{14}$$

where dimensionless parameter Θ represents the ratio between plasma flow work and heat conduction into the workpiece. Conduction energy is removed by convection at the bottom surface of the workpiece

$$-K^* \frac{\partial \lambda}{\partial \xi} = Bi\lambda \tag{15}$$

Temperature at the solid-liquid interface maintains the melting point

$$\lambda_s = \lambda_l = \lambda_m \tag{16}$$

The initial condition is $\lambda = 0$ at $\tau = 0$.

Numerical Method. A discretized form of Eq. (12) is given by [23,24]

$$a_{j-1}\lambda_{j-1} + a_j \lambda_j + a_{j+1}\lambda_{j+1} = a_R \tag{17}$$

where a's are discretization coefficients. Assuming a linear approximation for temperature, Stefan boundary condition of Eq. (13) can be used to determine the solid-liquid interface in the interval $[\xi_j, \xi_{j+1}]$

$$\delta^* = \xi_j + \frac{(\lambda_i - \lambda_j)\Delta\xi_j}{(\lambda_i - \lambda_j) + K_l^*(\lambda_{j+1} - \lambda_i)} \tag{18}$$

A successive relaxation method with a relaxation factor 0.3 was used. Among testing different grid systems 101 and 201 in uniform spaces, it was found that choosing a grid system 101 is quite good to obtain solutions independent of the variation in meshes. The solution procedure was as follows:

1. specify initial and working conditions, and properties of plasma and the workpiece;
2. solve Eqs. (7) and (11) to obtain electrical potentials at the sheath edge and surface;
3. calculate the total energy flux to the surface from Eq. (10),
4. solve Eq. (17) satisfied by Eqs. (14)–(16),
5. determine interface locations from Eq. (18),
6. determine liquid fraction at the interface locations; and
7. check convergence of temperature and total energy balance of the workpiece to relative errors less than 10^{-7}, and 10^{-3}, respectively. Otherwise, go to step 4.

The error, Dawson, and incomplete gamma functions were numerically integrated by a Simpson's rule. Errors were less than 10^{-6} by comparing grids of 1000 and 500.

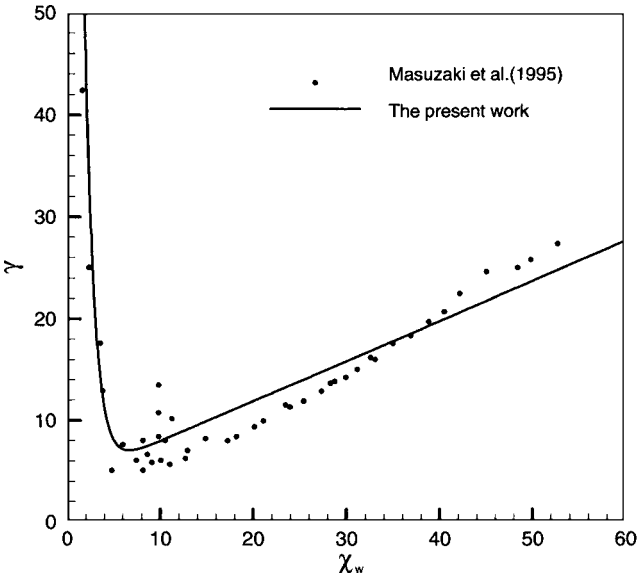

Fig. 2 A comparison between the measurements [25] and predicted energy transmission factor as a function of dimensionless wall potential

Results and Discussion

In this study, independent parameters governing the temperature distribution in the workpiece are ρ, ρ_e, M, Z_i, κ, E_i^*, Ste, θ_m, K, Θ and Bi. To confirm relevancy and accuracy of this model, the predicted energy transmission factor between a helium plasma and tungsten workpiece as a function of dimensionless wall potential is compared with experimental data provided by Masuzaki et al. [25], as shown in Fig. 2. The energy transmission factor γ is defined as [3]

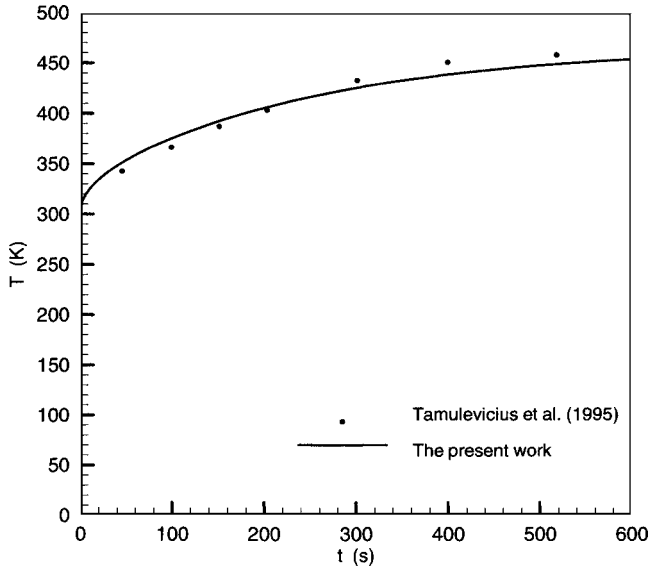

Fig. 3 A comparison between the measurements [26] and predicted surface temperature of a workpiece as a function of time

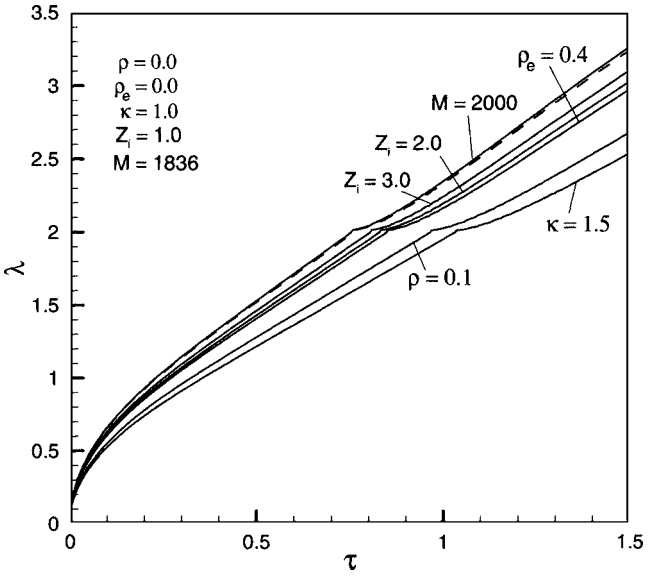

Fig. 4 Dimensionless surface temperature of a workpiece as a function of time for different reflectivities of ions and electrons, ion-to-electron mass ratios, charge numbers, and electron-to-ion source temperature ratios

$$\gamma = \frac{Q_{\text{totw}}}{k_B T_e n_{ib}\left(\frac{k_B T_e}{m_i} + \frac{k_B T_i}{m_i}\right)^{1/2}} = \frac{Q^*_{\text{totw}}}{n^*_{ib}}\left(1 + \frac{1}{\kappa}\right)^{-1/2} \tag{19}$$

where the electron temperature at the sheath edge is considered to be identical to that at the presheath edge, while the ion temperature at the sheath edge is the ion source temperature at the presheath edge. Choosing dimensionless parameters $Z_i=1$, $\rho=0.5$, $\rho_e=0$, $M=7344$, $\kappa=10$, $E_i^*=14.3$, the predicted energy transmission factor as a function of wall potential agrees quite well with experimental data [25]. The deviation can be due to the unavailable ion and electron temperatures at the sheath edge. A good comparison between the predicted and measured surface temperature as a function of time [26] for a nitrogen plasma and titanium workpiece is also shown in Fig. 3. In this case, the data chosen for comparison are $L=3.65\times10^5$ J/kg, $c_p=1228$ J/kg K, $T_0=T_\infty=300$ K, $T_m=1940$ K, $k_\ell=22$ W/m K, $k_s=22$ W/m K, $\rho=4510$ kg/m^3, $s=0.04$ m, $h_\infty=2.2\times10^3$ W/m^2 K, and $n_{e0}=5\times10^{18}$ m^{-3}, $m_i=2.34\times10^{-26}$ kg, $T_{e0}=2\times10^4$ K, $E_i=14.6$ eV.

Figure 4 shows the effects of plasma parameters, including reflectivities of electrons and ions, charge number, ion-to-electron mass ratio, and electron-to-ion source temperature ratio at the presheath edge, on dimensionless time-dependent surface temperature in the workpiece. The dashed line (and following figures) is the predicted results based on the referenced dimensionless parameters from Table 1, which are estimated from the data for a hydrogen plasma and aluminum workpiece as listed in Table 2. Different lines specified by different values of dimensionless parameters represent these parameters being different from those of the referenced parameters. Symbols and their values in the legend are referred to the dashed line. In the case of the referenced case, it can be seen that the dimensionless surface temperature increases rapidly to 0.7 at a dimensionless time of 0.15 after the plasma is in contact with the workpiece. The corresponding dimensional surface temperature is 510 K at time of 0.214 s. As time further proceeds, the dimensionless surface temperature gradually increases until a dimensionless time of 0.75 ($\approx$1.07 s) is reached. The corresponding dimensionless surface temperature $\lambda=2(=\theta_m-1)$, indicating the onset of surface melting. In view of the latent heat required for phase transition, the surface temperature maintains the melting temperature for a short period of time. After the solid-liquid phase transition is ended, the dimensionless surface temperature continues to increase with time.

It can be seen that an increase in ion-to-electron mass ratio results in an increase of surface temperature. This is because an increase in ion-to-electron mass ratio increases dimensionless wall potential [3,10,11], which enhances ion energy or total energy transport from the plasma to the workpiece. In this case, the ion

Table 1 Values of the reference dimensionless parameters

ρ	0
ρ_e	0
M	1836
Z_i	1
κ	1
E_i^*	0
Ste	0.8
θ_m	3
K_ℓ^*	0.5
Θ	0.3
Bi	5×10^{-4}

Table 2 Values of the data (hydrogen plasma and aluminum workpiece) used for estimating the reference dimensionless parameters

L	3.95×10^5 J/kg
c_p	1130 J/kg K
T_0, T_∞	300 K
T_m	933 K
k_ℓ	100 W/m K
k_s	200 W/m K
ρ	2520 kg/m^3
s	0.01 m
h_∞	10 W/m^2 K
n_{e0}	5×10^{20} m^{-3}
m_i	1.67×10^{-27} kg
T_{e0}	2×10^4 K

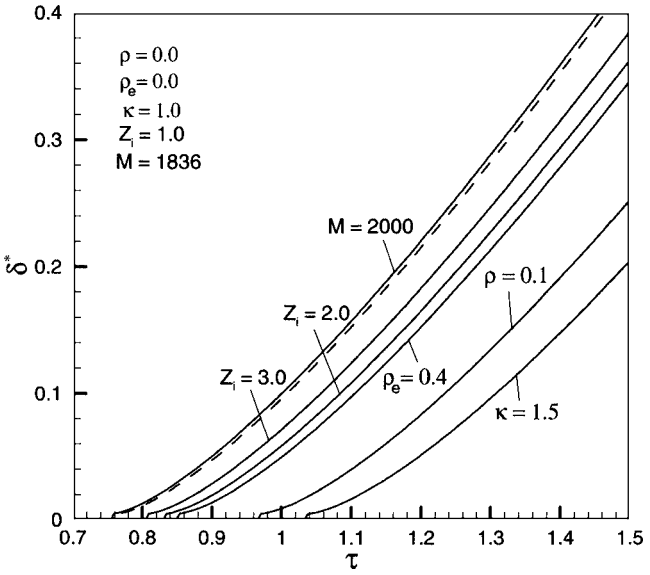

Fig. 5 Dimensionless thickness of the molten layer in a workpiece as a function of time for different reflectivities of ions and electrons, ion-to-electron mass ratios, charge numbers, and electron-to-ion source temperature ratios

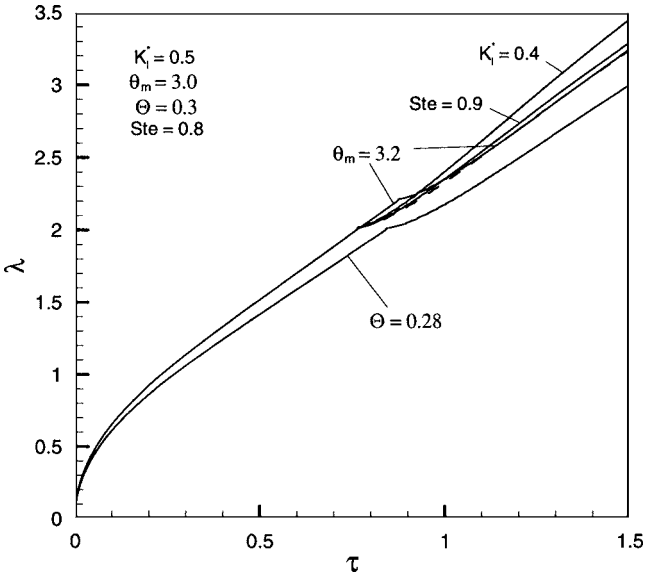

Fig. 6 Dimensionless surface temperature of a workpiece as a function of time for different Stefan numbers, dimensionless liquid conductivities, melting temperatures, and plasma flow work-to-heat conduction ratios

and electron currents are constants and independent of the ion-to-electron mass ratio. Even though dimensionless wall potential is increased with ion reflectivity, decreases in ion and electron currents [10,11] reduce total energy input and surface temperature of the workpiece. On the other hand, an increase in electron reflectivity decreases dimensionless wall potential [10,11]. Since ion and electron currents are independent of electron reflectivity [10,11], an increase in electron reflectivity reduces energy transport to the surface. Dimensionless surface temperature therefore is reduced with increasing electron reflectivity. A high electron-to-ion source temperature ratio indicates that generation of ions is low. To balance electron current, a high dimensionless wall potential is required and results in reduction of electron current (and ion current) [10,11]. Energy transport to the surface and dimensionless surface temperature are therefore decreased. It is interesting to find that as the charge number is equal to 2, the dimensionless surface temperature exhibits the minimum. The minimum surface temperature and energy transport to the workpiece is attributed to a decrease in ion energy and an increase in electron energy with increasing charge number [11]. In other words, an increase in charge number increases ion and electron currents, and decreases the difference in potentials between the workpiece surface and sheath edge. The minimum energy transport to the surface therefore takes place at a charge number of 2.

The corresponding dimensionless thickness of the molten layer as a function of time in the workpiece is shown in Fig. 5. Referring to Fig. 4, it is evidently seen that a high dimensionless surface temperature results in an early melting, rapid growth and thickness of the molten layer. The growth rates of the molten thickness are quite similar. The onset time for melting is decreased, while thickness and growth rate of the molten layer are increased by increasing the ion-to-electron mass ratio, and decreasing ion and electron reflectivities and electron-to-ion source temperature ratio. The minimum thickness is achieved at a charge number around 2. The results show that the effects of plasma parameters such as charge number, electron-to-ion source temperature ratio, and electron and ion reflectivities on heating, melting, and growth of the molten thickness are significant.

The effects of independent dimensionless parameters governing thermal properties of the workpiece on dimensionless surface temperature as a function of time are shown in Fig. 6. It is found that dimensionless surface temperature and its increasing rate are decreased, and time for melting is delayed by decreasing the plasma flow work-to-heat conduction ratio. This is attributed to a reduction of internal energy required to raise temperature. Even though the physical model for the melting process is different from a previous work for the cooling [24], it can still be seen that the surface temperature as a function of time before melting remains the same for different Stefan numbers, melting temperatures and liquid conductivities. An increase in dimensionless melting temperature, however, delays the melting. Increasing Stefan number, indicating a decrease in latent heat for melting, results in an increase in dimensionless surface temperature after melting takes place. After melting occurs, a decrease in dimensionless liquid conductivity implies a decrease in energy transport to the solid. This results in increase of the dimensionless surface temperature and its changing rate.

The corresponding dimensionless thickness of the molten layer in the workpiece as a function of time is shown in Fig. 7. It can be seen that thickness and growth rate of the molten layer are increased with increasing plasma flow work-to-heat conduction ratio and decreasing melting temperature. The effect of the melting temperature on the growth rate is comparatively slight. An increase of Stefan number increases thickness and growth rate of the molten layer. In view of less energy transport to the solid-liquid interface, a decrease in dimensionless liquid conductivity reduces thickness and growth rate of the molten layer.

Figure 8 shows dimensionless temperature as a function of location in the bulk workpiece for different dimensionless times. It can be seen that dimensionless temperature is decreased in the depthwise direction and increased with time. At a dimensionless time of 0.5, a monotonic decrease of temperature in the depthwise direction indicates a heating process in the solid in the absence of the liquid phase. However, surface melting takes place after dimensionless time is slightly around 1. This is revealed by the discontinuity of temperature gradients, resulting from absorption of latent heat and distinct thermal conductivities of the solid and liquid.

The dimensionless temperature in the workpiece at a given dimensionless time of 1.5 ($\approx$2.14 s) for different plasma parameters is shown in Fig. 9. In view of enhanced energy input from plasma as can be evaluated from the temperature gradient at the surface, temperatures and thickness of the molten layer in the workpiece

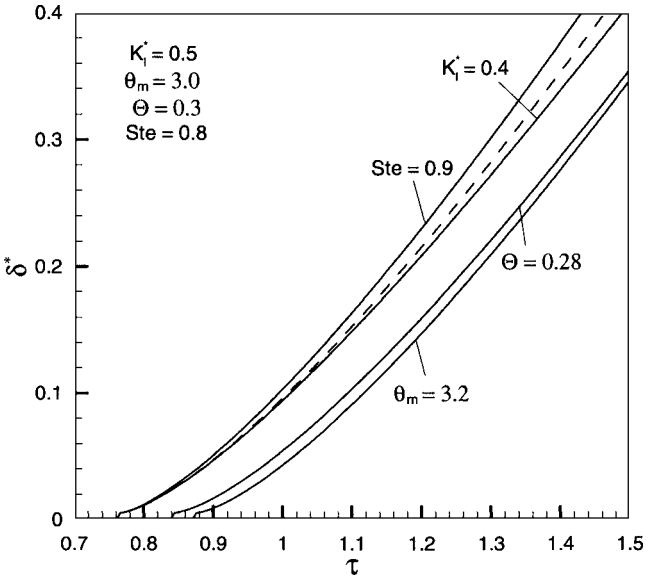

Fig. 7 Dimensionless thickness of the molten layer in a workpiece as a function of time for different Stefan numbers, dimensionless liquid conductivities, melting temperatures, and plasma flow work-to-heat conduction ratios

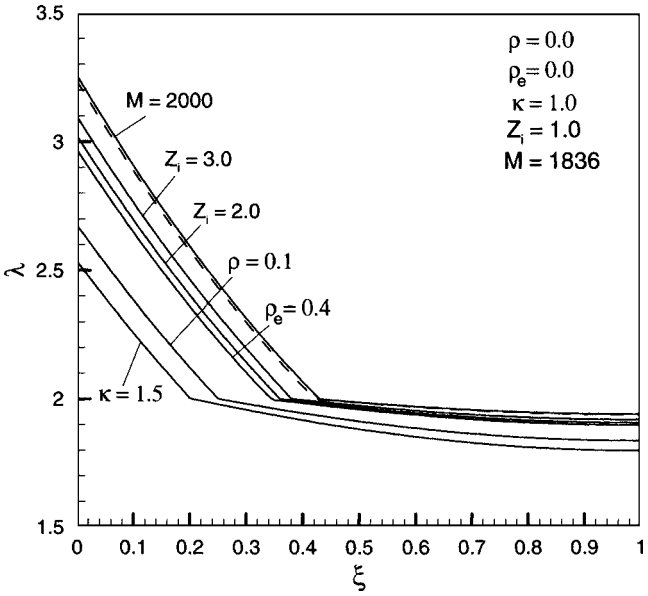

Fig. 9 Dimensionless temperature in a workpiece at a dimensionless time τ=1.5 for different reflectivities of ions and electrons, ion-to-electron mass ratios, charge numbers, and electron-to-ion source temperature ratios

are increased by increasing ion-to-electron mass ratio, and decreasing ion and electron reflectivities and electron-to-ion source temperature ratio. At charge number Z_i of 2, temperature and thickness of the molten layer exhibit the minimum. Figure 10 shows that temperatures and thickness of the molten layer in the workpiece are increased with plasma flow work-to-heat conduction ratio and Stefan number. A high temperature gradient is induced by decreasing dimensionless liquid conductivity, which results in a high surface temperature and thin thickness of the molten layer, as discussed previously.

Recombination energy is the difference between the ionization energy and work function. The effects of the dimensionless ionization energy on dimensionless surface temperature and thickness of the molten layer in the workpiece are, respectively, seen in Figs. 11 and 12. The dimensionless ionization energy of 8.0 corresponds to dimensional ionization energy of 13.6 eV for hydrogen plasma. In view of a significant energy release from recombination of the ions and electrons on the surface, the dimensionless surface temperature and thickness of the molten layer in the workpiece are increased with dimensionless ionization energy. Referring to the previous figures, the recombination energy plays the most important role in the energy transport to the workpiece. For example, accounting for recombination energy increases dimensionless surface temperature from 2 to 5.5 at a dimensionless time of 0.9, corresponding to dimensional temperature of 900–1950 K at a time of 1.28 s.

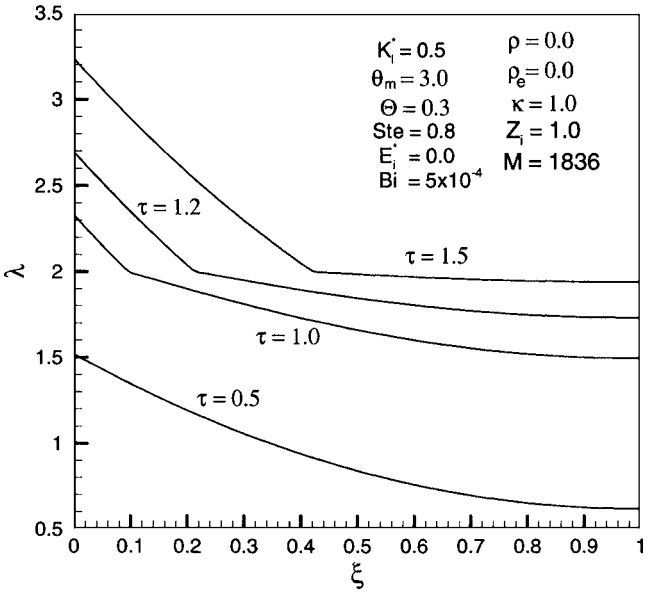

Fig. 8 Dimensionless temperature in a workpiece for different dimensionless times

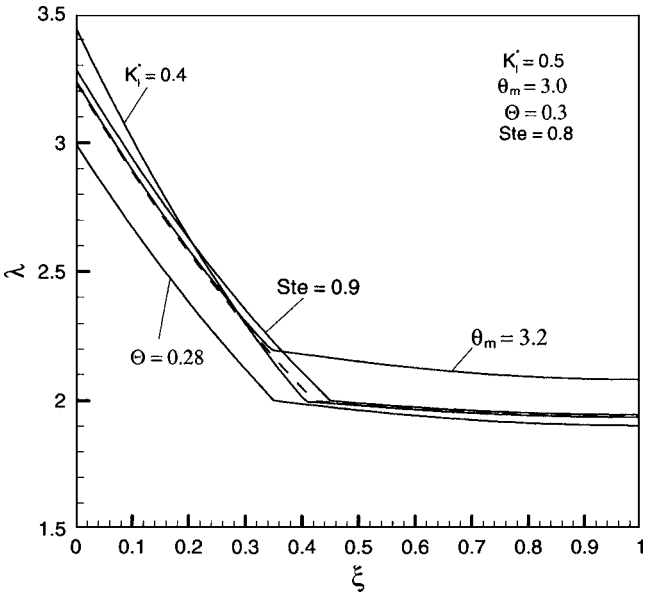

Fig. 10 Dimensionless temperature in a workpiece at a dimensionless time τ=1.5 for different Stefan numbers, dimensionless liquid conductivities, melting temperatures, and plasma flow work-to-heat conduction ratios

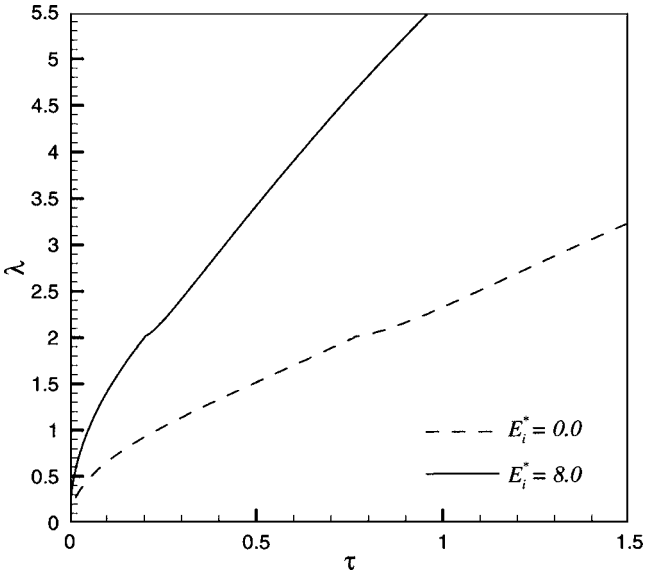

Fig. 11 Dimensionless surface temperature of a workpiece as a function of time for different dimensionless ionization energies

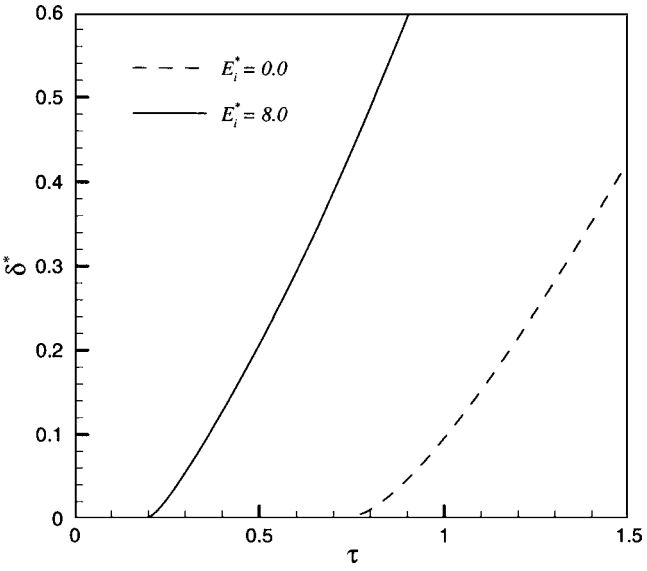

Fig. 12 Dimensionless thickness of the molten layer in a workpiece as a function of time for different dimensionless ionization energies

Conclusions

The conclusions drawn are the following:

1. The dimensionless temperature, thickness and growth rate of the molten layer in a workpiece can be increased by decreasing reflectivities of ions and electrons, electron-to-ion source temperature ratio, and increasing ion-to-electron mass ratio.
2. Dimensionless surface temperature and its increasing rate decrease with reducing the plasma flow work-to-heat conduction ratio. The surface temperature as a function of time before melting remains the same for different values of Stefan number, melting temperature and liquid conductivity. Onset time for melting is delayed by reducing the plasma flow work-to-heat conduction ratio and increasing melting temperature. After melting takes place, surface temperature and its changing rate are increased with increasing Stefan number and decreasing the dimensionless liquid conductivity.
3. Thickness and growth rate of the molten layer in the workpiece are increased by increasing the plasma flow work-to-heat conduction ratio, Stefan number and dimensionless liquid conductivity, and decreasing melting temperature. The effect of the melting temperature on the growth rate is comparatively slight.
4. Energy release from recombination of the ions and electrons on the surface plays the most important role in energy transport to the surface. Recombination energy can contribute the deviation of surface temperature to 1000 K.
5. Plasma heating and melting of the workpiece is important for plasma processing. Melting at the surface is detrimental for operation of fusion devices. In deposition process, temperature of the substrate affected by plasma heat transfer becomes one of the most important technological parameter-defining properties of the coating. It is crucial to control the temperature of the substrate to prevent softening and possible distortion of the finished tool. This work provides quantitative results applicable to determine the temperature and the thickness of the molten layer evolution in the workpiece. The effects of plasma parameters on heating, melting and growth of the molten thickness in the workpiece are found to be significant.

Nomenclature

Bi = Biot number, $Bi = h_\infty s/k_s$
c_p = specific heat
D = Dawson function, as defined in [10,11]
e = electron charge
E_i = ionization energy, $E_i^* = E_i/k_B T_{e0}$
f = liquid fraction, $f = (h - c_p T)/L$
h = enthalpy, or heat transfer coefficient
j = current density, $j^* = j/en_{e0}(k_B T_{e0}/m_i)^{1/2}$
K = dimensionless thermal conductivity ratio, $K = k/k_s$
k_B = Boltzmann constant
L = latent heat
m = particle mass
M = ion-to-electron mass ratio, $M = m_i/m_e$
n = particle density, $n^* = n/n_{e0}$
Q = total energy flux, $Q^* = Q/[n_{e0}k_B T_{e0}(k_B T_{e0}/m_i)^{1/2}]$
s = workpiece thickness, m
Ste = Stefan number, $\mathrm{Ste} = c_p T_\infty/L$
T = temperature
t = time
x, y, z = Cartesian coordinate
Z_i = charge number

Greek letter

γ = energy transmission factor defined in Eq. (19)
Θ = plasma flow work-to-thermal conduction ratio, $\Theta = n_{e0}k_B T_{e0}(k_B T_{e0}/m_i)^{1/2}/(k_s T_\infty/s)$
φ = work function, $\varphi^* = \varphi/k_B T_{e0}$
κ = electron-to-ion source temperature ratio at the presheath edge, $\kappa = T_{e0}/T_{i0}$
θ = dimensionless temperature, $\theta = T/T_\infty$
λ = $(T - T_\infty)/T_\infty = \theta - 1$
ξ = dimensionless coordinate, $\xi = x/s$
ρ = reflectivity, or density
δ = liquid thickness, $\delta^* = \delta/s$
τ = dimensionless time, $\tau = k_s t/\rho c_p s^2$
ϕ, χ = dimensional and dimensionless potential, $\chi = -e\phi/k_B T_{e0}$
Ω, Ω_{1b} = functions, defined in Eqs. (6) and (9)

Superscript

$*$ = dimensionless quantity

Subscript

ab = absorption
b = boundary between sheath and presheath
e = electron
ew = electron variables at the wall
i = ion
ib, iw = ion variables at the sheath edge and wall
ℓ = liquid
m = melting
rec = recombination
s = solid
tot = total
w = wall
0 = initial, or coordinate origin at $\phi = 0$ as shown in Fig. 1
∞ = ambient

References

[1] Chen, F. F., 1974, *Introduction to Plasma Physics*, Plenum Press, New York, Chap. 8.

[2] Bohm, D., 1949, "Minimum Ionic Kinetic Energy for a Stable Sheath," in *The Characteristics of Electrical Discharges in Magnetic Fields*, A. Guthrie and R. Wakerling, eds., McGraw–Hill, New York, Chap. 3, pp. 77–86.

[3] Stangeby, P. C., 1984, "Plasma Sheath Transmission Factors for Tokamak Edge Plasmas," Phys. Fluids, **27**, pp. 682–690.

[4] Benilov, M. S., and Marotta, A., 1995, "A Model of the Cathode Region of Atmospheric Pressure Arcs," J. Phys. D, **28**, pp.1869–1882.

[5] Costanzo, L., Gunn, J. P., Loarer, T., Colas, L., Corre, Y., Ghendrih, Ph., Grisolia, C., Grosman, A., Guilhem, D., Monier-Garbet, P., Reichle, R., Roche, H., and Vallet, J. C., 2001, "Analysis of Energy Flux Deposition and Sheath Transmission Factors during Ergodic Divertor Operation on Tore Supra," J. Nucl. Mater., **290–293**, pp. 840–844.

[6] Mändl, S., Manova, D., and Rauschenbach, B., 2002, "Balancing Incident Heat and Ion Flow for Process Optimization in Plasma Based Ion Implantation," J. Phys. D, **35**, pp. 1141–1148.

[7] Schmitz, H., and Riemann, K.-U., 2002, "Analysis of the Cathodic Region of Atmospheric Pressure Discharges," J. Phys. D, **35**, pp.1727–1735.

[8] Hussla, I., Enke, K., Grünwald, H., Lorenz, G., and Stoll, H., 1987, "In Situ Silicon-Wafer Temperature Measurements during RF Argon-Ion Plasma Etching Via Fluoroptic Thermometry," J. Phys. D, **20**, pp. 889–896.

[9] Emmert, G. A., Wieland, R. M., Mense, A. T., and Davidson, J. N., 1980, " Electric Sheath and Presheath in a Collisionless, Finite Ion Temperature Plasma," Phys. Fluids, **23**, pp. 803–812.

[10] Wei, P. S., and Yeh, F. B., 2000, "Fluid-Like Transport Variables in a Kinetic, Collisionless Plasma Near a Surface With Ion and Electron Reflection," IEEE Trans. Plasma Sci., **28**, pp.1233–1243.

[11] Yeh, F. B., and Wei, P. S., 2004, "Plasma Energy Transport to an Electrically Biased Surface," Int. J. Heat Mass Transfer, **47**, pp. 4019–4029.

[12] Visser, R. J., 1989, "Determination of the Power and Current Densities in Argon and Oxygen Plasmas by in situ Temperature Measurements," J. Vac. Sci. Technol. A, **7**, pp. 189–194.

[13] Zhou, X., Heberlein, J., and Pfender, E., 1994, "Theoretical Study of Factors Influencing Arc Erosion of Cathode," IEEE Trans. Compon., Packag. Manuf. Technol., Part A, **17**, pp. 107–112.

[14] Ye, M. Y., Masuzaki, S., and Shiraishi, K., 1996, "Nonlinear Interactions between High Heat Flux Plasma and Electron-Emissive Hot Material Surface," Phys. Plasmas, **3**, pp. 281–292.

[15] Takamura, S., Ye, M. Y., Kuwabara, T., and Ohno, N., 1998, "Heat Flows through Plasma Sheaths," Phys. Plasmas, **5**, pp. 2151–2158.

[16] Raffray, A. R., and Federici, G., 1997, "RACLETTE: A Model for Evaluating the Thermal Response of Plasma Facing Components to Slow High Power Plasma Transients. Part I: Theory and Description of Model Capabilities," J. Nucl. Mater., **244**, pp. 85–100.

[17] Takaki, K., Takahashi, A., and Fujiwara, T., 1998, "Experimental Study on Heat Flux From an Argon RF Plasma Using Laser Interferometry Method," Jpn. J. Appl. Phys., Part 1 **37**, pp. 3514–3520.

[18] Tsvetkov, I. V., and Tanabe, T., 1999, "The Influence of Electron Emission on Heat Load to the Plasma Facing Materials under Space Charge Limited Condition With an Oblique Magnetic Field," J. Nucl. Mater., **266–269**, pp. 714–720.

[19] Kersten, H., Deutsch, H., Steffen, H., Kroesen, G. M. W., and Hippler, R., 2001, "The Energy Balance at Substrate Surfaces during Plasma Processing," Vacuum, **63**, pp. 385–431.

[20] Bachet, G., Ch e rigier, L., and Doveil, F., 1995, "Ion Velocity Distribution Function Observations in a Multipolar Argon Discharge," Phys. Plasmas, **2**, pp. 1782–1788.

[21] Goeckner, M. J., Goree, J., and Sheridan, T. E., 1992,"Measurements of Ion Velocity and Density in the Plasma Sheath," Phys. Fluids B, **4**, pp. 1663–1670.

[22] Stangeby, P. C., 1986, "The Plasma Sheath," in *Physics of Plasma Wall Interactions in Controlled Fusion* (D. E. Post and R. Behrisch, eds.), Proceedings of NATO Advanced Study Institute, 30 July–10 Aug., 1984, Val-Morin, Quebec, Canada, Plenum, New York, pp. 41–97.

[23] Wei, P. S., and Yeh, F. B., 2000, "Heat Transfer Coefficient in Rapid Solidification of a Liquid Layer on a Substrate," ASME J. Heat Transfer, **122**, pp. 792–800.

[24] Yeh, F. B., Wei, P. S., and Chiu, S. H., 2003, "Distinct Property Effects on Rapid Solidification of a Thin Liquid Layer on a Substrate Subject to Self-Consistent Melting," J. Cryst. Growth, **247**, pp. 563–575.

[25] Masuzaki, S., Ohno, N., and Takamura, S., 1995, "Experimental Study on Plasma Heat Flow to Plasma-Facing Materials," J. Nucl. Mater., **223**, pp. 286–293.

[26] Tamulevičius, S., Babilius, K., and Matiukas, A., 1995, "Temperature Conditions During Arc Discharge Plasma Deposition of Titanium Nitride," Surf. Coat. Technol., **71**, pp. 250–253.

A Two-Temperature Model for Solid-Liquid Phase Change in Metal Foams

Shankar Krishnan

Jayathi Y. Murthy

Suresh V. Garimella[1]
e-mail: sureshg@ecn.purdue.edu

Cooling Technologies Research Center, School of Mechanical Engineering, Purdue University, West Lafayette, Indiana 47907-2088

Transient solid-liquid phase change occurring in a phase-change material (PCM) embedded in a metal foam is investigated. Natural convection in the melt is considered. Volume-averaged mass and momentum equations are employed, with the Brinkman-Forchheimer extension to the Darcy law to model the porous resistance. Owing to the difference in the thermal diffusivities between the metal foam and the PCM, local thermal equilibrium between the two is not assured. Assuming equilibrium melting at the pore scale, separate volume-averaged energy equations are written for the solid metal foam and the PCM and are closed using an interstitial heat transfer coefficient. The enthalpy method is employed to account for phase change. The governing equations are solved implicitly using the finite volume method on a fixed grid. The influence of Rayleigh, Stefan, and interstitial Nusselt numbers on the temporal evolution of the melt front location, wall Nusselt number, temperature differentials between the solid and fluid, and the melting rate is documented and discussed. The merits of incorporating metal foam for improving the effective thermal conductivity of thermal storage systems are discussed. [DOI: 10.1115/1.2010494]

Introduction

Solid-liquid phase change in porous media occurs in many practical applications, such as thermal energy storage, freezing of moist soils, and manufacture of metal-matrix composites. Of particular interest to this study are thermal energy storage units with thermal conductivity enhancers (e.g., metal foams) for transient thermal control of electronics. Here, the phase-change material (PCM) is impregnated into a metal foam. The latent heat of the PCM serves to absorb the heat generated by the electronics, whereas the metal foam helps transport heat from the heat source into the volume of the PCM and helps utilize the PCM more effectively. It is important to understand the flow, heat transfer, and phase change in these systems to better design phase-change energy storage systems for electronics cooling.

Melting and solidification of pure materials coupled with natural convection in the liquid melt has been studied extensively over the years [1–3]. A detailed review of the literature on solid-liquid phase-change heat transfer is given in [4]. Solid-liquid phase-change processes in porous media have also received wide attention as they have many practical applications. Beckermann and Viskanta [5] performed a combined experimental and numerical investigation of phase change occurring in a porous medium. Experiments were performed in a square enclosure with glass beads saturated with gallium. In their mathematical model, they assumed local thermal equilibrium between the glass beads and gallium. Their numerical results, which showed reasonable agreement with experiments, revealed that the solid-liquid interface shape was profoundly influenced by natural convection in the melt and heat conduction in the solid. Jany and Bejan [6] reported a scaling analysis of melting in porous media with local thermal equilibrium between the porous matrix and the PCM; melt convection was also incorporated. They found that the general behavior of the phase change process with a porous medium was similar to that of phase change without the porous medium. The melting phenomenon in porous media was shown to pass through four distinct regimes, each regime being characterized by distinct Nusselt numbers. Bejan [7] reported an analytical study of melting in a confined porous medium saturated with a PCM. Non-Darcian effects were ignored as was the initial subcooling. The local thermal equilibrium assumption was also invoked between the solid and PCM. The liquid Stefan number was found to have a profound effect on the heat transfer and melting rates. Chellaiah and Viskanta studied, numerically and experimentally, the melting of ice in a bed of glass [8] and aluminum [9] beads. They assumed local thermal equilibrium for the numerical model and found reasonable agreement with their experimental results. With the aluminum beads, the agreement between the numerical results and experiments was poor at high Rayleigh numbers, and deviation from local thermal equilibrium was suggested as the cause. A review of the literature on phase-change heat transfer in porous media is available in [10].

Ellinger and Beckermann [11] experimentally investigated the heat transfer enhancement in a rectangular domain partially occupied by a porous layer of aluminum beads. They found that the introduction of a porous layer caused the solid-liquid interface to move faster initially during the conduction-dominated regime. However, the overall melting and heat transfer rates were found to be lower with the porous layer present due to low porosity and permeability. They recommended the use of porous media of higher porosity and permeability with higher Rayleigh numbers for enhancement of melting and heat transfer rates. Tong et al. [12] performed a numerical analysis of the enhancement of melting and heat transfer rates obtained upon incorporating a metal matrix into water, under the assumption of local thermal equilibrium. An order-of-magnitude increase was observed in the heat transfer rate with the metal matrix present. Vesligaj and Amon [13] investigated the passive thermal control of portable electronics using PCMs with thermal conductivity enhancers under unsteady thermal workloads. An epoxy polymer was used as the PCM. The operational performance of portable electronics was found to improve when such a passive thermal storage device was used. Alawadhi and Amon [14] reported numerical and experimental studies on the effectiveness of a thermal control unit composed of an organic PCM and a metal matrix. Modeling the metal matrix using modified effective thermophysical properties was found to yield good agreement with the experiments. Harris et al. [15] presented an approximate theoretical model to analyze the

[1]Author to whom correspondence should be addressed.

Contributed by the Heat Transfer Division for publication in the JOURNAL OF HEAT TRANSFER. Manuscript received July 21, 2004. Final manuscript received November 13, 2004. Review conducted by: N. K. Anand.

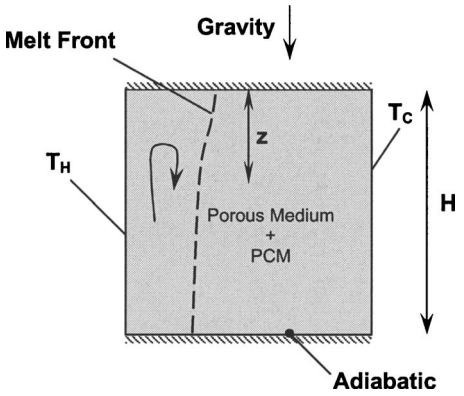

Fig. 1 Schematic of the problem under investigation

phase-change process in a porous medium. Assuming equilibrium melting at the pore scale, a parametric study based on a semi-heuristic conduction model was formulated. The conditions for the existence of local thermal equilibrium were explored. A number of studies have discussed the validity of assuming local thermal equilibrium in porous media saturated by a fluid [16–20].

The objective of the present study is to investigate nonequilibrium thermal transport associated with phase change in a rectangular enclosure containing a metal foam impregnated with PCM. Recently, metal foams have been proposed for thermal management of electronics. Applications studied include heat exchanger units [21], thermal storage units [22], and others [23]. Since the thermal conductivity of the phase-change material considered in the present study is two orders of magnitude lower than that of the metal foam, as is typical of organic PCMs, nonequilibrium thermal effects may play a significant role. A two-temperature model is developed, with separate energy equations for the metal foam and the PCM, including phase change in the PCM. This work builds on a previous analysis of natural convection in a PCM-foam domain, but in which change of phase was not considered [16]. Issues investigated and discussed in this work include natural convection in the melt, the effects of Rayleigh, Stefan, and interstitial Nusselt numbers on the temporal evolution of the melt front location, heat transfer rate, the temperature differentials between the solid and fluid, and the melting rate under local thermal nonequilibrium. The results are compared to local thermal equilibrium models, and the validity of the local thermal equilibrium assumption is discussed.

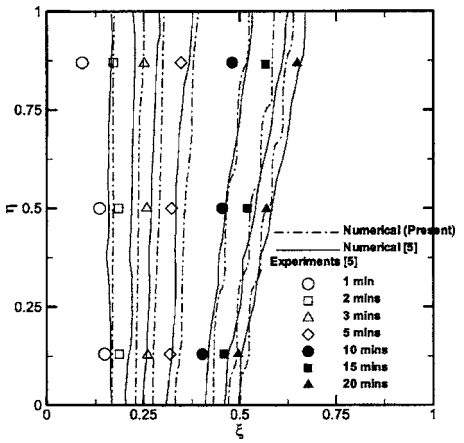

Fig. 2 Comparison of experimentally measured [5] and predicted (from [5] and present work) interface locations at various times

Table 1 Interstitial Nusselt number [26–32]

		Interstitial Nusselt Number, $Nu_{i,d}=\frac{h_i d^2}{k_f}$	Analysis Type	Remarks
1	Wakao and Kaguei [26]	$6(1-\varepsilon)\left[2+1.1(\mathrm{Re})^{0.6}(\mathrm{Pr})^{1/3}\right]$	Experimental, Analytical	For forced convective flow over spheres ($0 < \mathrm{Re} < 8500$, $\varepsilon \sim 0.4$)
2	Hwang et al. [27]	$0.376(\mathrm{Re})^{0.641}(\mathrm{Pr})^{0.37}$	Experimental	For forced flow across metal foams ($40 < \mathrm{Re} < 200$)
3	Calmidi and Mahajan [28]	$(a_{sf}d)C\,\mathrm{Re}^{0.5}\,\mathrm{Pr}^{0.37}$	Experimental	Correlation for forced flow across metal foams ($C = 0.52$, $40 < \mathrm{Re} < 1000$). Originally proposed for forced flow across cylinder.
4	Phanikumar and Mahajan [29]	$(a_{sf}d)C\,\mathrm{Re}^{0.5}\,\mathrm{Pr}^{0.37}$	Experimental	Correlation for forced flow across metal foams ($C = 0.52$, $10^5 < \mathrm{Ra} < 5\times10^5$). Originally proposed for forced flow across cylinder.
5	Kuwahara et al. [30]	$4(1-\varepsilon)\left[\left(1+\frac{4(1-\varepsilon)}{\varepsilon}\right)+\frac{1}{2}(1-\varepsilon)^{1/2}\,\mathrm{Re}^{0.6}\,\mathrm{Pr}^{1/3}\right]$	Numerical	Forced flow across arbitrary geometry ($0 < \mathrm{Re} < 8000$, $0.2 < \varepsilon < 0.9$)
6	Morgan [31]	$\frac{2}{\ln\left(\frac{d_o}{d_m}\right)}$	Analytical	For an infinitely long cylinder in an infinite space.
7	Frankel and Acrivos [32]	$\frac{2a_{sf}d}{(1.372+0.5\ln 2-0.5\ln(\mathrm{Re}\cdot\mathrm{Pr}))}$	Analytical	For shear flow across freely suspended cylinders. The derived solution is for $\mathrm{Re}.\mathrm{Pr}\to 0$.
8	Acrivos and Taylor [32]	$\frac{2}{\ln(\mathrm{Re}\cdot\mathrm{Pr})}$	Analytical	For low Reynolds number flows over cylinders under $\mathrm{Re}.\mathrm{Pr}\to 0$.
9	Resistance Analysis	$\frac{a_{sf}}{\left[\frac{d}{2k_f}+\frac{d_m}{2k_m}\right]}$	Analytical	Resistances in series

Mathematical Formulation and Numerical Modeling

A schematic of the problem under investigation is shown in Fig. 1. A square domain of height H encloses the porous metal foam, which is filled with solid phase change material (PCM). The melting point of the PCM is T^*_{melt}, and the right wall is maintained at T^*_C ($<T^*_{\mathrm{melt}}$). The top and bottom walls are adiabatic. Initially, the solid metal foam and the PCM are at equilibrium at temperature T^*_C. At time $\tau=0$, the left wall temperature is raised to T^*_H ($>T^*_{\mathrm{melt}}$) and the PCM is allowed to melt. The thermophysical properties of the solid metal foam and the PCM are assumed to be constant over the range of temperatures considered. In the liquid state, the PCM is assumed to be incompressible, Newtonian, and subject to the Boussinesq approximation. The densities of the solid and liquid PCM are assumed to be equal, i.e., the volume change upon phase change is ignored. Thermal dispersion effects may be important for very high Rayleigh numbers [24], but are neglected in the present work because of the lack of available models for metal foams. The volume-averaged governing mass and momentum equations in dimensionless terms, subject to the above assumptions, are

$$\nabla\cdot\mathbf{U}=0 \tag{1}$$

$$\frac{1}{\mathrm{Pr}}\left(\frac{1}{\varphi}\frac{\partial\mathbf{U}}{\partial\tau}+\frac{1}{\varphi^2}(\mathbf{U}\cdot\nabla)\mathbf{U}\right)=-\nabla\mathbf{P}+\frac{1}{\varphi}\nabla^2\mathbf{U}-\left(\frac{1}{\mathrm{Da}^2}+\frac{F}{\mathrm{Pr}\cdot\mathrm{Da}}|\mathbf{U}|\right)\mathbf{U}+\mathrm{Ra}\,T^*_f\frac{\mathbf{g}}{|\mathbf{g}|} \tag{2}$$

In Eq. (2), F is the inertial coefficient and $\varphi(=V_l/V)$ is the fraction of liquid PCM in the given volume.

The governing energy equations are written for the metal foam and PCM separately and are closed using an interstitial Nusselt number. Assuming equilibrium melting at the pore scale, i.e., ignoring kinetics effects, the dimensionless energy equations are

$$(1-\varepsilon)\Omega\frac{\partial T^*_m}{\partial\tau}=(1-\varepsilon)\lambda\nabla^2T^*_m-\mathrm{Nu}_i(T^*_m-T^*_f) \tag{3}$$

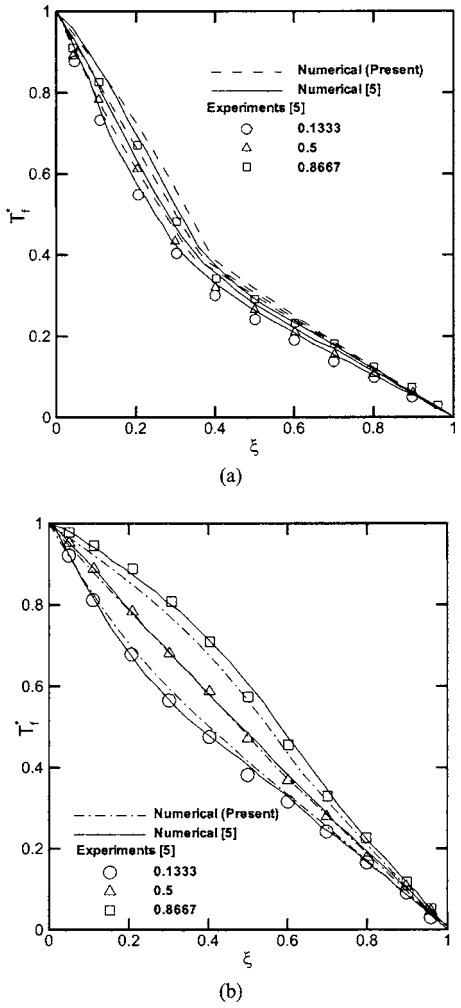

Fig. 3 Comparison of measured [5] and predicted (from [5] and present work) temperature distributions at three different vertical locations at a dimensionless time of (*a*) 1.829 (5 min) and (*b*) 7.314 (20 min)

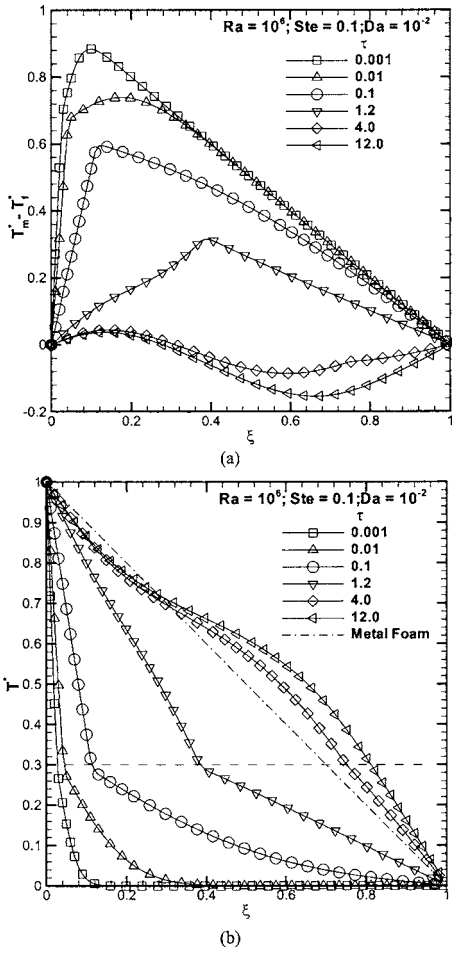

Fig. 4 Predicted temporal evolution of the thermal field for Ra=10^6, Nu_i=0, Ste=0.1, Pr=50, and Da=10^{-2} at the midheight of the domain (η=0.5): (*a*) solid-to-fluid temperature difference, and (*b*) solid and fluid temperature distributions. Also plotted in the figure is the nondimensional melting temperature (horizontal dashed line).

$$\varepsilon\frac{\partial T_f^*}{\partial \tau} + (\mathbf{U}\cdot\nabla)T_f^* = \varepsilon\nabla^2 T_f^* - \frac{\varepsilon}{\mathrm{Ste}}\frac{\partial \gamma}{\partial \tau} - \mathrm{Nu}_i(T_f^* - T_m^*) \tag{4}$$

In Eq. (4), $\gamma(=V_l/V_f)$ is the fraction of liquid in the PCM. As an alternative, if local thermal equilibrium can be assumed, the energy equations (3) and (4) may be replaced by a single energy equation given by

$$[\varepsilon + (1-\varepsilon)\Omega]\frac{\partial T^*}{\partial \tau} + (\mathbf{U}\cdot\nabla)T^* = [\varepsilon + (1-\varepsilon)\lambda]\nabla^2 T^* - \frac{\varepsilon}{\mathrm{Ste}}\frac{\partial \gamma}{\partial \tau} \tag{5}$$

Equation (5) can be obtained from Eqs. (3) and (4) by setting $T_m^* = T_f^* = T^*$ and adding Eqs. (3) and (4). If no porous medium were present, the governing mass, momentum, and energy equations would be obtained by setting $\varepsilon = 1$ and $\mathrm{Da} = \infty$ in Eqs. (1), (2), and (5). The following dimensionless variables are used in deriving Eqs. (1)–(5):

$$\xi = \frac{x}{H};\quad \eta = \frac{y}{H};\quad \tau = \frac{t\alpha_f}{H^2};\quad U = \frac{uH}{\alpha_f};\quad P = \frac{pH^2}{\rho_f \upsilon_f \alpha_f}$$

$$T_s^* = \frac{(T_m - T_C)}{(T_H - T_C)};\quad T_f^* = \frac{(T_f - T_C)}{(T_H - T_C)};\quad T^* = \frac{(T - T_C)}{(T_H - T_C)}$$

The relationship between φ, ε, and γ in the above equations can be expressed as follows:

$$\varphi = \begin{cases} \varepsilon & \text{for } T_f^* \geq T_{\mathrm{melt}}^* + \Delta T^* \\ \varepsilon\left(\dfrac{T_f^* - T_{\mathrm{melt}}^* + \Delta T^*}{2\Delta T^*}\right) & \text{for } T_{\mathrm{melt}}^* - \Delta T^* < T_f^* < T_{\mathrm{melt}}^* + \Delta T^* \\ 0 & \text{for } T_f^* \leq T_{\mathrm{melt}}^* - \Delta T^* \end{cases}$$

Here, phase change is assumed to occur over a small but finite temperature range ΔT^* for numerical stability. For all computations performed in this study a ΔT^* of 0.04 or less was used. In order to model solid-liquid phase-change phenomena in the same grid, the third term in Eq. (2) was used to immobilize the material in the fully solid regime by imposing a small value of K (=1×10^{-10} m^2).

The dimensionless parameters describing the heat and fluid flow processes are

$$\mathrm{Pr} = \frac{\upsilon_f}{\alpha_f};\quad \mathrm{Ra} = \frac{g\beta_f H^3(T_H - T_C)}{\alpha_f \upsilon_f};\quad \mathrm{Da} = \frac{\sqrt{K}}{H}$$

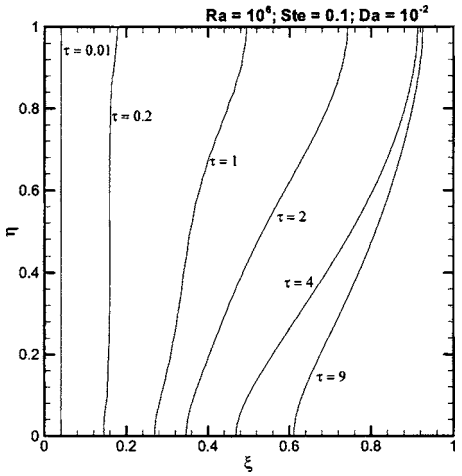

Fig. 5 Predicted temporal evolution of the melt front location for Ra=10^6, Nu_i=0, Ste=0.1, Pr=50, and Da=10^{-2}

$$\mathrm{Nu}_i = \frac{h_v H^2}{k_f}; \quad \mathrm{Ste} = \frac{(C_p)_f (T_H - T_C)}{\Delta H}$$

$$\lambda = \frac{k_m}{k_f}; \quad \lambda_e = \frac{k_{eq}}{k_f} = \varepsilon + (1-\varepsilon)\lambda; \quad \Omega = \frac{(\rho C_p)_m}{(\rho C_p)_f}; \quad F; \quad \varepsilon$$

The effective conductivity is given by $k_{eq}=\varepsilon k_f+(1-\varepsilon)k_m$. The inertial coefficients F for flow over a packed bed of particles [16] and metal foams [25], are $1.75/\sqrt{150\varepsilon^3}$ and 0.068, respectively. For metal foams, a constant porosity of 0.8 is used for all the computations.

The computational domain is discretized into finite volumes using a rectangular mesh. All the variables are stored at the cell centroids. A central-differencing scheme with a deferred correction [26] is used for convective fluxes. A central-differencing scheme is used for discretizing diffusive fluxes as well. The transient terms are discretized using a second-order-accurate three-time-level scheme [26]. The SIMPLE algorithm is used for obtaining the velocity fields, and the linearized systems of equations are solved using a strongly implicit procedure (SIP). The calculations are terminated when the dimensionless residual [26] has dropped at least below 10^{-4} for all governing equations.

Code Validation

The code used in this work was previously validated [16] against the available numerical and experimental studies on natural convection in porous enclosures, but without phase change. Since experimental results are not available in the literature for solid-liquid phase change in metal foams, the code was validated against a study of melting of gallium in a packed bed of glass spheres [5]. The height of the square domain was 4.76 cm and the porosity of the enclosure was 0.385. The boundary conditions were the same as illustrated in Fig. 1. Further details about the experiments and the numerical model are available in [5]. The dimensionless governing parameters used for the present computations for this comparison are $\mathrm{Ra}=8\times10^5$, $\mathrm{Da}=3.7\times10^{-3}$, Ste =0.124, Pr=0.0208, d/H=0.126, λ=0.046, Ω=0.786, and T_m^* =0.3912. The permeability for liquid flow through a packed bed of spherical particles is calculated from [5]

$$K(\varphi) = \frac{d^2\varphi^3}{175(1-\varphi)^2}$$

For closing the two energy equations (3) and (4), the correlation proposed by Wakao and Kaguei [27] was used and is given below

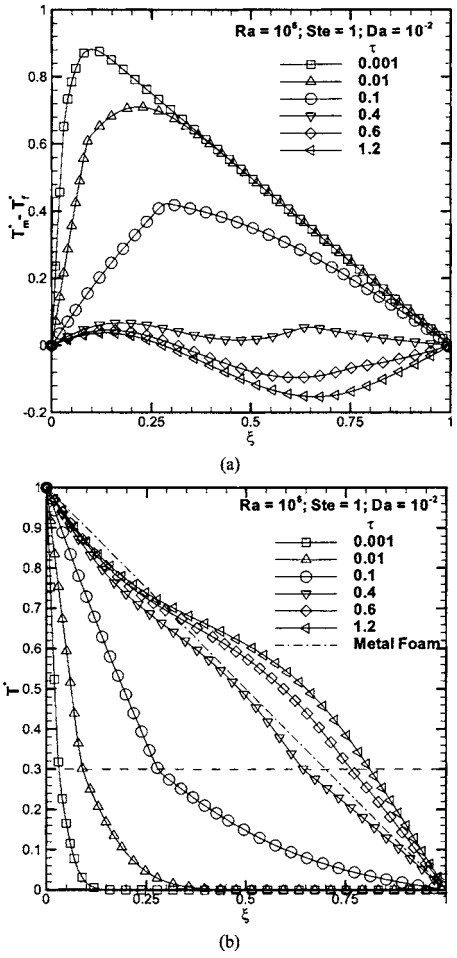

Fig. 6 Predicted temporal evolution of thermal field for Ra =10^6, Nu_i=0, Ste=1.0, Pr=50, and Da=10^{-2} at the midheight of the domain (η=0.5): (*a*) Solid-to-fluid temperature difference, and (*b*) Solid and fluid temperature distributions. Also plotted in the figure is the nondimensional melting temperature (horizontal dashed line).

$$\mathrm{Nu}_{i,d} = 6(1-\varepsilon)[2 + 1.1(\mathrm{Re})^{0.6}(\mathrm{Pr})^{1/3}] \tag{6}$$

This correlation covers a broad range of Reynolds numbers and asymptotes to a constant value for the diffusion-only limit (Re $\rightarrow$0) for spheres. Though this correlation was reported for forced convection, it is assumed to be approximately valid for natural convection in the melt as well. The Reynolds number in Eq. (6) is interpreted as the local Reynolds number based on the local mean velocity, i.e., $u_{\mathrm{mean}}d/\upsilon$. Figure 2 shows the comparison of the computed melt front locations from the present study with those in [5]. The primary difference in the present mathematical model from that in [5] is the relaxation of the assumption of local thermal equilibrium between the solid and the interstitial fluid. The temperature distributions predicted from the present study are compared to those in [5] in Fig. 3 at different vertical (η-direction) locations at two different times. The current predictions show satisfactory agreement with experiments and also agree reasonably well with the numerical predictions in [5], despite the assumption of thermal equilibrium in the latter. This agreement between the numerical results can be attributed to the fact that the system is conduction dominated ($\mathrm{RaDa}^2\sim11$).

Grid independence of the solution for the meshes used in the present simulations was also established. A Rayleigh number of 10^6, Darcy number of 10^{-2}, Prandtl number of 50, Stefan number of 0.1, and porosity of 0.8 were used for this set of calculations.

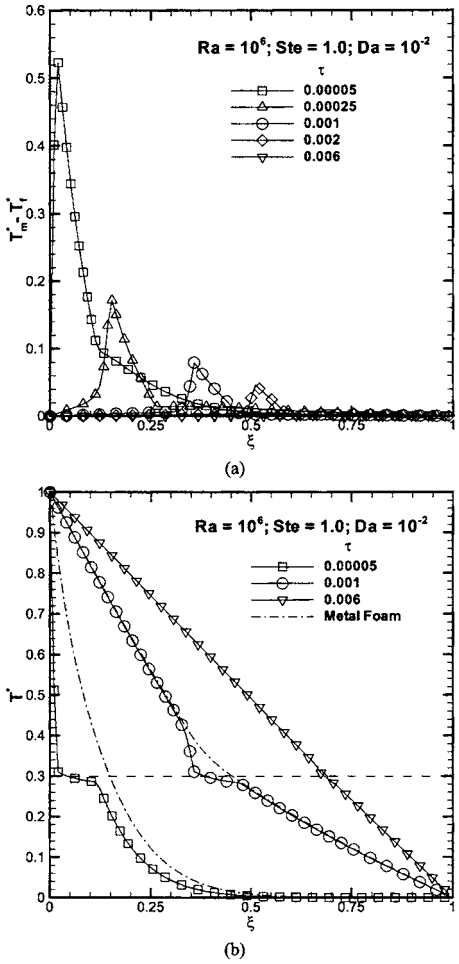

Fig. 7 Predicted temporal evolution of thermal field for Ra $=10^6$, $Nu_{id}=5.9$, Ste=1.0, Pr=50, and $Da=10^{-2}$ at the midheight of the domain ($\eta=0.5$): (*a*) Solid-to-fluid temperature difference, and (*b*) solid and fluid temperature distributions. Also plotted in the figure is the nondimensional melting temperature (horizontal dashed line).

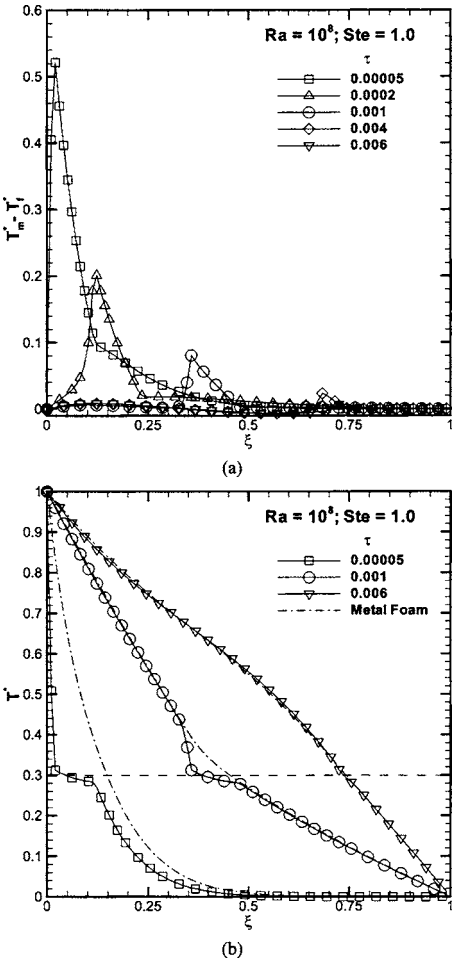

Fig. 9 Predicted temporal evolution of thermal field for Ra $=10^8$, $Nu_{i,d}=5.9$, Ste=1.0, Pr=50, and $Da=10^{-2}$ at the midheight of the domain ($\eta=0.5$): (*a*) Solid-to-fluid temperature difference, and (*b*) solid and fluid temperature distributions. Also plotted in the figure is the nondimensional melting temperature (horizontal dashed line).

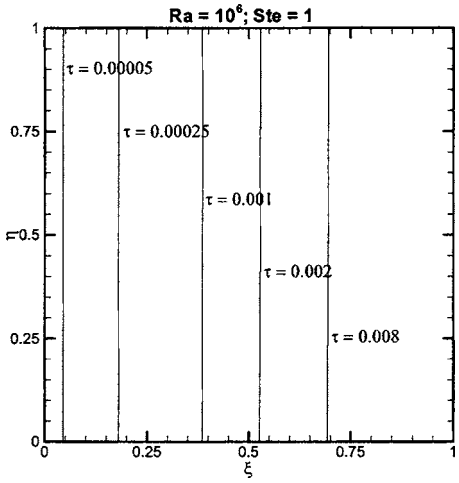

Fig. 8 Predicted temporal evolution of melt front locations ($\gamma=0.5$) for Ra$=10^6$, $Nu_{i,d}=5.9$, Ste=1.0, Pr=50 and $Da=10^{-2}$

Grid sensitivity was tested on three different grids, 48×48 (grid 1), 102×102 (grid 2), and 186×186 (grid 3). For grid 1, deviations of 7.5% and 2% were observed, respectively, in the minimum and maximum solid-to-fluid temperature differences with respect to grid 3 at time $\tau=0.225$. For grid 2 at $\tau=0.225$, the corresponding deviations with respect to grid 3 reduced to 1% and 1.7%. The melt front shapes were almost identical in these latter two cases. The intermediate grid of 102×102 was found to be sufficient for all the calculations presented in this study.

Results and Discussion

The porosity of the metal foam considered is held constant at 0.8 and the pore size (d/H) is 0.0135. The typical ratio of the average ligament diameter d_m of the foam to the mean cell size d is 0.1875, with the average ligament diameter of 0.36 mm [25]. The ratio of the metal foam-to-PCM thermal conductivity λ is 1000. The Prandtl number of the PCM is fixed at 50, which is typical of the value for many organic PCMs.

A correlation similar to Eq. (6) (which was for spherical beads) that covers a broad range of Reynolds numbers was not found in the literature for metal foams. For high-Prandtl-number fluids undergoing phase change in porous enclosures the velocities encountered are small (e.g., the vertical velocity v (m/s) is $O(10^{-3})$ or

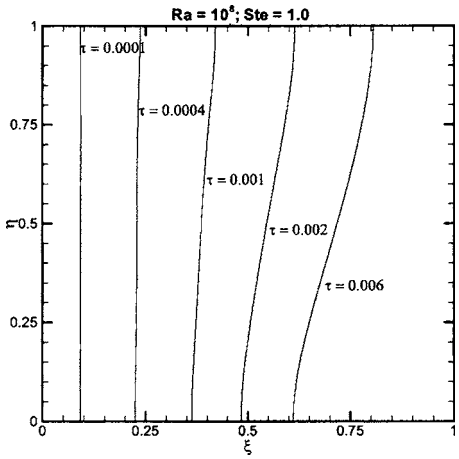

Fig. 10 Predicted temporal evolution of melt front locations (γ=0.5) for Ra=10^8, $Nu_{i,d}$=5.9, Ste=1.0, Pr=50, and Da=10^{-2}

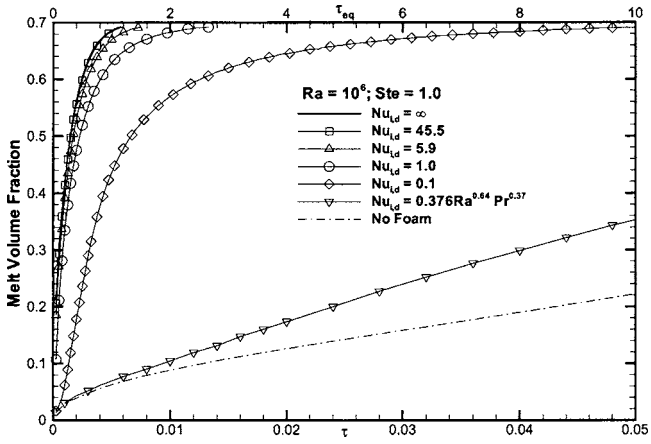

Fig. 11 Predicted melt volume fractions as a function of τ for Ra=10^6, Da=10^{-2}, Ste=1.0, and Pr=50 for various interstitial Nusselt numbers ($Nu_{i,d}$). Also shown are the τ_{eq} (=$\alpha_{eq}t/H^2$) values for comparison.

less for $RaDa^2 \leqslant 10^4$). Also, the heat transfer between the metal foam and the solid PCM is only by conduction during the initial transient. As the system is largely conduction dominated, it is critical to establish the diffusion limit for the interstitial heat transfer coefficients. Table 1 [25,27–32] lists the various models used in the present study for closing the energy equations (3) and (4). Though some of the correlations in Table 1 are for forced convection, they are assumed to be approximately valid for natural convection in the melt as well. The Reynolds number in the equations is interpreted as the local Reynolds number based on the local mean velocity, i.e., $u_{\text{mean}}d/\nu$. As $\text{Re}\rightarrow 0$, some of the equations yield $\text{Nu}_{i,d}=0$, which does not correctly represent the conduction limit. In the equations listed in Table 1, a_{sf} is the specific surface area of the metal foams and is given by the relation [28]

$$a_{sf}=\frac{3\pi d_m}{0.59d^2}\left\{1-\exp\left[-\left(\frac{1-\varepsilon}{0.04}\right)\right]\right\}$$

In the discussion that follows, the "fluid" phase refers to the PCM, whether solid or melted, whereas the "solid" phase refers to the metal foam. In order to understand the effect of interphase heat transfer on the melting of PCM, the case of zero interphase heat transfer ($\text{Nu}_i=0$) is first considered. Under this condition, there is no thermal interaction between the metal foam and the PCM, and the melt experiences only the flow resistance offered by the porous foam. Figure 4(*a*) shows the temporal evolution of the dimensionless solid-to-fluid temperature difference along η=0.5 for Ra=10^6, Pr=50, Da=10^{-2}, $\lambda=10^3$, Ω=1, and T'_{melt}=0.3. The Stefan number for this case is 0.1. Figure 4(*b*) shows the PCM and metal foam temperature distributions at the midheight of the domain. In Fig. 4(*b*) and in other similar figures that follow, the dimensionless metal foam temperature distribution is represented using dotted-dashed lines, whereas the PCM is represented using solid lines with open symbols. Also, the dimensionless melting point is shown as a horizontal dashed line. In the limit of zero interphase heat exchange, the metal foam and PCM develop independently and the temperature difference between them is determined by the relative response of the two phases. The metal foam reaches a steady state in a time scale of order (H^2/α_m), or a dimensionless time scale of $\tau_m\sim\Omega/\lambda$. For low Rayleigh numbers and Ste$<$1, the time for the PCM to reach a steady state is governed by the effective inertia associated with phase change. It scales as H^2/α_{ef} where $\alpha_{ef}=k_f/(\rho_f C_{p_{ef}})$ and $(C_p)_{ef}=(\Delta H\varepsilon)/\Delta T$. The corresponding dimensionless time scale is $\tau_f\sim\varepsilon/\text{Ste}$. The metal foam is seen to have reached a steady state well before the temperature field in the fluid has started to develop. Thus at early times, the temperature differential in the domain is very large, of $O(1)$. The temperature difference progressively decreases with time, reaching a steady-state value over the PCM time scale. Furthermore, the maximum temperature difference between the metal foam and PCM occurs near the solid-liquid interface. This is expected because the phase-change process constrains the PCM temperature to T^*_{melt} at the interface. The thickness of the warm boundary layer ($\sim[\text{RaDa}^2]^{-0.25}$) near the heated wall ceases to grow at a time of order $\varepsilon/(\text{Ste}\sqrt{\text{RaDa}^2})$ [3]. This is the time at which a convective regime in the melt [3] sets in. The time predicted for the onset of the convective regime by Benard et al. [33] is $4.59\varepsilon/(\text{Ste}\sqrt{\text{RaDa}^2})$.

Figure 5 shows the temporal evolution of melt front location for $\text{Nu}_i=0$, Ra=10^6, Ste=0.1, Da=10^{-2}, Pr=50, $\lambda=10^3$, Ω=1, and T^*_{melt}=0.3. Initially, the process is conduction-dominated and the melt front is planar. The horizontal intrusion layer appears in the top half of the domain at a dimensionless time of 0.2 because of the development of natural convection. This denotes the beginning of the convection-plus-conduction regime [3]. The vertical height (see Fig. 1) of the upper portion of the domain z, where convection dominates conduction scales as $(\text{RaDa}^2[\tau_f\,\text{Ste}/\varepsilon]^2)$ [3]. At a nondimensional time of approximately $\varepsilon/(\text{Ste}\sqrt{\text{RaDa}^2})$, the thermal boundary layer ceases to grow and the quasi-steady regime commences. This can also be seen from Figs. 4(*a*) and 4(*b*), where the boundary layer thickness is approximately the same after a nondimensional time of 1.2. In this quasi-steady regime, the movement of the melt front is slow enough that the convective process reaches a steady state before the melt front moves to any significant extent.

The predicted dimensionless solid-to-fluid temperature difference for a higher Stefan number of 1.0 at different times along η=0.5 for all other parameters remaining the same as above ($\text{Nu}_i=0$, Ra=10^6, Da=10^{-2}, Pr=50, $\lambda=10^3$, Ω=1, and T^*_{melt}=0.3) are shown in Fig. 6(*a*). As expected, the increase in Stefan number from 0.1 in Fig. 4 to 1.0 in Fig. 6 expedites the melt front propagation. As noted previously, the metal foam reaches a steady state over a dimensionless time of Ω/λ and the PCM reaches a steady state over a dimensionless time of ε/Ste. A comparison of Figs. 4(*b*) and 6(*b*), in which the temporal evolution of the solid and fluid temperature distributions along η=0.5 is plotted, reveals that the temperature distributions at steady state are identical for the two different Stefan numbers, as expected from Eq. (4). The melt front location for Ste=1.0 is similar to that in Fig. 5, except for the faster evolution of the melt interface, and hence is not shown for brevity. For cases of practical interest, the Stefan number is not large enough to compete with the time scale for the evolution of

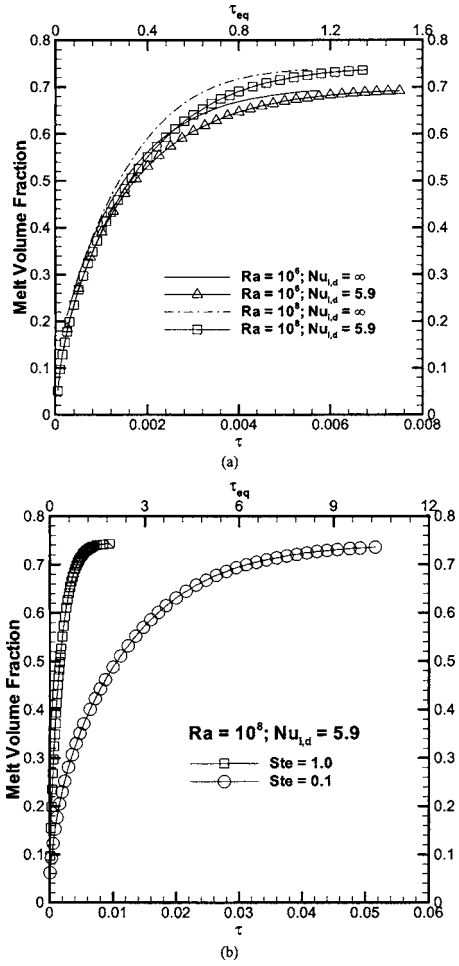

Fig. 12 Predicted melt volume fractions as a function of τ for different Rayleigh, Stefan, and interstitial Nusselt numbers. Also shown are the τ_{eq} values for comparison.

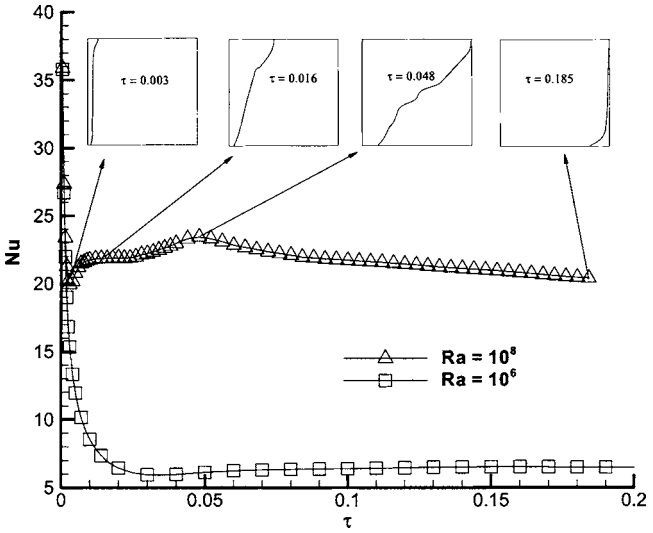

Fig. 13 Predicted hot wall Nusselt number for the no-foam case as a function of τ for Ste=1 and two different Rayleigh numbers. Also shown are the melt fronts at several critical time instants during flow evolution.

the solid temperature profile, and the overall behavior described in Figs. 5 and 6 is expected to be typical for $Nu_i=0$.

The next case considered is one for which the metal foam and PCM exchange energy through interphase transfer ($Nu_i \neq 0$). Figure 7(*a*) shows the dimensionless solid-to-fluid temperature difference at various times along $\eta=0.5$, for $Ra=10^6$, Ste=1.0, $Da=10^{-2}$, $d/H=0.0135$, Pr=50, $\lambda=10^3$, $\Omega=1$, and $T_m^*=0.3$. The interstitial Nusselt number ($Nu_{i,d}$) based on the pore diameter used for the calculations is 5.9. This Nusselt number was obtained from the expression by Morgan [31] in Table 1 using a d_∞/d_m ratio of 10^4. Figure 7(*b*) shows the dimensionless metal foam and PCM temperature distributions along $\eta=0.5$ for the same set of parameters. The metal foam-to-PCM temperature difference is determined by the heat exchange between the metal foam and PCM. If the response time for the heat exchange between the PCM and metal foam ($\tau_i \sim [(1-\varepsilon)\Omega/Nu_i]$) is long compared to the response times of the two phases, the two phases evolve separately, large solid-to-fluid temperature differences exist, and the time to steady state is determined by the slower phase. On the other hand, if the response time for heat exchange is short compared to the response times of the two phases, then the two phases develop together in a coupled manner. For $Nu_i > [(1-\varepsilon)\lambda]$, the interphase exchange time is shorter than the diffusion time for metal foam. For the case in Fig. 7, the interphase exchange time is shorter than both the diffusion time for metal foam as well as that for the PCM (i.e., $\tau_i < \tau_m,\ \tau_f$) and hence the metal foam and the PCM develop together in a coupled manner. Initially, the metal foam-to-PCM temperature difference is very high, but it progressively decreases with time and is driven to a value of zero at steady state. It may be noted that a steady state is reached on a time scale of $O(\Omega/\lambda)$. In the earlier case of $Nu_i=0$, the fluid phase was seen to respond on a time scale of $\tau \sim O(1)$. Here, however, the fluid is seen to evolve faster, on a scale closer to that of the metal foam, as a result of interface exchange. Initially, the metal foam responds faster than the PCM at the hot wall boundary. But since the heat exchange time is shorter than the diffusion scale τ_f for the PCM, heat from the hot boundary travels through the metal and the metal temperature imprints itself on the fluid. Also, as seen in the previous case of $Nu_i=0$, the maximum solid-to-fluid temperature difference occurs at the interface, which is held at T_m^* because of phase change. It may also be noted that the dimensionless solid-to-fluid temperature difference for the uncoupled (Fig. 4) case is not zero at steady state, whereas in the present case, a zero temperature difference is obtained at steady state. Since the fluid temperature distribution is linear across the domain, the amount of melted PCM is less for $Nu_i \neq 0$ than that of $Nu_i=0$; this aspect will be discussed, in detail, later in this paper, as will the effect of variations in the interstitial Nusselt number and Stefan number.

The predicted temporal evolution of the front location for $Ra=10^6$, $Nu_{i,d}=5.9$, Ste=1.0, Pr=50, and $Da=10^{-2}$ is shown in Fig. 8. Contours of the liquid fraction, $\lambda=0.5$ corresponding to the melting temperature (T_{melt}^*) of 0.3, are plotted in Fig. 8. It may be noted, initially at $\tau=0.00005$, from Fig. 7(*b*) that the mushy zone "thickness" is large, i.e., the mushy zone occupies several computational cells because of the presence of the metal matrix. Eventually at steady state ($\tau=0.006$), the mushy zone thickness is confined to a single computational cell. It can be seen from Fig. 8 that the heat transfer process is conduction dominated. The melt front shape is planar throughout the melting process and little natural convection is observed when compared to the $Nu_i=0$ case in Fig. 5.

The effect of increasing Rayleigh number on the dimensionless solid-to-fluid temperature difference is discussed next. Figure 9(*a*) shows the dimensionless solid-to-fluid temperature difference along $\eta=0.5$ for $Ra=10^8$, $Da=10^{-2}$, Ste=1, Pr=50, and $Nu_{i,d}=5.9$. Figure 9(*b*) shows the dimensionless temperature distributions in the metal foam and PCM along $\eta=0.5$ for these parameters. The overall behavior is similar to the $Ra=10^6$ case, albeit with greater convective effects. The solid and fluid temperature

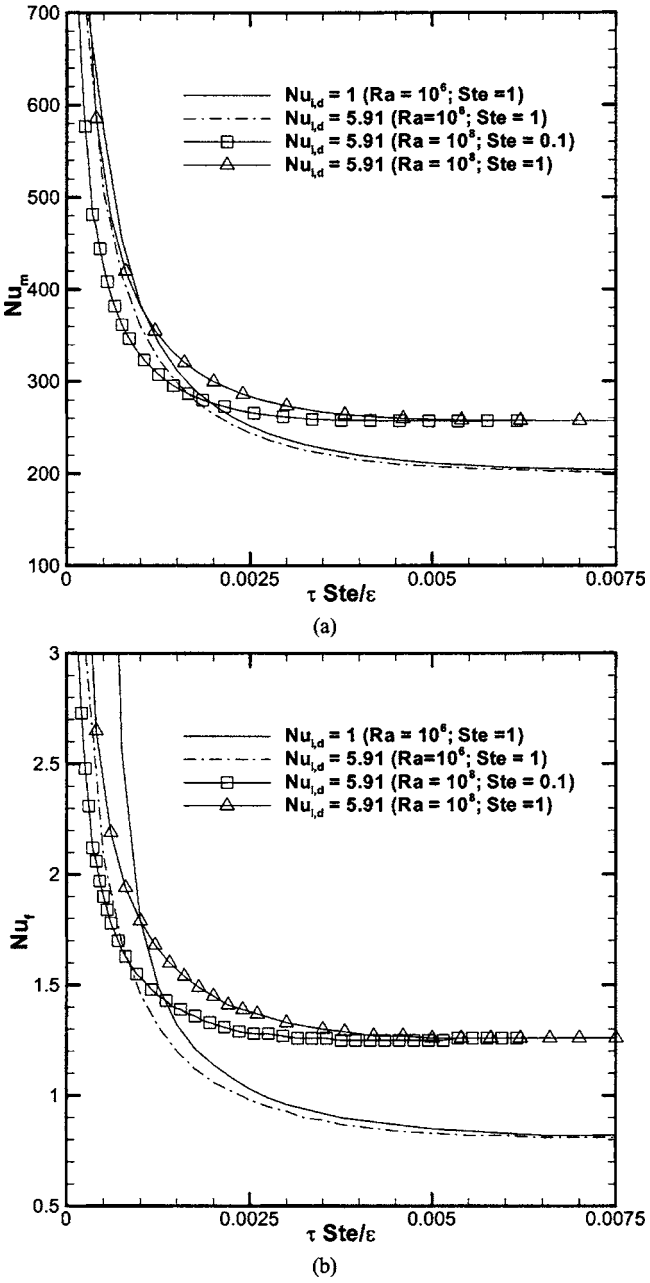

Fig. 14 Predicted hot wall Nusselt number for (*a*) metal foam and (*b*) PCM for various Rayleigh, Stefan, and interstitial Nusselt numbers

profiles are seen to be nearly identical at steady state and exhibit curvature due to convection. The system is driven to steady state on a time scale $O(\Omega/\lambda)$. Figure 10 shows the temporal evolution of the melt front locations for $\mathrm{Ra}=10^8$, $\mathrm{Da}=10^{-2}$, $\mathrm{Ste}=1$, $\mathrm{Pr}=50$, and $\mathrm{Nu}_{i,d}=5.9$. The influence of natural convection on the melt front shape is clear.

A detailed discussion of temperature profiles and melt front shapes for a different Nu_i correlation is outlined in [34]. It is not included here for brevity.

Melt Volume Fraction. From an engineering standpoint, the melt volume fraction and time-dependent average melt front location are of interest in foam-enhanced PCM units. The effect of interstitial heat transfer coefficient on the melted volume is first discussed. Figure 11(*a*) shows the melt volume fraction $(=\Sigma_{\mathrm{cells}}\gamma\Delta x\Delta y)$ as a function of τ for $\mathrm{Ra}=10^6$, $\mathrm{Ste}=1$, $\mathrm{Da}=10^{-2}$, $\mathrm{Pr}=50$, and for different interstitial Nusselt numbers (obtained from various Nu_i relations listed in Table 1 for $\varepsilon=0.8$). Also plotted in the figure for comparison is the nondimensional time τ_{eq} based on the effective conductivity of the system (foam+PCM). As expected, the higher the interstitial Nusselt number, the faster is the rate at which a steady state is achieved. The time to steady state is dictated by the metal foam response time, as discussed previously. For the parameters considered here, the final steady-state profile for both solid and fluid is a straight line for all $\mathrm{Nu}_{i,d}$, and the melt volume fraction is thus the region $T^*>T^*_{\mathrm{melt}}$. Consequently, the melt volume fraction is the same for all the different $\mathrm{Nu}_{i,d}$ values, with the asymptote being $(1-T^*_{\mathrm{melt}})$. For values of $\mathrm{Nu}_{i,d}\geqslant 1$, little difference in the time to steady state is seen as $\mathrm{Nu}_{i,d}$ is increased. For $\mathrm{Nu}_{i,d}>5.9$, the transient response is not particularly distinguishable from that of the equilibrium model $(\mathrm{Nu}_{i,d}\rightarrow\infty)$.

Though not shown here, the melt volume fraction at steady state for $\mathrm{Nu}_i=0$ is 0.8 for the parameter set in this study. For the case when there is no foam, the melt volume fraction is 0.92 at steady state. In the presence of the foam, convective flow in the melt is retarded due to low values of the parameter RaDa^2 (=100) and conduction-dominated profiles result, limiting the melt volume fraction to $(1-T^*_{\mathrm{melt}})$. But for the uncoupled $(\mathrm{Nu}_i=0)$ and the no-foam cases, the fluid temperature distribution is not linear at steady state and convection in the fluid increases the overall melted volume. However, the response time of the system is substantially slower than for the $\mathrm{Nu}_{i,d}>0$ cases. In practical terms, this means less effective cooling during the transient.

In Fig. 12(*a*) the effect of varying the Rayleigh number on the evolution of the melt volume fraction is shown. Also plotted in Fig. 12 is τ_{eq} as in Fig. 11. As the Rayleigh number increases, the convection contribution increases and the melting rate and the melt volume fraction of the PCM also increase somewhat. In Fig. 12(*b*), the effect of decreasing the Stefan number is examined. A decrease in Stefan number from 1.0 to 0.1 with $\mathrm{Ra}=10^8$ decreases the rate of melting due to the thermal inertia associated with phase change and the concomitant increase in the latent heat of fusion. Both cases are computed upto a melt volume fraction of 0.74.

Wall Nusselt Number. In order to compare the performance of the PCM with and without the metal foam, the average Nusselt number at the hot wall for the case without the metal foam case is discussed. The average Nusselt number at the wall is defined as

$$\mathrm{Nu}=\frac{hH}{k_f}=(-1)\int_0^1\left[\frac{\partial T^*}{\partial\xi}\right]_{\xi=0}d\eta$$

In the above equation, T^* is the nondimensional PCM temperature. Figure 13 shows the average Nusselt number at the hot wall for two different Rayleigh numbers (10^6 and 10^8) and $\mathrm{Ste}=1.0$ as a function of dimensionless time. Also plotted in Fig. 13 are the melt front locations for $\mathrm{Ra}=10^8$ for different flow regimes. Initially, at $\tau=0$, when the left wall temperature is raised to T_H, the heat transfer from the wall to the PCM is large, but the Nusselt number falls rapidly as the PCM heats up. Over a time scale $\tau\sim(1-T^*_{\mathrm{melt}})^{5/4}\,\mathrm{Ra}^{-1/2}$ [3], the Nusselt number reaches a low value corresponding to the pure conduction limit [3,34] and starts to increase as convection sets in (referred to as conduction-plus-convection regime in [3]). The increase in Nu $(\sim\tau^{-0.5}+\mathrm{Ra}(\tau)^{3/2}$ [3]) in the convection-plus-conduction regime is very small for $\mathrm{Ra}=10^6$. The "quasi-steady" regime or the convection-dominated regime sets in over a time scale $\tau\sim(\mathrm{Ra})^{-1/2}$ [3]. The Nusselt number is constant in this regime and is computed to be approximately 22 and 7 for $\mathrm{Ra}=10^8$ and 10^6, respectively. The Nusselt number starts to increase again as the melt front nears the cold wall and peaks when the melt front touches the cold wall on a time scale τ of $O(\mathrm{Ra}^{-0.25})$ [3]. The Nusselt number drops again

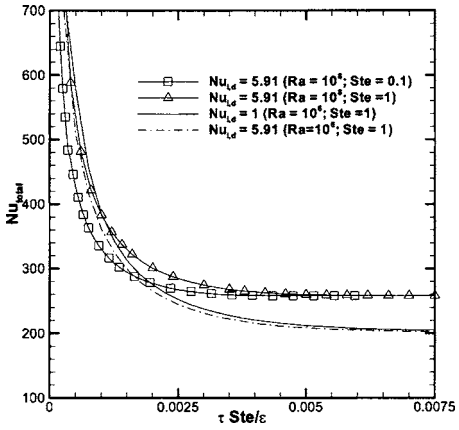

Fig. 15 Predicted total hot wall Nusselt number for various Rayleigh, Stefan, and interstitial Nusselt numbers

when the melt front traverses along the right wall.

The behavior in the presence of the metal foam is markedly different. Figure 14 shows the Nusselt number at the hot wall in this case. The Nusselt number corresponding to the metal foam, Nu_m, and that corresponding to the PCM, Nu_f, are shown. Figure 15 shows the total heat transfer from the hot wall to the system. This Nusselt number is defined as

$$\mathrm{Nu}_{\mathrm{total}} = \mathrm{Nu}_m + \mathrm{Nu}_f = -(1-\varepsilon)\lambda \int_0^1 \left[\frac{\partial T_m^*}{\partial \xi}\right]_{\xi=0} d\eta - \varepsilon \int_0^1 \left[\frac{\partial T_f^*}{\partial \xi}\right]_{\xi=0} d\eta$$

The case of $\mathrm{Ra}=10^6$, $\mathrm{Da}=10^{-2}$, and $\mathrm{Ste}=1$ is considered first. Initially, at $\tau=0$, the heat transfer from the wall is large, but drops rapidly as both the metal and PCM heat up. In the presence of the foam, heat transfer is conduction dominated and at steady state, the dimensionless temperature gradient at the wall for both metal foam and PCM is unity. Hence, $\mathrm{Nu}_{\mathrm{total}} \sim \varepsilon + (1-\varepsilon)\lambda$. This is true for both the $\mathrm{Nu}_{i,d}$ values plotted in Fig. 14. As the Rayleigh number is increased, the Nusselt number at the wall increases due to increased natural convection. The increase in the Nusselt number for metal foam is manifested as a distortion in the metal foam isotherms because of coupling with the PCM (see Figure 9(*b*)). The greatest contribution to sensible heat transfer from the hot wall is due to the metal. The fluid primarily contributes to the phase change heat transfer and heat from the hot wall is conveyed to it by the metal.

Conclusions

A parametric study of the transient melting of PCMs integrated into metal foams for enhanced effective thermal conductivity has been investigated for the case of a step change in boundary temperature. A number of important results have been obtained. For the range of parameters considered, for metal foams with interstitial Nusselt numbers $\mathrm{Nu}_{i,d} > 5.9$, a single-temperature model is sufficient for analysis. But for smaller $\mathrm{Nu}_{i,d}$ values, the metal foam and the PCM are sufficiently out of equilibrium that a two-temperature model is necessary. The metal foam is seen to act in two ways. First, it substantially dampens convective flow because of frictional resistance. Second, since the metal responds far faster than the fluid, the linear temperature profile in the metal tends to imprint itself on the fluid, leading to conductionlike temperature profiles for $\mathrm{Ra} \leqslant 10^6$. Even at $\mathrm{Ra}=10^8$, only a mild departure from the conduction temperature profile is seen. As a result, the melt volume fraction at steady state, which is a measure of the total heat that can be absorbed, is approximately $(1-T^*_{\mathrm{melt}})$. This value may be less than that obtained without the metal foam because of the damping of convective flow. The metal foam acts to substantially decrease the response time of the system and may, thus, lead to far less overheating during the transient, despite the smaller melt volume fraction at steady state.

This study has investigated the transients due to a step change in boundary temperature. In many applications, periodic pulsed heating may be used. The difference in response time between systems with and without metal foam enhancers has important implications for the management of transient energy pulses. If the time scale of the energy pulse is short compared to the response time of the system, local overheating is possible. Since the metal foam response time is typically far faster than typical energy pulse time scales, it would tend to perform far better than systems without metal foams. These aspects must be investigated further to gain a clearer understanding of pulsed heating.

Acknowledgment

Support for this work from industry members of the Cooling Technologies Research Center, an NSF Industry/University Cooperative Research Center (www.ecn.purdue.edu/CTRC), is gratefully acknowledged.

Nomenclature

a_{sf} = specific surface area, m^{-1}
$\mathrm{C_p}$ = isobaric specific heat, $\mathrm{JKg^{-1}\,K^{-1}}$
Da = Darcy number
d = particle diameter or mean pore diameter, m
F = inertial coefficient
$\mathbf{g}$ = gravity vector, $\mathrm{ms^{-2}}$
H = height of the enclosure, m
h_v = volumetric heat transfer coefficient, $\mathrm{Wm^{-3}\,K^{-1}}$
K = permeability, $\mathrm{m^2}$
k = thermal conductivity, $\mathrm{Wm^{-1}\,K^{-1}}$
k_e = equivalent thermal conductivity, $\mathrm{Wm^{-1}\,K^{-1}}$
Nu = Nusselt number based on the porous foam height
Nu_i = interstitial Nusselt number $(h_v H^2/k_f)$
$\mathrm{Nu}_{i,d}$ = interstitial Nusselt number based on pore diameter $(h_v d^2/k_f)$
P = pressure, $\mathrm{Nm^{-2}}$
Pr = Prandtl number
Ra = Rayleigh number
Re = Reynolds number
Ste = Stefan number
T = temperature, K
t = time, s
$\mathbf{U}$ = velocity vector, $\mathrm{ms^{-1}}$
V = volume
u, v = velocity in x and y directions, $\mathrm{ms^{-1}}$
x, y = Cartesian coordinates

Greek Symbols

α = thermal diffusivity, $\mathrm{m^2\,s^{-1}}$
β = coefficient of thermal expansion, $\mathrm{K^{-1}}$
ΔH = enthalpy of freezing/melting, $\mathrm{JKg^{-1}}$
ΔT = mushy zone thickness, $\mathrm{K^{-1}}$
ε = porosity
γ = fraction of liquid melt in the PCM
η = dimensionless y coordinate
φ = fraction of liquid PCM $(=\varepsilon\gamma)$
λ = ratio of thermal conductivities of metal foam and fluid
λ_e = ratio of equivalent thermal conductivity to fluid thermal conductivity
μ = dynamic viscosity, $\mathrm{N\,sm^{-2}}$
υ = kinematic viscosity, $\mathrm{m^2\,s^{-1}}$
ρ = density, $\mathrm{kg\,m^{-3}}$

τ = dimensionless time
ξ = dimensionless x coordinate
Ω = ratio of volumetric heat capacities of metal foam and fluid

Subscripts

C = cold
d = diameter
ef = effective fluid property
eq = equivalent
f = fluid (PCM)
H = hot/height of enclosure
l = liquid
p = pore or particle
m = metal foam
s = solid (PCM)

Superscripts

$*$ = dimensionless quantity
n = time step n

References

[1] Sparrow, E. M., Patankar, S. V., and Ramadhyani, S., 1977, "Analysis of Melting in the Presence of Natural Convection in the Melt Region," ASME J. Heat Transfer, **99**, pp. 520–526.
[2] Gau, C., and Viskanta, R., 1986, "Melting and Solidification of a Pure Metal on a Vertical Wall," ASME J. Heat Transfer, **108**, pp. 174–181.
[3] Jany, P., and Bejan, A., 1988, "Scaling Theory of Melting With Natural Convection in an Enclosure," Int. J. Heat Mass Transfer, **31**, pp. 1221–1235.
[4] Yao, L. S., and Prusa, J., 1989, "Melting and Freezing," Adv. Heat Transfer, **19**, pp. 1–95.
[5] Beckermann, C., and Viskanta, R., 1988, "Natural Convection Solid/Liquid Phase Change in Porous Media," Int. J. Heat Mass Transfer, **31**, pp. 35–46.
[6] Jany, P., and Bejan, A., 1988, "Scales of Melting in the Presence of Natural Convection in a Rectangular Cavity Filled With Porous Medium," ASME J. Heat Transfer, **110**, pp. 526–529.
[7] Bejan, A., 1989, "Theory of Melting With Natural Convection in an Enclosed Porous Medium," ASME J. Heat Transfer, **111**, pp. 407–415.
[8] Chellaiah, S., and Viskanta, R., 1990, "Natural Convection Melting of a Frozen Porous Medium," Int. J. Heat Mass Transfer, **33**, pp. 887–899.
[9] Chellaiah, S., and Viskanta, R., 1990, "Melting of Ice-Aluminum Balls Systems," Exp. Therm. Fluid Sci., **3**, pp. 222–231.
[10] Viskanta, R., 1991, "Phase Change Heat Transfer in Porous Media," *Proc. of 3rd Int. Symp. on Cold Region Heat Transfer*, University of Alaska, Fairbanks, pp. 1–24.
[11] Ellinger, E. A., and Beckermann, C., 1991, "On the Effect of Porous Layers on Melting Heat Transfer in an Enclosure," Exp. Therm. Fluid Sci., **4**, pp. 619–629.
[12] Tong, X., Khan, J. A., and Amin, M. R., 1996, "Enhancement of Heat Transfer by Inserting a Metal Matrix into a Phase Change Material," Numer. Heat Transfer, Part A, **30**, pp. 125–141.
[13] Vesligaj, M. J., and Amon, C. H., 1999, "Transient Thermal Management of Temperature Fluctuations During Time Varying Workloads on Portable Electronics," IEEE Trans. Compon. Packag. Technol., **22**, pp. 541–550.
[14] Alawadhi, E. M., and Amon, C. H., 2003, "PCM Thermal Control Unit for Portable Electronic Devices: Experimental and Numerical Studies," IEEE Trans. Compon. Packag. Technol., **26**, pp. 116–125.
[15] Harris, K. T., Haji-Sheikh, A., and Agwu Nnanna, A. G., 2001, "Phase-Change Phenomena in Porous Media—A Non-Local Thermal Equilibrium Model," Indian J. Pure Appl. Phys., **44**, pp. 1619–1625.
[16] Krishnan, S., Murthy, J. Y., and Garimella, S. V., 2004, "A Two-Temperature Model for Analysis of Passive Thermal Control Systems," ASME J. Heat Transfer, **126**, pp. 628–637.
[17] Minkowycz, W. J., Haji-Sheikh, A., and Vafai, K., 1999, "On Departure From Local Thermal Equilibrium in Porous Media Due to a Rapidly Changing Heat Source: The Sparrow Number," Int. J. Heat Mass Transfer, **42**, pp. 3373–3385.
[18] Nield, D. A., and Bejan, A., 1992, *Convection in Porous Media*, Springer-Verlag, New York.
[19] Vafai, K., and Sozen, M., 1990, "An Investigation of a Latent Heat Storage Porous Bed and Condensing Flow Through it," ASME J. Heat Transfer, **112**, pp. 1014–1022.
[20] Kaviany, M., 1995, *Principles of Heat Transfer in Porous Media*, Springer-Verlag, New York.
[21] Boomsma, K., Poulikakos, D., and Zwick, F., 2003, "Metal Foams as Compact High Performance Heat Exchangers," Mech. Mater., **35**, pp. 1161–1176.
[22] Price, D. C., 2003, "A Review of Selected Thermal Management Solutions for Military Electronic Systems," IEEE Trans. Compon. Packag. Technol., **26**, pp. 26–39.
[23] Ashby, M. F., Evans, A., Fleck, N. A., Gibson, L. J., Hutchinson, J. W., and Wadley, H. J. G., 2000, *Metal Foams: A Desgin Guide*, Butterworth-Heinemann, Boston.
[24] Amiri, A., and Vafai, K., 1994, "Analysis of Dispersion Effects and Non-Thermal Equilibrium, Non-Darcian, Variable Porosity Incompressible Flow Through Porous Media," Int. J. Heat Mass Transfer, **37**, pp. 939–954.
[25] Hwang, J. J., Hwang, G. J., Yeh, R. H., and Chao, C. H., 2002, "Measument of Interstitial Convective Heat Transfer Coefficient and Frictional Drag for Flow Across Metal Foams," ASME J. Heat Transfer, **124**, pp. 120–129.
[26] Ferziger, J. H., and Peric, M., 1995, *Computational Methods for Fluid Dynamics*, Springer-Verlag, Berlin.
[27] Wakao, N., and Kaguei, S., 1982, *Heat and Mass Transfer in Packed Beds*, Gordon and Beach, New York, NY.
[28] Calmidi, V. V., and Mahajan, R. L., 2000, "Forced Convection in High Porosity Metal Foams," ASME J. Heat Transfer, **122**, pp. 557–565.
[29] Phanikumar, M. S., and Mahajan, R. L., 2002, "Non-Darcy Natural Convection in High Porosity Metal Foams," Int. J. Heat Mass Transfer, **45**, pp. 3781–3793.
[30] Kuwahara, F., Shirota, M., and Nakayama, A., 2001, "A Numerical Study of Interfacial Convective Heat Transfer Coefficient in Two-Energy Equation Model for Convection in Porous Media," Int. J. Heat Mass Transfer, **44**, pp. 1153–1159.
[31] Morgan, V. T., 1975, "The Overall Convective Heat Transfer From Smooth Circular Cylinders," Adv. Heat Transfer, **11**, pp. 199–264.
[32] Frankel, N. A., and Acrivos, A., 1968, "Heat and Mass Transfer From Small Spheres and Cylinders Freely Suspended in Shear Flow," Phys. Fluids, **11**, pp. 1913–1918.
[33] Benard, C., Gobin, C., and Martinez, F., 1985, "Melting in Rectangular Enclosures: Experiments and Numerical Simulations," ASME J. Heat Transfer, **107**, pp. 794–803.
[34] Krishnan, S., Murthy, J. Y., and Garimella, S. V., 2004, "A Two-Temperature Model for Solid/Liquid Phase Change in Metal Foams," *Proc. ASME Heat Transfer/Fluids Engineering Summer Conf.*, ASME, New York, ASME Paper No. HT-FED2004-56337, Charlotte, NC, July 2004.

Thermal Behavior and Geometry Model of Melt Pool in Laser Material Process

Lijun Han

Frank W. Liou[1]

Srinivas Musti

Department of Mechanical and Aerospace Engineering,
University of Missouri-Rolla,
Rolla, MO 65409, USA

Melt pool geometry and thermal behavior control are essential in obtaining consistent building performances, such as geometrical accuracy, microstructure, and residual stress. In this paper, a three dimensional model is developed to predict the thermal behavior and geometry of the melt pool in the laser material interaction process. The evolution of the melt pool and effects of the process parameters are investigated through the simulations with stationary and moving laser beam cases. The roles of the convection and surface deformation on the heat dissipation and melt pool geometry are revealed by dimensionless analysis. The melt pool shape and fluid flow are considerably affected by interfacial forces such as thermocapillary force, surface tension, and recoil vapor pressure. Quantitative comparison of interfacial forces indicates that recoil vapor pressure is dominant under the melt pool center while thermocapillary force and surface tension are more important at the periphery of the melt pool. For verification purposes, the complementary metal oxide semiconductor camera has been utilized to acquire the melt pool image online and the melt pool geometries are measured by cross sectioning the samples obtained at various process conditions. Comparison of the experimental data and model prediction shows a good agreement. [DOI: 10.1115/1.2005275]

Keywords: Laser Processing, Melt Pool, Convection, Free Surface

1 Introduction

Laser material interaction is encountered in a variety of industrial manufacturing processes, such as laser aided material deposition, part repair, surface hardening, alloy, and welding. Although the individual applications vary greatly, a general description of the laser manufacturing process involves utilizing a laser to melt the substrate surface to form the melt pool. The dimensions and shape of the melt pool are determined by the process conditions such as laser power and processing speed. Accurate prediction of the melt pool geometry will facilitate obtaining an optimum building performance. Compared to the conventional technologies, laser aided manufacturing technology has the ability to produce parts requiring high accuracy and flexibility. However, due to the highly localized heating property of the laser beam, a huge thermal gradient exists across the melt pool and into the bulk base material. Since mechanical properties are dependent on the microstructure of material, which in turn is a function of the thermal history of solidification, a deep understanding of the melt pool thermal behavior is of special interest.

Since Rosenthal [1] first derived conductive analytical solutions for linear two- and three-dimensional heat flow across a semi-infinite thin substrate with point, linear, and plane heat source, solutions of the moving heat source problem have been approached further. In the area of laser application, conduction based analytical solutions have been adapted widely for process control due to the fast response requirement. In order to obtain an analytical solution, some conductive models [2–7] have simplified melt pool behavior by assuming that the melt pool has a uniform temperature distribution and fixed geometry or neglecting latent heat release/absorption during melting/solidification process. However, as stated in [8] convection plays prominent roles in the molten region and the conduction model lacks the ability to accurately predict the melt pool behavior and the geometry. In fact, many physical phenomena occurred during the process are nonlinear, such as phase change, surface tension, Marangoni effect, and vapor recoil pressure, etc. In such a situation, it is extremely challenging to find an analytical solution for a comprehensive model which can account for the above complicated phenomena. Due to the importance of the convection, various numerical models have been developed in the past two decades to simulate the heat transfer and fluid flow in the melt pool for both steady state and transient situations. In order to simplify the implementation or to concentrate on special issues, some of them [9–11] assumed that the top surface of the melt pool is flat. However, this assumption may induce the noticeable difference with the real cases under high laser power level circumferences, in which the large interfacial forces such as surface tension and thermocapillary force will cause apparent deformation of the melt pool surface. Based on previous reviews, it can be said that although the analysis and investigation of melt pool thermal behavior have been well documented, it is still of essential interest to develop a comprehensive model, which does not preassume the melt pool shape; at the same time, effects of various factors can be quantitatively compared. In very high laser power situations, accurate prediction of melt pool thermal behavior need to consider the plasma phenomenon, which has not been included in the current model.

Interaction process between laser beam and base material determines the part geometry accuracy and properties; hence, sensory monitoring of the melt pool thermal behavior is of primary importance in understanding the nature and mechanisms. In past years, numerous experiments have been conducted to calibrate melt pool shape and temperature. Voelkel and Mazumder [12] obtained a direct image of the weld pool using a CCD video camera with a telephoto lens to monitor the melt pool geometry. Lim et al. [13] suggest an in-process monitoring method utilizing a point infrared sensor to measure the absorbed energy and temperature for the pulsed laser spot welding. Beersiek [14] presented a monitoring system to observe the welding process based on a CMOS camera. Some other attempts on capturing the image of the melt pool have been reported in [15–18].

[1]Corresponding author; E-mail address: liou@umr.edu

Contributed by the Heat Transfer Division for publication in the JOURNAL OF HEAT TRANSFER. Manuscript receieved: September 1, 2004. Final manuscript received: April 25, 2005. Review conducted by: Ranga Pitchumani.

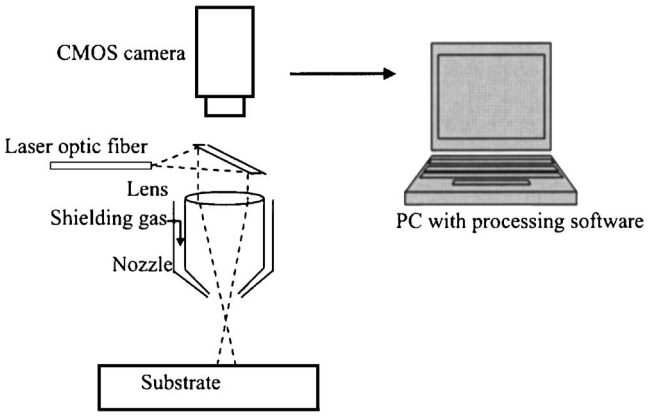

Fig. 1 Experimental apparatus and setup

In this paper, the experimental setup and technique used for the measurement of the melt pool geometry is discussed. The CMOS camera was installed right above the nozzle head to obtain a better view of the melt pool image. The experimental samples were cross sectioned for the melt pool geometry analysis. Following the description of the experimental procedure, a comprehensive 3D mathematical model was presented, and the model considered most physical phenomena taking place in the processing. Simulation predictions were compared to the experimental results for both the stationary laser case and moving laser case at various process conditions. The effects of convection and surface deformation on the heat transfer and melt pool shape are analyzed. The relative importance of three interfacial forces which determine the melt pool thermal dynamics are further discussed. The paper ends with a brief section summarizing the conclusions.

2 Experimental Setup

The experiments were conducted on the close-loop controlled LAMP system, which consists of four units: 2.5 kw Rofin Sinar Nd:YAG laser, Fadal 5-axis CNC machine, powder-feeder subsystem and monitoring subsystem. The experimental apparatus and setup is illustrated in Fig. 1. The laser was operated at continuous wave (cw) mode and defocused to a beam spot of 0.7 mm diameter. The monitoring subsystem includes a CMOS camera and image process software. The smart digital CMOS camera is a powerful standalone vision-capture device and has the capability to measure the melt pool and adjacent region simultaneously. Compared to the typical CCD camera, the CMOS camera converts the light intensity to voltage in a logarithmic manner other than linear which expands measurement range. This feature allows the CMOS camera to work efficiently at such a strong light intensity circumference as the laser material process. In these experiments, due to the small distance between the nozzle and substrate, the CMOS camera was mounted coaxially on the top of the nozzle head to have a direct view of the melt pool without blocking it. Moreover, coaxial installation has an advantage over a system viewing at an angle since it provides direct dimensions of the melt pool without the need for additional transformations. Although the image monitoring subsystem together with the image process software can obtain the melt pool length and width dynamically, online measurement of the melt pool depth remains a difficult issue. In order to validate the model prediction of the melt pool geometry, especially for melt pool penetration, the samples were cross sectioned by an abrasive cutoff wheel and polished to 3 μm surface finish, and then etched by HNO_3 to identify the profile of the fusion zone. The materials selected as the substrate are H13 tool steel and stainless steel 304. The thermal material properties used in the simulations are summarized in Table 1.

Table 1 Material properties and process conditions used in the simulation (Ref. [27])

Property	Symbol	Value (unit)
Solid specific heat	c_s	460 J/kgK
Liquid specific heat	c_l	480 J/kgK
Solid thermal conductivity	k_s	29 W/mK
Liquid thermal conductivity	k_l	29 W/mK
Solid density	ρ_s	7760 kg/m^3
Liquid density	ρ_l	7000 kg/m^3
Latent heat of fusion	L_m	2.5×10^5 J/kg
Latent heat of evaporation	L_v	6.0×10^6 J/kg
Melting temperature	T_m	1730 K
Boiling temperature	T_v	3400 K
Laser absorptivity	η	0.2
Dynamic viscosity	μ_l	6×10^{-3} kg/ms
Radiation emissivity	ε	0.3
Laser power	P	300–1000 W
Process speed	V	6.3–17 mm/s
Laser beam radius	r	3.5×10^{-4} m
Surface tension coefficient	γ	1.9 N/m
Surface tension coeff. with temperature	$\frac{\partial\gamma}{\partial T}$	-4.3×10^{-4} N/mK
Atmosphere pressure	P_∞	1.013×10^5 Pa
Stefan-Boltzmann's constant	σ	5.67×10^{-8} W/m^2 K^4
Vaporization constant	B_0	1.78×10^{10} Pa
Ambient pressure coefficient	A	0.55
Magnitude of the sound velocity	V_0	4512 m/s

3 Mathematical Model

When the intense laser beam irradiates on the substrate surface, the melt pool will appear beneath the laser beam and it moves along with the motion of the laser beam. In order to interpret the interaction mechanisms between laser beam and substrate, computational domain in this study includes the melt pool and adjacent region. The governing equations [19,20] for the conservation of mass, momentum, and energy can be expressed in the following form:

$$\frac{\partial}{\partial t}(\rho) + \nabla\cdot(\rho\mathbf{V}) = 0, \tag{1}$$

$$\frac{\partial}{\partial t}(\rho\mathbf{V}) + \nabla\cdot(\rho\mathbf{V}\mathbf{V}) = \nabla\cdot\left(\mu_l\frac{\rho}{\rho_l}\nabla\mathbf{V}\right) - \nabla p - \frac{\mu_l}{K}\frac{\rho}{\rho_l}(\mathbf{V}-\mathbf{V}_s) + \rho\mathbf{g}, \tag{2}$$

$$\frac{\partial}{\partial t}(\rho h) + \nabla\cdot(\rho\mathbf{V}h) = \nabla\cdot(k\nabla T) - \nabla\cdot[\rho(h_l-h)(\mathbf{V}-\mathbf{V}_s)], \tag{3}$$

where ρ, $\mathbf{V}$, p, μ, T, k, and h are density, velocity vector, pressure, molten fluid dynamic viscosity, temperature, conductivity, and enthalpy, respectively. K is the permeability of mushy zone, $\mathbf{V}_s$ is moving velocity of substrate with respect to laser beam and subscriptions of s and l represent solid and liquid phases. Since the solid and liquid phases may coexist in the same calculation cell at the mushy zone, mixed types of thermal physical properties [19,20] are applied in the numerical implementation as shown below:

$$\rho = g_s\rho_s + g_l\rho_l, \tag{4}$$

$$c = f_s c_s + f_l c_l, \tag{5}$$

$$k = g_s k_s + g_l k_l, \tag{6}$$

$$h = f_s h_s + f_l h_l, \tag{7}$$

$$\mathbf{V} = f_s \mathbf{V}_s + f_l \mathbf{V}_l, \tag{8}$$

here, f_s and f_l refer to mass fractions of solid and liquid phases, and g_s and g_l are volume fractions of solid and liquid phases. The mixture properties are also valid in melt pool region and solid region since corresponding volume fractions will go to zero or unity. Absorbed or released latent heat during the melting and solidification process is incorporated in the enthalpy terms for solid and liquid, which can be defined as:

$$h_s = \int_0^T c_s dT = c_s T, \tag{9}$$

$$h_l = \int_0^{T_s} c_s dT + L_m + \int_{T_s}^T c_l dT = c_l T + (c_s - c_l) T_s + L_m. \tag{10}$$

The melting and solidification phenomena occur at a certain range of temperature, which corresponds to the solidus and liquidus temperatures and this leads to the presence of the mushy zone between solid and liquid phases. The mushy zone is modeled as porous media by introducing the damping term to the momentum equation. The permeability of the two-phase mushy zone K has the following form:

$$K = \frac{K_0 g_l^3}{(1 - g_l)^2 + \varepsilon_0}, \tag{11}$$

where K_0 is a permeability coefficient and ε_0 is a small number to avoid a zero denominator. The damping term disappears in the liquid region and approaches to infinity in the solid region, thus the momentum equation is valid for both solid and liquid phases as well.

Liquid/vapor interface is the most difficult boundary for numerical implementation in this study since many physical phenomena and interfacial forces are involved there, such as surface evolution, evaporation, surface tension, thermocapillary force, and vapor pressure. In order to solve those interfacial forces, the information of the melt pool geometry is required. Due to the advantages of the level set method [21,22] in accurately tracking surface evolution and topology changes, it is employed to acquire the solution of the melt pool free surface. According to the definition of level set function, the melt pool surface evolution satisfies the following formula:

$$\frac{\partial \phi}{\partial t} + F|\nabla \phi| = 0, \tag{12}$$

where ϕ is the level set function representing the distance from the calculation cell to the melt pool surface, and the melt pool surface corresponds to the zero level set. F is the speed function, which mainly results from the surface tension, and thermocapillary force as well as gas pressure.

To avoid numerical instability arising from the physical property jump at the liquid/vapor interface, the Heaviside function $H(\phi)$ is introduced to define a transition region where the physical properties are mollified. The smoothed Heaviside function $H(\phi)$ is given by:

$$H_\varepsilon(\phi) = \begin{cases} 0 & \text{if } \phi < -\varepsilon \\ 0.5\left[1 + \dfrac{\phi}{\varepsilon} + \dfrac{1}{\pi}\sin\left(\dfrac{\pi\phi}{\varepsilon}\right)\right] & \text{if } |\phi| \leqslant \varepsilon \\ 1 & \text{if } \phi > \varepsilon \end{cases}, \tag{13}$$

where ε is transition region thickness and corresponding mollified physical properties in the transition region can be expressed as:

$$\rho_\varepsilon = \rho_1 H_\varepsilon(\phi) + [1 - H_\varepsilon(\phi)]\rho_2, \tag{14}$$

$$\mu_\varepsilon = \mu_1 H_\varepsilon(\phi) + [1 - H_\varepsilon(\phi)]\mu_2, \tag{15}$$

where ρ_1 and μ_1 denote properties of liquidus metal, and ρ_2 and μ_2 denote gas properties.

The delta function $\delta(\phi)$, a derivative of the Heaviside function, is applied to guarantee that those interfacial forces are valid only for surface cells as shown below:

$$F_n = (p_v + \sigma\kappa)\delta(\phi), \tag{16}$$

$$F_t = -\frac{d\sigma}{dT}\nabla_s T \delta(\phi), \tag{17}$$

where σ is the surface tension, κ is the curvature, p_v is the gas pressure, and ∇_s is the nabla operator. F_n and F_t are the interfacial force components in normal and tangential directions, respectively. Melt pool surface normal direction and curvature can be represented in terms of level set function ϕ as seen below:

$$\mathbf{n} = \left.\frac{\nabla \phi}{|\nabla \phi|}\right|_{\phi=0}, \tag{18}$$

$$\kappa = \nabla \cdot \left.\left(\frac{\nabla \phi}{|\nabla \phi|}\right)\right|_{\phi=0}. \tag{19}$$

It is essential to point out that the gas pressure consists of shielding gas pressure and recoil vapor pressure. Under the low laser power processing conditions, the recoil vapor pressure is negligible; however, with the increase of the laser power, it becomes dominant at the melt pool center in comparison to other interfacial forces. Study of [23] has shown that during laser material interaction under typical industrial conditions, only surface evaporation can occur and evaporation intensity is a function of surface temperature. This is quite different with the assumption of volumetric evaporation, which treats evaporation as a threshold phenomenon and melt pool surface temperature cannot exceed boiling point. Based on the assumption presented in [24], the calculation of the recoil evaporation pressure is given by:

$$p_v = AB_0\sqrt{T_{\text{surf}}}\exp(-U/T_{\text{surf}}), \tag{20}$$

where A is the ambient pressure dependent coefficient. As suggested by Ref. [24], the coefficient A varies from 0.55 for evaporation in vacuum to 1 for the case of evaporation under a high ambient pressure. For practical values of the ambient pressure, the coefficient A is close to its minimal value of 0.55. B_0 is the evaporation constant, which takes a value of 1.78×10^{10} Pa in the simulation based on the analysis of Ref. [24]. U is the energy of evaporation per Avogadro's number atoms and T_{surf} is surface temperature.

Surface temperature is determined by the energy balance between the input laser energy and heat loss induced by the evaporation, convection, and radiation. The laser beam intensity profile is assumed to be Gaussian distribution; hence, laser heat influx can be expressed as:

$$q_{\text{laser}} = \frac{2\eta P_{\text{laser}}}{\pi R^2}\exp\left(-\frac{2r^2}{R^2}\right), \tag{21}$$

where P_{laser} is the laser power, R is the beam spot radius, r is the distance from calculation cell to the beam center, and η is absorptivity coefficient. The heat loss on the liquid/vapor interface is given by:

$$q_{\text{loss}} = h_c(T - T_\infty) + \varepsilon\sigma(T^4 - T_\infty^4) + \rho_l V_{dv} L_v. \tag{22}$$

The terms on the right-hand side are convective heat loss, radiation heat loss, and evaporation heat loss, respectively. In Eq. (22), h_c is the convective coefficient, ε is radiation emissivity, σ is the Stefan–Boltzmann constant, T_∞ is the ambient temperature, L_v is the latent heat by evaporation, ρ_l is the molten fluid density, and V_{dv} is the boundary moving speed resulting from evaporation. The relationship between V_{dv} and surface temperature is assumed to

have a little difference with that of recoil vapor pressure, and the following equation is used to calculate V_{dv}:

$$V_{dv} = V_0 \exp(-U/T_{\text{surf}}), \tag{23}$$

where V_0 is the order of magnitude of the sound velocity in the material and a value of 4512 m/s is utilized in the simulation. U and T_{surf} have the same meaning as in Eq. (20). Equation (20) indicates that evaporation will cause loss of mass; therefore, the boundary moving speed is referred as mass loss speed by evaporation as well. It is along the surface normal direction and points to liquid side. Since evaporation partially contributes to the change of free surface location, it will be incorporated into the boundary condition in the calculation of surface advance using Eq. (12). The boundary moving speed from evaporation is quite low in comparison to the speed resulting from those interfacial forces. However, the value of the latent heat of evaporation is a large number, which causes the energy loss from evaporation to be non-negligible. The calculation shows that heat loss is dominated by evaporation when the surface temperature is higher than 3000 K. For the cases analyzed in this paper, the amounts of surface location change and mass loss from evaporation are relatively small.

4 Consideration of Numerical Implementation

In this study, a semi-implicit finite difference algorithm is utilized for the solution of continuity and momentum equations. The thermal energy transport equation is solved using an explicit control volume method. It needs to be noted that Eq. (12) is only applicable for zero level set. In order to maintain the level set function as a signed distance, a reinitialization operation is required. A detailed scheme is depicted below.

4.1 Third Order ENO Reinitialization Scheme. The following equation is applied to the calculation domain after Eq. (12) is updated:

$$\phi_\tau = S_\varepsilon(\phi^{(0)})(1 - |\nabla \phi|), \tag{24}$$

where S_ε is a smooth factor and τ is artificial time.

For a given initial data $\phi^{(0)}$, solving Eq. (24) to steady state provides a new value for ϕ with the property that $|\nabla \phi| = 1$. In this study, Eq. (24) is solved based on the third order ENO method [25]. The solution of Eq. (24) can be achieved by iterating the following two equations until the specified order of the method:

$$L(\phi^{(0)}, \phi^{(i-1)}) = S_\varepsilon(\phi^{(0)})(1 - |\nabla \phi^{(i-1)}|), \tag{25}$$

$$\phi^{(i)} = \sum_{k=0}^{i-1} [\alpha_{ik}\phi^{(k)} + \beta_{ik}\Delta t L(\phi^{(0)}, \phi^{(k)})], \tag{26}$$

where $i = 1 \ldots r$. r is the order of the method and it equals 3 in this study. Δt is artificial time and it is taken as $\Delta x/2$, which satisfies stability conditions. The discretization of the spatial derivatives in Eq. (24) employs an upwind scheme for stability.

4.2 Volume Conservation Algorithm. Due to the slight shift of the zero level set ϕ_0 caused by the reinitialization operation, partial volume loss of the surface cell is observed. Based on Sussam's work [26], the following constraint is placed in each computational cell Ω to keep the volume constant after reinitialization:

$$\frac{\partial V}{\partial \tau} = \frac{\partial}{\partial \tau}\int_\Omega H(\phi) d\Omega = 0, \tag{27}$$

where V is the volume of the computational cell. Equation (27) can be rewritten as:

$$\int_\Omega H'(\phi)\phi_\tau d\Omega = 0. \tag{28}$$

In order to compensate for the volume loss, reinitialization Eq. (25) is modified as:

$$L(\phi_0, \phi) = \phi_\tau = \text{sign}(\phi_0)(1 - |\nabla \phi|) + \lambda \cdot f(\phi). \tag{29}$$

The second term on the right-hand side is a compensation term, which consists of two parts. Function $f(\phi)$ is based on observation [26] and it has the form:

$$f(\phi) \equiv H'(\phi)|\nabla \phi|. \tag{30}$$

λ is a cell related constant, and following formula can be obtained by combining Eqs. (28)–(30):

$$\lambda = \frac{-\int_\Omega H'(\phi)L(\phi_0, \phi)d\Omega}{\int_\Omega H'(\phi)f(\phi)d\Omega}, \tag{31}$$

where the smoothed Heaviside function is used in the above equation for derivative. The integration term for λ can be calculated by weighted sum of the surface cell and its neighbor cells. $L(\phi_0, \phi)$ obtained through the previous step is used here for the calculation of the product of function $f(\phi)$ and λ. Once the compensation term is achieved, $L(\phi_0, \phi)$ will be updated.

5 Results and Discussion

5.1 Model Validation. The three-dimensional image of the melt pool shape and surface temperature distribution obtained by the simulation for the stationary laser beam is shown in Fig. 2(a). The laser beam used in the simulation is 1000 W, which is the same as the practical parameters for comparison. The plot presents the view of the melt pool at the fully developed stage; at this point the energy balance is reached between the thermal influx from the laser beam and heat sink into the substrate as well as heat losses on the top surface including evaporation, radiation and convection. Figure 2(b) illustrates the experimental observation acquired by the CMOS camera from the top of the melt pool. Although the presence of the strong reflection inside the melt pool obscures geometrical information there, it can be noted that a circular crater has been created in the laser–substrate interaction region. The formation of the crater can be interpreted that in laser irradiation zone, the substrate surface is heated up to a temperature much higher than the melting point, and strong thermocapillary force induced by huge temperature gradient pulls the molten fluid from the melt pool center to the edge; as a result, the hump is generated around the molten zone.

Figure 3(a) presents the simulation result for surface geometry and temperature distribution in the moving laser beam case with a scanning speed of 12.7 mm/s and laser power level 1000 W. In the simulation, the calculation domain has been chosen large enough to avoid the end effect. As the laser beam moves away, the displaced surface fluid flows back and the substrate surface restores to be flat. The motion of the laser beam causes the temperature contours to be compressed in the front of the laser beam and stretched behind the laser beam, which can be seen from the plot. In a high laser power situation, the melt pool tail may appear in the opposite direction of the laser beam traveling and the melt pool exhibits a pear shape. Corresponding experimental observation on the melt pool is shown in Fig. 3(b) and the high temperature zone is consistent with the simulation result.

A quantitative comparison for the melt pool geometry at different laser power levels and process speeds were further conducted by calibrating the fusion zone size. Figures 4(a)–4(d) show the cross section images of four typical laser power levels, which are 300, 500, 750, and 1000 W. Figures 5(a)–5(d) correspond to re-

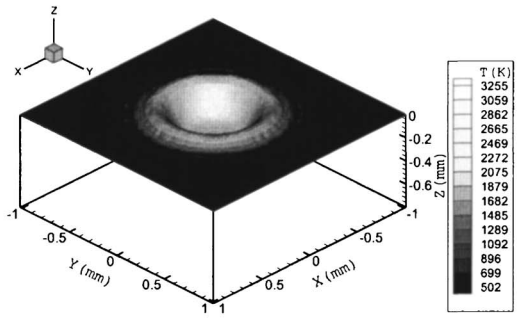

(*a*) Simulation result of the melt pool shape and surface temperature distribution with stationary laser beam at laser power level 1000 W

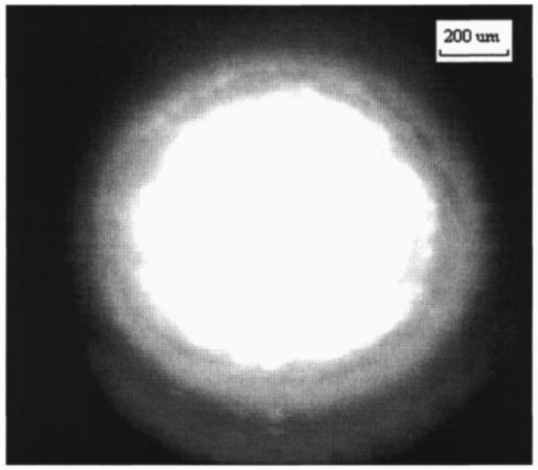

(*b*) Melt pool shape acquired by CMOS camera from top view with stationary laser beam at laser power level 1000 W

Fig. 2 Melt pool shape comparison between experimental data and simulation result with stationary laser beam

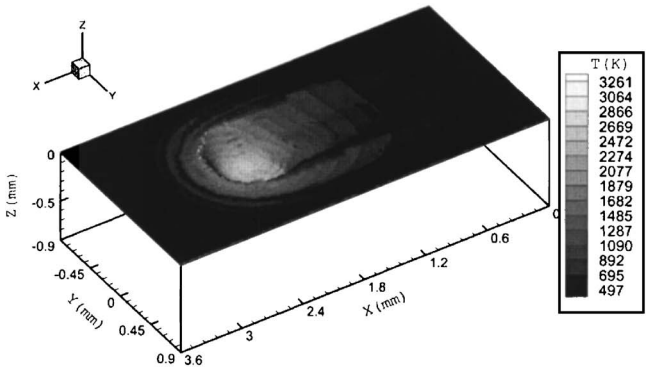

(*a*) Simulation result of melt pool shape and surface temperature with moving laser beam

(*b*) Experimental result of melt pool shape with moving laser beam case

Fig. 3 Melt pool shape comparison between simulation and experiment with moving laser beam

sults of different process speeds at 6.3, 8.5, 12.7, and 17.0 mm/s (10–40 ipm) with 750 W laser power. For the simulation, information of the melt pool cross-section perpendicular to the moving direction is extracted at the quasistatic stage. Figures 6 and 7 present the melt pool velocity field and temperature distribution from the top and side views at 1000 W laser power and 12.7 mm/s process speed. The cross section for side view in Fig. 7 is located at beam center ($x=0$ mm). From top view of velocity field, it can be seen that due to the effect of moving laser, surface fluid will flow backward and forms a melt pool tail. As a result, a low melt pool shoulder forms at the cross section $x=0$ mm, and the location of highest melt pool shoulder lags behind the position of the beam center. When the laser beam moves forward, strong interfacial forces will pull the fluid on the melt pool shoulder back to the melt pool center and flatten the depressed melt pool surface.

Figures 8(a) and 8(b) provide a comparison of melt pool width and depth as a function of laser power level between experimental measurement and simulation prediction. There is an over prediction in the simulation for the melt pool width, however, depth prediction is much closer to the experimental data, especially at low power levels. For example, the discrepancy in depth between experimental data and simulation results is within 0.02 mm for laser power of 300 and 500 W, while the difference in width is about 0.08 mm. Moreover, it can be noted from both the experi-

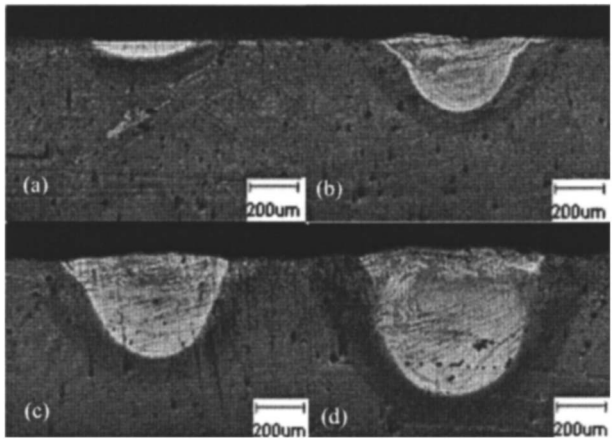

Fig. 4 Cross section image of the fusion zone for different laser power levels at 300, 500, 750, and 1000 W

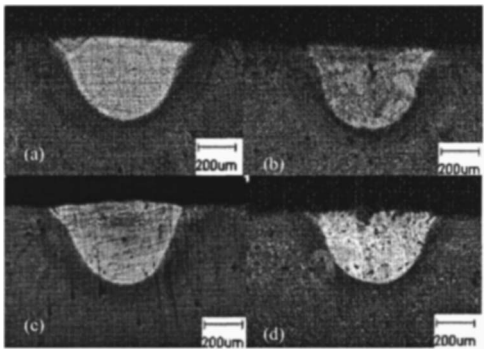

Fig. 5 Cross section image of the fusion zone for different process speeds at 10, 20, 30, and 40 ipm

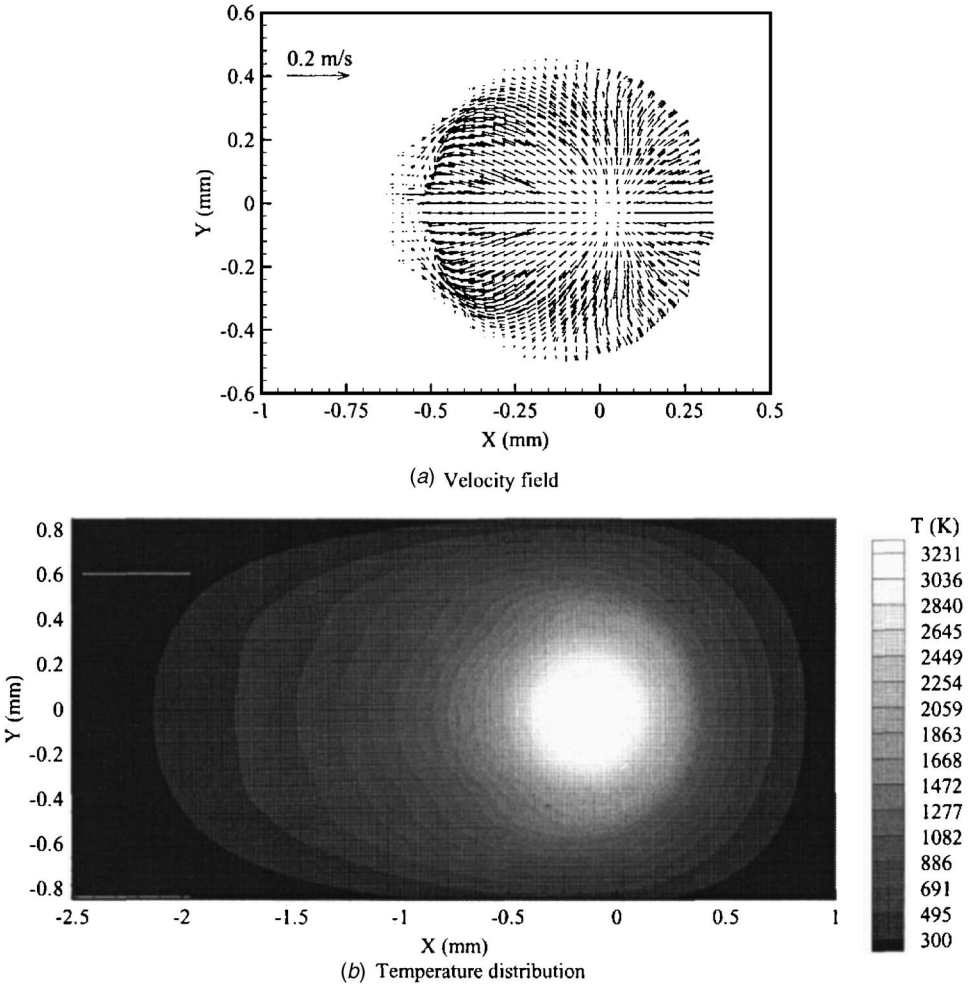

Fig. 6 Melt pool velocity field and temperature distribution from the top view

mental and simulation results that the laser power level has a more prominent effect on depth than width, and this reflects that convection facilitates to bring the higher temperature surface fluid to the bottom of the melt pool, and thus partially increases the melt pool penetration.

In Figs. 9(a) and 9(b), the melt pool width and depth are plotted as a function of processing speed. The variation of the experimentally determined values for width and depth are 9.4% and 9.9% from 6.3 to 17.0 mm/s, and corresponding values in the simulation are 11.4% and 14.5%. Compared with the influence of laser power, the alternation of processing speed has much less effect on the melt pool geometry. Although there is about 10%–15% over prediction in the melt pool dimensions, it can be noted that the trend of the melt pool geometry variation with the processing speed has a good agreement between experimental data and simulation results.

5.2 Melt Pool Evolution. In order to give some insight on the melt pool formation procedure, the evolution of the solid/liquid and liquid/vapor interfaces are tracked with a stationary laser beam case. Figure 10 presents the surface temperature distribution with respect to the radial distance at different times. The effect from the latent heat of fusion can be identified through the curves at $t=0.4$ ms and $t=0.6$ ms. During this period, the substrate starts to melt and the formation of a thin mushy zone results in the change of the temperature gradient as seen in the $t=0.6$ ms curve. From the temperature evolution plot, it can be seen that surface temperature at beam center rises rapidly and reaches the melting point and boiling point sequentially at about 0.4 and 2.0 ms. The change rate of the maximum temperature has a tendency to become smaller with time since heat loss from evaporation increases with the rise of surface temperature. Evaporation not only significantly affects the surface temperature, but also produces the recoil pressure, which partially contributes to the surface depression. Figure 11(a) presents the melt pool surface evolution, and the surface under the beam center sinks gradually under the combined action of thermal-capillary force, surface tension, shielding gas pressure, and recoil vapor pressure. The displaced fluid from the melt pool center bulges up around the melt pool to form the melt pool shoulder; at the same time, it also carries high temperature fluid to the melt pool edge which assists in widening the melt pool boundary. During the period of the top surface evolution, the solid/liquid interface expands as well as shown in Fig. 11(b). It can be observed from the plot that in the initial stage, the melt pool extends primarily in the radial direction, and then in the depth direction after the melt pool diameter is comparable to the beam spot. As a consequence, the melt pool aspect ratio of width to depth is about 4.0 at 5 ms, and it reduces to a value of around 2.3 at 30 ms. After the laser beam is turned off, the fluid on the melt pool shoulder will flow back to melt pool center, while surface fluid flowing from center to edge becomes less. As seen in Fig. 11(b), the final shape of the melt pool tends to be flat.

5.3 Influence of Convection and Surface Deformation. Thermal flux from the laser beam is dissipated through conduction and convection in the melt pool region. The relative importance of the heat conduction and convection is evaluated by the Peclet number *Pe*, which is given by:

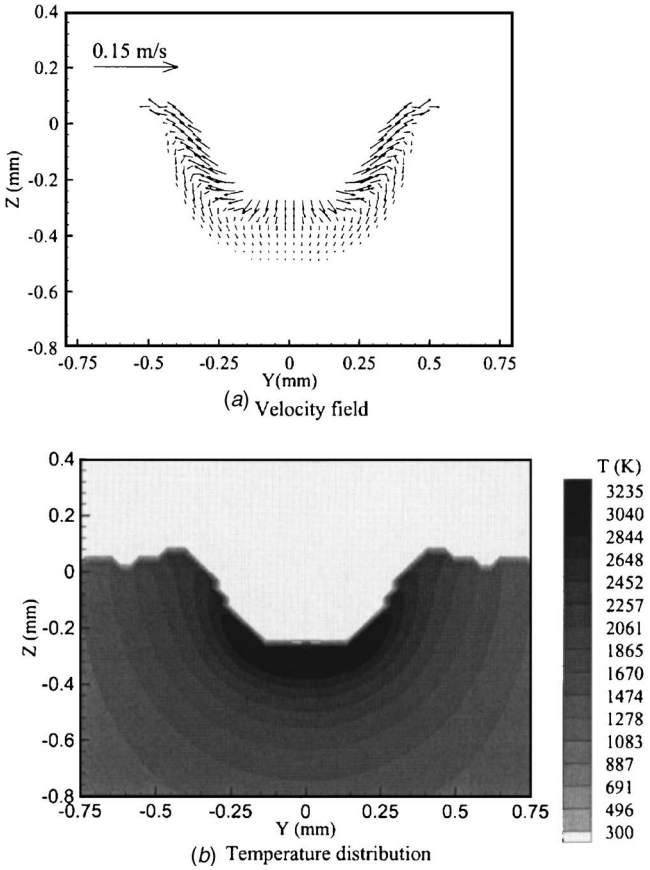

Fig. 7 Melt pool velocity field and temperature distribution at cross section

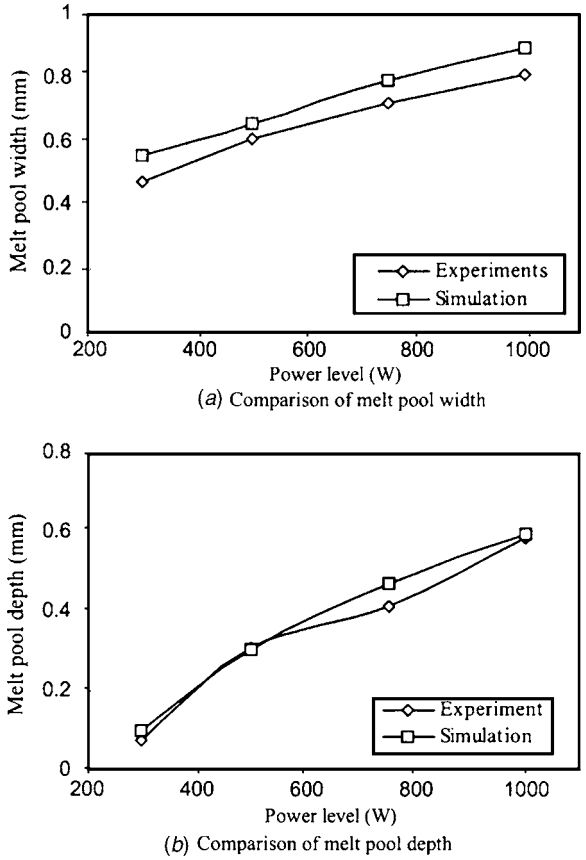

Fig. 8 Comparison of melt pool geometry between simulation and experiment for different power levels at 300, 500, 750, and 1000 W

$$\mathrm{Pe} = \frac{\mathbf{V}L}{\alpha},$$

where **V** is the average velocity of the fluid flow in the melt pool, L is the characteristic length and α is the thermal diffusivity.

Figure 12 gives the Peclet number variation with time at three different laser power levels. At the initial stage, the Peclet numbers increase rapidly due to the fast expansion of the melt pool diameters, and then they approach relatively stable values. Since the melt pool development considerably depends on the process parameters, the relative importance of the convection will vary with the parameters; for example as shown in Fig. 12, the Peclet number increases from 1.27 at 750 W to 1.96 at 1250 W. In all three cases, the Peclet numbers are larger than unity at the fully developed stage, which indicates that convection plays essential roles on the heat dissipation and melt pool shape; therefore, the conduction model may result in a striking difference in the prediction of the melt pool shape.

Quantitative investigation on the effect of the surface deformation is further conducted and Fig. 13 shows the melt pool ratio for the cases with surface deformation and without surface deformation at 750 W laser power. It can be clearly noted from the plot that the melt pool ratio of the flat surface case is much smaller than that of the surface deformation case. With the surface deformation, strong thermocapillary force and vapor pressure pull the surface fluid at the melt pool center to the edge, which reduces the thickness of the liquid layer under the beam center. The depressed surface in turn facilitates the heat dissipation in the depth direction; accordingly, the melt pool penetration increases.

5.4 Comparison of Interfacial Forces. Melt pool deformation and fluid flow are mainly contributed by three types of surface driven forces in this study, which are surface tension, thermocapillary force, and vapor pressure. Surface tension and vapor pressure act on the melt pool surface in the normal direction while the thermocapillary force is in the tangential direction. The magnitude of the thermocapillary force and vapor pressure are dependent on the surface temperature distribution. In the simulation, it is observed that the evaporation phenomenon primarily occurs in the melt pool center region where the surface temperature is around 3000 K or higher. The evaporation attributes to the surface deformation in two aspects: on the one hand, it produces the vapor pressure which pushes the melt pool surface downward; on the other hand, evaporation causes the apparent heat loss and weakens the surface temperature gradient, thereby the thermocapillary force. In order to demonstrate the relative importance of vapor pressure and thermocapillary force, the comparisons for different melt pool development stages and laser power levels are conducted under the stationary laser beam condition. Figure 14 presents the relative magnitude ratio of recoil vapor pressure to thermocapillary force with respect to the dimensionless melt pool radius for 1250 W laser power level at 12, 24, and 36 ms. It can be seen that the force ratio decreases dramatically along the radial direction and it is close to zero at $r^*=0.5$, which corresponds to the half laser beam radius. In this region, the recoil vapor pressure drops rapidly from the melt pool center to its periphery, while the thermocapillary force rises with the increase of the surface temperature gradient. Before the melt pool reaches the fully developed stage, surface temperature increases with time; however, the temperature gradient changes less; correspondingly, the force ratio rises from 6.96 at $t=12$ ms up to 9.03 at $t=36$ ms.

Among those process parameters, laser power level has a prominent influence on the force ratio. As shown in Fig. 15, maximum force ratio at 1250 W is more than 6 times higher than that of 750 W at $t=24$ ms. Based on the nonvolumetric evaporation

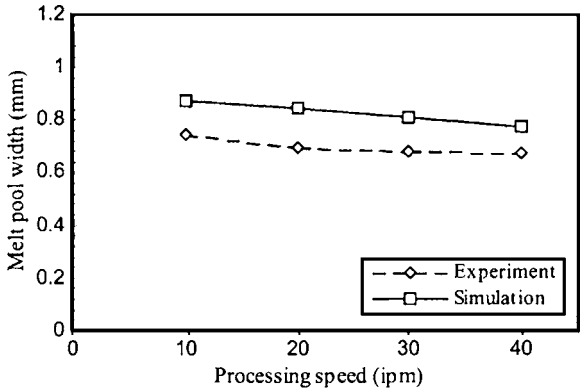

(*a*) Comparison of melt pool width

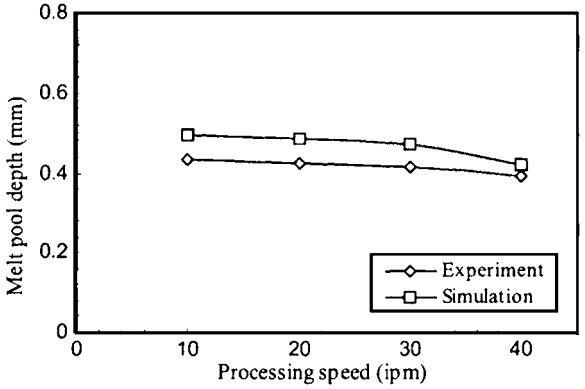

(*b*) Comparison of melt pool depth

Fig. 9 Comparison of melt pool geometry between simulation and experiment for different process speeds at 10, 20, 30, and 40 ipm

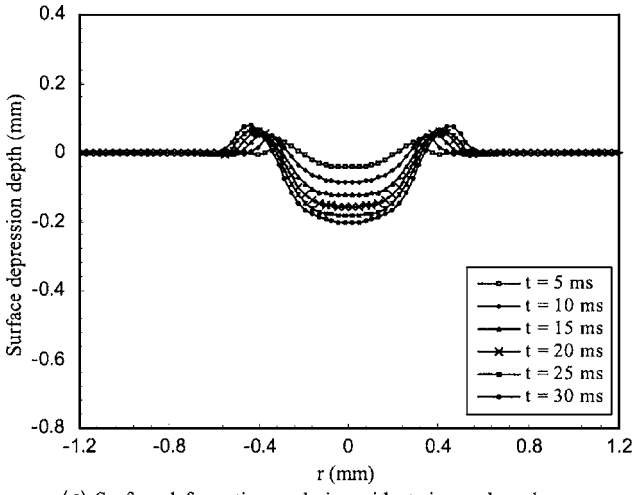

(*a*) Surface deformation evolution with stationary laser beam

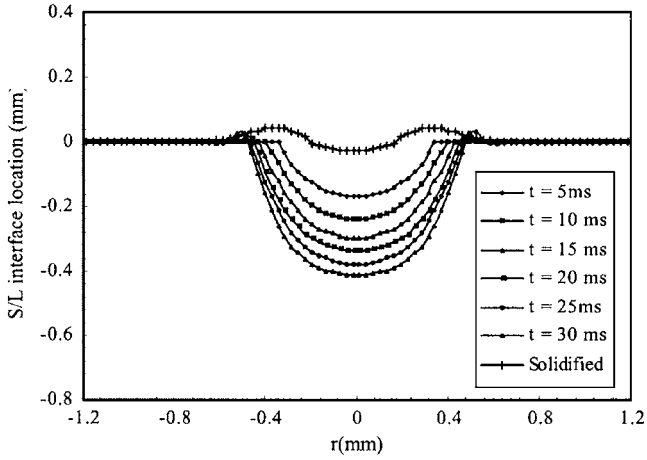

(*b*) Solid/liquid interface evolution for stationary laser beam

Fig. 11 Melt pool interfaces evolution with stationary laser beam

assumption that melt pool peak temperature is proportional to the intensity of heat influx from the laser beam, a higher peak temperature at the melt pool center leads to stronger recoil vapor pressure, which enhances the force ratio.

Relative importance of thermocapillary force versus surface tension is characterized by the Capillary number Ca, which is expressed as:

$$\mathrm{Ca} = \frac{\left|\frac{\partial \sigma}{\partial T}\right| \Delta T}{\sigma_{\mathrm{ref}}}, \tag{32}$$

where σ is the surface tension coefficient, and ΔT is the temperature difference between melt pool center and melt pool edge.

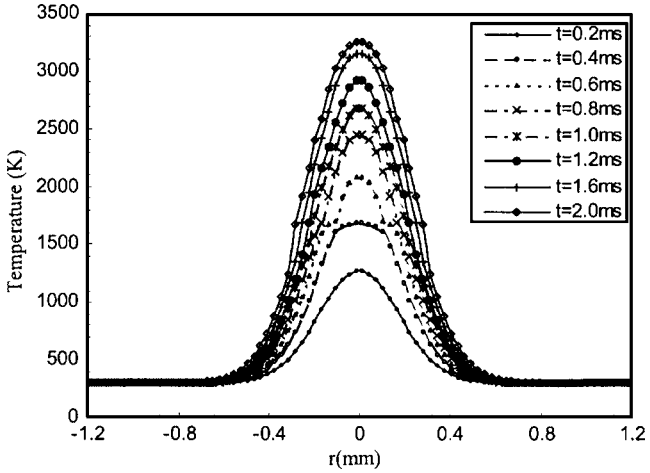

Fig. 10 Surface temperature evolution with stationary laser beam

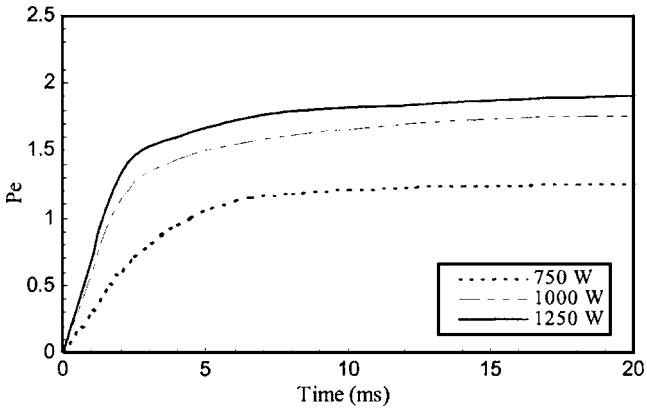

Fig. 12 Peclet number comparison at different laser power levels

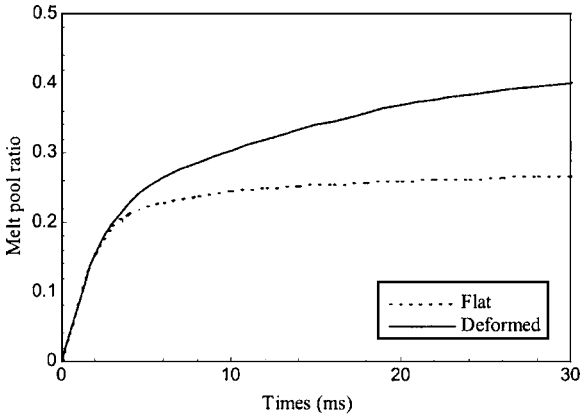

Fig. 13 Melt pool ratio comparison between deformed surface case and flat surface case

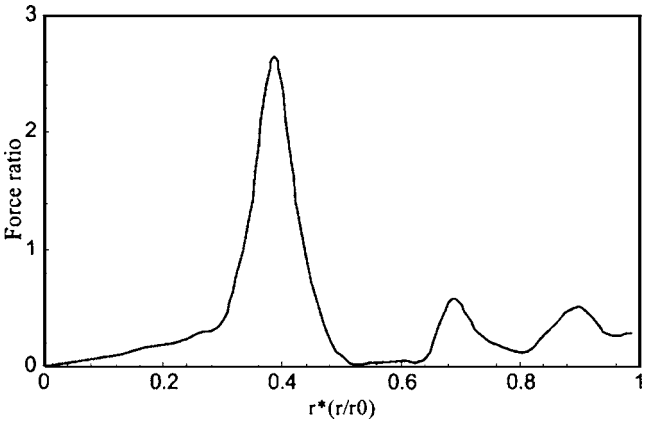

Fig. 16 Force ratio of thermocapillary force to surface tension at laser power level 750 W

Based on the thermal property listed in Table 1 and melt pool temperature distribution at the fully developed stage for 750 W laser power case, the Ca is around 0.39. The distribution of force ratio of thermocapillary force to surface tension along the radial direction is presented in Fig. 16. Intensity distributions of these two forces along the radial direction are not consistent, which results in the fluctuation of the force ratio. This curve will vary with different process conditions; however, it reveals that surface tension is critical to the melt pool behavior and shape.

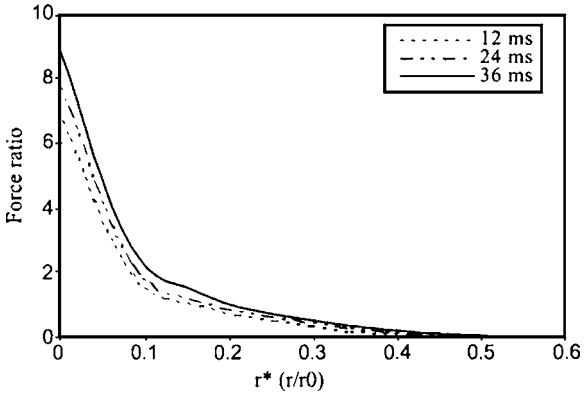

Fig. 14 Force ratio of recoil vapor pressure to thermocapillary force at different times for 1250 W laser power level

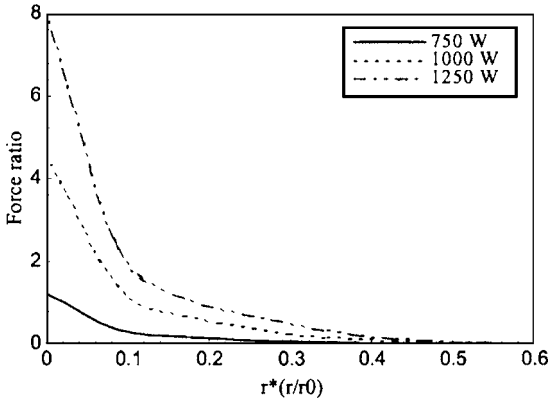

Fig. 15 Force ratio of recoil vapor pressure to thermocapillary force at different laser power levels

6 Conclusions

A three dimensional transient model of the melt pool with stationary and moving laser beam has been established and the simulations are conducted at different laser power levels and process speeds. The results show a good agreement with the experimental data. The model shows that convection plays significant roles on heat dissipation and the melt pool shape; moreover, an assumption of a flat free surface may cause an apparent discrepancy in the melt pool geometry prediction with the real situation. The melt pool deformation mainly results from three interfacial forces and their magnitudes rely on the surface temperature and geometry. At the melt pool center, recoil vapor pressure usually is several times higher than thermocapillary force and surface tension; whereas, it drops dramatically along the radial direction and becomes negligible at the melt pool edge in comparison with the thermal capillary force and surface tension. Since the underlying mechanisms investigated also occur in other laser processes, such as laser welding and laser deposition, the results of this study will give some insight into the practical applications.

Acknowledgments

This research was supported by the National Science Foundation Grant No. DMI-9871185, the Grants from the U.S. Army Aviation and Missile Command (AMCOM), and the support from the Intelligent Systems Center at the University of Missouri-Rolla. Their support is greatly appreciated.

References

[1] Rosenthal, D., 1946, "The Theory of Moving Source of Heat and its Application to Metal Treatment," Trans. ASME, **68**, pp. 849–866.
[2] Doumanidis, C., and Kwak, Y. M., 2001, "Geometry Modeling and Control by Infrared and Laser Sensing in Thermal Manufacturing with Material Deposition," ASME J. Manuf. Sci. Eng., **123**, pp. 45–52.
[3] Kaplan, A. F. H., and Groboth, G., 2001, "Process Analysis of Laser Beam Cladding," ASME J. Manuf. Sci. Eng., **123**, pp. 609–613.
[4] Tsai, F. R., Elijah, K. A. Jr., 2002, "Modeling of Conduction Mode Laser Welding Process for Feedback Control," ASME J. Manuf. Sci. Eng., **122**, pp. 420–428.
[5] Hu, D., Mei, H., and Kovacevic, R., 2002, "Improving Solid Freeform Fabrication by Laser-based Additive Manufacturing," Proc. Inst. Mech. Eng., Part B, **216**, pp.1253–1264.
[6] Vasinonta, A., Beuth, J. L., and Griffith, M. L., 2001, "A Process Map for Consistent Build Conditions in the Solid Freeform Fabrication of Thin-Walled Structures," ASME J. Manuf. Sci. Eng., **123**, pp. 615–622.
[7] Cline, H. E., and Anthony, T. R., 1977, "Heat Treating and Melting Material with a Scanning Laser or Electron Beam," J. Appl. Phys., **48**, pp. 2895–3900.
[8] Mazumder J., 1991, "Overview of Melt Dynamics in Laser Processing," Opt. Eng., **30**, pp.1208–1219.
[9] Mahrle, A., and Schmidt, J., 2002, "The Influence of Fluid Flow Phenomena on the Laser Beam Welding Process," Int. J. Heat Fluid Flow, **23**, pp. 288–297.
[10] Lange, D. F., and Postma, S., 2003, "Modeling and Observation of Laser Welding: the Effect of Latent Heat," ICALEO, Jacksonville, FL.

[11] He, X., Fuerschbach, P. W., and DebRoy, T., 2003, "Heat Transfer and Fluid Flow during Laser Spot Welding of 304 Stainless Steel," J. Phys. D **36**, pp. 1388–1398.
[12] Voelkel, D. D., and Mazumder, J., 1990, "Visualization and Dimensional Measurement of the Laser Weld Pool," ICALEO, pp. 422–429.
[13] Lim, D. C., Cho, Y. B., and Gweon, D. G., 1998, "A Robust in Process Monitoring of Pulsed Laser Spot Welding Using a Point Infrared Sensor," Proc. Inst. Mech. Eng., Part B, **212**, pp. 241–250.
[14] Beersiek, J., 2002, "New Aspects of Monitoring with a CMOS Camera for Laser Materials Processing," ICALEO, Scottsdale, AZ.
[15] Bicknell, A., 1994, "Infrared Sensor for Top Face Monitoring of Weld Pools," Meas. Sci. Technol. **5**, pp. 371–387.
[16] Romer, G. W., Hoeksma, M., and Meijer, J., 1997, "Industrial Imaging Controls Laser Surface Treatment," Photonics Spectra, **31**, pp. 104–109.
[17] Beersiek, J., 2001, "A CMOS Camera as a Tool for Process Analysis Not Only for Laser Beam Welding," ICALEO, Jacksonville, FL.
[18] Hu, D., Labudovic, M., and Kovacevic, R., 1999, "On Line Sensing of Laser Surface Modification Process by Computer Vision," *Proceedings of ASW Ninth International Conference on Computer Technology in Welding*, pp. 417–424.
[19] Bennon, W., and Incropera, F., 1987, "A Continuum Model for Momentum, Heat, and Species Transport in Binary Solid-Liquid Phase Change Systems I: Model Formulation," Int. J. Heat Mass Transfer, **30**, pp. 2161–2170.
[20] Bennon, W., and Incropera, F., 1987, "A Continuum Model for Momentum, Heat, and Species Transport in Binary Solid-Liquid Phase Change Systems-II," Int. J. Heat Mass Transfer, **30**, pp. 2171–2187.
[21] Sethian, J. A., 1999, *Level Set Method and Fast Marching Methods*, 2nd ed., Cambridge University Press, Cambridge, UK
[22] Ki, H., Mohanty, P. S., and Mazumder, J., 2002, "Modeling of Laser Keyhole Welding: Part I. Mathematical Modeling, Numerical Methodology, Role of Recoil Pressure, Multiple Reflections and Free Surface Evolution," Metall. Mater. Trans. A **33**, pp. 1817–1830.
[23] Afanasiev, Y. V., and Krokhin, O. N., 1967, Sov. Phys. JETP, **25**, p. 639.
[24] Semak, V., and Matsunawa, A., 1997, "The Role of Recoil Pressure in Energy Balance During Laser Materials Processing," J. Phys. D **30**, pp. 2541–2552.
[25] Shu, C. W., and Osher, S. J., 1989, "Efficient Implementation of Essentially Nonoscillatory Shock Capturing Schemes II," J. Comput. Phys., **83**, pp. 32–78.
[26] Sussman, M., Fatemi, E., Smereka, P., and Osher S., 1998, "An Improved Level Set Method for Incompressible Two-Phase Flows," Comput. Fluids," **27**, pp. 663–680.
[27] Wang, Y., and Tsai, H. L., 2001, "Effect of Surface Active Elements on Weld Pool Fluid Flow and Weld Penetration in Gas Metal Arc Welding," Metall. Mater. Trans. B, **32B**. pp. 501–515.

Wei Shang
Department of Mechanical Engineering,
University of Saskatchewan,
57 Campus Drive,
Saskatoon, S7N 5A9 Canada
Phone: (306) 966-5452
Fax: (306) 966-5427
e-mail: wes153@mail.usask.ca

Hong Chen
Petroleum Engineering Department,
University of Tulsa,
2950 E Marshall Street,
Tulsa OK 74110 USA
Phone: (918) 631-5137
e-mail: hong-chen@utulsa.edu

Robert W. Besant
Department of Mechanical Engineering,
University of Saskatchewan,
57 Campus Drive,
Saskatoon, S7N 5A9 Canada
Phone: (306) 966-5452
Fax: (306) 966-5427

Frost Growth in Regenerative Wheels

An experimental investigation was carried out for frost growth in a desiccant-coated regenerative wheel. The test facility was set up following ASHRAE Standard 84-1991R. Temperature, relative humidity, mass flow rate, and pressure drops were measured at each measuring station. Photos of frost within energy wheel flow channels show frost accumulation. The problem of frost growth within the narrow parallel flow passages of a regenerative heat or energy rotary wheel is formulated for a very cold-temperature ventilation application. Frost growth is assumed to grow as a porous media while the wheel is exposed to warm humid airflow on the exhaust side. While the wheel is exposed to cold dry airflow on the supply side, the frost is cooled but no frost grows. This cyclic frost growth and cooling process is continued with each wheel rotation. An analytical/numerical model is developed to simulate these frost properties over the depth of the wheel and as a function of time. Simulation results are used to interpret experimental data for the early stage of frost growth on a typical energy wheel with a cold supply air temperature of −40 °C, a warm exhaust temperature of 20 °C and 40% relative humidity. Pressure drop measurements across a wheel taken for constant mass flow conditions revealed some very significant fluctuations of up to 100% of original pressure drop with a period ranging from 2 to 4 min for a wheel speed of 20 rpm. Each fluctuation in pressure drop is interpreted to imply a catastrophic failure of the outer frost layer sequenced over 1–2 min throughout the wheel followed by another frost growth period on top of a slightly thicker frost base. [DOI: 10.1115/1.2005274]

1 Introduction

Using regenerative air-to-air heat exchangers for ventilation air energy recovery in cold climates may result in frost growth inside the airflow passages. These devices are commonly used to reclaim waste heat (i.e., heat wheels) and typically operate at 5–10 rpm or they reclaim both heat and moisture (i.e., energy or enthalpy wheels) and typically operate at 15–45 rpm. The airflow passages within a rotating regenerative wheel will be subject to potential icing or frost blockage for cyclic variations of warm humid airflow from exhaust air, typically 20–25 °C, and cold dry supply airflow with temperatures less than −25 °C in very cold weather conditions. Increasing the exhaust relative humidity or flow rate relative to the supply flow rate will raise the ambient inlet supply air temperature when icing or frost blockage problems may occur. The rotational speed of the wheel and its internal geometry must be known to determine the magnitude of frost accumulation.

Frost growth, due to forced convection of humid air with relative humidity less than 100% over initially clean cold surfaces, can be divided into several characteristic time periods: an early, and relatively short, droplet deposition, droplet freezing period, a single dendretic crystal perpendicular to the surface as an extension period for the droplets also of short duration, and a fully developed frost layer growth period of long duration where the frost density is low, and, for air supply temperatures above freezing, a final freeze–thaw cyclic fluctuation period characterized by a significant increase in frost density [1]. Of course, if the surface temperature is not below the dew point temperature of the inlet air flow no deposition of liquid or solid water occurs. If the cold surface is close to the freezing point (e.g., $T_c > -5$ °C) for warm supply air temperature (e.g., $T_a > 20$ °C) no low density frost will occur [2]. If both the air supply and the surface temperature are below the freezing point temperature the final freeze–thaw fluctuations will not occur—so the fully developed frost growth period may continue indefinitely provided it is not sheared off [2]. If the inlet air is supersaturated, with water droplets or ice crystals present, the entire deposition process will be very different from that described above. In this study the inlet air is not supersaturated, but all the other modes of frost growth occur as warm humid exhaust air flows through one side of a regenerative wheel heat exchanger and very cold supply air flows through the other side in a counterflow arrangement.

Frost growth on cold surfaces has attracted the attention of many researchers over the past 50 years. Although frost inside a regenerative wheel forms and grows under complex operating conditions involving perhaps all types of frost growth characteristics as briefly described in Sec. 1, modeling of the frost during the fully developed frost growth period may be the best means of developing an understanding of the process. When the frost has reached a certain height inside narrow flow channels it completely fails structurally due to the high reversing local air speed accompanying the high pressure drops. After such a structural failure of the frost, a new fully developed type of frost growth can resume on top of the remaining frost on the surface.

In recent years new measuring techniques and more sophisticated numerical models have been developed that account for the growth and densification of frost [3–5]. Na and Webb [6,7] presented data which are supported by theoretical and empirical equations to show that supersaturation conditions exist on most cold surfaces when frost first forms. In another paper in the series, Na and Webb [8] utilize the supersaturation model to predict frost growth and compare the simulation results with three independent data sources. This model includes a new correlation for frost thermal conductivity but they did not compare their correlation with those of Dettinberger [9]. The recent experimental and theoretical work of Thomas et al. [10] and Chen et al. [11] for frost properties under freeze operating conditions were not considered.

For very cold surfaces this early growth period of droplet deposition, freezing, and single crystal growth may be only a few seconds or minutes and therefore it can be omitted from the frost growth models with little change in the results. The model in this paper is applied to the second or fully developed frost growth

Contributed by the Heat Transfer Division for publication in the JOURNAL OF HEAT TRANSFER. Manuscript received: July 19, 2004. Final manuscript received: April 20, 2005. Review conducted by: Suresh V. Garimella

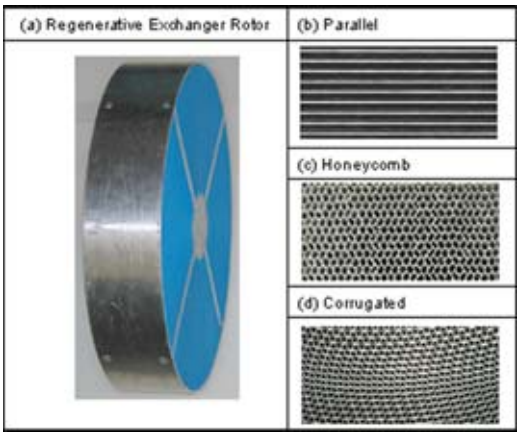

Fig. 1 (*a*) Rotor of a typical regenerative heat exchanger and three different geometry matrices: (*b*) parallel surface; (*c*) hexagonal honeycomb; and (*d*) corrugated geometry

period, which may represent many minutes or hours of the frost layer development. During this period, the frost layer is characterized by a somewhat uniform canopy of frost which is modeled as a low density porous ice matrix filled with humid air. Except adjacent to the solid surface, this porosity is typically high, i.e., more than 80%–90% [2,3]. The governing equations for the heat and mass transport processes in a porous medium were derived using the local volume averaging technique for mass and energy transport [3].

Several theoretical studies have been done on regenerative wheels to investigate the effect of cold supply air inlet temperatures on the onset of condensation and frost growth. Holmberg [12,13] developed a numerical model for heat and moisture transfer in desiccant coated wheels and simulated performance characteristics of a regenerative wheel for the cold supply air inlet temperature down to −10 °C while the exhaust inlet temperature was 20 °C. Simonson and Besant [4] used a somewhat similar model to show that, depending on the exhaust air humidity, uncontrolled frost growth could occur for balanced air flows below −20 °C for the supply inlet when the exhaust air inlet is 20°C. This prediction for the onset of frosting problems is consistent with operating experience for energy wheels. Bilodeau et al. [14] investigated frost formation in energy wheels experimentally for different operating conditions and numerically using a frost growth model which includes several simplifying assumptions that appear to need more investigation. Freund et al. [15] investigated frost control strategies for energy wheels for balanced and unbalanced air flows over a range of operating conditions and predicted a frost threshold temperature. The energy implications of several frost control strategies are included. Except for the new model for frost growth in regenerative heat exchangers by Shang et al. [16], there have been no simulation studies of substantial frost growth in regenerative exchangers operating under very cold frosting conditions. It is the purpose of this paper to investigate this frost growth phenomenon experimentally and theoretically.

A typical rotary regenerative heat exchanger is shown in Fig. 1(*a*). Regenerative wheels used in cold climate applications are commercially available often with a matrix constructed of aluminum foil, plastic film, or sometimes paper. They are designed with different kinds of matrix shapes, such as parallel surface, hexagon honeycomb, corrugation geometry, as shown in Figs. 1(*b*), 1(*c*), and 1(*d*). When these matrices are coated with a desiccant, they can be used to transfer both heat and moisture between the exhaust and supply air. Without this coating they are referred to as heat wheels. As frost accumulates inside a desiccant-coated regenerative wheel, the moisture transfer effectiveness will drop toward zero and both the heat wheel and the energy wheel will have similar frost accumulation characteristics.

2 Experimental Investigation

The laboratory-experimental test facility for frost growth, shown in Fig. 2(*a*), was designed to measure accurately the mass flow of air and its bulk mean temperature and humidity at each of the four measuring stations [17]. All the ducting was completely sealed and well insulated to result in negligible air leaks except perhaps through the wheel seals (estimated to be less than 1% of the total flow) and small heat gains or losses at steady state operating conditions (estimated to be less than 2% of the total heat rate) [18]. For this test facility, the inlet air properties are uniform throughout the inlet flow ducts and the velocity is very nearly uniform as it approaches the wheel face at inlets at stations 1 and 3 in Fig. 2(*b*). Nonuniformity of air flow toward the face of the energy wheel was less than 5% of the maximum except near the wall. The large pressure drop across the energy wheel (e.g., 100–1000 Pa) compared to the dynamic pressure of the face velocity (e.g., 2.4 Pa) would ensure a uniform face velocity. Flow mixers were used after each flow outlet to ensure uniform properties at measuring stations 2 and 4. The sensors at each flow station were calibrated against NIST traceable standards.

Devising a measuring system to determine the frost properties inside a rotating regenerative wheel would be extremely difficult. Consequently, only the external inlet and outlet properties are measured continuously (i.e., the inlet and outlet pressures, temperatures, and humidities), a laser beam indicated the existence of frost blockage and some photos were taken periodically of the exhaust air side outlet when the wheel was briefly stopped as shown in Fig. 3. Figure 3(*a*) shows a method for photographing a few air flow channels at the exhaust outlet of the wheel. A boroscope is used to observe and photograph frost growth inside the wheel flow channels at various times during one test. Figure 3(*b*) shows the laser beam frost scanning scheme, where beam diameter was 1.7 mm at the 90% falloff intensity was used, and the pressure drops across the regenerative wheel at supply air side and exhaust air side were measured using the static pressure ports on Pitot-static tubes. A small amount of heat was supplied to the optical fiber in (a) and the adjustable mirror in (b) to avoid any frost on these surfaces during the test.

The properties for the regenerative desiccant coated wheel tested for frost growth is presented in Table 1. The matrix core aluminum sheet thickness was 0.052 mm leaving the desiccant coating thickness on each side of the sheet of 0.016 mm so the total thickness is $0.052+2\times0.016=0.084$ mm.

Photos before and after frost growth are presented in Fig. 4. Figure 4(*a*) shows a typical photo of the corrugated geometry matrix without frost. Figures 4(*b*), 4(*c*), and 4(*d*) show that frost inside several flow channels of the energy wheel at three different locations on the wheel surface after 20 min of operation.

Temperature measurements were taken using T-type thermocouples with a calibration uncertainty of ±0.1 °C; however, because the downstream temperatures were taken downstream of the air flow mixers and flow straighteners they do not show any transient fluctuations of short duration. Conduction effects in the thermocouple lead wires were made small by long emersion lengths. The temperature data at stations 1–4 are presented in Fig. 5. The air speed through this flow channel can be many times greater with frost than without. The added resistance of the frost layer reduces the heat rate as the frost layer grows in each channel. This reduction in heat rate is indicated by the decreasing sensible energy effectiveness, ε_s, defined by the equation

$$\varepsilon_s = \frac{(\dot{m}c_p)_s(T_1 - T_2)}{(\dot{m}c_p)_{\min}(T_1 - T_3)}, \tag{1}$$

where ${}_s(\dot{m}c_p)$ and $(\dot{m}c_p)_{\min}$ are nearly constant during the test when the variation in c_p with T is small.

For typical regenerative wheel the flow velocity in flow channels is between 1.5 and 4 m/s and the corresponding Reynolds numbers are 120 and 320, respectively. For this test wheel the

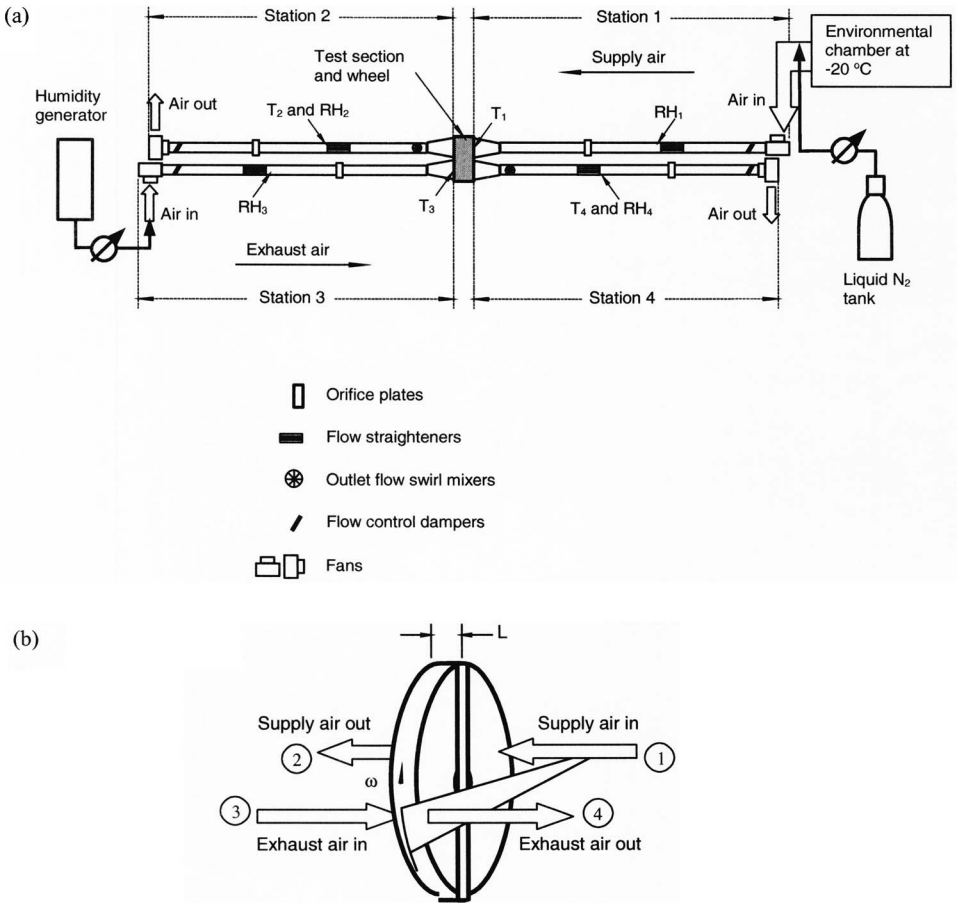

Fig. 2 (*a*) **Schematic diagram of the laboratory experimental test facility for frost growth within a regenerative wheel and instrumentation and** (*b*) **a schematic diagram showing the air flow through a regenerative wheel**

velocity is 2 m/s and Re=160. The starting value of f' Re is 10.4 for the corrugated flow channels with aspect ratio $\eta=0.4$ and when frost grows in the flow channels the value of f' Re is expected to approach f' Re=16 which is the value for circular tubes.

Figure 6 shows $\varepsilon_s(t)$ where the vertical bars indicate the uncertainty. Humidity measurements were taken using calibrated sensors with a calibration uncertainty of ±2% for relative humidity between 5% and 95%. The Vaisala capacitance type humidity sensors were used for these tests which have a measured response time 15 s for 90% of the humidity change. Calibration of these humidity sensors were done over the range of temperatures used in the test using a factory calibrated chilled mirror. The humidity ratio, W, at each station was calculated using the ASHRAE equations [19]. Figure 7 shows the data for the humidity ratio where the uncertainty is ±0.0002 on a relative basis and ±0.0004 absolute when $W>0.0004$. The air flow rates were measured using standard orifice plates and calibrated pressure transducers at each of the four measuring stations and these mass flow rates were each set to maintain a constant mass flux of dry air of 2.41 ± 0.04 kg/(s m^2) as shown in Fig. 8.

The problem with more realistic tests such as the case of using a particular fan with its own flow versus pressure drop characteristics is that the fan selection significantly alters the results. This effect can be seen in the frosting study by Chen et al. [20] where it was shown that axial flow and centrifugal fans will result in different increasing pressure drops and decreasing flow rates and they result in different frost growth characteristics on fins for the same frost growth starting condition. In this study the mass flow rate was maintained at a selected typical value so that the physics of the process would be more clearly understood even though this condition is not likely to occur in practice.

Figure 9 shows the pressure drop, Δp, across the frosted regenerative wheel with time during a 120 min test where $\Delta p_{00}=35$ Pa is the pressure drop with no frost. The calibration uncertainty in these pressure drop data is ±3 Pa. Line (a) shows that the pressure drop ratio increases with time in supply air side and (b) shows it for the exhaust side. The somewhat surprising pressure drop fluctuations with time on both sides of the wheel imply a very different physical phenomenon than just the steady mass accumulation rate of frost as given by $\dot{m}_f=\dot{m}(W_3-W_4)$ after 5 min using the data in Figs. 7 and 8. The rapid rise in pressure drop for each fluctuation is a consequence of frost growth while the rapid fall in pressure drop for each pressure fluctuation is a consequence of the frost fracture and removal of part of the frost layer in many, but not necessarily all, of the flow tubes. Furthermore, these frost fractures due to frost layer fatigue phenomena [21], are sequenced over 1–2 min among the large number of flow channels the supply and exhaust sides of the exchanger. For any tube, not all the frost is removed after any decrease in pressure drop so there is a gradual increase in the mean value of these pressure drops with time. Generally, the cycle period for each pressure fluctuation increases slowly with time and is related to the speed of wheel rotation (i.e., $\omega=20$ rpm) only in that the minimum and maximum pressure drop on one side is expected to lag behind that of the other side where the frost first fractures by less than one half

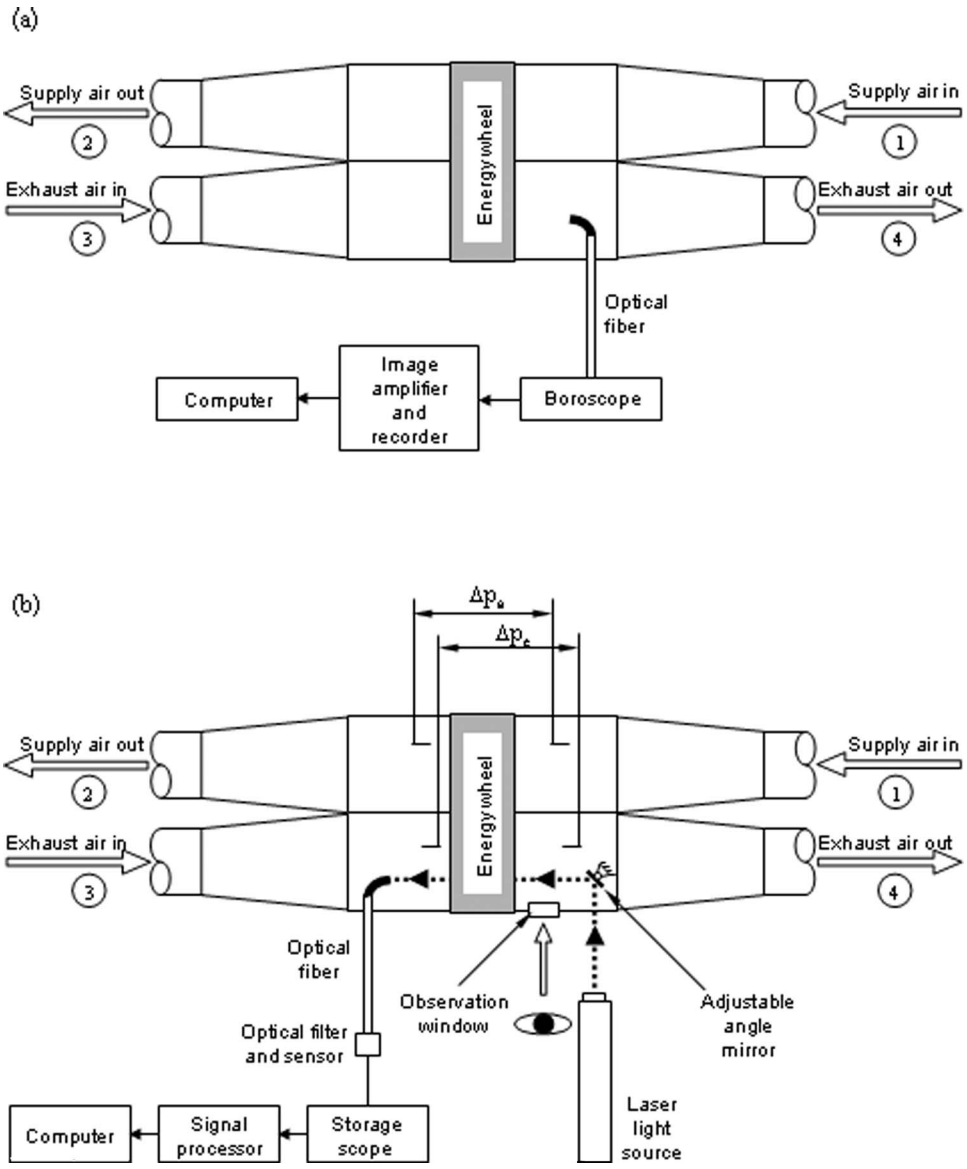

Fig. 3 Frost growth measurement system: (*a*) frost photosystem with a boroscope and (*b*) static pressure drop measurement and laser detector system

rotation (i.e., 1.5 s). The relative magnitude of these pressure drop fluctuations increases significantly with time up to about 75 min and then remains nearly constant.

It is also noted that after 60 min of frost growth the magnitude of the exhaust side pressure drop differs slightly from that of the supply side. These differences may be caused by slightly different frost fracture characteristics in the two flow channels. It is noted that small differences existed between the supply and exhaust pressure differences at all times as shown in Fig. 10.

Figure 10 shows these data in more detail for two cycles near 40 min after the start of the test. It shows that the pressure rise and fall durations are nearly equal at about 1.3 min each indicating that the frost fracture is not occurring at the same time for each flow tube because the expected duration of frost transmission through frost moves with the average air speed. Given that there are nearly 100 000 flow tubes on each side of the exchanger, the pressure drop will appear to be continuous and not abrupt if the flow tubes that have a frost fracture are sequential in time. When

Table 1 Geometric properties for the regenerative wheel

Pore material	Pore shape	Pore wall thickness (mm)	Pore hydraulic diameter (mm)	Wheel diameter (mm)	Wheel thickness (mm)	Hub diameter (mm)
Aluminum	Corrugated	0.084 ± 0.005	1.00 ± 0.07	508.0 ± 0.5	99.0 ± 0.5	80.0 ± 0.5

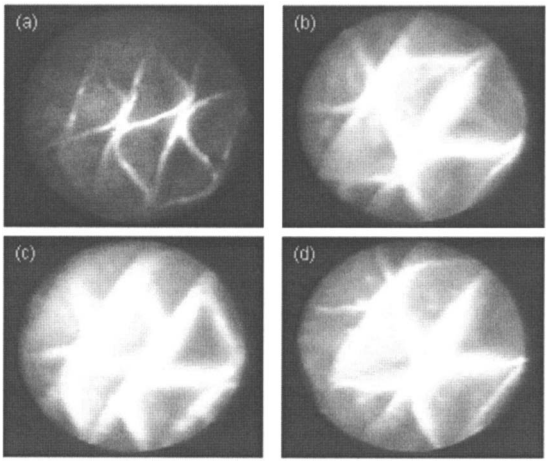

Fig. 4 Photos of some energy wheel flow channels: (*a*) before frost growth (amp. factor=10); (*b*), (*c*), and (*d*) after frost growth (amp. factor=12), T_1=−40 °C, ϕ_1=50%, g_1=2.41 kg/(s m^2), $\Delta p_{1-2}(t=0)$=35 Pa, T_3=20 °C, ϕ_3=40%, g_3=2.41 kg/(s m^2), $\Delta p_{3-4}(t=0)$=38 Pa, and wheel speed is ω=20 rpm

the pressure drop decreases to a small enough value this frost fracture process stops and the pressure drop begins to rise again.

Understanding the physics of frost fracture is not considered part of this study but the consequences of this fracture are part of the study. That is, variations in frost thickness from one flow tube

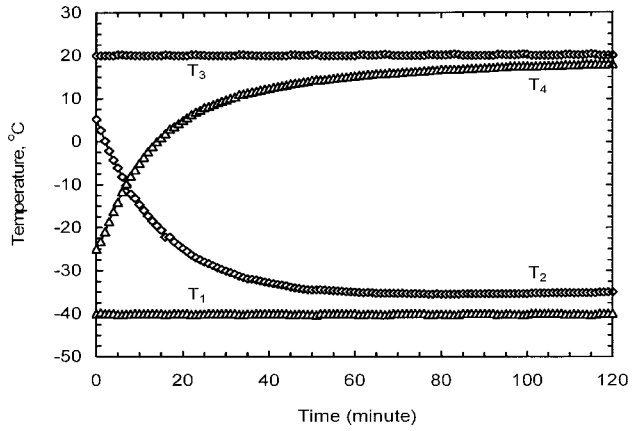

Fig. 5 Temperature data at stations 1–4, $\bar{g}_a$=2.41 kg/(s m^2)

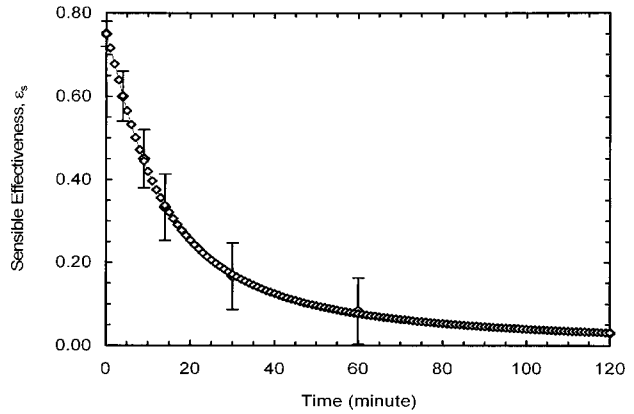

Fig. 6 Sensible effectiveness of the regenerative wheel vs time during frost growing

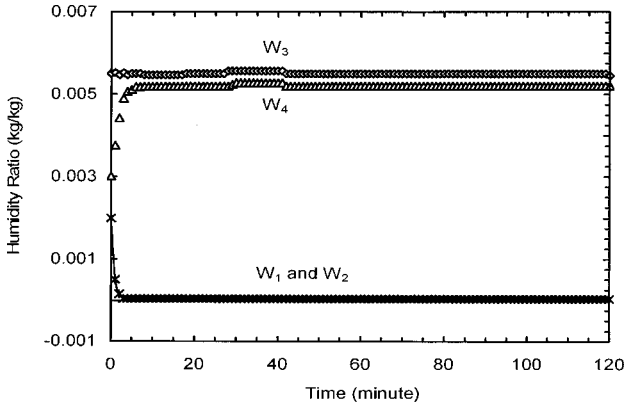

Fig. 7 Humidity ratio data at stations 1–4 with temperatures and flow rate as in Fig. 5

to another will significantly alter the pressure drop compared to the same wheel with no frost thickness differences [22]. The fluctuations in the laser beam sensor readings imply a correlation with the pressure drop fluctuations especially for the first 50 min and then the peak signals decrease to less than 10% of the first peak at

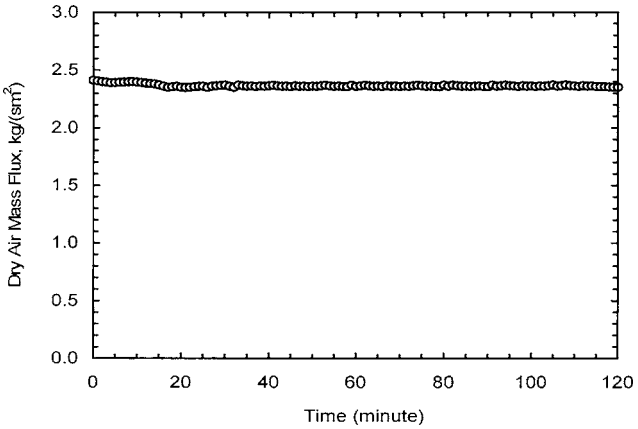

Fig. 8 Dry air mass flux vs time with air flow properties as in Figs. 5 and 7

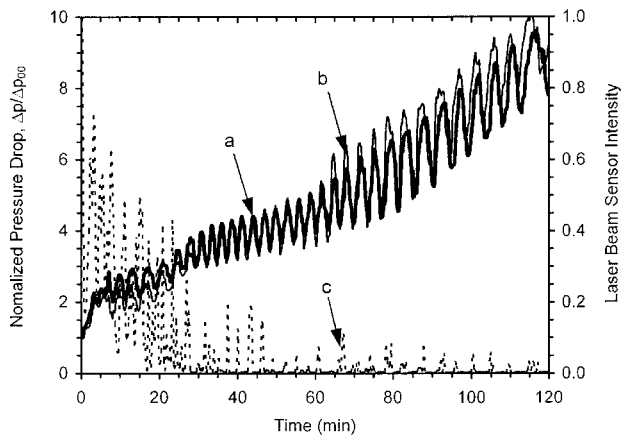

Fig. 9 Pressure drop across the wheel vs time for (*a*) the supply air side; (*b*) the exhaust air side; and (*c*) the laser beam sensor: T_1=−40 °C, ϕ_1=50%, g_1=2.41 kg/(s m^2), $\Delta p_{1-2}(t=0)$=35 Pa, T_3=20 °C, ϕ_3=40%, g_3=2.41 kg/(s m^2), $\Delta p_{3-4}(t=0)$=38 Pa, and wheel speed is ω=20 rpm

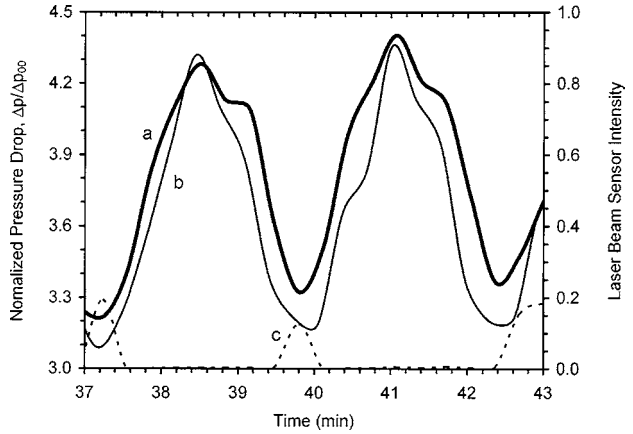

Fig. 10 Two typical cycles of pressure drop across the wheel vs time for (*a*) the supply air side, (*b*) the exhaust air side, and (*c*) the laser beam sensor from 37 to 43 min in Fig. 9

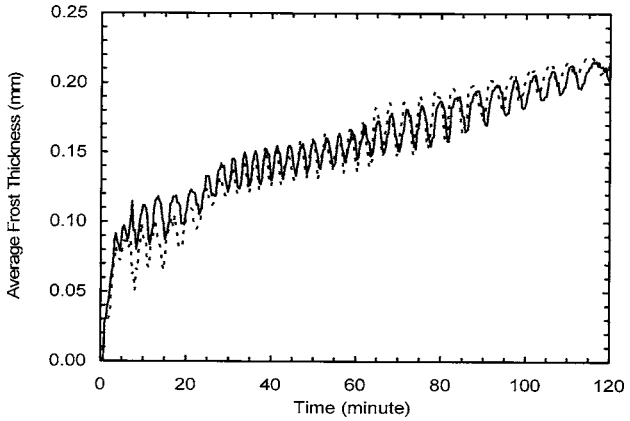

Fig. 11 Calculated average frost thickness vs time

$t<1$ min and optically the frost blockage becomes nearly complete while the pressure fluctuations continue while the total mass flow of dry air was very nearly constant as shown in Fig. 8. Generally, the peak laser signal decreases with time; however, during any frost growth cycle, it increases while the fluctuating pressure drop signal decreases to near its minimum and the optical signal decreases again during the pressure drop increase. The variability of the optical signal from cycle to cycle is consistent with the physical explanation that the pattern of frost fracture among the many flow tubes of the wheel is somewhat erratic from cycle to cycle of pressure drop fluctuation. Generally, the strength of the peak laser beam signal decreases each pressure drop cycle for the first 18 frost growth cycles (50 min) when the optical peaks decrease to less than 10% of the first one—but they still persist, at least a few percent, over the remainder of the test duration. These data imply that, at least for the peak optical signal, the frost does not completely block a straight line laser path through the air flow channels. On the other hand, after 30 min or nine pressure drop cycles the minimum optical signal drops to essentially zero indicating that the frost completely blocks the laser signal over most of the cycle period. The frost accumulation restarts after each pressure cycle fracture from an elevated frost base of unfractured frost and, although this base may be irregular with respect to axial distance through the channel, a straight line air flow channel remains for a small fraction of the pressure fluctuation cycle. These results imply that each air flow channel may be somewhat tortuous during most of the pressure drop fluctuation cycle but not entirely immediately following the fracture because some laser beam signals were cyclically recorded over the entire 120 min test duration.

3 Analysis of the Pressure Drop

For fully developed laminar flow in a tube of a general cylinder shape the pressure drop gradient at any point in the tube can be written [23]:

$$\frac{dp}{dx} = 2f' \frac{1}{D} \rho V^2. \tag{2}$$

At any time the pressure drop for all the tubes are the same and for flow outside the frost layer it can be expressed for any tube, i, of length, L, and hydraulic diameter, D_i, in the form

$$\Delta p(t) = 128 \frac{\mu \dot{m}_i}{\rho} \int_0^L \frac{dx}{K_{Pi} D_i^4} = 128 \frac{\mu \dot{m}_i L}{\rho \overline{K_P} \overline{D_i^4}}, \tag{3}$$

where $\overline{D_i}$ is the length averaged hydraulic diameter.

If the hydraulic diameter were uniform for each flow channel giving value of $\overline{D_0}$ at any time then for a total mass flow rate, $\dot{m}$, through one half of a wheel with N flow channels the corresponding pressure drop would be

$$\Delta p(t) = \frac{256 \mu \dot{m} L}{N \rho \overline{K_P} \overline{D_0^4}}, \tag{4}$$

using $\overline{K_P} = \pi$ for frost growth in the shape of a circular tube, Eq. (4) can be used to calculate $\overline{D_0}$ at any time. Using the pressure drop data from Fig. 9 the frost thickness at any time is calculated as $\delta_f = (D_{00} - \overline{D_0})/2$ and the result is plotted in Fig. 11.

For the same total mass flow rate through the wheel at any time we can show that

$$\frac{\Delta p}{\Delta p_0} = \left[\frac{1}{N} \sum_{i=1}^{N} \left(\frac{\overline{D_i}}{\overline{D_0}} \right)^4 \right]^{-1}, \tag{5}$$

where Δp_0 is the pressure drop for frost uniformly distributed on all flow channels of length averaged hydraulic diameter of $\overline{D_0}$ which initially have an average hydraulic diameter of D_{00} [22]. In general, this pressure drop ratio could start at one value [i.e., with no frost $(\Delta p/\Delta p_0)_0$] and change with time for each redistribution of frost. The average frost thickness data in Fig. 11, when compared with the flow channel hydraulic diameter of 1.0 mm and the optical transmission data of Fig. 9, imply that frost thickness is usually not distributed uniformly along the flow channels.

4 Numerical Model of Frost Growth on a Wall

Two cases are to be considered in this analysis: (1) frost growth during the first frost growth cycle and before the first frost fracture and (2) frost growth after many frost fracture cycles or pressure drop fluctuations. It is noted that the model presented here is only for the frost growth not the time duration between frost fractures. These fracture events are expected to be somewhat random and unpredictable.

A schematic of the expected frost layer inside one flow channel is presented in cross section in Fig. 10 for a symmetric channel before the first frost fracture. Cold and dry supply air with a known mass flow rate, temperature, T_1, and humidity ratio, W_1, passes through an initially clean and smooth airflow channel within the wheel matrix in the $-x$ direction. Then warm and humid exhaust air with known mass flow rate, temperature, T_3, and humidity ratio, W_3, passes through the channel for the same time period in the opposite (x) direction.

The objective of the numerical model is to predict the frost properties at a point (x,z,t) inside a flow channel. Figure 12 shows this frost configuration for the first cycle of frost growth in

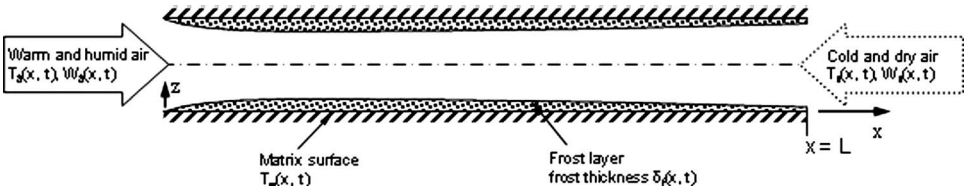

Fig. 12 Schematic of frost distribution on the cold matrix surfaces for one flow channel during the first cycle of frost growth

a flow channel. Variations in the frost properties in the x direction is primarily a consequence of variations in the boundary conditions, i.e., wall temperature, $T_w(x,t)$, airflow temperatures, $T_1(x,t)$ and $T_3(x,t)$, airflow humidity ratios, $W_1(x,t)$, and $W_3(x,t)$.

After many pressure drop cycles (case 2), the frost distribution fracture cycle is schematically shown in Fig. 13 for the case of the laser beam not completely obstructed after the frost fracture but obstructed after the new frost growth where line (a) represents the frost distribution immediately after a fracture and line (b) represents the frost distribution just before the next fracture. The same frost growth model is applied for the restart of each frost growth cycle except that the restarting frost thickness distribution is assumed to be somewhat irregular but still continuous as shown in Fig. 13.

The major assumptions used to arrive at the governing equations and boundary conditions for the frost growth model are:

(a) the transport of heat and mass in the frost layer is transient, macroscopically one dimensional and dependent only on the boundary conditions at $z=0$ and $z=\delta_f$, (i.e., the variation frost properties in the x direction depend on these boundary conditions [3]).
(b) the total pressure of the gaseous phase (water vapor plus air) in the frost ice matrix is constant for each half rotation of the wheel when the matrix is first exposed to the supply side and then the exhaust side,
(c) both the case of local thermodynamic equilibrium inside the frost layer, i.e., the gas phase temperature and solid (ice) temperature are the same so that the assumptions used for porous media maybe used and the case of supersaturated conditions on the surface of the frost will be investigated.
(d) gas-phase convection inside the frost layer is negligible so the transfer of water vapor is by molecular diffusion.
(e) during the frost accumulation period, the desiccant coating on energy wheels does not alter the characteristics of the frost.

4.1 Frost Growth Model for Each Warm Cycle. The governing equations presented here are similar to those of Tao et al. [24] and Chen et al. [3]. Somewhat different are the boundary conditions used for the volume fraction of ice on the cold plate and the convective heat and mass transfer coefficients at the outer edge of the frost layer. Within the frost layer, the following equations apply at every point (z,t):

Energy equation

$$\rho_f c_p \frac{\partial T}{\partial t} + \dot{m} h_{sg} = \frac{\partial}{\partial z}\left(k_{\text{eff}} \frac{\partial T}{\partial z}\right). \tag{6}$$

Water vapor diffusion equation

$$\frac{\partial(\varepsilon_a \rho_v)}{\partial t} - \dot{m} = \frac{\partial}{\partial z}\left(D_{\text{eff}} \frac{\partial \rho_v}{\partial z}\right), \tag{7}$$

where D_{eff} is the effective diffusion coefficient for water vapor within frost layer and ε_a is the volume fraction of air within the frost.

Ice phase continuity equation

$$\frac{\partial \varepsilon_b}{\partial t} + \frac{\dot{m}}{\rho_b} = 0, \tag{8}$$

where ε_b is the volume fraction of ice within the frost.

Volumetric constraint

$$\varepsilon_a + \varepsilon_b = 1. \tag{9}$$

Thermodynamic relations

$$p_a = p_t - p_v, \tag{10}$$

$$p_a = R_a \rho_a T, \tag{11}$$

$$p_v = R_v \rho_v T, \tag{12}$$

where p_a is the air pressure, p_v is vapor pressure, and p_t is the total gas phase pressure. R_a is the specific gas constant of air and R_v is the specific gas constant of water vapor.

The supersaturated conditions for frost growth within regenerative wheels can be defined by the supersaturation degree at the frost surface defined by [7]

$$S \equiv (p_v - p_{vs})/p_{vs}. \tag{13}$$

Experiments of Na and Webb [7] showed that water vapor is supersaturated at the frost surface. For supersaturation at the frost surface, they developed the following equation,

$$S_{fs} = 0.808(p_{v,\infty}/p_{vs,\infty})(p_{vs,fs}/p_{vs,\infty})^{-0.657} - 1. \tag{14}$$

In this model, Eq. (14) is used to determine the humidity ratio at the frost surface for calculating the mass transfer rate from the air

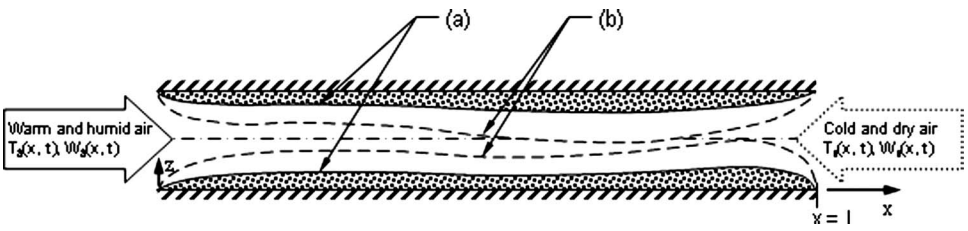

Fig. 13 Schematic of frost distribution (*a*) immediately after one frost fracture and (*b*) just before the next frost fracture

stream to the frost surface. Using Eqs. (13) and (14), the water vapor pressure at the frost surface can be calculated.

In the governing equations, the frost properties are defined as follows:

$$\rho_f = \varepsilon_a(\rho_v + \rho_a) + \varepsilon_b\rho_b, \tag{15}$$

$$c_p = \frac{\varepsilon_a(\rho_a c_a + \rho_v c_v) + \varepsilon_b\rho_b c_b}{\rho_f}. \tag{16}$$

Dietenberger [9] in his paper reviewed ten independent databases for the averaged thermal conductivity of a frost layer and found a wide range of calculated thermal conductivity data (e.g., ±50% about the mean and biases up to 50% as a result of systematic errors where a wide range of frost density was reported). Major difficulties in all the measurements were the determination of the frost–air interface thickness and temperature because optical temperature indicators carry significant bias and direct contact sensors to measure frost thickness or temperature disturbs the frost and cause transient effects of unknown magnitude. He found that both the frost temperature and density effects are important, especially at low temperatures and densities. Dietenberger [9] recommends a complex semiempirical relationship to calculate the local average conductivity of frost in the form

$$k_{\text{eff}} = f(k_a, k_i, \rho_f, T), \tag{17}$$

where the range of frost density and temperature are $50 < \rho_f < 600$ kg/m^3 and $136 < T < 267$ K. This correlation equation is used in this study. It implies that variations in frost density and temperature will alter the local frost effective thermal conductivity. Although no explicit uncertainty analysis was presented, the uncertainty implied in his data comparisons suggest there may be a ±15% to 20% uncertainty in k_{eff} using Eq. (17).

The effective diffusion coefficient is:

$$D_{\text{eff}} = \varepsilon_a D_{AB}/\tau, \tag{18}$$

where D_{AB} is the binary diffusion coefficient for water vapor in air at the film temperature and the tortuosity coefficient, τ, is assumed to be 1.0 for frost. The tortuosity value used in frost growth modeling has been investigated by Chen et al. [25] and found to be not a sensitive factor when the frost density is low.

4.2 Boundary Conditions for the Frost Growth Model during Each Warm Cycle. At the frost–air interface, the mass transfer boundary condition for water vapor is taken to be

$$h_{mf}(x)[W_0 - W(z = \delta_f, t)] = D_{eff,s}\frac{\partial\rho_v(z = \delta_f, t)}{\partial z} + \rho_f\frac{d\delta_f}{dt}, \tag{19}$$

where $h_{mf}(x)$ is the local convective mass transfer coefficient, W_0 is the air flow humidity ratio, and W is the humidity ratio where

$$W = 0.6218\frac{p_v}{p_t - p_v}. \tag{20}$$

The diffusion coefficient at the frost–air interface is defined as

$$D_{\text{eff},s} = \varepsilon_a(z = \delta_f)D_{AB}. \tag{21}$$

The boundary condition for heat transfer at the air–frost interface is:

$$h_f(x)[T_0 - T(z = \delta_f, t)] = k_{\text{eff}}\frac{\partial T(z = \delta_f, t)}{\partial z} - h_{sg}\rho_f\frac{d\delta_f}{dt}. \tag{22}$$

The temperature boundary condition at $z=0$ for the first cycle of frost growth is:

$$T(z = \delta_f, t) = T_w \tag{23}$$

In this model the temperature boundary condition at the cold surface must be specified as either a constant or a known function of x. In this study, T_w is taken to be the mean temperature between the warm exhaust air temperature and the cold supply air temperature at each point x in the flow path.

The local Nusselt number Nu_x was determined for fully developed laminar flow in a round tube with a constant heat flux (i.e., Nu=4.36) [26]. It is assumed in this study that for mass transfer

$$\text{Sh}_x = \text{Nu}_x. \tag{24}$$

Therefore $h_{mf}(x)$ and $h_f(x)$ can be obtained from Sh_x and Nu_x in Eq. (24).

At the cold surface, the volume fraction of ice is taken to be

$$\varepsilon_b(z = 0, t) = 0.3. \tag{25}$$

The selection of boundary condition (25) for the ice volume fraction, ε_b, needs more discussion. In their study of the early growth period of frost growth on a cold plate supplied by room air at a high relative humidity, Tao et al. [2] showed that a large fraction (typically 52% to 72%) of the surface on which frost grows is covered by water droplets [typically 20–70 μm average diameter for a plate temperature of −25 °C (−13 °F)] before these droplets suddenly freeze after a time duration of 15–100 s. Some subcooling of the water droplets is expected during this period. Shortly after these droplets all suddenly freeze, individual dendretic frost crystals start to grow on each frozen droplet which very shortly branch into a fully developed frost layer after about 200 s for cold plate temperatures less than −25 °C (−13 °F). Ramaswamy et al. [27] showed similar results for the early growth period of frost on smooth cold surfaces with airflow at room temperature.

The boundary condition for the fully developed frost ice fraction on the cold plate in this study is set equal to 30% [i.e., $\varepsilon_b(z=0)=0.3$]. Chen et al. [3] found this value to give a good fit between the theoretical simulations and the experimental data but a slightly higher value may be justified for warmer cold plate temperatures. A sensitivity study of this boundary condition did not reveal a strong sensitivity, except for the boundary condition selected by Tao [24] which lead to a very low unrealistic value of ε_b. The values obtained by Le Gall [28] were not compatible with these more recent findings because they are also physically unlikely.

4.3 Conditions for the Start of Each Frost Growth Cycle for the Warm Humid Air Flow. The thickness of frost to start each wheel switch from cold to warm of the cold surface is assumed to not change while the cold dry air flows, i.e.,

$$\delta_f(x, t = t_j) = \delta_{fj}(x), \tag{26}$$

where δ_{fj} is the frost thickness at the end of the previous part of the warm air flow. At the start of the first cycle $t=0$, δ_{fj} is assumed to be 0.01 mm.

The frost temperature, on the other hand, changes significantly during the cold air flow—so the temperature distribution is taken to be that at the end of the cold air flow.

$$T(x, z, t = t_j) = T_j(x, z). \tag{27}$$

The initial volume fraction condition at time zero is:

$$\varepsilon_b(x, z, t = 0) = 0.3. \tag{28}$$

As discussed in Tao et al. [24], an implicit finite difference formulation of these equations was used to solve this numerical model with the properties evaluated from the previous time step.

4.4 Model for Heat Conduction for Each Cooling Period. The model for heat conduction in the frost during the cyclic exposure to cold air is determined only by a heat conduction equation with no phase change,

$$\rho_f c_f\frac{\partial T}{\partial t} = \frac{\partial}{\partial z}\left(k_{\text{eff}}\frac{\partial T}{\partial z}\right). \tag{29}$$

The initial conditions for the temperature is the same as Eq. (27) except that $T(z)$ is the frost temperature at the end of the warm

Table 2 Inlet air conditions and wheel speed

	Temperature (°C)	W_0 (kg/kg)	Mass flux (kg/s·m^2)	Wheel speed (rpm)
Supply	-40	0.00004	2.41	20
Exhaust	+20	0.0058	2.41	20

cycle.

The boundary condition at δ_f is given by

$$h_f[T_0 - T(z=\delta_f,t)] = k_{\text{eff}}\frac{\partial T(z=\delta_f,t)}{\partial z}, \tag{30}$$

and at $z=0$ it is given by the equation for heat conduction on the cold surface.

In this model, the temperature of the cold surface must be known. This temperature is estimated by using a time-averaged energy balance between the supply and exhaust air flows and assuming that the time-averaged temperature of the cold surface at any point along the airflow path varies linearly with distance from the leading edge. Simonson and Besant [4] show that this surface temperature varied a few degrees over each wheel cycle and decreased linearly with x. These cyclic variations of the matrix surface temperature are expected to decrease as the frost layer grows. So the assumption of a constant surface temperature at each point, x, in the flow passage will result in a negligible error in frost characteristics.

A discussion of the verification of this frost growth model is presented in the Appendix.

5 Simulated Results

The frost growth in a regenerative heat or energy wheel will depend upon several geometric and operative conditions. In this study, the regenerative wheel has a depth of 100 mm and spacing between the flat matrix surfaces of the wheel. The wheel speed was 20 rpm. At higher speeds the cyclic changes are more rapid but the cyclic average frost properties are the same at each instant in time. Since the thermal mass of the wheel changes through a very small temperature range, it is assumed that the cold base temperature of the wheel remains constant for a given steady operating condition and is equal to the time average of the supply and exhaust air temperatures at that point in the wheel. The supply and exhaust inlet air conditions for the simulations are shown in Table 2. In the following graphs of simulated results the case of frost growth is presented for frost growth after any frost fracture cycles.

The simulated frost thickness, average density, air–frost interface temperature, and average mass accumulation rate are shown at one location 0.05 m from the exhaust inlet and midway between the inlet and outlet of the wheel in Figs. 14(*a*), 14(*b*), and 14(*c*). Simulation results for other positions within the wheel showed only small property variations with respect to this midpoint. A time duration of 300 s was chosen for this frost growth period before any frost fracture in spite of the fact that some frost fracture appears to occur over a shorter time. The step changes in frost thickness every 1.5 s in Fig. 14(*a*) corresponds to one 1.5 s of frost growth while the warm supply air flows, followed by one 1.5 s of no growth during the cold supply air flow. The average frost density in Fig. 14(*b*) shows only very small changes with each cycle and a slow gain over a long time indicating that the frost not only gains mass at its outer limit, $z=\delta_f$, but internally also. The air–frost interface temperature in Fig. 14(*c*) shows significant variations with each half of the cyclic exposure from warm to cold air, and over many cycles, as the frost grows. Expanding one 2-min cycle, shows more detail on this frost thickness, average density, and interface temperature variation with time in Fig. 15. Figure 16 presents the frost property simulation results at 40 min after the start of the test beginning at the time of the frost fracture in one flow channel similar to Fig. 14. The simulation start point at 40 min was selected as typical a midtest frost fracture time. The simulated averaged frost mass accumulation rate, presented in Fig. 17, is consistent with the measured average frost mass accumulation rate of $0.000\,12 \pm 0.0001$ kg/s but the large uncertainty in the small difference in the humidity difference $(W_3 - W_4)$ implies too large an uncertainty to be a meaningful comparison.

6 Summary and Conclusions

Data are presented for frost growth inside a regenerative wheel operating with a constant mass flow of very cold supply air

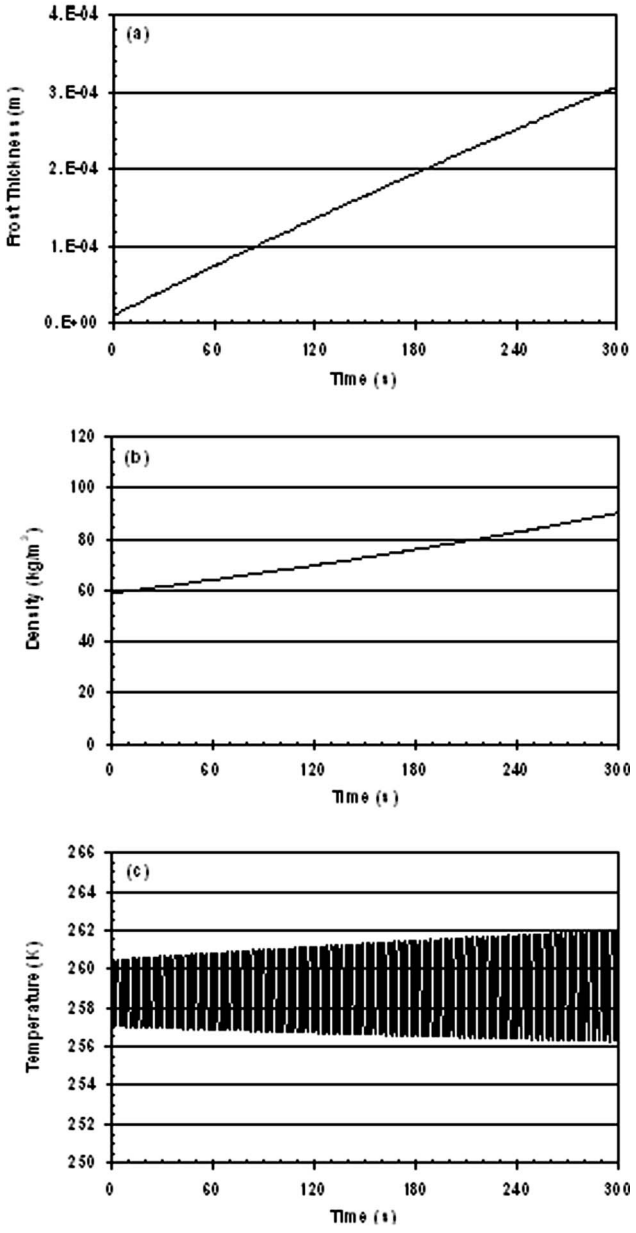

Fig. 14 Simulated results of (*a*) frost thickness, (*b*) frost density, and (*c*) frost-air interface temperatures for 300 s of frost grow period at a distance $x=50$ mm for $T_1=-40$ °C, $\phi_1=50\%$, $g_1=2.41$ kg/(s m^2), $T_3=20$ °C, $\phi_3=40\%$, $g_3=2.41$ kg/(s m^2), and wheel speed is $\omega=20$ rpm

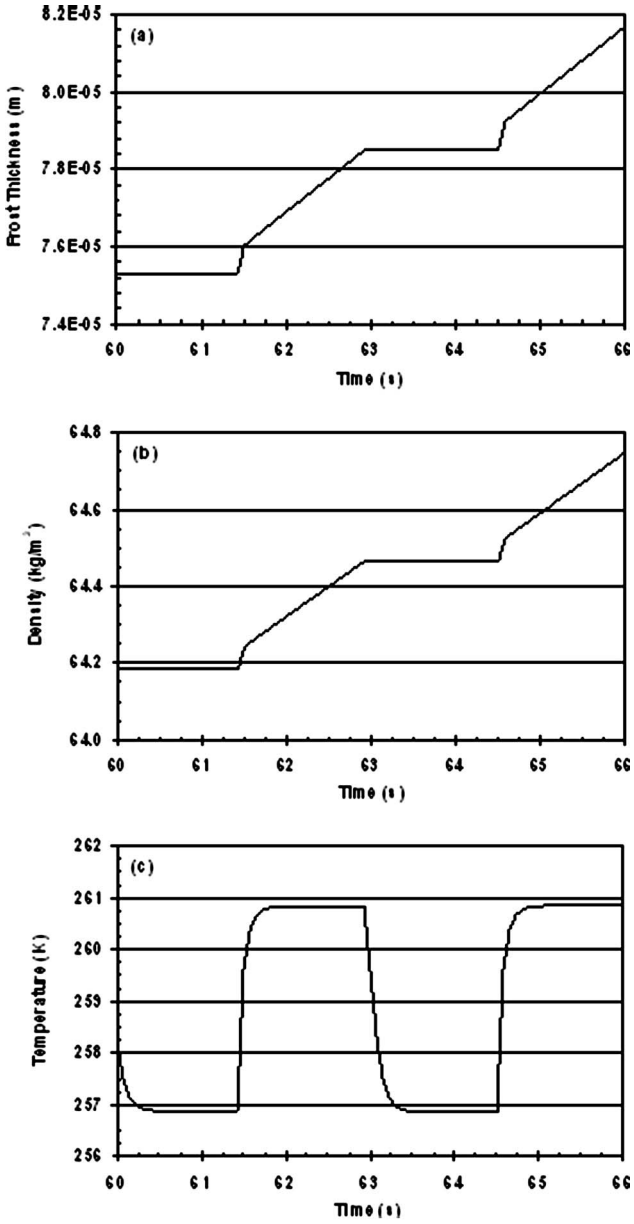

Fig. 15 Simulated results of (*a*) frost thickness; (*b*) frost density; and (*c*) frost–air interface temperatures variation with time for a typical two rotations for conditions as in Fig. 14

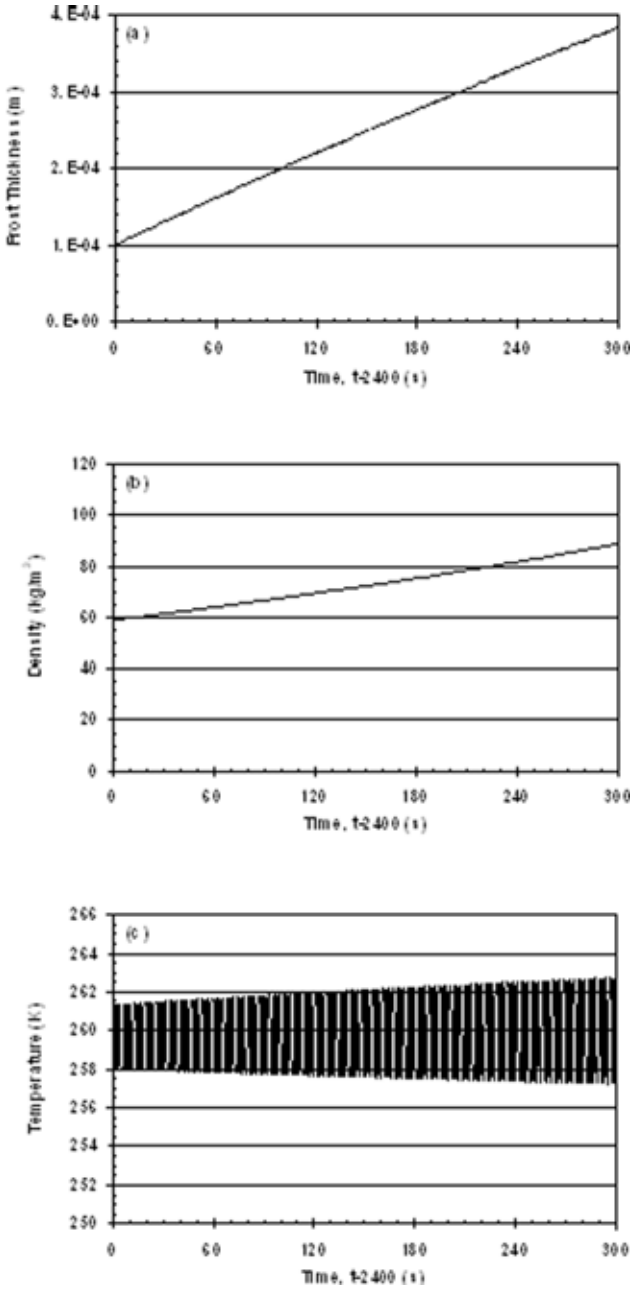

Fig. 16 Simulated results of (*a*) frost thickness; (*b*) frost density; and (*c*) frost–air interface temperatures for a period of 300 s of frost growth after frost fracture at 40 min at a distance $x = 50$ mm for flow conditions as in Fig. 14

(−40 °C) and humid room temperature exhaust air (20 °C). The measurement of the air pressure drop across the wheel, rotating at 20 rpm, revealed cyclic fluctuations and a gradual increase in the average pressure drop over 2 h. A laser beam passing through the wheel showed coincident transmission fluctuations and a gradual decrease in the average laser signal. These fluctuations are interpreted to result from frost growth over many rotations of the wheel followed by a sudden fracture of the outer layers of frost in various flow channels within the wheel. These frost fractures do not occur at the same time for all the flow channels; rather, they are phased over 1.0–2.0 min at which time they stop and the frost growth again becomes the main feature.

This paper presents the equations for a frost growth model on the inside surfaces of a regenerative heat or energy wheel. This numerical model was tested against measured data and then used to simulate frost properties within a regenerative heat or energy wheel. This model permits the modeling of frost growth with time over the period of many rotational cycles.

For the selected operating conditions it is concluded that the frost thickness will increase with time most significantly in the middle of the wheel and cause 50% blockage in 20 min of exposure. The slow cyclic variation and slow increase in frost density over time indicates that frost gains mass internally as well as at its outer limit. Finally, the model predicts a significant temperature variation at the air–frost interface during each cycle and a gradual increase in average air–frost interface temperature as the frost layer thickens with time.

Acknowledgments

Funding for this research work was provided by Venmar CES, and NSERC, Canada. The regenerative exchangers used for testing were provided by Venmar CES, Saskatoon, SK, Canada.

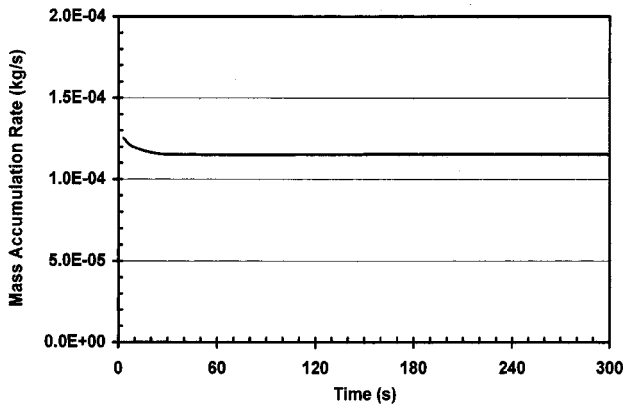

Fig. 17 Simulated averaged frost accumulation rate for 300 s of frost grow period within the regenerative wheel for flow conditions as in Figure 14

Nomenclature

c_a = specific heat of air, J/(kg K)
c_b = specific heat of solid ice, J/(kg K)
c_v = specific heat of water vapor, J/(kg K)
c_p = specific heat, J/(kg K)
D = hydraulic diameter of flow channels, m
$\overline{D_0}$ = length averaged hydraulic diameter for uniform frost distribution in flow channels, *m*
D_{00} = averaged hydraulic diameter of flow channels without frost, *m*
D_{AB} = binary diffusion coefficient for water vapor in air, m^2/s
D_{eff} = effective diffusion coefficient for water vapor within frost layer, m^2/s
f' = flow channel averaged skin friction factor, dimensionless
g_a = dry air mass flux rate, $kg/(s\ m^2)$
h_{fg} = evaporation specific enthalpy of saturated liquid water, $h_g - h_f$, J/kg
h_{mf} = local convective mass transfer coefficient, kg/m^2
h_{sg} = enthalpy of sublimation, J/K
i = individual flow channel, 1, 2, 3,…
k_a = thermal conductivity of air, W/(m K)
k_b = thermal conductivity of ice, W/(m K)
k_{eff} = effective thermal conductivity of frost, W/(m K)
K_p = flow channel geometry constant, dimensionless
L = length of flow channel or wheel thickness, *m*
$\dot{m}$ = phase change rate or mass flow rate, $kg/(s\ m^3)$ or kg/s
N = number of flow channels on half of a wheel, dimensionless
Nu_x = local Nusselt number, $h \cdot x/k$, dimensionless
p_a = air pressure, Pa
p_t = total gas phase pressure, Pa
p_v = water vapor pressure, Pa
Δp = pressure drop, Pa
Δp_0 = pressure drop across energy wheel for frost uniformly distributed on all flow channels, Pa
Δp_{00} = pressure drop across energy wheel with no frost, Pa
R_a = specific gas constant of air, J/(kg K)
R_v = specific gas constant of water vapor, J/(kg·K)
Re = Reynolds number, $\rho VD/\mu$, dimensionless
S = supersaturation degree, dimensionless
Sh_x = local Sherwood number, $h_m \cdot x/D$, dimensionless
t = time, s
T = temperature, K
V = mean flow velocity, m/s
W_0 = air flow humidity ratio, $kg_{\text{vapor}}/kg_{\text{dry air}}$
W = humidity ratio, $kg_{\text{vapor}}/kg_{\text{dry air}}$
x = distance from the leading edge, *m*
z = position normal to the cold surface, *m*

Greek

δ = frost height, *m*
ε = volume fraction or effectiveness, dimensionless
ε_a = volume fraction of air within frost, dimensionless
ε_b = volume fraction of ice within frost, dimensionless
ε_s = sensible energy effectiveness, dimensionless
η = aspect ratio, corrugated wave length divided by wave height, dimensionless
μ = viscosity, Pa s
ρ = density, kg/m^3
ϕ = relative humidity, dimensionless
ω = wheel speed, rad/s
τ = tortuosity coefficient, dimensionless

Subscripts

a = air
b = ice
c = cold air
e = exhaust air
f = frost
fs = frost surface
h = warm air
i = individual flow channel, 1, 2, 3,…
j = frost growth cycle in energy wheel, 1, 2, 3,…
l = latent heat
min = minimum value
s = surface of frost, sensible heat, or supply air
t = total value
v = water vapor
w = wall of the matrix
0 = mean value
1 = station 1
2 = station 2
3 = station 3
4 = station 4
∞ = free stream

Appendix: Model Verification

The basic equations and boundary conditions were presented to model the frost growth inside a regenerative heat or energy wheel. It was shown by Chen et al. [3] that frost models need validation using carefully devised experiments that include a rigorous uncertainty analysis. In the present study, the data of Mao et al. [29] for humid airflow over a cold flat plate (surface temperatures −35 to −42 °C) was chosen to validate the frost growth model. Complete validation of the model for humid airflow through a regenerative wheel would require the development of a test facility with sophisticated instrumentation that can accurately measure frost accumulation and thickness distributions throughout the rotating wheel. This type of validation is beyond the scope of this study.

Mao et al. [29] presented an experimental database of the frost growth on a cold flat plate including 20 sets of data for 20 different test conditions. To develop an accurate numerical model, it is essential to identify those test conditions and results that would not give rise to large uncertainties in the data. It was noted that uncertainties in the supply air humidity ratio (W_0) might be large

when the air humidity ratio is low with respect to the test variations in humidity ratio (e.g., up to 0.0001). Also, it was noted that these experimental data for rough frost, or partially rough frost, have an uncertainty of ±0.15 to ±0.4 mm for the thickness measurement when the frost layer is thin (i.e., less than 4 mm). Uncertainty in frost mass per unit area is somewhat smaller and is most significant for very thin layers of frost, similar to that for frost thickness. Uncertainty in frost density combines data from these two measurements. Uncertainty in the temperature difference between the airflow and cold surface was large when the temperature difference is less than 12 °C (21.6 F).

The main elements of this model for frost growth on a flat plate were also verified in the paper by Chen et al. [25] and for frost growth on heat exchanger fins in the papers by Chen et al. [3] where frost concentration, frost thickness, surface temperature, and all the inlet air flow properties were measured. A large number of test conditions were compared to the simulations and the uncertainty limits were stated for all the test data. These studies included spatial and temporal grid checks and sensitivity studies for the specified boundary conditions.

References

[1] Hayashi, Y., Aoki, A., Adachi, S., and Hori, K., 1977, "Study of Frost Properties Correlating with Frost Formation Types," ASME J. Heat Transfer, **99**, pp. 239–245.

[2] Tao, Y-X, Besant, R. W., and Mao, Y., 1993, "Characteristics of Frost Growth on a Flat Plate during the Early Period," ASHRAE Trans., **99**, pp. 739–745.

[3] Chen, H., Thomas, L., and Besant, R. W., 2000, "Modeling Frost Characteristics on Heat Exchanger Fins: Part I: Numerical Model and Part II: Model Validation and Limitations," ASHRAE Trans., **106**, pp. 357–376.

[4] Simonson, C. J., and Besant, R. W., 1998, "Heat and Moisture Transfer in Energy Wheels during Sorption, Condensation and Frosting Conditions," ASME J. Heat Transfer, **120**, pp. 699–708.

[5] Lee, K. S., Kim, W. S., and Lee, T. H., 1997, "A one-dimensional model for frost formation on a cold flat surface," Int. J. Heat Mass Transfer, **40**, pp. 4359–4365.

[6] Na, B., and Webb, R. L., 2004a, "Mass Transfer On and Within a Frost Layer," Int. J. Heat Mass Transfer, **47**, pp. 899–911.

[7] Na, B., and Webb, R. L., 2004b, "New Model for Frost Growth Rate," Int. J. Heat Mass Transfer, **47**(5), pp. 925–936.

[8] Na, B., and Webb, R. L., 2003, "A Fundamental Understanding of Factors Affecting Frost Nucleation," Int. J. Heat Mass Transfer, **46**, pp. 3797–3808.

[9] Dietenberger, M. A., 1983, "Generalized Correlation of the Water Frost Thermal Conductivity," Int. J. Heat Mass Transfer, **26**, pp. 607–619.

[10] Thomas, L., Chen, H., and Besant, R. W., 1999, "Measurement of Frost Characteristics on Heat Exchanger Fins, Part I: Test Facility and Instrumentation," ASHRAE Trans., **105**, pp. 283–293.

[11] Chen, H., Thomas, L., and Besant, R. W., 1999, "Measurement of Frost Characteristics on Heat Exchanger Fins, Part II: Data and Analysis," ASHRAE Trans., **105**, pp. 294–302.

[12] Holmberg, R. B., 1977, "Heat and Mass Transfer in Rotary Heat Exchangers with Non-Hygroscopic Rotor Materials," ASME J. Heat Transfer, **99**, pp. 196–202.

[13] Holmberg, R. B., 1979, "Combined Heat and Mass Transfer in Regenerators with Hygroscopic Materials," ASME J. Heat Transfer, **101**, pp. 205–210.

[14] Bilodeau, S., Brosseau, P., Lacroix, M., and Mercadier, Y., 1999, "Frost Formation in Rotary Heat and Moisture Exchangers," Int. J. Heat Mass Transfer, **42**, pp. 2605–2619.

[15] Freund, S., Klein, S. A., and Reindl, D. T., 2003, "A Semi-Empirical Method to Estimate Enthalpy Exchanger Performance and a Comparison of Alternative Frost Control Strategies," HVAC&R Res., **9**, pp. 493–508.

[16] Shang, W., Chen, H., Evitts, R. W., and Besant, R. W., 2001, "Frost Growth in Regenerative Heat Exchangers: Part I: Problem Formulation and Method of Solution and Part II: Simulation and Discussion," *Proceedings of 2001 ASME International Mechanical Engineering Congress and Exposition*, New York, NY.

[17] ASHRAE, 1991, *ANSI/ASHRAE Standard 84-1991R, Method of Testing Air-to-Air Heat Exchangers*, American Society of Heating, Refrigerating and Air-Conditioning Engineers, Inc., Atlanta, GA.

[18] Shang, W., Wawryk, M., and Besant, R. W., 2001, "Air Crossover in Rotary Wheels Used for Air-to-Air Heat and Moisture Recovery," ASHRAE Trans., **107**, pp. 72–83.

[19] ASHRAE, 2001, *2001 ASHRAE Handbook - Fundamentals*, American Society of Heating, Refrigerating and Air-Conditioning Engineers, Inc., Atlanta, GA.

[20] Chen, H., Thomas, L., and Besant, R. W., 2003, "Fan Supplied Heat Exchanger Fin Performance under Frosting Conditions," Int. J. Refrig., **26**, pp. 142–152.

[21] Fletcher, 1970, *The Chemical Physics of Ice*, Cambridge University Press, Cambridge.

[22] Shang, W., and Besant, R. W., 2005, "Effects of Pore Size Variations on Regenerative Wheel Performance," ASME J. Eng. Gas Turbines Power, **127**, pp. 121–135.

[23] Shah, R. K., and London, A. L., 1978, *Laminar Flow Forced Convection in Ducts*, Supplement 1 to Advances in Heat Transfer, Academic Press, New York.

[24] Tao, Y.-X, Besant, R. W., and Rezkallah, K. S., 1993b, "A Mathematical Model for Predicting the Densification and Growth of Frost on a Flat Plate," Int. J. Heat Mass Transfer, **36**, pp. 353–363.

[25] Chen, H., Besant, R. W., and Tao, Y. X., 1999, "Frost Characteristics and Heat Transfer on a Flat Plate under Freezer Operating Conditions: Part II: Numerical Modeling and Comparison with Data," ASHRAE Trans., **105**, pp. 252–259.

[26] Kays, W. M., and Crawford, M. E., 1993, *Convective Heat and Mass Transfer*, McGraw-Hill, New York.

[27] Ramaswumy, M., Georgiadis, J. G., and Tenbusch, A., 1995, "Microscopic Study of Frost Inception: Effects of Substrate, Supercooling, and Grazing Flow," *Proceedings of 1995 ASME International Mechanical Engineering Congress and Exposition*.

[28] Le Gall, R., Grillot, J. M., and Jallut, C., 1997, "Modeling of Frost Growth and Densification," Int. J. Heat Mass Transfer, **40**, pp. 3177–3187.

[29] Mao, Y., Besant, R. W., and Rezkallah, K. S., 1992, "Measurement and Correlations of Frost Properties with Airflow over a Flat Plate," ASHRAE Trans., **98**, pp. 65–78.

Numerical Simulation of Mixed Convective Flow Over a Three-Dimensional Horizontal Backward Facing Step

J. G. Barbosa Saldana
Graduate Research Assistant

N. K. Anand
Professor and Assistant Dean for Graduate Programs

Department of Mechanical Engineering,
Texas A&M University,
College Station, TX 77843, USA

V. Sarin
Assistant Professor
Department of Computer Science,
Texas A&M University,
College Station, TX 77843, USA

Laminar mixed convective flow over a three-dimensional horizontal backward-facing step heated from below at a constant temperature was numerically simulated using a finite volume technique and the most relevant hydrodynamic and thermal features for air flowing through the channel are presented in this work. The channel considered in this work has an aspect ratio AR=4*, and an expansion ratio* ER=2*, while the total length in the streamwise direction is 52 times the step height* (L=52 s) *and the step length is equal to 2 times the step height* (l=2 s)*. The flow at the duct entrance was considered to be hydrodynamically fully developed and isothermal. The bottom wall of the channel was subjected to a constant high temperature while the other walls were treated to be adiabatic. The step was considered to be a thermally conducting block.*
[DOI: 10.1115/1.2005272]

Keywords: Numerical Simulation, Backward-Facing Step, Mixed Convection

Introduction

Separation and reattachment flows is a phenomenon that is found in several industrial devices such as in pieces of electronic cooling equipment, cooling of nuclear reactors, cooling of turbines blades, flow in combustion chambers, flow in wide angle diffusers, and valves. In other situations the separation is induced in order to induce more favorable heat transfer conditions as in the case of compact heat exchangers [1–3].

In the last decade several numerical studies have been conducted to gain a better knowledge and understanding of the hydrodynamic and thermal aspect of the separated flow. In this aspect the backward-facing step has been the main target of several researchers. Even though the geometry is simple it is rich in physics as it captures complex flow and heat transfer features associated with separation and reattachment. For this reason flow over a backward facing step has been used as a benchmark problem for validating numerical codes and numerical procedures [4].

The recent developments in terms of computing speed and memory storage has permitted the solution to problems that demands an extremely high computational resources as in the case of numerical simulations of three-dimensional flows, including fluid flow and heat transfer phenomenon over a three-dimensional backward facing step problem [5–7]. However, none of the previous cited publications include the effects of buoyant forces or mixed convective flow, even though the effects of buoyancy forces become significant when dealing with laminar flow regime with strong temperature gradients.

The mixed convective flow over a three-dimensional backward facing step is not a very common topic found in the literature. Nie, Armaly, Li, and co-workers [8,9] have considered the effect of buoyancy force (mixed convection effects) in vertical ducts wherein the gravitational vector and flow direction are parallel.

Iwai et al. studied mixed convection in vertical ducts with backward facing step by varying the duct angle of inclination [2]. However, their study was confined to extremely weak buoyancy forces. For example, when the backward facing step is aligned with the horizontal axis the modified Richardson number was chosen to be equal to 0.03 (Ri^*=0.03). This value is associated with not strong enough buoyancy effects to alter the velocity field and temperature distributions from the pure forced convection values. Therefore, the flow in the cited report can be judged and qualified as being a pure forced convective flow.

Thus the work that comes close to the configuration considered in this study is that of Iwai et al. [2]. Hence it is concluded that there is no work reported on mixed convective flows over a horizontal three-dimensional backward facing step to date in the literature.

In this work, numerical simulation of three-dimensional mixed convective air flow over a horizontal backward facing step heated from below at a constant temperature is presented. The simulation is carried out for dominant free convective flow and the results for limiting cases are compared with those of pure force convective three-dimensional flow. Also, the back step is considered as a conductive block which is another unique aspect of this study.

Model Description and Numerical Procedure

The geometry considered in this study is shown in Fig. 1. The duct aspect ratio and expansion ratio were fixed in relation to the step height (s) as AR=4 and ER=2, respectively. The total length of the channel is equal to 52 times the step height L=52 s and the length of the step is fixed as 2 times the step height l=2 s. This particular geometry was chosen to study the strong three-dimensional behavior of the flow over the backward facing step.

Flow was assumed to be steady and the Boussinesq approximation was invoked. Based on these simplifying assumptions the steady three-dimensional mass conservation, momentum equations, and energy equation governing the fluid flow and heat transfer problem are reduced to the following forms [10,11]:
continuity equation:

$$\frac{\partial(\rho u)}{\partial x}+\frac{\partial(\rho v)}{\partial y}+\frac{\partial(\rho w)}{\partial z}=0, \tag{1}$$

X momentum equation:

Contributed by the Heat Transfer Division for publication in the JOURNAL OF HEAT TRANSFER. Manuscript received: May 27, 2004. Final manuscript received: April 27, 2005. Review conducted by: Sumanta Acharya.

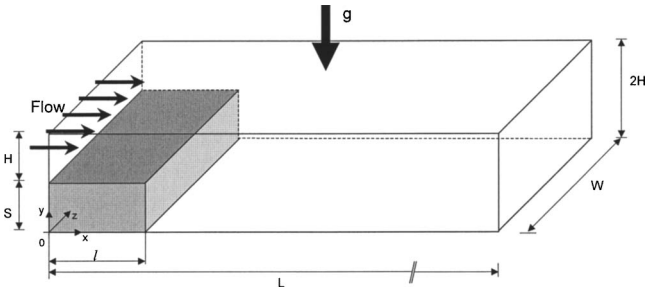

Fig. 1 Schematic of the three-dimensional backward facing step

$$\left(u\frac{\partial(\rho u)}{\partial x}+v\frac{\partial(\rho u)}{\partial y}+w\frac{\partial(\rho u)}{\partial z}\right)=-\frac{\partial p}{\partial x}+\left[\frac{\partial}{\partial x}\left(\mu\frac{\partial u}{\partial x}\right)+\frac{\partial}{\partial y}\left(\mu\frac{\partial u}{\partial y}\right)+\frac{\partial}{\partial z}\left(\mu\frac{\partial u}{\partial z}\right)\right], \tag{2}$$

Y momentum equation:

$$\left(u\frac{\partial(\rho v)}{\partial x}+v\frac{\partial(\rho v)}{\partial y}+w\frac{\partial(\rho v)}{\partial z}\right)=-\frac{\partial p}{\partial y}+\rho_0\beta(T-T_0)g_y+\left[\frac{\partial}{\partial x}\left(\mu\frac{\partial v}{\partial x}\right)+\frac{\partial}{\partial y}\left(\mu\frac{\partial v}{\partial y}\right)+\frac{\partial}{\partial z}\left(\mu\frac{\partial v}{\partial z}\right)\right], \tag{3}$$

Z momentum equation:

$$\left(u\frac{\partial(\rho w)}{\partial x}+v\frac{\partial(\rho w)}{\partial y}+w\frac{\partial(\rho w)}{\partial z}\right)=-\frac{\partial p}{\partial x}+\left[\frac{\partial}{\partial x}\left(\mu\frac{\partial w}{\partial x}\right)+\frac{\partial}{\partial y}\left(\mu\frac{\partial w}{\partial y}\right)+\frac{\partial}{\partial z}\left(\mu\frac{\partial w}{\partial z}\right)\right], \tag{4}$$

energy equation:

$$\left(u\frac{\partial(\rho CpT)}{\partial x}+v\frac{\partial(\rho CpT)}{\partial y}+w\frac{\partial(\rho CpT)}{\partial z}\right)=\left[\frac{\partial}{\partial x}\left(k\frac{\partial T}{\partial x}\right)+\frac{\partial}{\partial y}\left(k\frac{\partial T}{\partial y}\right)+\frac{\partial}{\partial z}\left(k\frac{\partial T}{\partial z}\right)\right]. \tag{5}$$

The Y momentum Eq. (2) contains the buoyancy effects and according to the Boussinesq approximation the density variation due to the buoyancy effect is related to the volumetric thermal expansion coefficient (β) of the fluid.

At the channel entrance the flow was treated as a three-dimensional fully developed flow [12] with uniform temperature. No-slip condition was applied at the channel walls, including the step. The bottom wall of the channel ($0\leqslant x\leqslant L$; $0\leqslant z\leqslant W$) was subjected to a constant temperature (T_w) and the rest of the walls were treated as adiabatic.

In this work the step was considered to be conducting with a thermal conductivity k_s. The conjugate problem of conduction convection at the solid–fluid interface of the step was solved by a pseudo-solid-specific heat method as suggested by Xi and Han [13].

The physical properties of air in the numerical procedure were treated as constants and evaluated at the inlet temperature $T_0=293$ K, as $\rho=1.205$ kg/m^3, $\mu=1.81\times10^{-5}$ kg/m s, $C_p=1005$ J/kg K, $k_f=0.0259$ W/m K, and $\beta=0.003\,41$ K^{-1}. The thermal conductivity of the back step was set equal to $k_s=386$ W/m K.

The flow rate in the duct entrance was fixed such that the Reynolds number (Re) would have a constant value of 200 for all the numerical simulations. The Reynolds number was computed based on the inlet bulk velocity U_o and the channel height. The effects of the buoyancy forces on the velocity field and the temperature distribution was studied by varying the Richardson number from Ri=0 to 3 and then selecting the appropriate value for the bottom wall temperature (T_w).

A finite volume technique was implemented for discretizing the momentum and energy equations inside the computational domain. The SIMPLE algorithm was used to link the pressure and velocity fields. Solution to the one-dimensional convection-diffusion equation at the control volume interfaces was represented by the power law [14]. Velocity nodes were located at staggered locations in each coordinate direction while pressure and temperature nodes as well as other scalar properties were placed at the main grid nodes. At the channel exit the natural boundary conditions

$$\left(\frac{\partial()}{\partial x}=0\right)$$

were imposed for all the variables [14]. In addition, the overall mass flow in and out of the domain were computed and its ratio was used to correct the outlet plane velocity at the channel exit as proposed by Versteeg and Malalasekera [15].

A combination of line-by-line solver and Thomas algorithm was implemented for each plane in x, y, and z coordinate directions for the computation of the velocity components, pressure, and temperature inside the computational domain. To ensure convergence when solving the mixed convective flow over a three dimensional horizontal backward facing step a severe underrelaxation for the velocity components ($\alpha_u=\alpha_v=\alpha_w=0.4$), pressure ($\alpha_p=0.4$) and temperature ($\alpha_T=0.4$) was imposed. Convergence was declared when residuals for the velocity components (R_u,R_v,R_w) and for the pressure (R_p) were less than 1×10^{-8} and 1×10^{-10}, respectively. For the temperature field the convergence criterion required that the maximum relative change in temperature between successive iterations is less than 1×10^{-6}. The definitions for the residuals adopted for the velocity components, pressure, and temperature are presented in Eqs. (6), (7), and (8), respectively, [16]:

$$R_\phi=\frac{\sum_{\text{nodes}}|a_p\phi_p|-\left[\sum|a_{nb}\phi_{nb}|-A(p_\phi-p_{\phi+1})-b\right]_{\text{nodes}}}{\sum_{\text{nodes}}|a_p\phi_p|}\leqslant\varepsilon_\phi, \tag{6}$$

$$R_p=\sum_{\text{nodes}}|\rho A[(u_w-u_e)+(v_s-v_n)+(w_b-w_t)]|\leqslant\varepsilon_p, \tag{7}$$

$$R_T=\left(\left|\frac{T^{n+1}_{k,j,i}-T^{n}_{k,j,i}}{T^{n+1}_{k,j,i}}\right|\right)\leqslant\varepsilon_T. \tag{8}$$

In the Eq. (6) ϕ represents the u, v, and w velocity components and a coefficients are defined in context of the finite volume discretization technique [14].

A nonuniform grid was considered for solving the problem. In this sense, at the channel walls and at the edge of the step the grid was composed by small-size control volumes (fine grid) and the control volume size increased far away from the solid walls. The grid size was deployed by means of a geometrical expansion factor, such that each control volume is a certain percentage larger than its predecessor.

The grid independence study was conducted by using several grid densities for the most severe parametric values (Ri=3 and Re=200) considered in this study. The average Nusselt number

Table 1 Grid independence study

Grid Size (x-y-z):(100-40-40) Expansion factor (x-y):(1.025-1.35)				
Expansion factor for Z	Nusselt average at exit	% diff	u-max at the exit	% diff
Uniform grid	4.7743		0.1248	
1.04	4.5016	6.05	0.1326	5.91
1.08	4.1798	7.69	0.1324	0.11
1.10	4.0263	3.81	0.1326	0.08
1.12	3.8812	3.73	0.1326	0.0
1.14	3.7462	3.60	0.1324	0.15
1.16	3.6223	3.42	0.1323	0.07
1.18	3.5098	3.20	0.1322	0.07
1.20	3.4085	2.97	0.1322	0.0

distribution (Nu) and the maximum velocity (u_{max}) at the channel exit were monitored to declare grid independence.

A grid size of $100\times40\times40$ was chosen as the base case. By keeping the number of grid points constant several runs were made by varying the expansion factor in the z direction. The variation of the expansion factor did not increase the number of nodes but affected their allocation in the computational domain. In this sense, as the expansion factor increases a fine grid distribution is realized in the vicinity of the solid walls, so velocity, pressure, and temperature gradients in these specific zones could be resolved with greater accuracy.

Once the appropriate value for the expansion factor was obtained such that the monitored parameters have small deviations, the next step was to add grid points in each direction. However, further addition of grid points to the grid in the x, y, and z directions resulted in less than 1% change in the averaged Nusselt number and maximum u velocity at the channel exit. Accordingly, a nonuniform grid of $100\times40\times40$ and expansion factors $e_x=1.025$, $e_y=1.35$, and $e_z=1.20$ was chosen to make parametric runs. The result of this grid independence study is summarized in Table 1.

Lack of previous experimental or numerical data in the literature for the problem in question precludes the direct numerical validation of the numerical code developed for solving the mixed convective flow over a three dimensional horizontal backward facing step. Hence, two closely related problems to the mixed convective flow over a three dimensional backward facing step were considered to validate the numerical code developed for this research. For each verification test the hydrodynamic and thermal flow features were compared with the previously published works in the literature.

Test Case #1. The first test case was that for simulating pure forced convective flow over a three-dimensional backward facing step subjected to constant heat flux heating along the bottom wall [6]. The numerical predictions of reattachment lengths and Nusselt number distributions using the developed code was compared with the experimental data for Re=343 and numerical predictions for Re=400 presented by Nie and Armaly [6]. The comparisons are shown in Figs. 2 and 3.

Due to the symmetry for pure forced convection the literature presents values for half of the channel in the spanwise direction. However, this assumption was not considered in this research and computations were made by considering the entire spanwise width of the channel. In order to be consistent with the format in the referenced cited, the results are presented for only half of the channel width in Figs. 2 and 3.

The numerical predictions using the code developed for this research very closely agrees with both the experimental and numerical results in the published literature shown in Figs. 2 and 3.

Test Case # 2. The second test case was that for simulating mixed convective flow in straight horizontal channel with no

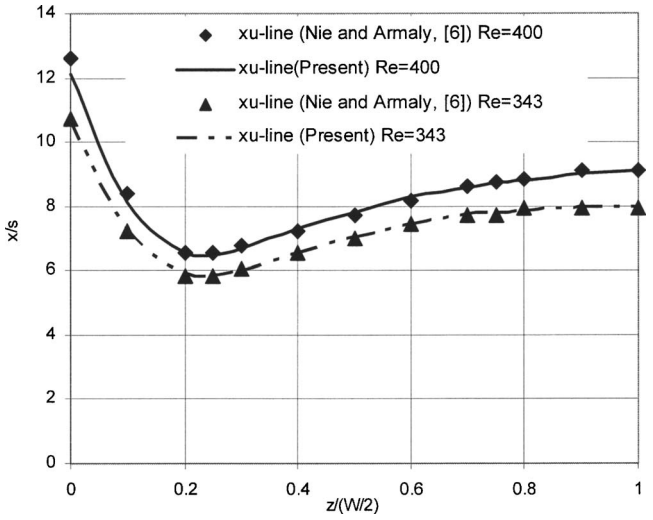

Fig. 2 x_u line for the stepped wall ($z/W=0$ wall and $z/W=1$ central plane)

blockage heated from below by subjecting the wall to a constant temperature [17]. The width to height channel's ratio was equal to 2. The numerical predictions using the code developed for this research closely agreed with the numerical predictions in the literature as shown in Fig. 4.

Results and Discussion

According to earlier studies [1,3–7], it is known that the flow over the backward facing step channel is extremely sensitive to the abrupt geometrical changes at the step. Downstream of the step and just behind the primary recirculation zone, the velocity profile is reattached and redeveloped approaching that of a fully developed flow as fluid flows towards the channel exit. However, the behavior described earlier for a pure force convective flow is completely distorted in presence of buoyancy forces. The last scenario considered is a mixed convective problem and is the central theme for this work.

The mixed convective flow is a process in which both the forced and the buoyancy effects are of significant importance in the convective process and primarily occurs in laminar and tran-

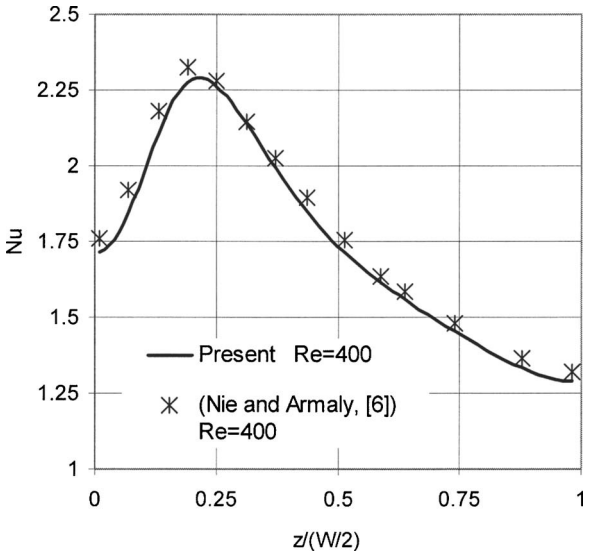

Fig. 3 Local Nusselt number distribution for the stepped wall at $x/s=6.6$ ($z/W=0$ wall and $z/W=1$ central plane)

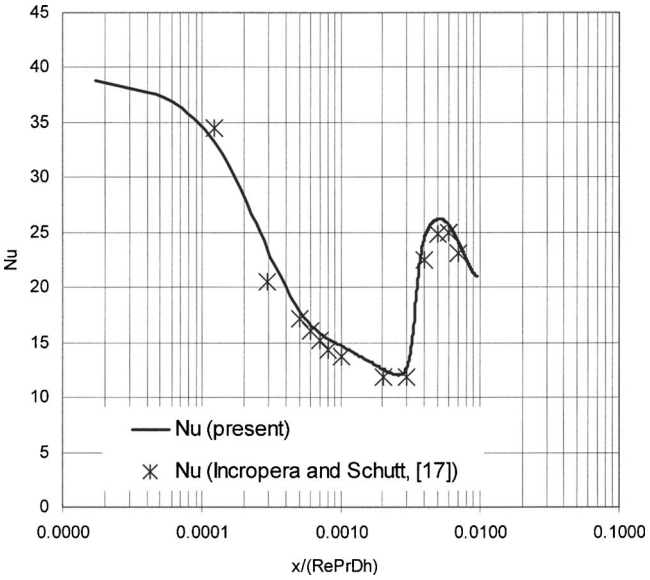

Fig. 4 Average Nusselt number for a mixed convective flow through a straight rectangular channel $Gr=1.55\times10^6$, Re=500 and Pr=6.5

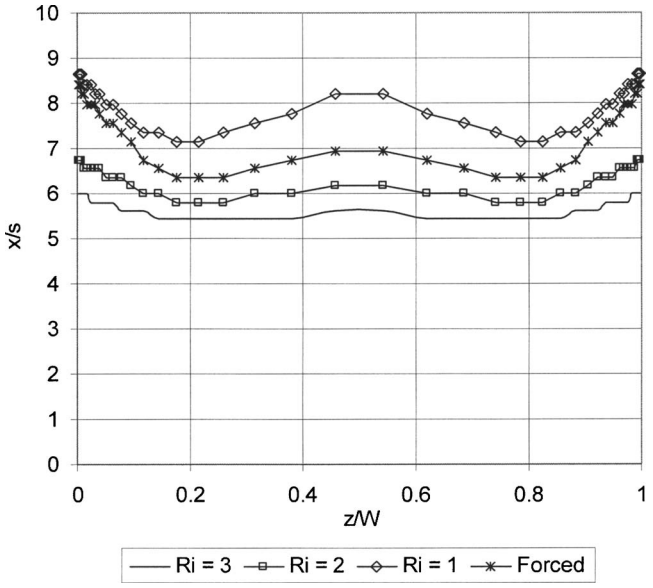

Fig. 5 x_u-line distribution for mixed convection over a 3D backward facing step

sitional flow regimes. Therefore, for all numerical simulations considered in this study the Reynolds number (Re) was fixed to be Re=200.

The variation in buoyancy forces was accomplished by altering the imposed temperature along the bottom wall which in turn alters the Richardson number (Ri). Mixed convective effects on the flow were studied by simulating flows for three different Richardson numbers (Ri=1, 2, and 3). When Ri=1 the forced and free convective forces are comparable and, as Ri increases the free convective effects become dominant over forced convective effects in the flow. The extreme case in this study is for Ri=3, where the free convective effects strongly prevail over the forced convective effects.

The mixed convective effects were studied by monitoring the so-called x_u line, the average Nusselt number, and some velocity profiles at specific planes by comparing with the results for mixed convective flow and those for pure forced convective flow.

In a two-dimensional problem flow over a backward facing step, the point where the shear stress is equal to zero is used to locate the reattachment length and to allocate the primary recirculation zone downstream of the step. However, for a three-dimensional flow the same definition represent a point in a horizontal plane and cannot be used to demarcate the recirculation zone. The common assumption for delimiting the recirculation zone in a three-dimensional case is the distribution in the spanwise direction of points along the axial direction where the streamwise component of the shear stress at the wall is equal to zero. Therefore, the limiting primary recirculation zone is bounded by a line in the spanwise direction named the x_u line.

Figure 5 shows the x_u line for different mixed convective and pure forced convective flows. The x_u lines present a symmetric behavior with respect to the middle plane in the spanwise direction. A minimum value is located approximately at $z/W=0.2$ and $z/W=0.8$. This effect is associated with the influence of the viscous effects and the no slip condition imposed at the lateral walls. The larger reattachment point is along the lateral walls.

For Ri=1 a very similar behavior as the pure forced convective flow is found. However, the location of x_u line for mixed convective flow Ri=1 is pushed further downstream. The mixed convection in ducts presents two different structures or convective rolls, and depending on the effects of the mixed convection the rolls can be transverse or longitudinal in nature [18]. The onset of transverse rolls occurs at low Grashof numbers (Gr). Therefore for Ri=1, the presence of longitudinal rolls is the reason why the x_u line is displaced downstream of the channel inlet ($x/s=0$).

On the other hand, for Ri=2 and 3 the location of x_u line is upstream of the x_u-line location for Ri=0. It is evident from the Fig. 5, that when Ri increases the recirculation zone is shortened due to the presence of strong buoyancy forces and higher v velocity components in the vicinity of the heated wall.

The average along the span-wise direction of the streamwise shear stress component at the channel's bottom wall is presented in Fig. 6. The negative values in Fig. 6 are associated with the primary recirculation zone and the point where τ_{wx} changes to a positive value could be interpreted as "*the averaged reattachment point*." This point is shifted upstream if Ri is large (Ri=3) and the

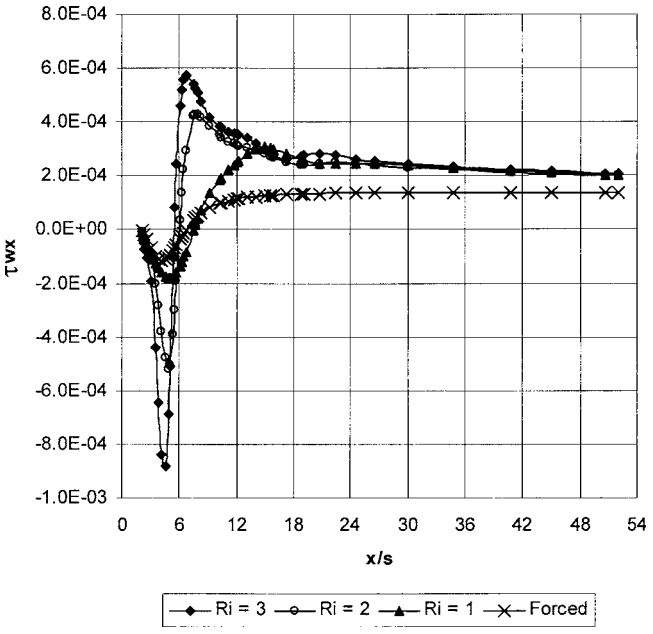

Fig. 6 Spanwise average of the streamwise shear stress component along the bottom wall

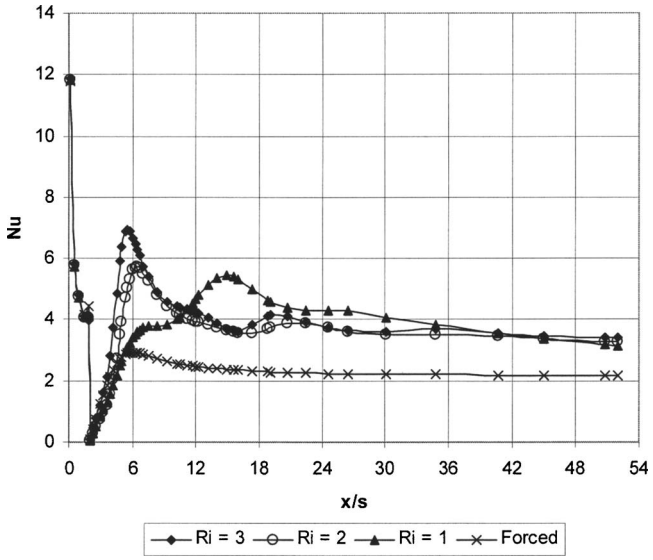

Fig. 7 Spanwise averaged Nusselt number distribution for the mixed convective flow over a 3D backward facing step

farthest point downstream happens to be for Ri=1 as a consequence of the earlier discussion following Fig. 5.

The spanwise averaged Nusselt number distribution for the mixed convective flow in a channel with a backward step is presented in Fig. 7. The averaged Nusselt number distribution at the entrance of the backward facing step channel has a high value and then monotonically decreases. At the edge of the step a dramatic change in the averaged Nusselt number distribution was found due to the flow separation and the abrupt change in the channel geometry. Figure 7 shows a similar tendency for the averaged Nusselt number distributions for the three mixed convective cases in consideration and the higher values are associated to higher Ri numbers.

For Ri=1, the location of the maximum Nusselt number is found further downstream of the step (step ends at $x/s=2$) while for Ri=3 and 2 the location of the maximum was found in the proximity of the step. Hence, the location of the maximum spanwise averaged Nusselt number shifts upstream with increase in Ri. After reaching a maximum value the Nusselt number decreases toward its fully developed value at the channel exit. It is also observed in this figure that after reaching the minimum value just behind the step, the Nusselt number distribution sharply increases to reach its maximum value inside the primary recirculation zone for Ri=3 and Ri=2. For Ri=1 the change from the minimum value of Nusselt number to the maximum is not as sharp as for Ri=3 and 2 due to presence of longitudinal rolls as described earlier (Fig. 5).

According to Fig. 7 the spanwise averaged Nusselt number distribution for pure forced convective flow has a similar behavior as for the mixed convective flow, but the spanwise values for the averaged Nusselt number distribution are considerably smaller for the pure forced convection than those for the mixed convection case. The minimum value in the spanwise averaged Nusselt number distribution for forced convection happens just behind the step

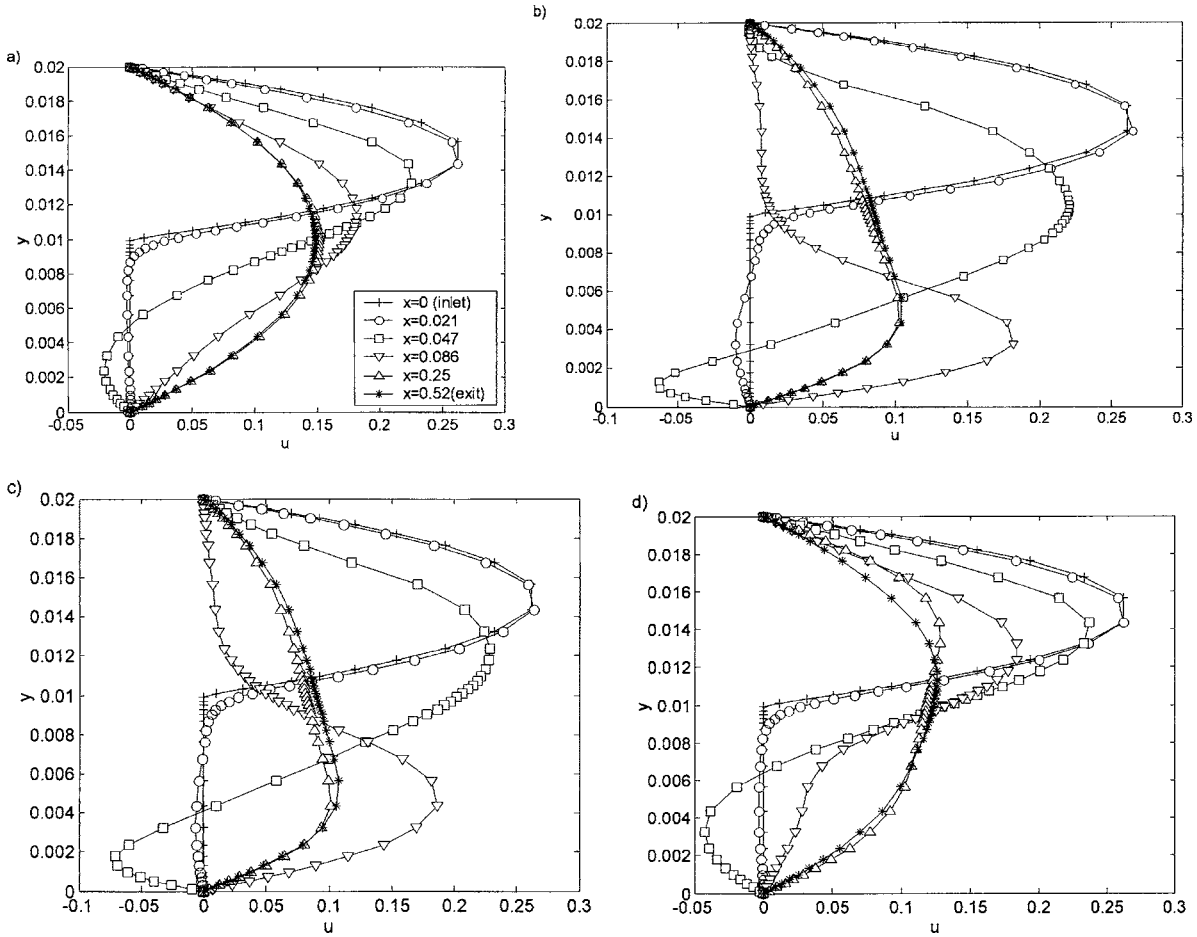

Fig. 8 *u*- velocity profiles at plane *z*=0.02 at different *x* positions (a) forced convection (b) Ri=3, (c) Ri=2, (d) Ri =1

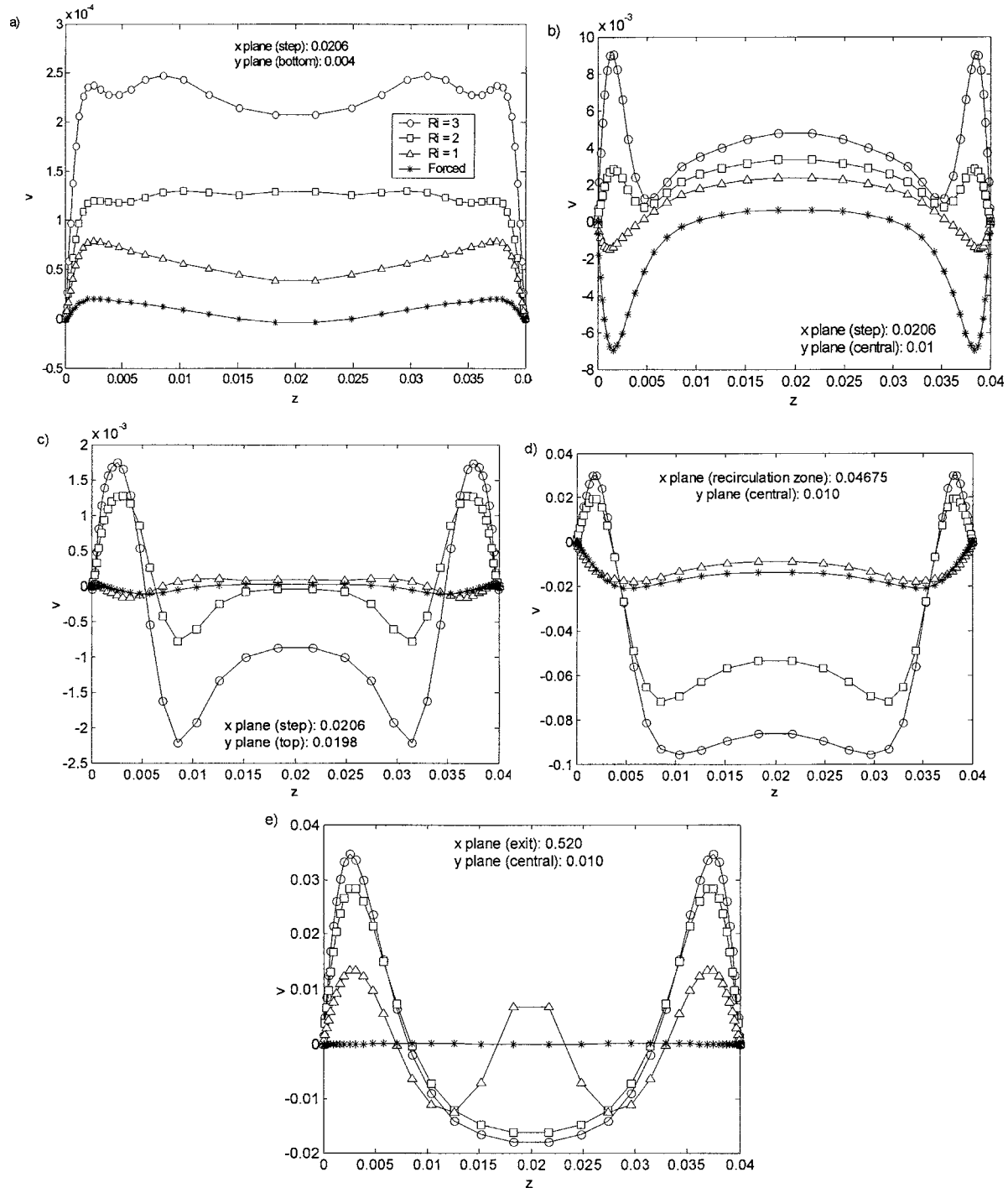

Fig. 9 *v* velocity at different *x* and *y* planes

and its maximum is reached inside the primary recirculation zone, and decreases monotonically towards its fully developed value at the channel exit.

Velocity distributions for each of the velocity components are presented in Figs. 8–10 in order to study the influence of the buoyancy forces on the flow field. Figure 8 shows the u velocity component for the central plane in the spanwise direction ($z/W=0.5$) at different x planes for pure forced convective flow and mixed convective flow. As previously mentioned, at the inlet ($x=0$) the flow is considered as hydrodynamically fully developed for all cases considered in this study.

In the vicinity of the step at $x=0.02$, the u velocity component has a slight deviation from the hydrodynamically fully developed flow values and the velocities at this point are slightly less than that for $x=0$ in region above the step. Also, u values were negative near the bottom of the channel and this effect is most pronounced for the case of Ri=3.

At a constant value of $x=0.047$ the recirculation of the flow becomes evident along the bottom of the channel. Also, the negative value of u next to the bottom wall of the channel increases with increase in Ri. On the other hand the maximum value of the u component in the positive direction occurs for the pure forced convective flow. As Ri increases, the vertical size of the recirculation zone is reduced. This effect is related to the buoyancy forces in the flow.

Figure 8(b) reveals the presence of a small recirculation zone

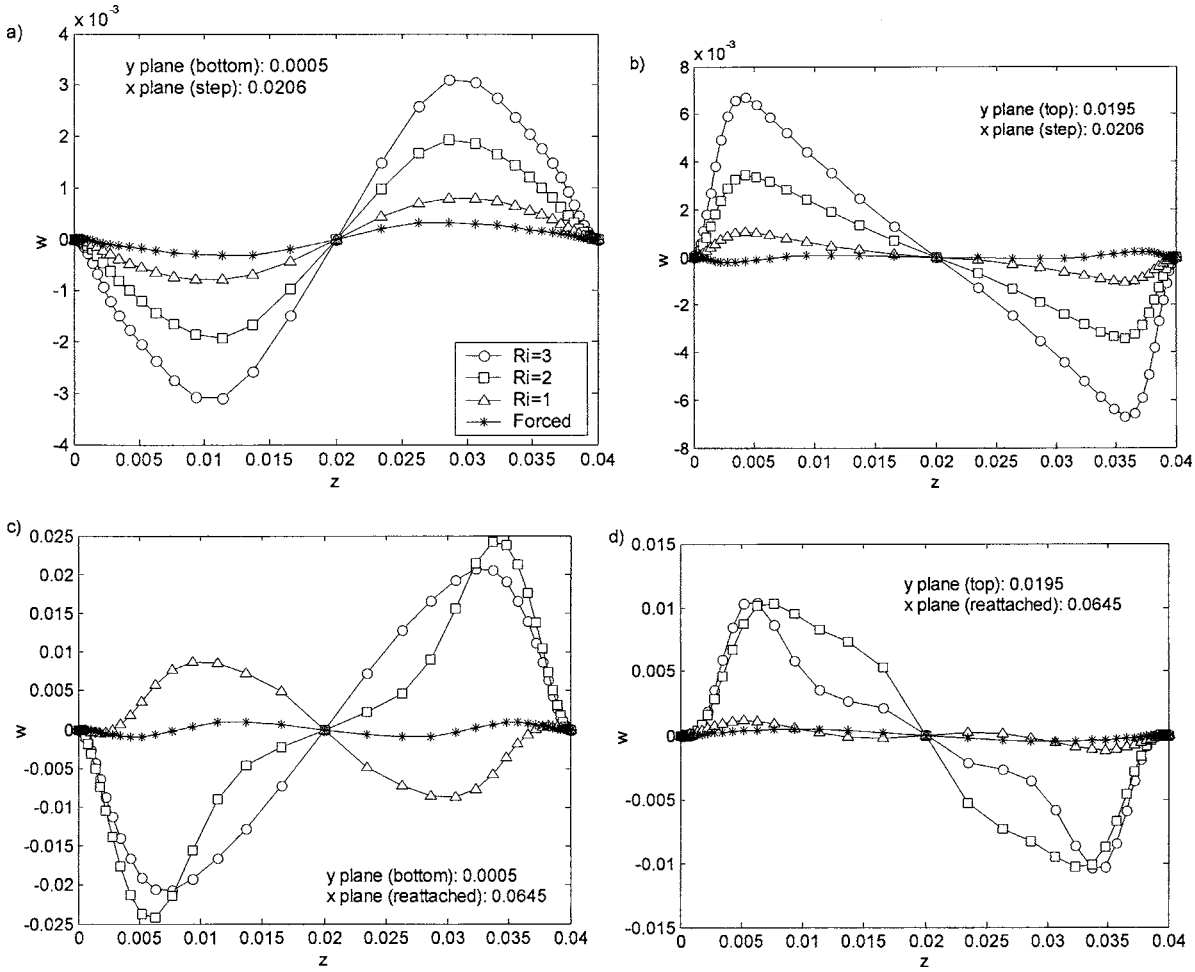

Fig. 10 ***w*** **velocity component at different** ***x*** **and** ***y*** **planes**

attached to the roof of the channel at $x=0.047$ and the effect extends up to $x=0.086$. This effect was found only for the Ri=3 and is due to the strength of the mixed convective flow in this case.

The u velocity profile at $x=0.25$ (half of the channel in the streamwise direction) reveals that for pure forced convective flow the u velocity component begins to show a fully developed behavior. For Ri=1 the u-velocity components tends to approach fully developed velocity profile. For Ri=3 and Ri=2 the velocity profile behavior is very different to be a fully developed flow. The maximum in the velocity profile is shifted towards the bottom of the channel. This behavior will be explained below.

It is evident from Fig. 8 that the length of the channel is long enough to accommodate fully developed flow for pure forced convection (Ri=0). None of the mixed convective flow cases considered in this study was able to reach the hydrodynamically fully developed conditions at the channel exit. The case of Ri=1 was the one of the mixed convective cases that appeared to be approaching fully developed flow conditions at the channel exit. The u-velocity components at the channel exit for mixed convective cases were found to be nonsymmetric with respect to the y axis. Even though the fully developed conditions were not achieved, it becomes clear that at the channel exit the u-velocity component does not present any negative values. Hence, at the channel exit a possible inflow condition is discarded and then the outflow boundary conditions imposed to the numerical code does not have a negative impact on the numerical predictions.

Figure 9 presents the v-velocity distribution. In these figures, the plane $y=0.01$ is the central plane while $y=0.004$ is a plane near to the bottom wall and $y=0.0198$ is a plane near to the top wall.

The magnitude of the velocity v component is extremely small near the top and bottom walls. It should be noted that higher values for the v component are for Ri=3 where the buoyancy effects dominate.

Figure 9(a) shows that for Ri=3 the v-velocity component values are three times larger than the values for pure forced convective flow. This effect is associated with the strength of the mixed convective flow as it was mentioned before; the effect of mixed convection is to reduce the size of the recirculation zone in both streamwise and vertical directions.

Figure 9(b) shows that at the edge of the back step, the line for pure forced convection does not have positive values for the v-velocity component, but the lines for Ri=3 and Ri=2 have the opposite behavior. In others words, at the edge of the step for pure forced convection the flow is descending while for mixed convection the flow is ascending due to the buoyancy forces. Figure 9(c) shows that at the top of the channel the v velocity has negative values along the spanwise direction and except a small region near the side walls where the values are positive.

Figure 9(d) shows the v velocity at x constant plane inside the primary recirculation zone and at the central constant y plane in the vertical direction. For Ri=3 and 2 the earlier mentioned effect of ascending flow near the side walls is observed. However, at the channel central region in the z-direction the v-velocity distribution shows high negative values and the flow is directed towards the

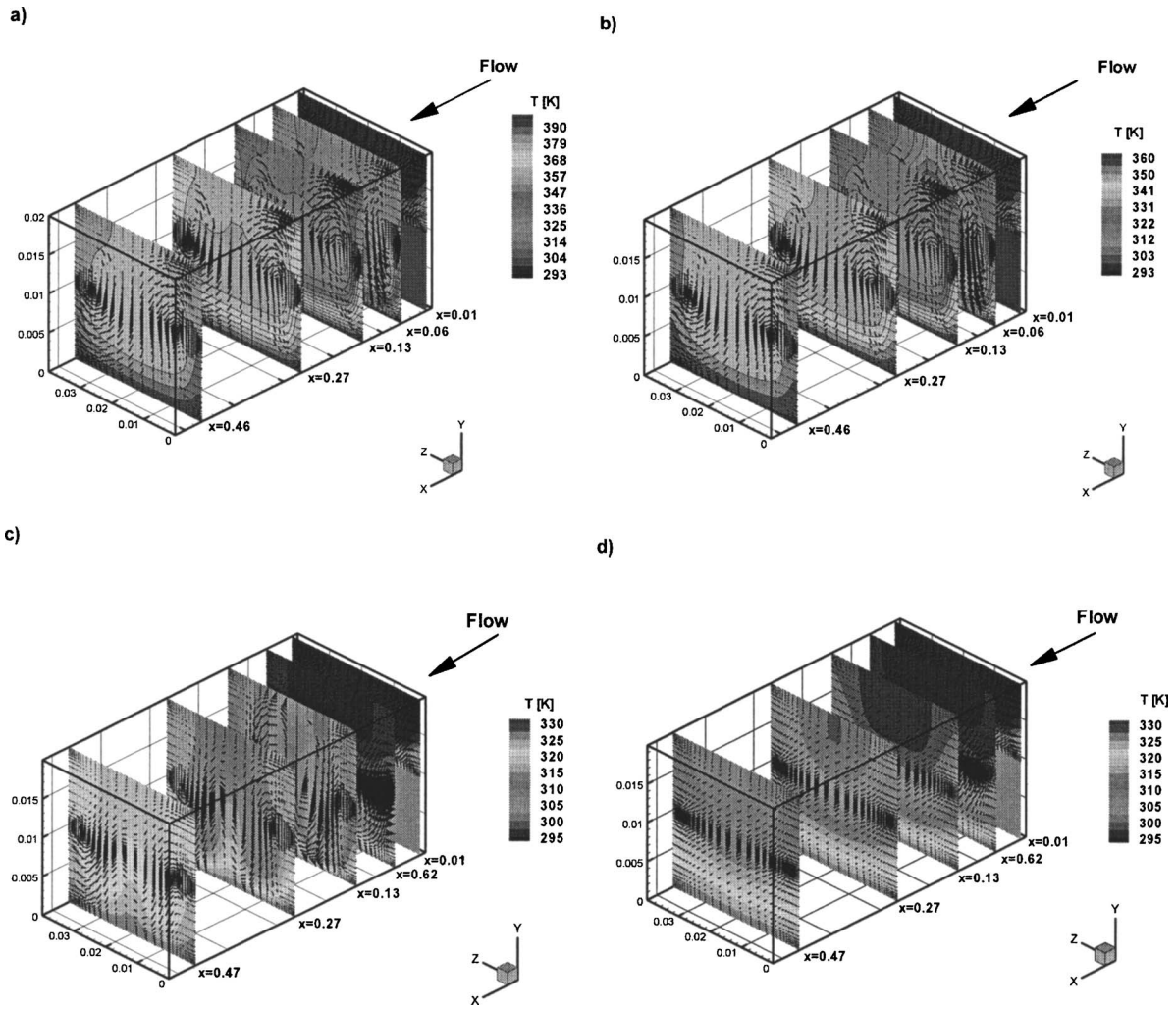

Fig. 11 Temperature contours and velocity vectors at constant *x* planes (a) Ri=3, (b) Ri=2, (c) Ri=1, (d) forced convection

bottom wall. This is the reason why the recirculation zone is not only reduced in the streamwise direction but also in the transverse direction (y direction).

Figure 9(e) confirms that at the channel exit the flow is fully developed for pure forced convective flow ($v=0$) and that for mixed convective flow, the v component of the velocity has considerable nonzero values. This figure also shows that for strong mixed convective flow (Ri=3 and Ri=2) positive values for the v-velocity component are present near the side walls and negative values are present in the middle of the channel. This is the reason why the maximum of u-velocity component in the central plane is shifted towards the bottom wall as seen in Figs. 8(b) and 8(c).

Figure 10 presents the spanwise velocity w distribution at different x and y planes. It is evident in Fig. 10 that for pure forced convective flow the change in the w-velocity component is minimal and also that the variation in w component in the spanwise direction is greater near the walls than in the middle of the channel. This behavior is associated with the formation of convective rolls in the flow. Even though the variation in the w-velocity component is minimal, this component cannot be neglected in the numerical discretization in order to save computational effort.

As expected, the higher values for the w-component velocities are associated with larger Ri values. In the vicinity of the back step [Figs. 10(a) and 10(b)] the w component of the velocity has extremely small values. Higher values for the w-velocity component occurs downstream of the backstep [Figs. 10(c) and 10(d)].

Analyzing Fig. 10 and considering the coordinate system proposed in Fig. 1 it is evident that near the top of the channel the w-velocity component acts towards the central plane in the spanwise direction ($z=0.02$), while near the bottom wall the flow is directed towards the side walls.

Figure 11 presents the temperature contours and the velocity vectors at different streamwise positions for the convective flows considered in this study.

A pair of longitudinal convective rolls is perfectly defined for Ri=3 and Ri=2 in Figs. 11(a) and 11(b). It is evident that the flow is ascending along the side walls and is moving towards the bottom wall near the middle plane in the spanwise direction ($z=0.02$). That is the reason why in Figs. 8(b) and 8(c) the maximum for the u velocity at the channel exit is shifted towards the bottom wall. For Ri=1 the longitudinal vortex are not completely defined even though the velocity structures tends to align with longitudinal vortices. For the pure forced convective case in Fig. 11(d) the flow structures do not show formation of the convective rolls, but they are more like a fully developed flow.

The temperature contours show the presence of high temperatures along the channel roof. According to the linear relationship between density and temperature this is an expected behavior. Flow with lower density and high temperature must be along the top wall of the channel. For the pure forced convective case the temperature contours reveals that the region of higher temperature are near to the heating zone.

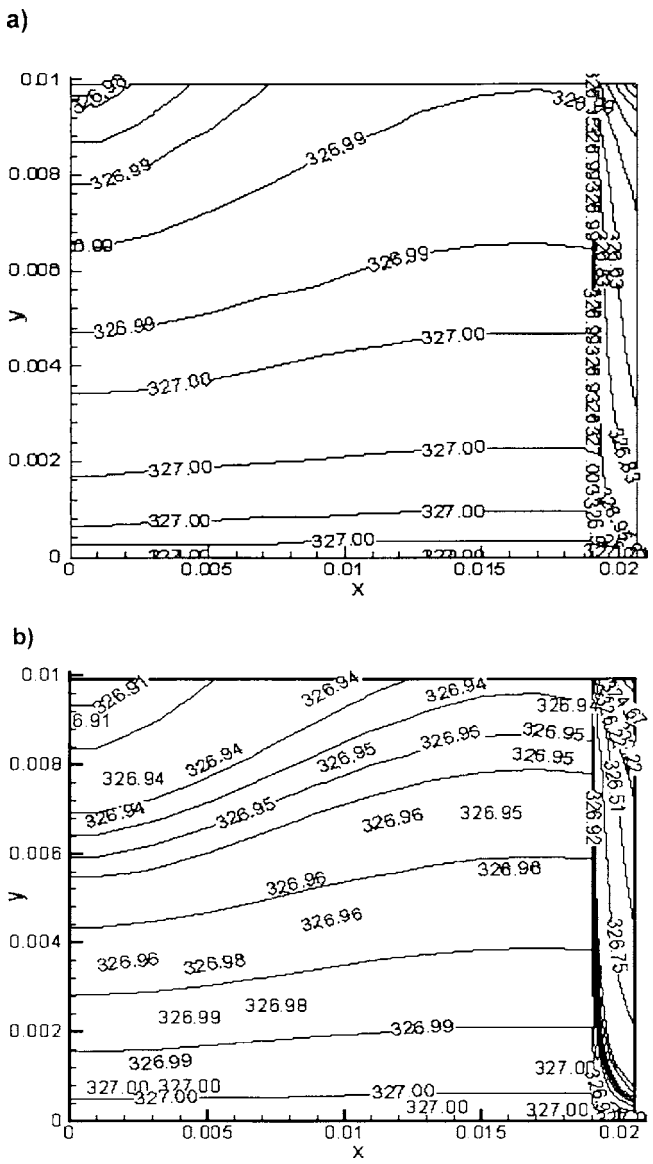

Fig. 12 Temperature distribution inside the back-step for the central plane $z=0.02$ (a) $k_s=386$ (copper) (b) $k_s=64$ (carbon steel AISI 1010)

The influence of the conducting block on the mixed convective flow was studied for two different block's thermal conductivity. Figure 12(*a*) shows the temperature distribution inside the block along the central plane in the spanwise direction for $k_s=386$ W/m K (copper). Similarly Fig. 12(*b*) for $k_s=64$ W/m K (carbon steel AISI 1010).

The thermal conductivity in the block does not impact the temperature distribution for mixed convective flow and the only effect is on the temperature distribution inside the back step. Even though the temperature gradients inside the block can be neglected it was found that a higher temperature gradient is found for the lower thermal conductivity ($k_s=64$ W/m K). It is important to mention here that the geometrical dimensions for the back step in the streamwise direction (x direction) is two times the step height while the total length of the channel is 52 times the step height.

Conclusions

The mixed convective flow over a three dimensional horizontal backward facing step heated from below was numerically simulated using a finite volume technique. The bottom wall of the channel was subjected to constant temperature. Numerical simulations were conducted for four different buoyancy parameters ($\mathrm{Ri}=\mathrm{Gr}/\mathrm{Re}^2$) ranging from pure forced convective flow to mixed convective flow (Ri=0,1, 2, and 3).

The numerical results show that the velocity field and temperature distribution features for the mixed convective flow are significantly different from that for pure forced convective flow, even for small Ri. Hence, the effects of buoyancy forces should be considered in simulation of mixed convective flows.

The effect of increase in Richardson number (Ri) on the mixed convective flow not only decreased the size of the primary recirculation zone in both streamwise and transverse directions, but also moved the location of maximum in the averaged Nusselt number distribution and maximum in the averaged streamwise shear stress distribution further upstream.

At the channel exit the fully developed conditions are not achieved for mixed convective flows. It should be noted that for pure forced convective flow (Ri=0) the flow does achieve fully developed flow condition at the channel exit.

Acknowledgment

Support for this work by ANUIES/IPN Mexico is greatly appreciated.

Nomenclature

a = discretization coefficients
A = area
AR = aspect ratio, AR=W/s
b = linearization for the source term
C_p = specific heat
e = expansion factor
ER = expansion ratio, $ER=2H/(2H\text{-}s)$
g = acceleration due to gravity
Gr = Grashof number, $\mathrm{Gr}=g\beta\Delta Ts^3/\nu^2$
H = channel height at the inlet
k = thermal conductivity
L = total length of the channel, $L=52$ s
l = total length of the step, $l=2$ s
n = iteration number
Nu = average Nusselt number, $\mathrm{Nu}=(d\overline{T}/dy)|_{y=0}2H/(T_{\mathrm{wall}}-T_b)$
p = pressure
Pr = Prandtl number
R = residuals
Re = Reynolds number $\rho U_0 2H/\mu$
Ri = Richardson number; $g\beta\Delta Ts^3/\nu^2\mathrm{Re}^2$
s = step height
R = residuals
T = temperature
U_o = bulk velocity at the inlet
u = velocity component in x direction
v = velocity component in y direction
w = velocity component in z direction
W = channel width
$2H$ = channel height
$x_{\text{u-line}}$ = $x_{u\text{-line}}=[(du/dy)_{z=\text{const}}]|_{y=0}$
x, y, z = Coordinate directions

Subscripts

b = bulk, back
e = east
f = fluid
max = maximum
n = north
nb = neighborhood points
s = solid, south

t = top
0 = inlet
w = wall, west

Greek letters

α = underrelaxation factor
β = coefficient of thermal expansion
ε = convergence stop criteria
μ = dynamic viscosity
τ_{wx} = average streamwise shear stress
$\tau_{wx} = \mu(d\overline{u}/dy)_{y=o}$
υ = kinematic viscosity
ρ = density
ϕ = general variable (velocity and pressure)

References

[1] Iwai, H., Nakabe, K., Suzuki, K., and Matsubara, K., 2000, "Flow and heat transfer characteristics of backward-facing step laminar flow in a rectangular duct," Int. J. Heat Mass Transfer, **43**, pp. 457–471.
[2] Iwai, H., Nakabe, K., Suzuki, K., and Matsubara, K., 2000, "The effects of duct inclination angle on laminar mixed convective flows over a backward-facing step," Int. J. Heat Mass Transfer, **43**, pp. 473–485.
[3] Nie, J. H., and Armaly, B. F., 2002, "Three-Dimensional Convective Flow Adjacent to Backward-Facing Step Effects of Step Height," Int. J. Heat Mass Transfer, **45**, pp. 2431–2438.
[4] Blackwell, B. F., and Pepper, D. W., 1992, Benchmark problems for heat transfer codes, ASME-HTD-222, ASME, NY.
[5] Armaly, B. F., Li, A., and Nie, J. H., 2003, "Measurements in three-dimensional laminar separated flow," Int. J. Heat Mass Transfer, **46**, pp. 3573–3582.
[6] Nie, J. H., and Armaly, B. F., 2003, "Reattachment of three-dimensional flow adjacent to backward-facing step," ASME J. Heat Transfer, **125**, pp. 422–428.
[7] Carrington, D. B., and Pepper, D. W., 2002, "Convective heat transfer downstream of a 3D backward-facing step," Numer. Heat Transfer, Part A, **41**, pp. 555–578.
[8] Nie, J. H., and Armaly, B. F., 2002, "Buoyancy effects on three-dimensional convective flow adjacent to backward-facing step," J. Thermophys. Heat Transfer, **17**, pp. 122–126.
[9] Li, A., and Armaly, B. F., 2000, "Mixed convection adjacent to a 3D backward facing step," HTD-Proc. ASME Heat Transfer Division, **2**, pp. 51–58.
[10] White, F. M., 1991, *Viscous Fluid Flow*, 2nd ed., McGraw-Hill, New York
[11] Kakac, S., and Yener, Y., 1995, *Convective Heat Transfer*, 2nd ed., CRC Press, Boca Raton, FL.
[12] Shah, R. K., and London, A. L., 1978, *Laminar Flow Forced Convection in Ducts*, Academic Press, New York, USA
[13] Xi, C., and Han, P., 2000, "A Note on the Solution of Conjugate Heat Transfer Problems Using SIMPLE-like algorithms," Int. J. Heat Fluid Flow, **21**, pp 463–467.
[14] Patankar, S. V., 1980, *Numerical Heat Transfer and Fluid Flow*, Taylor and Francis, USA.
[15] Versteeg, H. K., and Malalasekera, W., 1995, *An Introduction to Computational Fluid Dynamics. The Finite Volume Technique*, Prentice-Hall, Malaysia.
[16] Guo, Z., and Anand, N. K., 1997, "Three-Dimensional Heat Transfer in a Channel with Baffle in the Entrance Region," Numer. Heat Transfer, Part A, **31**, pp. 21–35.
[17] Incropera, F. P., and Schutt, J. A., 1985, "Numerical Simulation of Laminar Mixed Convection in the Entrance region of Horizontal Rectangular Ducts," Numer. Heat Transfer, **8**, pp. 707–729.
[18] Luijkx, J. M., Platten, J. K., and Legros, J. C. L., 1981, "On the existence of thermoconvective rolls, transverse to a superimposed mean Poiseuille flow," Int. J. Heat Mass Transfer, **24**, pp. 1287–1291.

A New Numerical Procedure for Coupling Radiation in Participating Media With Other Modes of Heat Transfer

Sandip Mazumder
Professor
Mem. ASME
Department of Mechanical Engineering,
The Ohio State University,
Columbus, OH 43202
e-mail: mazumder.2@osu.edu

Traditionally, radiation in participating media is coupled to other modes of heat transfer using an iterative procedure in which the overall energy equation (EE) and the radiative transfer equation (RTE) are solved sequentially and repeatedly until both equations converge. Although this explicit coupling approach is convenient from the point of view of computer code development, it is not necessarily the best approach for stability and convergence. A new numerical procedure is presented in which the EE and RTE are implicitly coupled and solved simultaneously, rather than as segregated equations. Depending on the average optical thickness of the medium, it is found that the coupled solution approach results in convergence that is between 2–100 times faster than the segregated solution approach. Several examples in one- and two-dimensional media, both gray and nongray, are presented to corroborate this claim.
[DOI: 10.1115/1.1929780]

Keywords: Thermal Radiation, Participating, Implicit Method, Numerical, Convergence Acceleration, Coupled Solution

1 Introduction

Radiation is the dominant mode of heat transfer in applications involving high temperature. In many such applications, the medium is radiatively participating either because of the presence of significant quantities of absorbing-emitting molecular gases, or due to the presence of particulates, such as soot. The radiation energy within a participating medium is tracked using the radiative transfer equation (RTE). In addition, energy conservation (first law of thermodynamics) has to be satisfied, when considering heat transfer by other modes, resulting in the overall energy equation (EE).

In a participating medium, the EE and RTE are coupled. The divergence of the radiative flux appears as a sink term in the EE [1], while the temperature at any point, which is obtained by solving the EE, influences local emission and radiative properties, thereby affecting the solution of the RTE. Traditionally, the two equations are solved sequentially within a larger global iteration loop (Fig. 1). First, the temperature distribution is guessed and the RTE is solved. The divergence of the radiative heat flux, which is calculated from the solution of the RTE, is then substituted into the EE, which is next solved to obtain a new temperature distribution. The procedure is repeated until both equations converge simultaneously. Despite the existence of a large volume of literature dating back to the early 1960s that discusses treatment of radiation in combined mode heat transfer problems (Chap. 21 of Ref. [1] and the references cited therein), it was impossible to identify a single paper that treats radiation using a numerical procedure that is different from the procedure outlined above.

In realization of the fact that the EE and RTE are coupled to each other through the temperature and radiation intensity, a new numerical procedure is developed in which the temperature and radiation intensity are solved simultaneously, rather than sequentially by splitting of operators. Simultaneous solution allows implicit treatment of the effects of the aforementioned two quantities on each other, thereby resulting in enhanced stability and accelerated convergence. To the best of the author's knowledge, such a procedure has never been attempted before in the solution of problems involving combined mode heat transfer and, therefore, represents significant advancement over the state of the art.

Contributed by the Heat Transfer Division for publication in the JOURNAL OF HEAT TRANSFER. Manuscript received: December 27, 2004. Final manuscript received: April 1, 2005. Review conducted by: Walter W. Yuen.

2 Numerical Procedure

In this section, the detailed numerical procedure and discretized equations for simultaneous solution of the EE and RTE are presented. This section is divided into four subsections. In Sec. 2.1, the governing equations for radiative transport (i.e., the RTE) and overall energy conservation, along with relevant boundary conditions, are presented. In Sec. 2.2, the new numerical procedure is described in the context of a combined conduction-radiation problem in one-dimensional plane parallel geometry with gray radiation. This simplified scenario is examined for three reasons. First, it allows writing of the coefficient matrices in explicit form, rather than in compact notation, which, in the opinion of the author, is necessary for thorough understanding of the new procedure. Second, the one-dimensional gray equations are vital to explaining important issues pertaining to stability and convergence, as is seen later. Third, the results for such a problem are available in the literature and can serve as benchmark solutions for validation. In Sec. 2.3, the numerical procedure for the same one-dimensional conduction-radiation problem is outlined for nongray radiation. In Sec. 2.4, the numerical procedure is outlined for the general case of multidimensional nongray medium involving all modes of heat transfer. The equations are presented using compact notations, amenable to computer program development.

2.1 Governing Equations. As mentioned earlier, for problems involving combined modes of heat transfer, the governing equations that have to be solved are the overall energy conservation equation (or EE) and the radiative transfer equation (RTE). The overall energy conservation equation, written with temperature as the primary dependent variable, is [2]

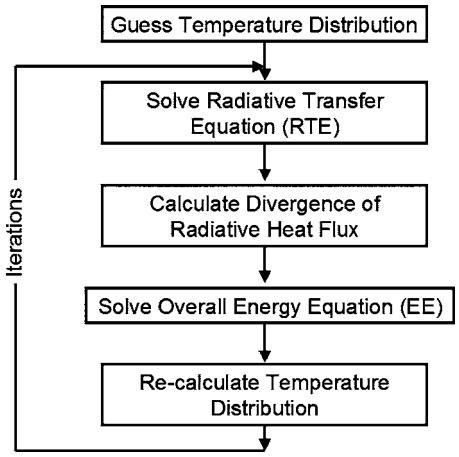

Fig. 1 Solution procedure used to date to solve combined mode heat transfer problems involving radiation in participating media

$$\rho c_p \frac{\partial T}{\partial t} + \rho c_p \mathbf{U} \bullet \nabla T = -\nabla \bullet \mathbf{q}^C - \nabla \bullet \mathbf{q}^R + \dot{S}_T \tag{1}$$

where ρ is the fluid density and c_p its specific heat capacity. The fluid velocity vector is denoted by $\mathbf{U}$, and $\dot{S}_T$ represents source of heat due to several different phenomena, such as viscous dissipation, work transfer, compressibility effects, and chemical reactions. The conductive and radiative heat fluxes are denoted by $\mathbf{q}^C$ and $\mathbf{q}^R$, respectively. In a single-component fluid, the conductive heat flux is given by the Fourier law of heat conduction [2], such that

$$\rho c_p \frac{\partial T}{\partial t} + \rho c_p \mathbf{U} \bullet \nabla T = \nabla \bullet (k_c \nabla T) - \nabla \bullet \mathbf{q}^R + \dot{S}_T \tag{2}$$

where k_c is the thermal conductivity of the medium.

It is clear from Eq. (2) that the divergence of the radiative heat flux, $\nabla \bullet \mathbf{q}^R$, appears as a sink in the overall energy transport equation and needs to be computed prior to the solution of Eq. (2). The computation of $\nabla \bullet \mathbf{q}^R$ requires solution of the RTE. The RTE is an integrodifferential equation whose solution requires special treatment, and several well-established methods are available to reduce it to a form that can be solved numerically with relative ease. Of these methods, the P_1 approximation [1,3], the discrete ordinates method [1,4,5], and the zonal method [6–8] appear to be the three most popular methods by virtue of being easily adaptable to the numerical framework traditionally used in computational fluid dynamic calculations. The P_1 method is particularly attractive because it results in a single elliptic partial differential equation, as opposed to several partial differential equations, which result from the discrete ordinates method. For the purposes of this paper, the P_1 approximation is used, with a note that the use of this method does not preclude the use of the coupled solution procedure to be described shortly. The advantages and disadvantages of using the P_1 approximation, relative to other methods of solution of the RTE, are well documented [1], and their discussion is not relevant for the current paper. Using the P_1 approximation, the RTE may be written as [1]

$$\nabla \bullet \left(\frac{1}{\kappa_\lambda + \sigma_{s\lambda}} \nabla G_\lambda \right) = -3\kappa_\lambda (4E_{b\lambda} - G_\lambda) \tag{3}$$

subject to the boundary condition

$$-\frac{2-\varepsilon_\lambda}{\varepsilon_\lambda}\frac{2}{3}\hat{\mathbf{n}} \bullet \nabla G_\lambda = (\kappa_\lambda + \sigma_{s\lambda})(4E_{bw\lambda} - G_\lambda) \tag{4}$$

where κ_λ and $\sigma_{s\lambda}$ are the spectral absorption and scattering coefficients of the medium, respectively, and G_λ is the spectral incident radiation. The blackbody emissive power is denoted by $E_{b\lambda}$ and is strongly temperature dependent. The emissivity of the boundary is denoted by ε_λ, and the surface normal at the boundary is denoted by $\hat{\mathbf{n}}$. Once the solution to Eq. (3), subject to Eq. (4), has been obtained, the divergence of the radiative heat flux can be calculated and Eq. (2) can be solved. The divergence of the radiative heat flux, which appears as a sink in Eq. (2), is written as [1]

$$\nabla \bullet q^R = \int_0^\infty \kappa_\lambda (4E_{b\lambda} - G_\lambda) d\lambda \tag{5}$$

Substitution of Eq. (5) into Eq. (2) yields

$$\rho c_p \frac{\partial T}{\partial t} + \rho c_p \mathbf{U} \bullet \nabla T = \nabla \bullet (k_c \nabla T) - \int_0^\infty \kappa_\lambda (4E_{b\lambda} - G_\lambda) d\lambda + \dot{S}_T \tag{6}$$

It is clear from the preceding description that Eqs. (3) and (6) represent a set of coupled equations. Furthermore, Eq. (6) is nonlinear because $E_{b\lambda}$ is a nonlinear function of temperature.

2.2 Conduction-Radiation in One-Dimensional Gray Media. Under the assumption of a gray nonscattering one-dimensional medium confined between gray isothermal boundaries, Eq. (6) may be written in nondimensional form as [1]

$$\frac{d^2\theta}{d\tau^2} = \frac{1}{N}(\theta^4 - g) \tag{7}$$

subject to the boundary conditions $\theta(0)=1$ and $\theta(\tau_L)=\theta_L$. Similarly, Eqs. (3) and (4) may be written in nondimensional form as [1]

$$\frac{d^2 g}{d\tau^2} = -3(\theta^4 - g) \tag{8}$$

subject to the boundary conditions

$$\left.\frac{dg}{d\tau}\right|_{\tau=0} + \frac{3}{2}\frac{\varepsilon_0}{2-\varepsilon_0}[1 - g(0)] = 0$$

$$\left.\frac{dg}{d\tau}\right|_{\tau=\tau_L} - \frac{3}{2}\frac{\varepsilon_L}{2-\varepsilon_L}[\theta_L^4 - g(\tau_L)] = 0 \tag{9}$$

In Eqs. (7)–(9), the optical length is defined as $\tau=\kappa x$, where x is the coordinate in the direction normal to the boundaries starting from 0 at the left boundary and going to L at the right boundary. The nondimensional temperature and incident radiation are defined as $\theta=T/T_0$ and $g=G/4\sigma T^4$, respectively. The subscript 0 is used to denote quantities at the left boundary, while the subscript L is used to denote quantities at the right boundary. The quantity N is the so-called conduction-to-radiation number, and is given by $N=k_c\kappa/4\sigma T_0^3$. Since Eqs. (7) and (8) are coupled nonlinear second-order ordinary differential equations, they necessitate solution by numerical means.

One common method to solve Eqs. (7) and (8) numerically is the finite-difference method [9]. Throughout this paper, this method is used for spatial discretization, although the extension of the formulations presented here to the finite-volume or finite-element method is straightforward. Using the finite-difference approximations to the second derivatives for a set of equally spaced nodes $[1,2,\ldots,i-1,i,i+1,\ldots,n-1,n]$, Eqs. (7) and (8) may be written as

$$\frac{\theta_{i-1}-2\theta_i+\theta_{i+1}}{\Delta\tau^2}-\frac{1}{N}(\theta_i^4-g_i)=0 \tag{10}$$

and

$$\frac{g_{i-1}-2g_i+g_{i+1}}{\Delta\tau^2}+3(\theta_i^4-g_i)=0 \tag{11}$$

where $\Delta\tau$ is the optical spacing between the nodes. For the purposes of stability, and to allow use of conventional linear algebraic equation solvers for solving Eqs. (10) and (11), they must first be linearized. This is best done using a Taylor series expansion, whereby $\theta_i^4 \cong \theta_i^{*4}+4\theta_i^{*3}(\theta_i-\theta_i^*)$, where θ_i^* is the value of θ_i at the previous iteration. Substitution of the linear form into Eqs. (10) and (11), followed by rearrangement yields

$$-\frac{1}{\Delta\tau^2}\theta_{i-1}+\left(\frac{2}{\Delta\tau^2}+\frac{4\theta_i^{*3}}{N}\right)\theta_i-\frac{1}{\Delta\tau^2}\theta_{i+1}=\frac{1}{N}g_i+\frac{3\theta_i^{*4}}{N} \tag{12}$$

and

$$-\frac{1}{\Delta\tau^2}g_{i-1}+\left(\frac{2}{\Delta\tau^2}+3\right)g_i-\frac{1}{\Delta\tau^2}g_{i+1}=12\theta_i^{*3}\theta_i-9\theta_i^{*4} \tag{13}$$

Equations (12) and (13) now represent two sets of coupled linear algebraic equations. In isolation, they can be solved most effectively using a tridiagonal matrix solver, such as the popular Thomas algorithm [9,10]. In the old approach, Eq. (13) is first solved by setting $\theta_i=\theta_i^*$ in the $12\theta_i^{*3}\theta_i$ term. This provides g_i, which is then substituted back into the right-hand side of Eq. (12). Equation (12) is subsequently solved to get a new θ_i, which then serves as a guess for the next iteration. Iterations are necessary in this approach for two reasons: (i) nonlinearity of the governing EE and (ii) explicit coupling between θ_i and g_i. It is worth noting that even if the EE were linear, the old method would still require iterations to address the explicit coupling between θ_i and g_i.

In the current approach, the implicitness of Eqs. (12) and (13) are preserved by re-writing them as

$$-\frac{1}{\Delta\tau^2}\theta_{i-1}+\left(\frac{2}{\Delta\tau^2}+\frac{4\theta_i^{*3}}{N}\right)\theta_i-\frac{1}{\Delta\tau^2}\theta_{i+1}-\frac{1}{N}g_i=\frac{3\theta_i^{*4}}{N} \tag{14}$$

$$-12\theta_i^{*3}\theta_i-\frac{1}{\Delta\tau^2}g_{i-1}+\left(\frac{2}{\Delta\tau^2}+3\right)g_i-\frac{1}{\Delta\tau^2}g_{i+1}=-9\theta_i^{*4} \tag{15}$$

Together, Eqs. (14) and (15) may be rewritten in matrix form as

$$\begin{bmatrix}\frac{2}{\Delta\tau^2}+\frac{4\theta_i^{*3}}{N} & -\frac{1}{N}\\ -12\theta_i^{*3} & \frac{2}{\Delta\tau^2}+3\end{bmatrix}\begin{bmatrix}\theta_i\\ g_i\end{bmatrix}+\begin{bmatrix}-\frac{1}{\Delta\tau^2} & 0\\ 0 & -\frac{1}{\Delta\tau^2}\end{bmatrix}\begin{bmatrix}\theta_{i-1}\\ g_{i-1}\end{bmatrix}$$

$$+\begin{bmatrix}-\frac{1}{\Delta\tau^2} & 0\\ 0 & -\frac{1}{\Delta\tau^2}\end{bmatrix}\begin{bmatrix}\theta_{i+1}\\ g_{i+1}\end{bmatrix}=\begin{bmatrix}\frac{3\theta_i^{*3}}{N}\\ -9\theta_i^{*4}\end{bmatrix} \tag{16}$$

For the set of nodes $[1,2,\ldots,i-1,i,i+1,\ldots,n-1,n]$, Eq. (16) represents a block tridiagonal system of equations of the form $[\mathbf{A}][\mathbf{X}]=[\mathbf{B}]$, where each element of the coefficient matrix $[\mathbf{A}]$ is a 2×2 matrix itself, whose elements are shown in Eq. (16). This block tridiagonal system of equations can also be solved using the Thomas algorithm, but rewritten in vector form [10,11], rather than in scalar form. The result vector $[\mathbf{X}]$ will now include both θ_i and g_i for all the nodes. Iterations will still be necessary to address the nonlinearity of the EE. If the EE were linear, unlike in the segregated solution approach, no iterations will be necessary, and the correct solution will have been generated after a single matrix inversion step. Even without performing any calculations, it is easy to understand why this implicit coupled approach will be computationally more efficient than the explicit segregated approach.

2.3 Conduction-Radiation in One-Dimensional Nongray Media. Under the assumption of a nongray non-scattering one-dimensional medium confined between nongray isothermal boundaries, Eq. (6) may be written as [1]

$$k_c\frac{d^2T}{dx^2}=\int_0^\infty \kappa_\lambda(4E_{b\lambda}-G_\lambda)d\lambda \tag{17}$$

subject to the boundary conditions $T(0)=T_0$ and $T(L)=T_L$. Similarly, Eqs. (3) and (4) may be written as

$$\frac{d^2G_\lambda}{dx^2}=-3\kappa_\lambda^2(4E_{b\lambda}-G_\lambda) \tag{18}$$

subject to the boundary conditions

$$\left.\frac{dG}{dx}\right|_{x=0}+\frac{3}{2}\frac{\varepsilon_{0\lambda}}{2-\varepsilon_{0\lambda}}\kappa_\lambda[4E_{b\lambda}(0)-G_\lambda(0)]=0$$

$$\left.\frac{dG}{dx}\right|_{x=L}-\frac{3}{2}\frac{\varepsilon_{L\lambda}}{2-\varepsilon_{L\lambda}}\kappa_\lambda[4E_{b\lambda}(L)-G(L)]=0 \tag{19}$$

where it has been assumed that both the thermal conductivity and the spectral absorption coefficient of the medium are invariant with space (and/or temperature).

In the nongray case, Eq. (18) must be solved for each wavelength λ. Several methods, of varying degree of fidelity, are available to address the spectral integration of the RTE. These include line-by-line integration [1,12], narrow-band models [13–15], wideband models [16], stepwise gray box model [1,17], the weight-sum-of-gray-gases model [1,18,19], and more recently developed models based either on narrowband k distributions [19–23] or full-spectrum k distributions [24]. Some of these methods, such as line-by-line calculations, narrowband models, and k-distribution models based on narrow bands, are prohibitively expensive for engineering calculations. Among the remaining models, the stepwise gray box model, the weighted-sum-of-gray-gases model, and the full-spectrum k-distribution models are computationally more efficient and amenable for engineering nongray calculations, and their use has been quite prolific. The stepwise gray box model is the default model employed in all commercial computational fluid dynamic codes, where the determination of the box height and width is left to the user.

Irrespective of what nongray model is used, the problem ultimately reduces to one where the incident radiation G has to be solved at several quadrature points to allow numerical integration of the right-hand side of Eq. (17). The exact form of the governing equation for G, and the interpretation of the quadrature points depends on whether the stepwise gray box model, the weighted-sum-of-gray-gases model, or the full-spectrum k-distribution model is used. In this paper, the discrete equations are formulated using the stepwise gray box model. Since both the weighted-sum-of-gray-gases model as well as the full-spectrum k-distribution model result in an RTE of the general form shown in Eq. (3), the current numerical procedure is just as easily extensible to these two models. Using the stepwise gray box model, Eqs. (17) and (18) may be rewritten as [1,17]

$$k_c\frac{d^2T}{dx^2}=\sum_{k=1}^{N_B+1}\kappa_k(4E_{bk}-G_k) \tag{20}$$

and

$$\frac{d^2G_k}{dx^2}=-3\kappa_k^2(4E_{bk}-G_k)\quad \forall\, k=1,2,\cdots,N_B+1 \tag{21}$$

where N_B is the number of gray boxes. The (N_B+1)th box represents the part of the spectrum that is outside of the defined boxes,

i.e., the so-called window [1,17]. The absorption coefficient in the kth box is a constant and is denoted by κ_k. The incident radiation for the kth box is denoted by $G_k=\int_{\Delta\lambda_k} G_\lambda d\lambda$, where $\Delta\lambda_k$ is the spectral width of the kth box. The emissive power within the k-th box is similarly given by [1]

$$E_{bk}(T)=\int_{\Delta\lambda_k} E_{b\lambda}(T,\lambda)d\lambda=[f(\lambda_{k,u}T)-f(\lambda_{k,l}T)]\sigma T^4 \quad (22)$$

where $\lambda_{k,u}$ and $\lambda_{k,l}$ are upper and lower wavelengths of the kth box, respectively, and f is the so-called fraction of blackbody radiation, which can be computed using a power series [25]. Following the procedure outlined in the preceding section, Eqs. (20) and (21) may be written in discretized form as

$$-\frac{k_c}{\Delta x^2}T_{i-1}+\left(\frac{2k_c}{\Delta x^2}+\sum_{k=1}^{N_B+1}4\kappa_k E'^{*}_{bk,i}\right)T_i-\frac{k_c}{\Delta x^2}T_{i+1}-\sum_{k=1}^{N_B+1}\kappa_k G_{k,i}$$
$$=-4\sum_{k=1}^{N_B+1}\kappa_k(E^{*}_{bk,i}-T^{*}_i E'^{*}_{bk,i}) \quad (23)$$

and

$$-12\kappa_k^2 E'^{*}_{bk,i}T_i+-\frac{1}{\Delta x^2}G_{k,i-1}+\left(\frac{2}{\Delta x^2}+3\kappa_k^2\right)G_{k,i}-\frac{1}{\Delta x^2}G_{k,i+1}$$
$$=12\kappa_k^2(E^{*}_{bk,i}-T^{*}_i E'^{*}_{bk,i}) \quad (24)$$

where the superscript astericks denote functional evaluations using values of independent variables at the previous iteration. The quantity E'_{bk} is defined as

$$E'_{bk}(T)=\int_{\Delta\lambda_k}\frac{dE_{b\lambda}}{dT}(T,\lambda)d\lambda=[h(\lambda_{k,u}T)-h(\lambda_{k,l}T)]4\sigma T^3 \quad (25)$$

Using Leibnitz's rule, it can be readily shown that

$$h(\lambda T)=f(\lambda T)+\frac{15}{4\pi^4}\frac{(C_2/\lambda T)^4}{\exp(C_2/\lambda T)-1} \quad (26)$$

where C_2 is the second constant of radiation. Once again, following the procedure described earlier, Eqs. (23) and (24) may be written in block-matrix form as

$$\begin{bmatrix} \frac{2k_c}{\Delta x^2}+\sum_k 4\kappa_k E'^{*}_{bk,i} & -\kappa_1 & \cdots & -\kappa_{N_B+1} \\ -12\kappa_k^2 E'^{*}_{bk,i} & \frac{2k_c}{\Delta x^2}+3\kappa_k^2 & 0 & 0 \\ \vdots & 0 & \ddots & \vdots \\ -12\kappa^2_{N_B+1}E'^{*}_{bN_B+1,i} & 0 & \cdots & \frac{2k_c}{\Delta x^2}+3\kappa^2_{N_B+1} \end{bmatrix}\begin{bmatrix} T_i \\ G_{1,i} \\ \vdots \\ G_{N_B+1,i} \end{bmatrix}$$
$$+\begin{bmatrix} -\frac{k_c}{\Delta x^2} & 0 & \cdots & 0 \\ 0 & \ddots & \ddots & \vdots \\ \vdots & \ddots & \ddots & 0 \\ 0 & \cdots & 0 & -\frac{k_c}{\Delta x^2} \end{bmatrix}\begin{bmatrix} T_{i-1} \\ G_{1,i-1} \\ \vdots \\ G_{N_B+1,i-1} \end{bmatrix}$$
$$+\begin{bmatrix} -\frac{k_c}{\Delta x^2} & 0 & \cdots & 0 \\ 0 & \ddots & \ddots & \vdots \\ \vdots & \ddots & \ddots & 0 \\ 0 & \cdots & 0 & -\frac{k_c}{\Delta x^2} \end{bmatrix}\begin{bmatrix} T_{i+1} \\ G_{1,i+1} \\ \vdots \\ G_{N_B+1,i+1} \end{bmatrix}$$
$$=\begin{bmatrix} -4\sum_k \kappa_k(E^{*}_{bk,i}-T^{*}_i E'^{*}_{bk,i}) \\ 12\kappa_1^2(E^{*}_{b1,i}-T^{*}_i E'^{*}_{b1,i}) \\ \vdots \\ 12\kappa^2_{N_B+1}(E^{*}_{bN_B+1,i}-T^{*}_i E'^{*}_{bN_B+1,i}) \end{bmatrix} \quad (27)$$

As before, for the set of nodes $[1,2,\ldots,i-1,i,i+1,\ldots,n-1,n]$, Eq. (27) represents a block tridiagonal system of equations of the form $[\mathbf{A}][\mathbf{X}]=[\mathbf{B}]$, where each element of the coefficient matrix $[\mathbf{A}]$ is now a $(N_B+2)\times(N_B+2)$ matrix itself. The treatment of the boundary nodes follows a similar procedure and is omitted here for the sake of brevity. The solution to this set of equations will simultaneously provide the temperature as well as the incident radiation at each box and at all spatial locations.

2.4 Combined Mode in Two-Dimensional Nongray Media. For a problem that involves all three modes of heat transfer, the full energy equation (Eq. (6)) needs to be solved. For a two-dimensional structured stencil, Eq. (6), after linearization, can be written in discretized form as

$$A^T_{i,j}T_{i,j}+A^T_{i-1,j}T_{i-1,j}+A^T_{i+1,j}T_{i+1,j}+A^T_{i,j-1}T_{i,j-1}+A^T_{i,j+1}T_{i,j+1}$$
$$+\sum_k A^{TG}_{k,i,j}G_{k,i,j}=S^T_{i,j} \quad (28)$$

where $A^T_{i-1,j}, A^T_{i+1,j}$, etc., denote the link coefficients between temperature at node $[i,j]$ to the temperature at the surrounding nodes, and $S^T_{i,j}$ is the linearized source term for the energy equation. The coefficient that couples temperature to incident radiation of the kth spectral box at the node $[i,j]$ is denoted by $A^{TG}_{k,i,j}$. Note that this term on the left-hand side of Eq. (28) preserves the implicitness between temperature and incident radiation. Similarly, the discretized RTE can be written as

$$A^G_{k,i,j}G_{k,i,j}+A^G_{k,i-1,j}G_{k,i-1,j}+A^G_{k,i+1,j}G_{k,i+1,j}+A^G_{k,i,j-1}G_{k,i,j-1}$$
$$+A^G_{k,i,j+1}G_{k,i,j+1}+A^{GT}_{k,i,j}T_{i,j}=S^G_{k,i,j} \quad \forall\, k=1,2,\cdots,N_B+1 \quad (29)$$

where $A^G_{k,i-1,j}, A^G_{k,i+1,j}$, etc., denote the link coefficients between the incident radiation of the kth spectral box and node $[i,j]$ to the incident radiation of the kth spectral box and surrounding nodes. The source term for the RTE of the kth spectral box is denoted by $S^G_{k,i,j}$. The coefficient that couples the incident radiation of the kth spectral box to the temperature at the node $[i,j]$ is denoted by $A^{GT}_{k,i,j}$. Following the procedure described in Secs. 2.2 and 2.3, Eqs. (28) and (29) may be written in the form of a block pentadiagonal system of equations. Three of the diagonals will be clustered in the center, while the remaining two will be displaced from the center. Thus, this system of equations cannot be solved directly using the Thomas algorithm. It is common practice to use the alternating direction implicit (ADI) method [9,10] to solve such systems. The ADI method constitutes an iterative procedure in which row- and columnwise sweeps are performed alternately and repeatedly. During a row-wise sweep (or i sweep), all j links are treated explicitly, while during a columnwise sweep (or j sweep) all i links are treated explicitly. Equations (28) and (29) can be written in block tridiagonal form for either row- or columnwise sweep. As an example, the block tridiagonal system for a row-wise sweep is shown below

$$
\begin{bmatrix} A^{T}_{i,j} & A^{TG}_{1,i,j} & \cdots & A^{TG}_{N_B+1,i,j} \\ A^{GT}_{1,i,j} & A^{G}_{1,i,j} & 0 & 0 \\ \vdots & 0 & \ddots & \vdots \\ A^{GT}_{N_B+1,i,j} & 0 & \cdots & A^{G}_{N_B+1,i,j} \end{bmatrix} \begin{bmatrix} T_{i,j} \\ G_{1,i,j} \\ \vdots \\ G_{N_B+1,i,j} \end{bmatrix}
$$

$$
+ \begin{bmatrix} A^{T}_{i-1,j} & 0 & \cdots & 0 \\ 0 & A^{G}_{1,i-1,j} & 0 & 0 \\ \vdots & 0 & \ddots & \vdots \\ 0 & 0 & \cdots & A^{G}_{N_B+1,i-1,j} \end{bmatrix} \begin{bmatrix} T_{i-1,j} \\ G_{1,i-1,j} \\ \vdots \\ G_{N_B+1,i-1,j} \end{bmatrix}
$$

$$
+ \begin{bmatrix} A^{T}_{i+1,j} & 0 & \cdots & 0 \\ 0 & A^{G}_{1,i+1,j} & 0 & 0 \\ \vdots & 0 & \ddots & \vdots \\ 0 & 0 & \cdots & A^{G}_{N_B+1,i+1,j} \end{bmatrix} \begin{bmatrix} T_{i+1,j} \\ G_{1,i+1,j} \\ \vdots \\ G_{N_B+1,i+1,j} \end{bmatrix}
$$

$$
= \begin{bmatrix} S^{T}_{i,j} + A^{T}_{i,j-1}T_{i,j-1} + A^{T}_{i,j+1}T_{i,j+1} \\ S^{G}_{1,i,j} + A^{G}_{1,i,j-1}G_{1,i,j-1} + A^{G}_{1,i,j+1}G_{1,i,j+1} \\ \vdots \\ S^{G}_{N_B+1,i,j} + A^{G}_{N_B+1,i,j-1}G_{N_B+1,i,j-1} + A^{G}_{N_B+1,i,j+1}G_{N_B+1,i,j+1} \end{bmatrix} \tag{30}
$$

Iterations will be necessary in this case on two accounts: (i) to address the nonlinearity in the EE and (ii) to address the splitting of spatial operators in the ADI method. Once again, in this new approach, iterations are not necessary to address the coupling between temperature and incident radiation.

It is clear from the above description that the current implicit method can be applied to a general multidimensional nongray problem involving combined modes of heat transfer. The main task in the use of this method is of writing the discrete equations in implicit block-matrix form. The above discussion also insinuates that tremendous savings in computational time are likely with this coupled implicit approach. Whether or not dramatic increase in computational efficiency is actually manifested remains to be assessed. In Sec. 3, several example problems are solved to quantify the gains in computational efficiency. Subsequently, an effort is made to distinguish between scenarios under which the computational savings will be tremendous versus scenarios under which the savings will only be marginal.

3 Results and Discussion

Computations were performed using the old and new methods for several different cases. The results are presented in Sec. 3.1–3.3. All computations were performed on a 1.2 GHz Intel Celeron processor with 256 MB of memory. CPU times were obtained using built-in function calls. In all cases, the residuals for the EE and RTE were computed separately and are given by

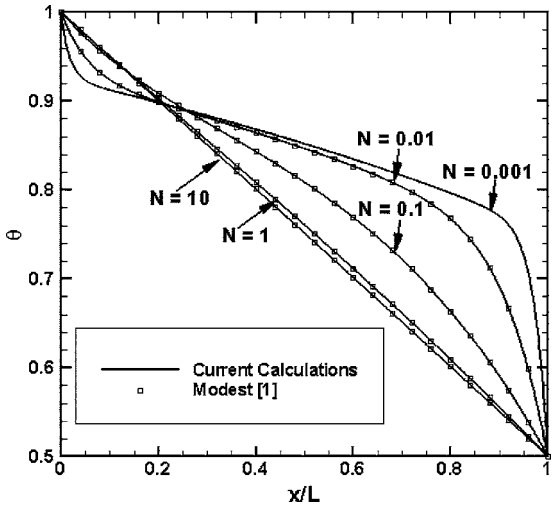

Fig. 2 Nondimensional temperature profiles for combined gray radiation conduction in a one-dimensional slab. $\varepsilon_0=\varepsilon_L=1$ and $\tau_L=\kappa L=1$ were used for these calculations

$$
R_T = \left[\sum_{i,j} (\mathrm{FDE}_{i,j})^2 \right]^{1/2}
$$

$$
R_G = \left[\sum_{k,i,j} (\mathrm{FDE}_{k,i,j})^2 \right]^{1/2} \tag{31}
$$

where $\mathrm{FDE}_{i,j}$ denotes the finite difference equation at node $[i,j]$ without linearization of the nonlinear terms. For the nongray case, the residual for the RTE includes summation over all spectral boxes, k. In each case, calculation was stopped when both residuals decreased by six orders of magnitude.

3.1 Conduction-Radiation in One-Dimensional Gray Media. Computations were first performed for a one-dimensional medium with combined conduction and gray radiation. The following data were used: $\varepsilon_0=\varepsilon_L=1$, $\tau_L=\kappa L=1$, and $\theta_L=0.5$. The necessary equations have already been presented in Sec. 2.2. The conduction-to-radiation number N was treated as a parameter. 1001 nodes were used for the numerical calculations, and a tridiagonal solver (scalar or vector form, depending on the method) was used in both cases. In the segregated method, no inner loop iterations were performed to solve the nonlinear EE within each global iteration loop. This method was chosen because it was found to have the best computational efficiency. The results produced by the two methods were identical, and are shown in Fig. 2. The results were also found to be identical to the results presented in Chap. 21 of Ref. [1], as shown in Fig. 2.

The number of global iterations required by the two methods is shown in Table 1. It is seen that the convergence of the segregated method is sensitive to the conduction-to-radiation number, whereas the convergence of the coupled method is independent of

Table 1 Number of global iterations required for a one-dimensional gray radiation-conduction problem using coupled and segregated solution methods

Conduction-to-Radiation Number, N	Coupled solution	Segregated solution
10	3	5
1	3	7
0.1	4	15
0.01	4	22
0.001	4	24

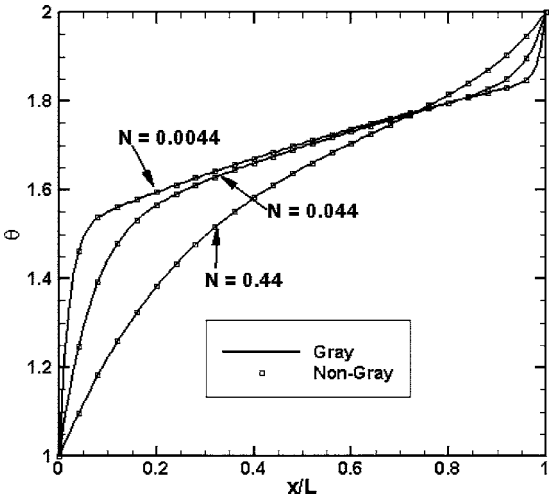

Fig. 3 Comparison of nondimensional temperature profiles computed using the gray and nongray formulations

this parameter. It is also quite clear that the convergence of the coupled method is vastly superior to the segregated method for this simple problem. In this study, since each calculation took <0.01 s, reliable CPU times could not be obtained. In this case, the convergence behavior of the coupled approach was found to be independent of the number of nodes, whereas that of the segregated approach deteriorated with increasing mesh size.

3.2 Conduction-Radiation in One-Dimensional Nongray Media. The next set of calculations was performed in the same one-dimensional geometry, but with a nongray model. The following data were used: $\varepsilon_0=\varepsilon_L=1$, $T_0=1000$ K, $T_L=2000$ K, $L=1$ m, and $k_c=1$ W/m/K. The stepwise gray model that was used to represent the spectrum consisted of three boxes, corresponding to the three bands of CO_2. The width of the boxes $\Delta\eta_k$ and their heights κ_k were evaluated at 1700 K, following the procedure described by Modest and Sikka [17], and were assumed to remain constant (i.e., invariant with temperature) for the sake of simplicity. The following values were used for the calculations: $\kappa_1=4.5$ m^{-1}, $\kappa_2=90.7$ m^{-1}, $\kappa_3=17.9$ m^{-1}, $\lambda_1=2.7$ μm, $\lambda_2=4.3$ μm, $\lambda_2=15$ μm, $\Delta\eta_1=445.3$ cm^{-1}, $\Delta\eta_2=377.6$ cm^{-1}, and $\Delta\eta_3=329.7$ cm^{-1}. In addition, a background constant gray absorption coefficient κ_B was also superimposed with the spectral box values, such that the "window" had an absorption coefficient κ_B. The background absorption coefficient was treated as a parameter in order to vary the average optical thickness of the medium. Once again, 1001 nodes were used. The nongray calculation procedure was first validated against the gray results of the preceding section by setting the absorption coefficient in each spectral box to be zero, such that the absorption coefficient defaulted to the background gray value. Results were found to be identical to the results produced by the gray code (Fig. 3). Next, calculations were performed with the two methods for several different values of the background absorption coefficient (optical thickness). The computational times and iterations required by the two methods are shown in Table 2.

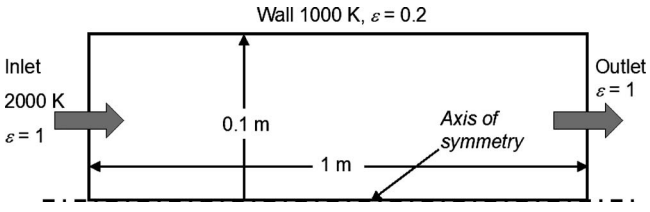

Fig. 4 Geometry and boundary conditions for the two-dimensional example problem

In this case, it is seen again that the convergence of the coupled solver is independent of variation in radiative properties, whereas that of the segregated solver is extremely sensitive to the properties used. As in the gray case, the computational savings due to the coupled solution procedure are tremendous. The choice to solve this nongray case in dimensional form was an intentional one. This choice was made to demonstrate that whether the dimensional or nondimensional form of the equations is used, the convergence of the segregated solution method is always sensitive to parametric variations, whereas that of the coupled solution method is almost insensitive to parametric variations.

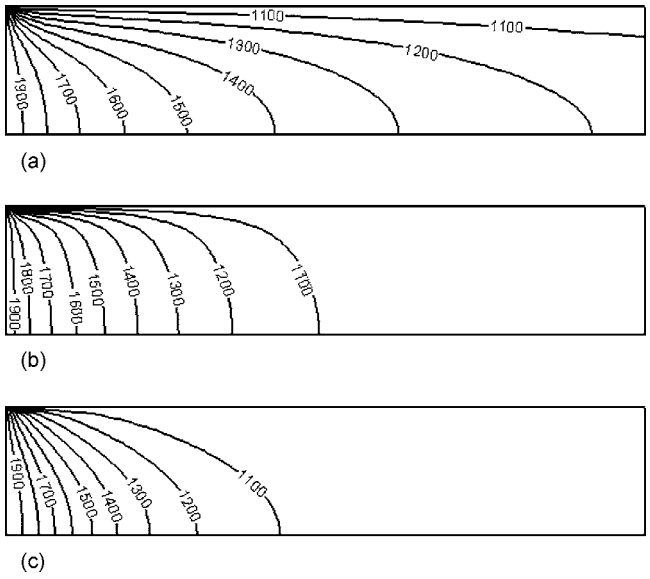

Fig. 5 Temperature distributions for various cases computed using a 51×51 mesh. Note that the figures have been stretched by a factor of two in the radial direction to enhance clarity. The lower boundary represents the axis of symmetry: (*a*) nongray radiation with three stepwise boxes and $\kappa_B=1$ m^{-1}, (*b*) nongray radiation with three stepwise boxes and $\kappa_B=10$ m^{-1}, and (*c*) nongray radiation with three stepwise boxes and $\kappa_B=100$ m^{-1}.

Table 2 Number of global iterations and CPU times required for a one-dimensional nongray radiation-conduction problem using coupled and segregated solution methods

κ_B (1/m)	Coupled solution		Segregated solution	
	Iterations	CPU time (s)	Iterations	CPU time (s)
1	6	0.45	137	15
10	7	0.54	615	67
100	6	0.45	23649	2571

Table 3 Computational time and iterations required for the two-dimensional example problem with all three modes of heat transfer and nongray radiation

Absorption coefficient of background = 1 m^{-1}

Mesh size (axial x radial)	Coupled-ADI		Segregated-ADI	
Aspect Ratio 10:1	CPU time	Iterations	CPU time	Iterations
11 x 11	2.19 s	165	4.56 s	182
21 x 21	30 s	590	50 s	561
51 x 51	17 mins	3392	26 mins	3000
101 x 101	4.32 hrs	12804	6.8 hrs	11738
Aspect Ratio 1:1				
51 x 6	2.5 mins	2086	4 mins	1794
101 x 11	15.2 mins	7309	23.1 mins	6272
201 x 21	3.6 hrs	26331	5.6 hrs	24102

Absorption coefficient of background = 10 m^{-1}

Mesh size (axial x radial)	Coupled-ADI		Segregated-ADI	
Aspect Ratio 10:1	CPU time	Iterations	CPU time	Iterations
11 x 11	0.33 s	24	2.2 s	88
21 x 21	3 s	60	11 s	123
51 x 51	1.5 mins	306	3.1 mins	357
101 x 101	22.9 mins	1151	39.6 mins	1181
Aspect Ratio 1:1				
51 x 6	5 s	161	12 s	198
101 x 11	1.3 mins	624	2.5 mins	671
201 x 21	18.8 mins	2302	31.6 mins	2261
401 x 41	5.4 hrs	8902	8.5 hrs	8733

Absorption coefficient of background = 100 m^{-1}

Mesh size (axial x radial)	Coupled-ADI		Segregated-ADI	
Aspect Ratio 10:1	CPU time	Iterations	CPU time	Iterations
11 x 11	0.27 s	21	12 s	500
21 x 21	1.35 s	27	42 s	473
51 x 51	17 s	57	4.2 mins	481
101 x 101	5 mins	181	23.35 mins	587
Aspect Ratio 1:1				
51 x 6	1 s	30	27 s	439
101 x 11	12 s	93	1.9 mins	461
201 x 21	2.8 mins	352	9.6 mins	684
401 x 41	44 mins	1320	111 mins	1569

3.3 Combined Mode in Two-Dimensional Nongray Media. In Secs., it was clearly demonstrated that the coupled solution approach is far superior to the traditionally used segregated solution approach. The next task was to investigate the effectiveness of the coupled solution procedure in a multidimensional geometry involving all three modes of heat transfer. For this purpose, a problem of combined mode heat transfer in a pipe was chosen. Hot gas at 2000 K entered a pipe whose walls were maintained at 1000 K. The geometry and boundary conditions are illustrated in Fig. 4. In order to avoid solution of the Navier-Stokes equation, it was assumed that the density of the gas is a constant (=0.22 kg/m^3, which is equal to its value computed using ideal gas law at 1700 K). This allowed use of the fully developed parabolic profile for the axial velocity of the fluid. The energy equation was discretized using the finite-difference technique. Second-order upwind differencing was used for the convection term, whereas central differencing was used for the conduction term [7]. The mean velocity of the flow was set to 1 m/s. The resulting equations were solved using the ADI method, described in Sec. 2.4. Typical temperature distributions are shown in Fig. 5 for various values of the background absorption coefficient.

A summary of the computational time and iterations required are shown in Table 3 for various mesh sizes. For optically thin situations (i.e., $\kappa_B=1\ m^{-1}$), the coupled solution approach is found to be approximately twice as efficient as the segregated solution approach, although the number of iterations required by both approaches is similar. This is indicative of the fact that one block tridiagonal matrix inversion is roughly twice as fast as five (EE+4 RTE spectral equations) individual tridiagonal matrix inversions. Unlike the one-dimensional case, the coupled solver is found to be sensitive to the optical thickness for the two-dimensional case. As the optical thickness is increased, the coupled solution approach becomes more and more efficient compared to the segregated solution approach, and the saving factor ranges between ~2 and 50, depending on the aspect ratio of the

grid and its coarseness. The reason for the sensitivity of the coupled solver to optical thickness for only the two-dimensional case has its roots in the ADI method and is best understood by reexamining the discrete RTE. For a two-dimensional Cartesian system, following the equations presented in Sec. 2.2, the gray RTE may be written in nondimensional discrete form as

$$\frac{g_{i-1,j}-2g_{i,j}+g_{i+1,j}}{\Delta\tau^2}+\frac{g_{i,j-1}-2g_{i,j}+g_{i,j+1}}{\Delta\tau^2}+3(\theta_{i,j}^4-g_{i,j})=0 \tag{32}$$

where $\Delta\tau=\kappa\Delta x=\kappa\Delta y$ has been used. Following lineraization, for a row-wise sweep of the ADI method, Eq. (31) may be rewritten as

$$g_{i,j}-\frac{1/\Delta\tau^2}{4/\Delta\tau^2+3}g_{i-1,j}-\frac{1/\Delta\tau^2}{4/\Delta\tau^2+3}g_{i+1,j}-\frac{12\theta_{i,j}^{*3}}{4/\Delta\tau^2+3}\theta_{i,j}$$
$$=\frac{1/\Delta\tau^2}{4/\Delta\tau^2+3}g_{i,j-1}+\frac{1/\Delta\tau^2}{4/\Delta\tau^2+3}g_{i,j+1}-\frac{9\theta_{i,j}^{*4}}{4/\Delta\tau^2+3} \tag{33}$$

Unlike the one-dimensional case, where all nodal values of the incident radiation are implicitly coupled, in this case, the nodes $[i,j-1]$ and $[i,j+1]$, which appear on the right-hand side of Eq. (33), are explicitly coupled to the node $[i,j]$. The convergence of the ADI method will depend on the magnitude of the coefficients premultiplying $g_{i,j-1}$ and $g_{i,j+1}$. If these coefficients are large, the convergence will be slow and vice versa. The limit of the coefficient $(1/\Delta\tau^2)/(4/\Delta\tau^2+3)$, as $\Delta\tau=\kappa\Delta x=\kappa\Delta y$ tends to zero, is 0.25, whereas its limit is zero as $\Delta\tau=\kappa\Delta x=\kappa\Delta y$ tends to infinity. Thus, when the optical thickness or grid spacing is small, convergence with the ADI method is expected to be poor. As the grid is coarsened, or the optical thickness in increased, the convergence will tend toward the convergence characteristics of the one-dimensional case. The data presented in Table 3 precisely follows this behavior. In summary, although implicit coupling between $G_{i,j}$ and $T_{i,j}$ helps enhance stability and convergence, the splitting of spatial operators in the ADI method adversely affects overall convergence. Such problems have been encountered before in computational fluid dynamics and are generally dealt with either by using block correction [10] or multigrid methods [10], both of which can be applied over and above the implicit procedure presented here to further enhance convergence.

4 Summary and Conclusions

Since radiation energy transport and overall energy transport are inherently coupled, implicit coupling between temperature and radiant energy is desirable. In this paper, the mathematical formulation to solve combined mode heat transfer problems using implicit coupling between radiation and overall energy was presented. It was shown through systematic numerical analysis that the coupled implicit treatment enhances convergence in almost all scenarios. In multidimensional problems, the choice of the method used for coupling the spatial operators is critical. It was found that with the ADI method in its un-enhanced form, the convergence of the coupled implicit method, although better than the segregated explicit method, becomes sensitive to the optical thickness of the medium. For optically thick situations, where the radiation does not propagate long distances, spatial coupling becomes weak and pointwise coupling between radiation intensity and temperature becomes dominant, the convergence is vastly superior using the coupled solution method. In the limiting case of nonparticipating medium (zero optical thickness), radiation does not affect the temperature of the medium and the coupled solution method essentially defaults to the segregated solution method. Overall, the new method demonstrates tremendous potential for convergence acceleration in problems involving combined modes of heat transfer with radiation in participating medium. This paper represents the first step in using the coupled approach. It presents the mathematical formulations for the implicit coupling between radiation and overall energy, along with a few examples demonstrating the potential gains of using this approach. Further research will be necessary to elucidate its advantages and disadvantages in full-scale calculations involving fluid flow and/or chemical reactions.

Acknowledgment

The author thanks Professor Michael Modest of the Pennsylvania State University for sharing the original files for the data used in Fig. 2.

Nomenclature

c_p = specific heat capacity of fluid, J/kg/K
E_b = blackbody emissive power, W/m^2
$E_{b\lambda}$ = blackbody emissive power, W/m^3
f = fraction of blackbody radiation (dimensionless)
G_λ = spectral incident radiation, W/m^3
g = dimensionless incident radiation
h = fraction of derivative of blackbody emissive power (Eqs. (25) and (26))
k_c = thermal conductivity, W/m/K
L = thickness, m
n = number of nodes
N = conduction to radiation number (dimensionless)
N_B = number of spectral boxes
$\hat{\mathbf{n}}$ = surface normal (dimensionless)
$\mathbf{q}^C$ = conductive heat flux, W/m^2
$\mathbf{q}^R$ = radiative heat flux, W/m^2
R_T = residual for energy equation, W/m^3
R_G = residual for radiative transfer equation, W/m^3
$\dot{S}_T$ = source term for energy equation, W/m^3
T = temperature, K
$\mathbf{U}$ = fluid velocity vector, m/s
x = spatial coordinate, m

Greek

ε_λ = spectral emissivity (dimensionless)
η = wave number, cm^{-1}
κ = absorption coefficient, m^{-1}
κ_λ = spectral absorption coefficient, m^{-1}
κ_B = absorption coefficient of background, m^{-1}
λ = wavelength, m
$\lambda_{k,u}$ = upper wavelength of kth spectral box, m
$\lambda_{k,l}$ = lower wavelength of kth spectral box, m
θ = dimensionless temperature
ρ = density of fluid, kg/m^3
σ = Stefan-Boltzmann constant $=5.67\times10^{-8}$Wm^{-2} K^{-4}
$\sigma_{s\lambda}$ = spectral scattering coefficient, m^{-1}
τ = optical thickness

References

[1] Modest, M. F., 2003, *Radiative Heat Transfer*, Second Edition, Academic Press, NY.
[2] Whitaker, S., 1983, *Fundamental Principles of Heat Transfer*, Krieger, Melbourne, FL.
[3] Modest, M. F., 1990, "The Improved Differential Approximation for Radiative Heat Transfer in Multi-Dimensional Media," ASME J. Heat Transfer, **112**, pp. 819–821.
[4] Fiveland, W., and Jamaluddin, A., 1991, "Three-dimensional Spectral Radiative Heat Transfer Solutions by the Discrete Ordinates Method," J. Thermophys. Heat Transfer, **5**(3), pp. 335–339.
[5] Chai, J. C., Lee, H. S., and Patankar, S. V., 1994, "Finite-Volume Method for Radiative Heat Transfer," J. Thermophys. Heat Transfer, **8**, pp. 419–425.
[6] Yuen, W., and Takara, E., 1994, "Development of a general zonal method for analysis of radiative transfer in absorbing and anisotropically scattering media," Numer. Heat Transfer, Part B, **25**, pp. 75–96.
[7] Shen, Z., Smith, T., and Hix, P., 1983, "Linearization of Thermal Radiation Terms for Improved Convergence by Use of the Zone Method," Numer. Heat Transfer, **6**, pp. 377–382.
[8] Smith, T. and Severin, S., 1985, "Development of the Finite Analytic with Radiation Method," ASME J. Heat Transfer, **107**, pp. 735–737.

[9] Cheney, W., and Kincaid, W., 1985, *Numerical Mathematics and Computing*, Second Edition, Brooks-Cole, Belmont, MA.
[10] Ferziger, J., and Peric, M., 1999, *Computational Methods for Fluid Dynamics*, Second Edition, Springer-Verlag, Berlin.
[11] Press, W., Teukolsky, S., Vetterling, W., and Flannery, B., 1996, *Numerical Recipes in Fortran 90*, Second Edition, Cambridge University Press, Cambridge, England.
[12] Hartmann, J. M., DeLeon, R., and Taine, J., 1984, "Line-by-line and Narrow Band Statistical Model Calculations for H_2O," J. Quant. Spectrosc. Radiat. Transf., **32**(2), pp. 119–128.
[13] Elsasser, W. M., 1942, "Heat Transfer by Infrared Radiation in the Atmosphere," Harvard Meterol., **6**, pp. 107–129.
[14] Ludwig, C. B., Malkmus, W., Reardon, J. E., and Thompson, J. A., 1973, *Handbook of Infrared Radiation from Combustion Gases*, NASA SP-3080, Scientific and Technical Information Office, Washington, DC.
[15] Malkmus, W., 1967, "Random Lorentz Band Model with Exponentially Tailed s-1 Line Intensity Distribution Function," J. Opt. Soc. Am., **57**(3), p. 323.
[16] Edwards, D. K., 1976, "Molecular Gas Band Radiation," Adv. Heat Transfer, **12**, pp. 115–193.
[17] Modest, M. F., and Sikka, K., 1992, "The Application of the Stepwise-Gray P-1 Approximation to Molecular Gas-Particulate Mixtures," J. Quant. Spectrosc. Radiat. Transf., **48**(2), pp. 159–162.
[18] Modest, M. F., 1991, "The Weighted Sum of Gray Gases Model for Arbitrary Solution Methods in Radiative Heat Transfer," ASME J. Heat Transfer, **113**(3), p. 650.
[19] Denison, M. K., and Webb, B. W., 1994, "k-Distributions and Weighted-Sum-of-Gray-Gases: A Hybrid Model," *Tenth International Heat Transfer Conference, Taylor & Francis, NY*, pp. 19–24.
[20] Lacis, A. A., and Oinas, V., 1991, "A Description of the Correlated *k* Distribution Method for Modeling Nongray Gaseous Absorption, Thermal Emission, and Multiple Scattering in Vertically Inhomogeneous Atmospheres," J. Geophys. Res., **96**(D5), pp. 9027–9063.
[21] Lee, P. Y. C., Hollands, K. G. T., and Raithby, G. D., 1996, "Reordering the Absorption Coefficient Within the Wide Band for Predicting Gaseous Radiant Exchange," ASME J. Heat Transfer **118**(2), pp. 394–403.
[22] Goody, R., West, R., Chen, L., and Crisp, D., 1989, "The Correlated-k Method for Radiation Calculations in Nonhomogeneous Atmospheres," J. Quant. Spectrosc. Radiat. Transf., **42**(6), pp. 539–560.
[23] Tang, K. C., and Brewster, M. Q., 1994, "*K*-Distribution Analysis of Gas Radiation With Nongray, Emitting, Absorbing, and Anisotropic Scattering Particles," ASME J. Heat Transfer, **116**, pp. 980–989.
[24] Modest, M. F., and Zhang, H., 2002, "The Full-Spectrum Correlated-k Distribution for Thermal Radiation From Molecular Gas-Particulate Mixtures," ASME J. Heat Transfer, **124**(1), pp. 30–38.
[25] Siegel, R. and Howell, J., 2001, *Thermal Radiation Heat Transfer*, Fourth Edition, Taylor and Francis-Hemisphere, NY.

Energy Transmission by Photon Tunneling in Multilayer Structures Including Negative Index Materials

C. J. Fu

Z. M. Zhang[1]
e-mail: zzhang@mail.me.gatech.edu

George W. Woodruff School
of Mechanical Engineering,
Georgia Institute of Technology, Atlanta, Georgia
30332, USA

D. B. Tanner
Department of Physics,
University of Florida, Gainesville, Florida 32611,
USA

The phenomenon of photon tunneling, which depends on evanescent waves for radiative transfer, has important applications in microscale energy conversion devices and near-field optical microscopy. In recent years, there has been a surge of interest in the so-called negative index materials (NIMs), which have simultaneously negative electric permittivity and negative magnetic permeability. The present work investigates photon tunneling in multilayer structures consisting of positive index materials (PIMs) and NIMs. Some features, such as the enhancement of radiative transfer by the excitation of surface polaritons for both polarizations, are observed in the predicted transmittance spectra. The influence of the number of layers on the transmittance is also examined. The results suggest that the enhanced tunneling transmittance by polaritons also depends on the NIM layer thickness and that subdividing the PIM/NIM layers to enhance polariton coupling can reduce the effect of material loss on the tunneling transmittance.
[DOI: 10.1115/1.2010495]

Keywords: Electromagnetic, Microscale, Properties, Radiation, Thin Films

1 Introduction

An evanescent wave is an electromagnetic field that decays exponentially in space and does not transfer energy. If two objects are separated by a very small distance (barrier), two evanescent waves that decay in opposite directions can interact with each other to produce a net energy flow through the barrier. This phenomenon, known as photon tunneling or radiation tunneling, is very important for radiative energy transfer between two bodies when the distance of separation is shorter than the dominant wavelength of the emitting source [1]. Cryogenic insulation is a practical example of when photon tunneling may be significant [2]. Advances in micro- and nanotechnologies have made it possible for radiative transfer by photon tunneling to be appreciable and even dominant at room temperature or above. Scanning near-field optical microscopy (SNOM) relies on the photon tunneling between the probe and the sample surface to provide images of the sample with a subwavelength spatial resolution [3,4]. The concept of microscale thermophotovoltaic devices utilizes photon tunneling to improve the efficiency, with the receiver placed in close proximity to the emitter [5]. Recent studies have shown that excitation of surface polaritons can greatly change the radiation spectrum so that nearly monochromatic emission occurs close to the surface of the emitter; consequently, both the net radiative energy flux and the energy conversion efficiency could increase tremendously at the microscale [6,7].

The concept of a negative refractive index ($n<0$) was first postulated by Veselago [8] for a hypothetical material that has both negative electric permittivity (ε) and negative magnetic permeability (μ) in the same frequency region. (Note that ε and μ in the present paper are relative to those of free space.) The lack of simultaneous occurrence of negative ε and μ in natural materials hindered further study on negative index materials (NIMs) for some 30 years. On the basis of theoretical work by Pendry et al. [9,10], Shelby et al. [11] first demonstrated that a metamaterial exhibits negative refraction at X-band microwave frequencies. In a NIM medium, the phase velocity of an electromagnetic (EM) wave is opposite to its energy flux. Light refracted from a conventional positive index material (PIM) into a NIM will bend to the same side of the surface normal as the incident beam (a phenomenon called negative refraction), and a flat slab of NIM can focus light [8]. Pendry [12] claimed that a NIM slab with $\varepsilon=\mu=-1$ performs the dual function of correcting the phase of the propagating components and amplifying the evanescent components, which normally exist only in the near field of the object. The combined effects could make a perfect lens that eliminates the limitations on image resolution imposed by diffraction for conventional lenses. Potential applications range from nanolithography to novel Bragg reflectors, phase-compensated cavity resonators, waveguides, and enhanced photon tunneling for microscale energy conversion devices [13–17]. Despite doubt cast by some researchers on the concept of a "perfect lens" and even on negative refraction, both hypotheses of negative refraction and the ability to focus light by a slab of NIM have been verified by analytical, numerical, and experimental methods [18–21].

A NIM layer of $\varepsilon=\mu=-1$, when placed together with a vacuum gap of the same thickness between two (semi-infinite) dielectric media, compensates the phase change in vacuum and causes evanescent wave amplification, so that radiative energy can be transmitted completely through the structure [16]. However, the ideal case of $\varepsilon=\mu=-1$ cannot exist at more than a single frequency because both ε and μ of a NIM must be inherently dependent on frequency [8]. Although some studies have dealt with nonideal cases [17,22], the effects of dispersion and loss on photon tunneling have not been completely understood. In the present study, the frequency-dependent complex ε and μ are considered, and enhanced photon tunneling is analyzed in terms of the excitation of a surface plasmon resonance. Furthermore, the effect of subdividing the NIM into thinner layers, which are placed alternately with vacuum gaps, is investigated to see whether structural changes can

[1]Corresponding author.

Contributed by the Heat Transfer Division for publication in the JOURNAL OF HEAT TRANSFER. Manuscript received: August 12, 2004. Final manuscript received: January 26, 2005. Review conducted by: Stefan Thynell.

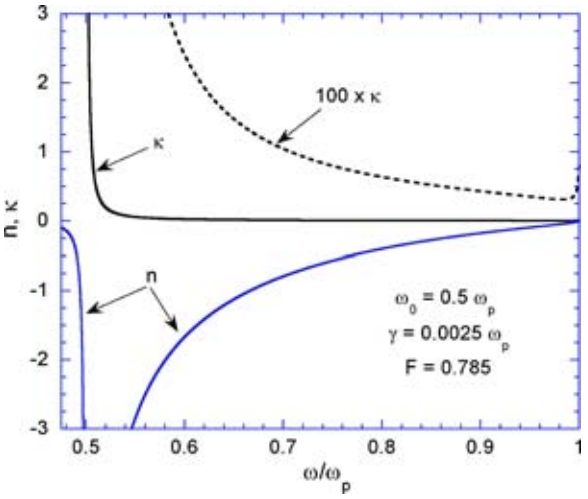

Fig. 1 Refractive index n and extinction coefficient κ of a NIM, calculated from Eqs. (1)–(3) as functions of the dimensionless frequency ω/ω_p. The dashed line shows the κ values multiplied by 100.

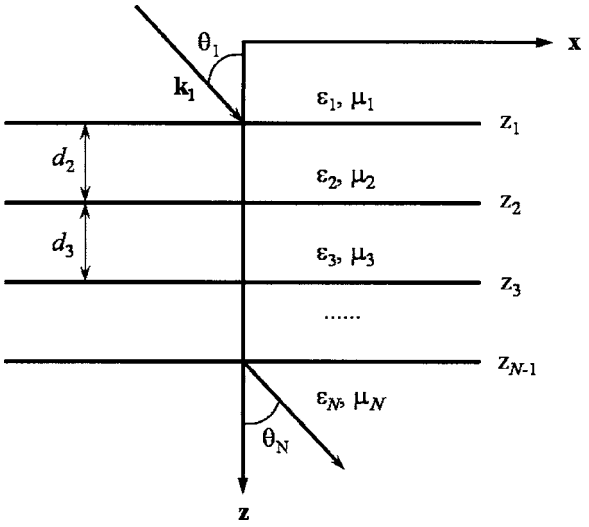

Fig. 2 Schematic illustration of a N-layer structure

significantly alter the radiative properties. Moreover, we provide a modified matrix formulation for use in the calculation.

2 Theory

Based on an effective medium approach, Pendry et al. [9,10] showed that the relative permittivity and permeability of the negative index metamaterial, consisting of repeated unit cells of interlocking copper strips and split-ring resonators, can be expressed as functions of the angular frequency ω as follows:

$$\varepsilon(\omega) = 1 - \frac{\omega_p^2}{\omega^2 + i\gamma_e\omega} \tag{1}$$

and

$$\mu(\omega) = 1 - \frac{F\omega^2}{\omega^2 - \omega_0^2 + i\gamma_m\omega} \tag{2}$$

where ω_p is the effective plasma frequency, ω_0 is the effective resonance frequency, γ_e and γ_m are the damping terms, and F is the fractional area of the unit cell occupied by the split ring. From Eqs. (1) and (2), both negative ε and μ can be realized in a frequency range between ω_0 and ω_p for an adequately small γ_e and γ_m. Here, the values of ω_0, ω_p, γ_e, γ_m, and F depend on the geometry of the unit cell that constructs the metamaterial. In the present study, the following parameters are chosen: $\omega_0 = 0.5\omega_p$, $F = 0.785$, and $\gamma_e = \gamma_m = \gamma$ with γ allowed to vary from zero to a small fraction of ω_p. Because of the scaling capability of the metamaterial [23], the frequency is normalized to ω_p in all the calculated results. The complex refractive index of the metamaterial depends on both ε and μ; hence,

$$\tilde{n}^2(\omega) = [n(\omega) + i\kappa(\omega)]^2 = \varepsilon(\omega)\mu(\omega) \tag{3}$$

Although the refractive index $n(\omega)$ may be negative, the extinction coefficient $\kappa(\omega)$ must be non-negative for a passive medium. The calculated n and κ are plotted in Fig. 1 as functions of the dimensionless frequency ω/ω_p for $\gamma = 0.0025\omega_p$. It can be seen that in the frequency range from ω_0 to ω_p, where the real parts of ε and μ are negative, n is negative and κ (for small values of γ) is small at frequencies not too close to ω_0.

The transfer matrix method is a standard and convenient technique for calculating the radiative properties of multilayer structures [24–27]. It is assumed that the incident light is in a plane-wave form. Some modifications are necessary for the matrix formulation to be applicable to absorbing media and with NIMs. Even in some recent publications involving NIMs [13,16,17,28,29], the equations were either not provided or given under restricted conditions. The multilayer structure containing N layers is shown in Fig. 2. Each layer is assumed isotropic and can be fully described by a relative permittivity ε_l and a relative permeability μ_l ($l = 1, 2, \ldots N$). The transmittance of this multilayer structure can be expressed as

$$T = \frac{\mathrm{Re}(k_{Nz}^*/\mu_N^*)}{\mathrm{Re}(k_{1z}^*/\mu_1^*)}\left|\frac{1}{M_{11}}\right|^2, \quad \text{for } s \text{ polarization} \tag{4}$$

and

$$T = \frac{\mathrm{Re}(k_{Nz}/\varepsilon_N)}{\mathrm{Re}(k_{1z}/\varepsilon_1)}\left|\frac{1}{M_{11}}\right|^2, \quad \text{for } p \text{ polarization} \tag{5}$$

Here, Re takes the real part of a complex number, the asterisk denotes the complex conjugate, k_{lz} is the normal component of the wave vector of the lth layer, and M_{11} is the element of the transfer matrix $\mathbf{M}$, which is given by

$$\mathbf{M} = \begin{pmatrix} M_{11} & M_{12} \\ M_{21} & M_{22} \end{pmatrix} = \prod_{l=1}^{N-1} \mathbf{P}_l \mathbf{D}_l^{-1} \mathbf{D}_{l+1} \tag{6}$$

where $\mathbf{D}_l^{-1}$ is the inverse matrix of $\mathbf{D}_l$, given by

$$\mathbf{D}_l = \begin{pmatrix} 1 & 1 \\ k_{lz}/\mu_l & -k_{lz}/\mu_l \end{pmatrix}, \quad \text{for } s \text{ polarization} \tag{7}$$

and

$$\mathbf{D}_l = \begin{pmatrix} 1 & 1 \\ k_{lz}/\varepsilon_l & -k_{lz}/\varepsilon_l \end{pmatrix}, \quad \text{for } p \text{ polarization} \tag{8}$$

and

$$\mathbf{P}_l = \begin{pmatrix} e^{-ik_{lz}d_l} & 0 \\ 0 & e^{ik_{lz}d_l} \end{pmatrix} \tag{9}$$

where d_l is the thickness of the lth layer except that d_1 is set to zero, and k_{lz} is calculated from

$$k_x^2 + k_{lz}^2 = \varepsilon_l\mu_l\omega^2/c^2 \tag{10}$$

where c is the speed of light in vacuum and k_x (the wave-vector component parallel to the surface) is the same in all layers as required by the phase-matching condition. Note that the imaginary part of k_{lz} calculated from Eq. (10) should not be less than zero. The reflectance of the multilayer structure for either polarization can be calculated by

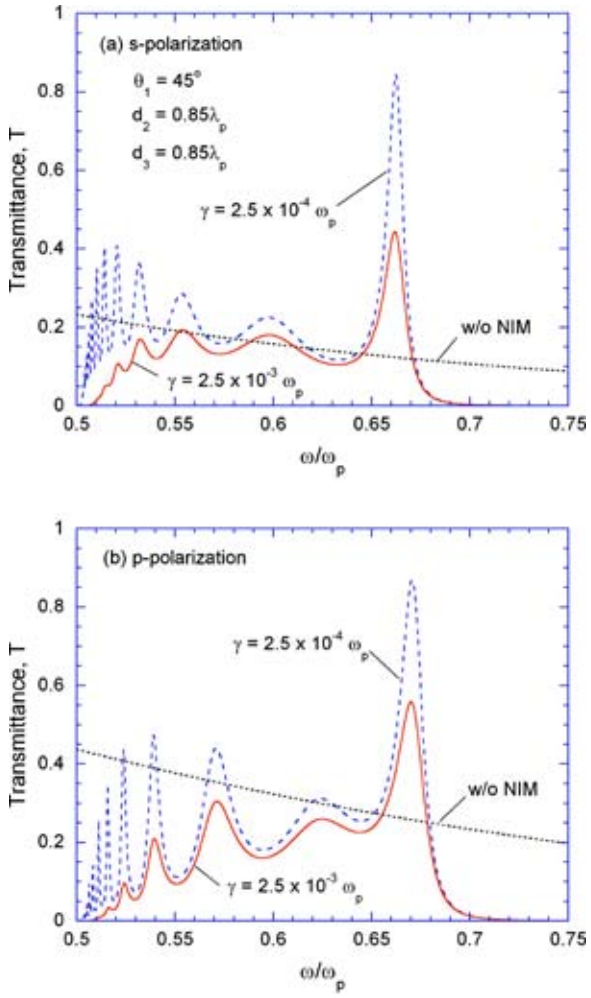

Fig. 3 Spectral transmittance of a four-layer structure at 45 deg incidence angle: (*a*) *s* polarization and (*b*) *p* polarization. For the dielectrics: $\varepsilon_1=\varepsilon_4=2.25$ and $\mu_1=\mu_4=1$; medium 2 is vacuum: $\varepsilon_2=\mu_2=1$; for the NIM: ε_3 and μ_3 are calculated from Eqs. (1) and (2) with $\omega_0/\omega_p=0.5$, $F=0.875$, and with different values of γ. The vacuum gap (VG) width and the NIM layer thickness are both taken to be $0.85\lambda_p$. The transmittance without a NIM layer ($d_3=0$) is also shown for comparison.

$$R=|M_{21}/M_{11}|^2 \tag{11}$$

It should be pointed out that the reflectance is ill defined when the first medium is dissipative because of the coupling between the reflected and incident waves [30]. However, Eqs. (4)–(11) are applicable if the last medium is dissipative.

3 Results and Discussion

Consider a four-layer ($N=4$) structure similar to that used in previous works [16,17]. The first and last media are semi-infinite dielectrics with $\varepsilon_1=\varepsilon_4=2.25$ ($n_1=n_4=1.5$). There are two intermediate layers: layer 2 is a vacuum gap (VG) and layer 3 is made of a NIM. In the present study, however, ε_3 and μ_3 are calculated from Eqs. (1) and (2). Without the NIM layer, the structure is similar to that used for the study of radiative transfer between two closely spaced plates [1,5]. For radiation from medium 1, the incidence angle should be greater than the critical angle $\theta_c=\arcsin(1/n_1)$ in order for photon tunneling to occur. This can be done by shaping the first dielectric like a prism, as in the attenuated total reflectance (ATR) configuration [31–33].

The calculated spectral transmittance at 45 deg angle of incidence is plotted in Fig. 3, for $\gamma=0.0025\omega_p$ and $0.00025\omega_p$, and compared to the case without the NIM layer ($d_3=0$). The VG width (d_2) and the NIM layer thickness (d_3) are both set to $0.85\lambda_p$, where $\lambda_p=2\pi c/\omega_p$ is the wavelength corresponding to the plasma frequency. The dimensionless approach allows the results to be scalable toward different electromagnetic spectral regions, once suitable negative index materials are available. For both polarizations, the transmittance oscillates in the frequency range from $0.5<\omega/\omega_p<0.7$, with a distinct peak between 0.65 and 0.68, and then goes to zero abruptly. The oscillation in the transmittance at $\omega/\omega_p<0.65$ is due to the interference of propagating waves inside the NIM layer, coupled with photon tunneling through the VG. On the other hand, the peak transmittance is due to the excitation of a surface plasma polariton (SPP) at the interface between the vacuum and NIM, to be discussed in the following.

A SPP is a coupled, localized electromagnetic wave that propagates along the interface of two different media and decay exponentially away from the interface [31]. In other words, there exists an evanescent wave in each medium whose amplitude is maximal at the interface. The excitation frequency of SPP depends not only on the electromagnetic properties of the materials but also on the wave-vector component k_x. At the interface between layer 2 (vacuum) and layer 3 (NIM) of the four-layer structure, the SPP dispersion relations satisfy the following simple equations when the thicknesses d_2 and d_3 extend to infinity and the loss (dissipation) in the NIM is negligible [32]:

$$\frac{\beta_2}{\mu_2}+\frac{\beta_3}{\mu_3}=0, \quad \text{for } s \text{ polarization} \tag{12}$$

and

$$\frac{\beta_2}{\varepsilon_2}+\frac{\beta_3}{\varepsilon_3}=0, \quad \text{for } p \text{ polarization} \tag{13}$$

where β_l is positive and is related to the wave vector by $\beta_l=(k_x^2-\varepsilon_l\mu_l\omega^2/c^2)^{1/2}$, $l=2$ or 3. Based on Eq. (10), for β to be positive, k_{lz} must be purely imaginary and evanescent waves occur in both media. Another necessary criterion for surface polariton to exist is that $\mu_3<0$ for s polarization and $\varepsilon_3<0$ for p polarization. The simultaneous negative ε and μ in a NIM allow SPPs to be excited for both polarizations in the same frequency region. Note that $k_x=(\omega n_1/c)\sin\theta_1$, Eqs. (12) and (13) can be recast as follows:

$$\sin\theta_1=\frac{1}{n_1}\left(\frac{\mu_3^2-\mu_3\varepsilon_3}{\mu_3^2-1}\right)^{1/2}, \quad \text{for } s \text{ polarization} \tag{14}$$

and

$$\sin\theta_1=\frac{1}{n_1}\left(\frac{\varepsilon_3^2-\varepsilon_3\mu_3}{\varepsilon_3^2-1}\right)^{1/2}, \quad \text{for } p \text{ polarization} \tag{15}$$

For a given angle of incidence θ_1 from a dielectric medium (layer 1), the frequency at which SPP can be excited, ω_{spp}, is the solution of Eq. (14) or (15) for each polarization. Generally speaking, θ_1 must be sufficiently large such that k_z is purely imaginary in both media 2 and 3. For the four-layer structure with finite thicknesses and nonzero γ, ω_{SPP} from Eq. (14) or (15) gives an approximate value to the excitation frequency of SPPs at the second interface. The excitation of polaritons causes a resonance transfer of the photon energy to a surface electromagnetic wave and is manifested in an ATR configuration as a sharp decrease in the reflectance [31]. In the case when a propagating wave exists in the last medium (layer 4), however, the excitation of SPPs can enhance the energy transmission via photon tunneling [33].

Table 1 compares ω_{SPP} calculated from Eqs. (14) and (15) at different incidence angles with the frequency ($\omega_{\max}$) that corresponds to the transmittance peak shown in Fig. 3 for $\gamma=0.0025\omega_p$. The agreement is very good, especially at larger incidence angles. The small deviation at θ_1 close to the critical angle θ_c (41.8 deg in this case) is caused by the disturbance of end layers. As can be seen from Fig. 3, $\omega_{\max}$ changes little with γ but

Table 1 Comparison of the SPP frequency ω_{spp} calculated from Eqs. (14) and (15) to the frequency ω_{max} corresponding to the transmittance peak for the four-layer structure with $\gamma = 0.0025\omega_p$.

Incidence angle (deg)	*s* polarization		*p* polarization	
	ω_{spp}/ω_p	ω_{max}/ω_p	ω_{spp}/ω_p	ω_{max}/ω_p
42	0.66600	0.66350	0.66650	0.66550
45	0.66325	0.66175	0.67075	0.67025
50	0.65975	0.65925	0.67625	0.67625
55	0.65750	0.65725	0.68025	0.68050
60	0.65550	0.65550	0.68325	0.68350

the magnitude of transmittance decreases significantly when γ is increased. The sharp peaks of transmittance due to SPP excitations suggest a possible way to build new optical resonators, similar to the Fabry-Perot resonators [26,34], which have important applications in optoelectronics and optical communications.

Because both d_2 and d_3 are finite, the matching of thickness is critical for transmittance enhancement [17]. In the lossless case, $\beta_2 d_2 = \beta_3 d_3$ is referred to as a phase-matching condition [16] because it will result in a transmittance of unity. When loss is included, the optimization condition can no longer be expressed by a simple relation. The peak transmittance of the four-layer structure as a function of d_3 is shown in Fig. 4 for different γ values, where the VG width d_2 is fixed to $0.85\lambda_p$. The frequency corresponding to the transmittance peak shifts slightly from the values (ω_{max}) listed in Table 1 as d_3 changes. The value of d_3 that results in a maximal transmittance depends on polarization because the SPP resonance frequencies are different. For a given γ, there exists an optimum d_3 at which the peak transmittance is the highest. Using $d_3 = d_2\beta_2/\beta_3$ and under the lossless assumption, one obtains $d_3 = 1.02\lambda_p$ for *s* polarization and $0.7\lambda_p$ for *p* polarization, close to optimum values for $\gamma = 0.00025\omega_p$ as shown in Fig. 4. As γ is increased to $0.0025\omega_p$, the optimum d_3 is reduced especially for *s* polarization.

Polaritons can be excited at both surfaces of a NIM slab [35]. If the media on both sides of the slab are identical, the two surface polaritons are coupled. On the other hand, a standing wave may exist inside a slab while the outside fields decay exponentially. Such a mode is called a waveguide mode or a bulk polariton [31]. Both coupled and bulk polaritons may affect the radiative properties [33]. Assume that a five-layer structure is constructed by equally subdividing the vacuum gap into two layers that sandwich the NIM layer. The two end layers are the same dielectric media as in the four-layer structure. The thickness of the NIM layer remains to be $0.85\lambda_p$, which is equal to the total thickness of the vacuum gaps. The results for both *s* and *p* polarizations are plotted in Fig. 5(*a*) for $\theta_1 = 45$ deg and Fig. 5(*b*) for $\theta_1 = 60$ deg. Compared to Fig. 3, the transmittance in Fig. 5(*a*) near the SPP frequency has increased remarkably. Furthermore, the full width at half maximum of the peak is significantly broadened. In particular, the peak at the SPP frequency for *s* polarization splits into two peaks. This change of the transmittance spectrum is because of the coupling between the SPPs at both surfaces of the NIM layer [31,35]. The split of the SPP mode depends on the field coupling strength. It follows that the split SPP modes tend to be more separated for a thinner NIM layer, whereas they shift to each other for a thicker NIM layer and eventually the fields inside the NIM decouple and the split SPP modes restore when the NIM thickness approaches infinity. The broadening of the transmittance peak shown in Fig. 5(*a*) is because the two split SPP modes are very close to each other, especially for *p* polarization, such that the corresponding two peaks overlap. The field reinforcement inside the NIM due to the coupling gives rise to the large enhancement of the tunneling transmittance, and this enhancement is more remarkable at larger incidence angles, such as the case shown in Fig. 5(*b*), where the transmittance near the SPP frequency is over 20 times greater than that without a NIM layer.

An alternative way to construct a five-layer structure is to place the vacuum gap in the middle and equally subdivide the NIM into two layers located between the VG and a dielectric. The transmittance of this five-layer structure is shown in Figs. 5(*c*) and 5(*d*) for an incidence angle equal to 45 and 60 deg, respectively. The label NIM/VG/NIM indicates that the vacuum gap is between two subdivided NIM layers. In the calculation, the VG thickness and the total NIM thickness remain to be $0.85\lambda_p$. The transmittance features due to SPP excitation are similar to those seen in Figs. 5(*a*) and 5(*b*), except that discernable split of the peak is for *p* polarization instead of *s* polarization. For $\omega/\omega_p < 0.6$, the transmittance shown in Figs. 5(*c*) and 5(*d*) is lower and less oscillating as compared to the corresponding results in Figs. 5(*a*) and 5(*b*). The reason for this difference is that the transmittance is enhanced in the case with VG/NIM/VG by the excitation of the waveguide modes or bulk polaritons inside the NIM layer. A slab should have a larger refractive index (absolute value) than its surrounding media in order to sustain bulk polaritons; this is the case for Figs. 5(*a*) and 5(*b*). Consequently, there are no bulk polaritons in Figs. 5(*c*) and 5(*d*). A detailed discussion of the dispersion relations of

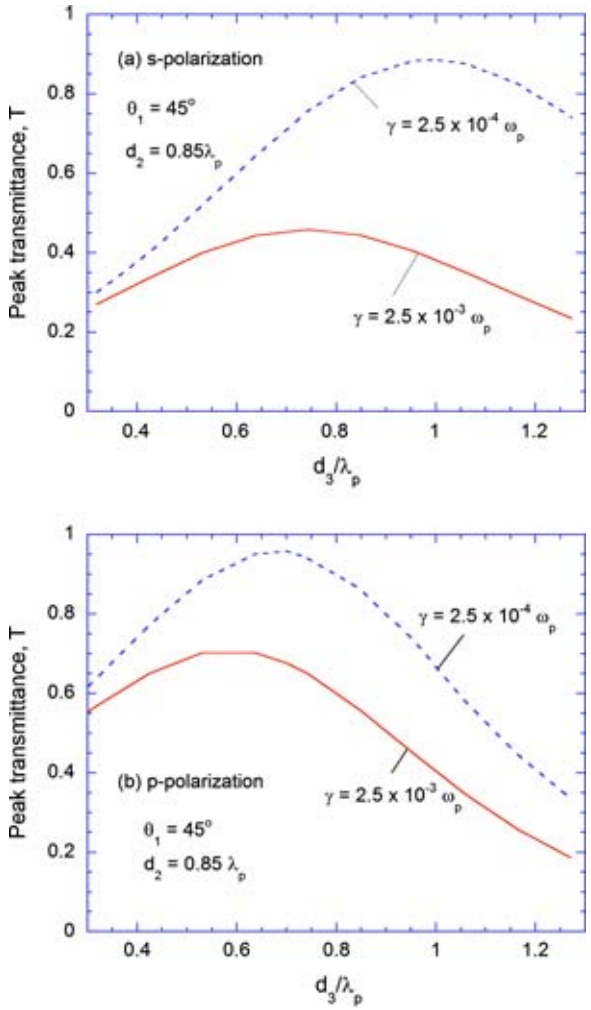

Fig. 4 Peak transmittance of the four-layer structure versus the thickness of the NIM for incidence angle of 45 deg, when d_2 is fixed at $0.85\lambda_p$: (*a*) *s* polarization and (*b*) *p* polarization.

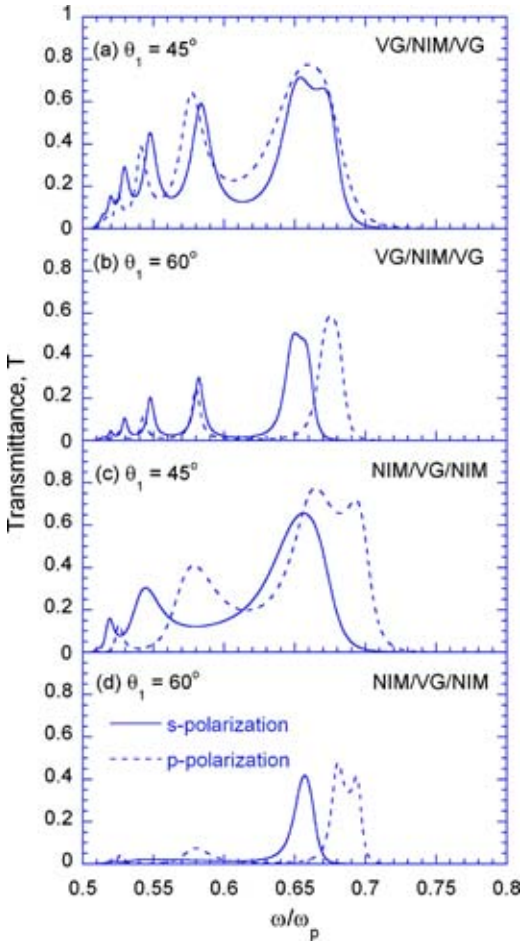

Fig. 5 The transmittance spectra of a five-layer structure for $\gamma=0.0025\omega_p$. In (*a*) and (*b*), the VG is equally divided into two layers sandwiching the NIM layer. The total thickness of the VGs and the thickness of the NIM layer are the same as in Fig. 4, i.e., $0.85\lambda_p$. In (*c*) and (*d*), the NIM layer is equally divided into two layers that sandwich the VG.

bulk polaritons can be found in the work of Park et al. [33]. The transmittance peaks for $\omega/\omega_p<0.6$ in Figs. 5(*a*) and 5(*b*) correspond to the modes of bulk polaritons excited in the NIM slab. Bulk polaritons have important applications in integrated optical waveguides [36] and for inducing resonant tunneling superlattices [37]. Figure 5 demonstrates that a NIM slab, which sustains bulk polaritons, can enhance radiative energy transmission via photon tunneling.

The focusing capability of a NIM slab may be the most promising application of these metamaterials. Challenges remain to reduce the losses in practical devices. It was shown [28,29] that the image resolution could be improved by dividing the NIM slab used in the imaging device into many thinner lamellae, and it was thought that the subdivision would result in a reduced absorption in the NIM. Many thinner NIM layers, when placed alternately with vacuum gaps, can cause stronger field coupling inside the structure when SPPs are excited. Therefore better enhancement of photon tunneling may be achieved. For instance, a six-layer structure can be made by equally dividing each VG and NIM layer into two sublayers and placing them alternately between the two end dielectrics. A ten-layer structure can be constructed by doubling the number of VGs and NIM layers without increasing the total thicknesses. The transmittance of multilayer structures calculated using the matrix formulation is shown in Figs. 6(*a*) for *s* polarization and 6(*b*) for *p* polarization, at 60 deg incidence angle. Clearly, the transmittance increases after each division and the frequency range over which significant tunneling can be observed is greatly broadened by subdividing the layers. The subdividing process results in more bulk polaritons or SPPs being excited and coupling inside the structure. The dispersion relations of bulk and surface modes are very complicated when the structure consists of many layers. Nevertheless, when the layers between the two end dielectrics become thinner and thinner, the stronger SPP coupling will split the surface modes into many branches: some modes will shift to higher frequencies and thus broaden the frequency range, whereas some others will shift to lower frequencies and can convert to bulk polaritons [33].

In order to understand the radiative properties for both propagating modes and evanescent modes, the transmittance and absorptance at a single frequency $\omega=0.665\omega_p$ is plotted in Figs. 7(*a*) for *s* polarization and 7(*b*) for *p* polarization, as a function of the incidence angle. When the incidence angle is smaller than the critical angle (at the dielectric-air interface), the radiative properties are affected by multiple reflections and interferences of the propagating waves in the layered structure. Consequently, a decrease in transmittance is observed when the layer number is increased from 4 to 10, presumably because of the enhancement of reflectance as more boundaries are added. On the other hand, when the incidence angle is greater than the critical angle, bulk polaritons and surface polaritons may be excited and may interact with each other to enhance the electromagnetic field in the structure, resulting in an enhancement in the transmittance as the num-

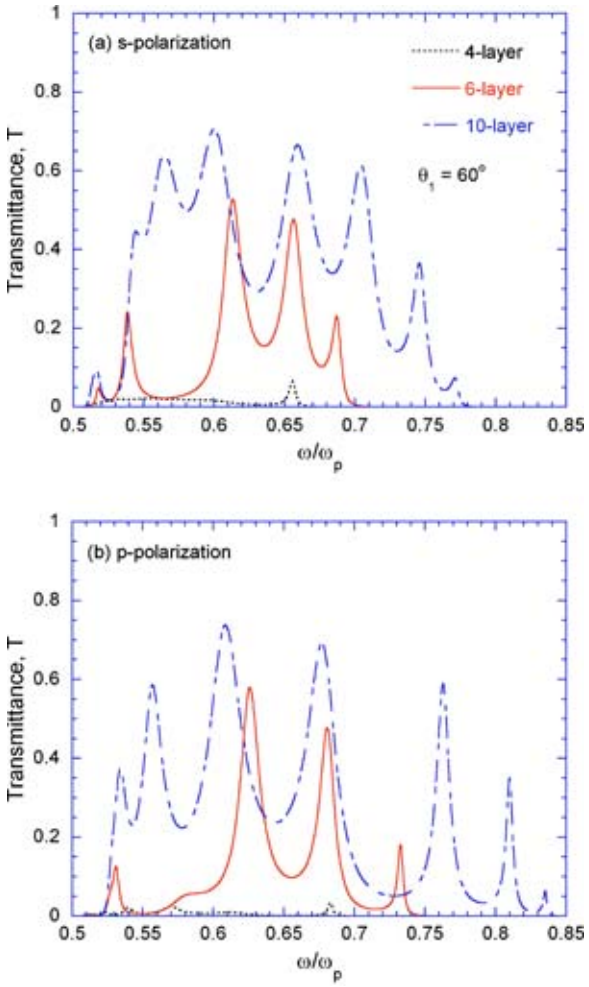

Fig. 6 The transmittance spectra of multilayer structures with different numbers of layers at an incidence angle θ_1=60 deg: (*a*) *s* polarization and (*b*) *p* polarization. Parameters for calculating $\varepsilon(\omega)$ and $\mu(\omega)$ of the NIM are the same as those used for Fig. 5. In each multilayer structure a VG and a NIM layer of the same thickness are alternately placed between the two end layers. The total thickness of the VGs is the same as the total thickness of the NIM layers and is set to $0.85\lambda_p$, the same as in Figs. 3 and 5.

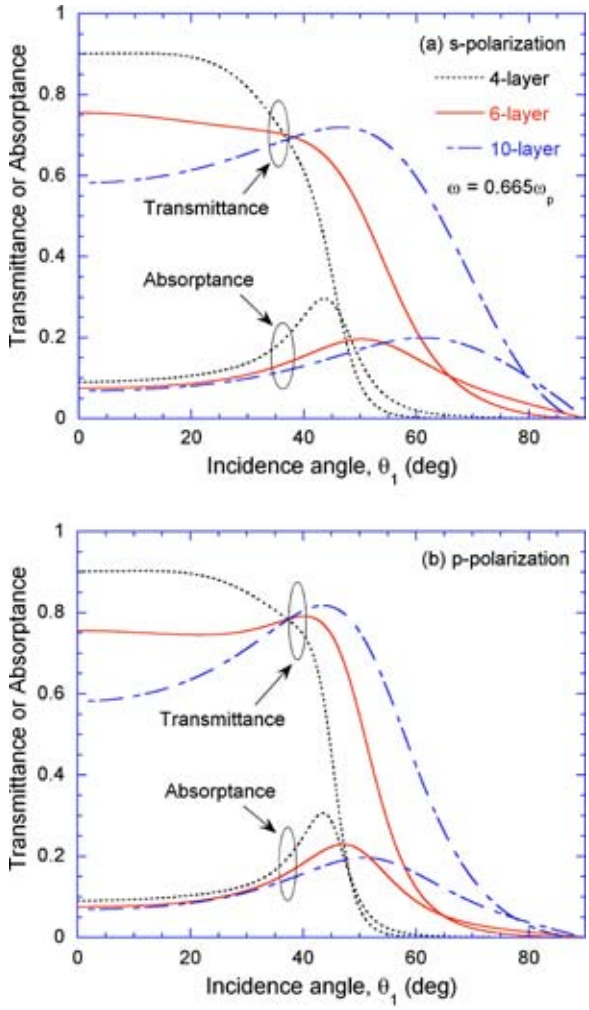

Fig. 7 The transmittance and absorptance of multilayer structures, with different number of layers, versus the incidence angle θ_1. (*a*) *s* polarization and (*b*) *p* polarization. The configurations are the same as corresponding ones in Fig. 6 and the frequency is fixed at ω=0.665ω_p.

ber of layers is increased. Increasing the magnitude of evanescent waves at the image plane is key to the improved image quality using NIM multilayer structures [28,29]. Contrary to intuition, however, the enhancement in transmission is not necessarily due to a reduction of absorption by subdivision of the NIM layers. It can be seen from Fig. 7 that the absorptance increases with the number of layers at large incidence angles. Hence, the enhanced transmission of evanescent waves is associated with a reduction of reflection.

4 Conclusions

The phenomenon of photon tunneling by using NIM layers in a multilayer structure is investigated. Enhanced energy transmission via photon tunneling is found when surface or bulk polaritons are excited. The enhancement depends on the thickness of the NIM layer that should be tuned to satisfy the phase matching condition between VG and NIM layer. Furthermore, it is found that subdividing the NIM layers into many thinner layers and placing them alternately with VGs can greatly enhance energy transmission, especially at large incidence angles. The enhancement is attributed to the coupling of surface or bulk polaritons that reinforce the EM fields in the structure. By coupling more photons into the structure, a large increase in the transmission of evanescent waves and a reduction of the reflectance are observed using multilayer structures. Devices that depend on photon tunneling to transfer energy or optical signals have wide applications in microscale energy conversion and optical communication. The result of the present study may benefit future applications of NIMs.

Acknowledgment

This work was supported by the National Science Foundation through Grants No. CTS-0082969, No. CTS-0236831, and No. CTS-0327117. Thanks to Keunhan Park and Bong Jae Lee for helpful comments.

Nomenclature

c = speed of light in vacuum, 2.998×10^8 m/s
d = layer thickness, m
F = fractional area of the unit cell occupied by the split ring
i = $\sqrt{-1}$
k_x = wave-vector component in the x direction, 1/m
k_z = wave-vector component in the z direction, 1/m
$\mathbf{M}$ = transfer matrix

n = real part of $\tilde{n}$
$\tilde{n}$ = complex refractive index
R = reflectance
T = transmittance

Greek Symbols

β = evanescent wave-decaying factor, 1/m
γ = damping term, rad/s
ε = relative (electric) permittivity
θ_1 = angle of incidence
κ = imaginary part of $\tilde{n}$
λ_p = wavelength corresponding to the plasma frequency, m
μ = relative (magnetic) permeability
ω = angular frequency, rad/s
ω_0 = resonance frequency, rad/s
ω_p = plasma frequency, rad/s
ω_{spp} = surface plasmon polariton resonance frequency, rad/s

References

[1] Cravalho, E. G., Tien, C. L., and Caren, R. P., 1967, "Effect of Small Spacing on Radiative Transfer Between Two Dielectrics," ASME J. Heat Transfer, **89**, pp. 351–358.
[2] Tien, C. L., and Cunnington, G. R., 1973, "Cryogenic Insulation Heat Transfer," Adv. Heat Transfer, **9**, pp. 349–417.
[3] Reddick, R. C., Warmack, R. J., and Ferrell, T. J., 1989, "New Form of Scanning Optical Microcopy," Phys. Rev. B, **39**, pp. 767–770.
[4] Kawata, S., 2001, "Near-Field Microscope Probes Utilizing Surface Plasmon Polaritons," in *Near-Field Optics and Surface Plasmon Polaritons*, S. Kawata, ed., Springer-Verlag, Berlin, pp. 15–27.
[5] Whale, M. D., and Cravalho, E. G., 2002, "Modeling and Performance of Microscale Thermophotovoltaic Energy Conversion Devices," IEEE Trans. Energy Convers., **17**, pp. 130–142.
[6] Mulet, J. P., Joulain, K., Carminati, R., and Greffet, J.-J., 2002, "Enhanced Radiative Heat Transfer at Nanometric Distance," Microscale Thermophys. Eng., **6**, pp. 209–222.
[7] Narayanaswamy, A., and Chen, G., 2003, "Surface Modes for Near Field Thermophotovoltaics," Appl. Phys. Lett., **82**, pp. 3544–3546.
[8] Veselago, V. G., 1968, "The Electrodynamics of Substances With Simultaneously Negative Values of ε and μ," Sov. Phys. Usp., **10**, pp. 509–514.
[9] Pendry, J. B., Holden, A. J., Stewart, W. J., and Youngs, I., 1996, "Extremely Low Frequency Plasmons in Metallic Mesostructures," Phys. Rev. Lett., **76**, pp. 4773–4776.
[10] Pendry, J. B., Holden, A. J., Rubbins, D. J., and Stewart, W. J., 1999, "Magnetism from Conductors and Enhanced Nonlinear Phenomena," IEEE Trans. Microwave Theory Tech., **47**, pp. 2075–2084.
[11] Shelby, R. A., Smith, D. R., and Schultz, S., 2001, "Experimental Verification of a Negative Index of Refraction," Science, **292**, pp. 77–79.
[12] Pendry, J. B., 2000, "Negative Refraction Makes a Perfect Lens," Phys. Rev. Lett., **85**, pp. 3966–3969.
[13] Gerardin, J., and Lakhtakia, A., 2002, "Negative Index of Refraction and Distributed Bragg Reflections," Microwave Opt. Technol. Lett., **34**, pp. 409–411.
[14] Engheta, N., 2002, "An Idea for Thin Subwavelength Cavity Resonators Using Metamaterials With Negative Permittivity and Permeability," IEEE Antennas Wireless Propag. Lett., **1**, pp. 10–13.
[15] Qing, D.-K., and Chen, G., 2004, "Enhancement of Evanescent Waves in Waveguides Using Metamaterials of Negative Permittivity and Permeability," Appl. Phys. Lett., **84**, pp. 669–671.
[16] Zhang, Z. M., and Fu, C. J., 2002, "Unusual Photon Tunneling in the Presence of a Layer With a Negative Refractive Index," Appl. Phys. Lett., **80**, pp. 1097–1099.
[17] Fu, C. J., and Zhang, Z. M., 2003, "Transmission Enhancement Using a Negative-Refraction Layer," Microscale Thermophys. Eng., **7**, pp. 221–234.
[18] Zhang, Z. M., and Park, K., 2004, "On the Group Front and Group Velocity in a Dispersive Medium Upon Refraction From a Nondispersive Medium," J. Heat Transfer, **126**, pp. 244–249.
[19] Foteinopoulou, S., Economou, E. N., and Soukoulis, C. M., 2003, "Refraction in Media With a Negative Refractive Index," Phys. Rev. Lett., **90**, pp. 107402/1–4.
[20] Parazzoli, C. G., Greegor, R. B., Li, K., Koltenbah, B. E. C., and Tanielian, M., 2003, "Experimental Verification and Simulation of Negative Index of Refraction Using Snell's Law," Phys. Rev. Lett., **90**, pp. 107401/1–4.
[21] Houck, A. A., Brock, J. B., and Chuang, I. L., 2003, "Experimental Observations of a Left-Handed Material That Obeys Snell's Law," Phys. Rev. Lett., **90**, pp. 137401/1–4.
[22] Smith, D. R., Schurig, D., Rosenbluth, M., Schultz, S., Ramakrishna, S. A., and Pendry, J. B., 2003, "Limitations on Subdiffraction Imaging With a Negative Refractive Index Slab," Appl. Phys. Lett., **82**, pp. 1506–1508.
[23] Yen, T. J., Padilla, W. J., Fang, N., Vier, D. C., Smith, D. R., Pendry, J. B., Basov, D. N., and Zhang, X., 2004, "Terahertz Magnetic Response From Artificial Materials," Science, **303**, pp. 1494–1496.
[24] Born, M., and Wolf, E., 1999, *Principles of Optics*, 7th Edition, Cambridge University Press, Cambridge, UK, pp. 54–74.
[25] Kong, J. A., 1990, *Electromagnetic Wave Theory*, 2nd Edition, Wiley, New York, pp. 126–138.
[26] Yeh, P., 1988, *Optical Waves in Layered Media*, Wiley, New York, pp. 102–113.
[27] Zhang, Z. M., Fu, C. J., and Zhu, Q. Z., 2003, "Optical and Thermal Radiative Properties of Semiconductors Related to Micro/Nanotechnology," Adv. Heat Transfer, **37**, pp. 179–296.
[28] Ramakrishna, S. A., Pendry, J. B., Wiltshire, M. C. K., and Stewart, W. J., 2003, "Imaging the Near Field," J. Mod. Opt., **50**, pp. 1419–1430.
[29] Gao, L., and Tang, C. J., 2004, "Near-Field Imaging by a Multilayer Structure Consisting of Alternate Right-Handed and Left-Handed Materials," Phys. Lett. A, **322**, pp. 390–395.
[30] Zhang, Z. M., 1997, "Reexamination of the Transmittance Formulae of a Lamina," J. Heat Transfer, **119**, pp. 645–647.
[31] Raether, H., 1988, *Surface Plasmons on Smooth and Rough Surfaces and on Gratings*, Springer-Verlag, Berlin, Chap. 2.
[32] Ruppin, R., 2000, "Surface Polaritons of a Left-Handed Medium," Phys. Lett. A, **277**, pp. 61–64.
[33] Park, K., Lee, B. J., Fu, C. J., and Zhang, Z. M., 2005, "Study of the Surface and Bulk Polaritons With a Negative Index Metamaterial," J. Opt. Soc. Am. B, **22**, pp. 1016–1023.
[34] Kumar, A. R., Boychev, V. A., Zhang, Z. M., and Tanner, D. B., 2000, "Fabry-Perot Resonators Built With $YBa_2Cu_3O_{7-\delta}$ Films on Si Substrates," ASME J. Heat Transfer, **122**, pp. 785–791.
[35] Ruppin, R., 2001, "Surface Polaritons of a Left-Handed Material Slab," J. Phys.: Condens. Matter, **13**, pp. 1811–1819.
[36] Buckman, B., 1992, *Guided Wave Photonics*, Sauders College Publishing, New York, pp. 35–85.
[37] Yeh, P., 1985, "Resonant Tunneling of Electromagnetic Radiation in Superlattice Structures," J. Opt. Soc. Am. A, **2**, pp. 568–571.

Journal of Heat Transfer

Technical Briefs

Natural Convection in a Vertical Microchannel

Cha'o-Kuang Chen
e-mail: ckchen@mail.ncku.edu.tw

Huei Chu Weng

Department of Mechanical Engineering, National Cheng Kung University, Tainan 701, Taiwan, Republic of China

It is highly desirable to understand the fluid flow and the heat transfer characteristics of buoyancy-induced micropump and microheat exchanger in microfluidic and thermal systems. In this study, we analytically investigate the fully developed natural convection in an open-ended vertical parallel-plate microchannel with asymmetric wall temperature distributions. Both of the velocity slip and the temperature jump conditions are considered because they have countereffects both on the volume flow rate and the heat transfer rate. Results reveal that in most of the natural convection situations, the volume flow rate at microscale is higher than that at macroscale, while the heat transfer rate is lower. It is, therefore, concluded that the temperature jump condition induced by the effects of rarefaction and fluid-wall interaction plays an important role in slip-flow natural convection.
[DOI: 10.1115/1.1999651]

Keywords: Natural Convection, Microfluidics, Micropump, Microheat Exchanger

Introduction

Microfluidic systems typically have characteristic lengths of the order of 1–100 μm. Rarefied gaseous flow in these microgeometries has frequently been observed. The Knudsen number Kn characterizing the effect of rarefaction is defined as the ratio of the molecular mean free path λ to the characteristic length. A classification of different flow regimes based on Kn is given in Schaaf & Chambre [1]. Here, we concern ourselves with a rarefied gas considered near the continuum region in the range $10^{-2} < \mathrm{Kn} < 10^{-1}$, the so-called slip flow. Using the Navier–Stokes equations, Arkilic et al. [2] and Liu et al. [3] found that the theoretical results for some microflows would fit the experimental data as the slip-flow condition induced by rarefaction effect is considered. More recently, Larrode et al. [4] and Yu and Ameel [5] considered the temperature jump condition and found that the effect of fluid-wall interaction is also important.

Natural convection of an enclosed fluid has received considerable attention in recent years due to its wide applications in engineering problems. Earlier work on this problem in isothermal parallel-plate channels was experimentally reported by Elenbaas [6]. Further investigations have been carried out for different thermal boundary conditions. An excellent review was given in the book Gebhart et al. [7]. All of the previous investigations were conducted at macroscale. A study on natural convection flow in microscale systems should be studied extensively.

The purpose of present study is to analyze the effects of rarefaction and fluid-wall interaction on steady fully developed natural convection in vertical parallel-plate microchannels. It should be noted that Aung [8] has studied the macroscale problem. Such type of study may be applicable to the designs of micropumps and microheat exchangers.

Problem Formulations

Consider a vertical parallel-plate microchannel of a width b, whose temperatures of the hotter and cooler plates are T_1 and T_2, respectively. Both ends of the channel are open to the ambient of density ρ_0 as shown in Fig. 1. Let x and y denote the usual rectangular coordinates, and let u and v denote the components of velocity field. Here constant physical properties are considered, internal heat generations are neglected, and the effect of compressibility for this typically low-speed microflow is negligible [9]. Under the usual Boussinesq approximation, the boundary layer equations described by continuity equation, momentum equation, and energy equation for two-dimensional steady flow with gravitational acceleration g are [10]

$$\frac{\partial u}{\partial x} + \frac{\partial v}{\partial y} = 0, \tag{1}$$

$$\rho_0\left(u\frac{\partial u}{\partial x} + v\frac{\partial u}{\partial y}\right) = -\frac{d\hat{p}}{dx} + \rho_0 g\beta(T - T_0) + \mu\frac{\partial^2 u}{\partial y^2}, \tag{2}$$

$$\rho_0 c\left(u\frac{\partial T}{\partial x} + v\frac{\partial T}{\partial y}\right) = k\frac{\partial^2 T}{\partial y^2} + \mu\left\{2\left[\left(\frac{\partial u}{\partial x}\right)^2 + \left(\frac{\partial v}{\partial y}\right)^2\right] + \left(\frac{\partial u}{\partial y} + \frac{\partial v}{\partial x}\right)^2\right\}, \tag{3}$$

where β is the thermal expansion coefficient, μ is the dynamic viscosity, c is the specific heat, k is the thermal conductivity, $\hat{p}$ is the pressure defect, T is the temperature, and T_0 is the free stream temperature.

Now we assume that the hydrodynamically fully developed condition $(\partial u/\partial x = 0, v = 0, d\hat{p}/dx = 0)$ can be achieved after the fluid reaches the position $y = l^*$. The dimensionless governing equations are

Contributed by the Heat Transfer Division for publication in the JOURNAL OF HEAT TRANSFER. Manuscript received by the Heat Transfer Division November 24, 2003; revision received April 20, 2005. Review conducted by: B. Farouk.

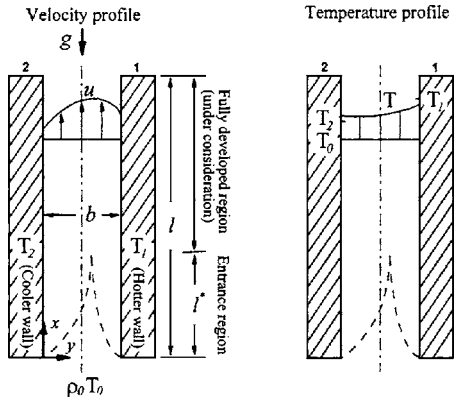

Fig. 1 Geometric sketch and parameters of natural convection in the microchannel

$$\frac{d^2U}{dY^2} = -\Theta, \tag{4}$$

$$\mathrm{Ra}U\frac{\partial\Theta}{\partial X} = \frac{\partial^2\Theta}{\partial Y^2} + \mathrm{Br}\left(\frac{dU}{dY}\right)^2, \tag{5}$$

where

$$X = \frac{x}{b}, \quad Y = \frac{y}{b}, \quad U = \frac{u}{U_c}, \quad \Theta = \frac{T - T_0}{T_1 - T_0},$$
$$\mathrm{Ra} = \frac{\rho_0 c U_c b}{k}, \quad \mathrm{Br} = \frac{\mu U_c^2}{k(T_1 - T_0)}, \quad U_c = \frac{\rho_0 g\beta(T_1 - T_0)b^2}{\mu}. \tag{6}$$

A solution of Eq. (4) in the form $U(Y)$ is only possible if Θ is a function of Y position only, i.e., $\partial\Theta/\partial X = 0$. It implies that the assumption of a hydrodynamically fully developed natural convection necessarily means that the natural convection is also thermally fully developed. Moreover, Br is known as the Brinkman number and is a characteristic dimensionless parameter for viscous dissipation. For rarefied gaseous micronatural convection (typically low-speed flow and low-Prandtl-number fluid), viscous dissipation term is negligible relative to the $d^2\Theta/dY^2$ term. The modified dimensionless energy equation then becomes

$$\frac{\partial^2\Theta}{\partial Y^2} = 0. \tag{7}$$

The boundary conditions which describe velocity slip and temperature jump conditions at the fluid-wall interface are [11–13]

$$U(0) = \beta_v \mathrm{Kn}\frac{dU(0)}{dY}, \quad U(1) = -\beta_v \mathrm{Kn}\frac{dU(1)}{dY},$$
$$\Theta(0) = \xi + \beta_v \mathrm{Kn}\, In\frac{\partial\Theta(0)}{\partial Y}, \quad \Theta(1) = 1 - \beta_v \mathrm{Kn}\, In\frac{\partial\Theta(1)}{\partial Y}, \tag{8}$$

where

$$\beta_v = \frac{2 - F_v}{F_v}, \quad \beta_t = \frac{2 - F_t}{F_t}\frac{2\gamma_s}{\gamma_s + 1}\frac{1}{\mathrm{Pr}}, \quad \mathrm{Kn} = \frac{\lambda}{b}$$
$$In = \frac{\beta_t}{\beta_v}, \quad \xi = \frac{T_2 - T_0}{T_1 - T_0}. \tag{9}$$

Here γ_s is the ratio of specific heats, Pr is the Prandtl number, F_v and F_t are the tangential momentum and thermal accommodation coefficients, respectively, and range from near 0 to 1, λ is the molecular mean free path, Kn is the Knudsen number, In is the fluid-wall interaction parameter, and ξ is the wall-ambient temperature difference ratio. Referring to the values of F_v and F_t given in Eckert and Drake [11] and Goniak and Duffa [13], the value of β_v is near unity, and the value of β_t ranges from near 1 to more than 100 for actual wall surface conditions and is near 1.667 for many engineering applications, corresponding to $F_v = 1$, $F_t = 1$, $\gamma_s = 1.4$, and $\mathrm{Pr} = 0.7$ ($\beta_v = 1, \beta_t = 1.667$). Equations (4) and (7) subjected to the boundary conditions (8) have the following analytical solutions:

$$\Theta(Y) = A_0 + A_1 Y, \tag{10}$$

$$U(Y) = B_0 + B_1 Y - \frac{A_0}{2}Y^2 - \frac{A_1}{6}Y^3, \tag{11}$$

where

$$A_0 = \xi + \frac{\beta_v \mathrm{Kn}\, In(1 - \xi)}{1 + 2\beta_v \mathrm{Kn}\, In}, \quad A_1 = \frac{1 - \xi}{1 + 2\beta_v \mathrm{Kn}\, In},$$
$$B_0 = \beta_v \mathrm{Kn}\left[\frac{1}{2}A_0 + \frac{(1 + 3\beta_v \mathrm{Kn})}{6(1 + 2\beta_v \mathrm{Kn})}A_1\right], \quad B_1 = \frac{1}{2}A_0 + \frac{(1 + 3\beta_v \mathrm{Kn})}{6(1 + 2\beta_v \mathrm{Kn})}A_1. \tag{12}$$

Two important parameters for buoyancy-induced microflow and microheat transfer are the volume flow rate m and heat transfer rate q, respectively. The dimensionless volume flow rate and heat transfer rate which is expressed as the Nusselt number are

$$M = \frac{m}{bU_c} = \int_0^1 U dY = B_0 + \frac{B_1}{2} - \frac{A_0}{6} - \frac{A_1}{24}, \tag{13}$$

$$\mathrm{Nu} = \frac{qb}{(T_1 - T_0)k} = \frac{d\Theta(0)}{dY} = \frac{d\Theta(1)}{dY} = A_1. \tag{14}$$

Results and Discussion

The present parametric study has been performed over the reasonable ranges $0 \leqslant \beta_v \mathrm{Kn} \leqslant 0.1$ and $0 \leqslant In \leqslant 10$. The product $\beta_v \mathrm{Kn}$ represents a measure of the departure from the continuum regime, while In represents a property of the fluid-wall interaction. The select reference values of $\beta_v \mathrm{Kn}$ and In for the analysis are 0.05 and 1.667, respectively. In Figs. 2–4, we check the results with those for the case $\beta_v \mathrm{Kn} = 0$ obtained by Aung [8] and with those for a physically impossible case $In = 0$ ($F_t = 2$). Note that the solutions (10) and (11) for $\beta_v \mathrm{Kn} = 0$ can reduce to

$$\Theta(Y) = (1 - \xi)Y + \xi, \tag{15}$$

$$U(Y) = \frac{(\xi - 1)}{6}Y^3 - \frac{\xi}{2}Y^2 + \frac{(2\xi + 1)}{6}Y. \tag{16}$$

Equations (15) and (16) are identical to the analytical expressions obtained by Aung [8].

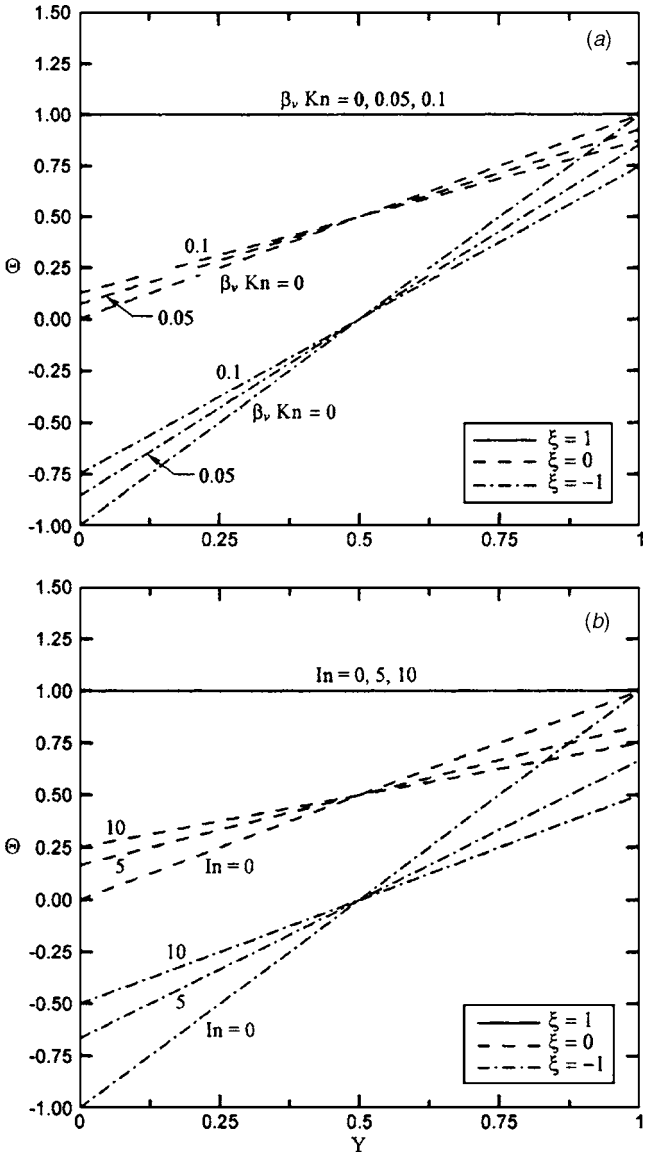

Fig. 2 Temperature distribution for (*a*) different values of β_vKn with *In*=1.667, (*b*) different values of *In* with β_vKn=0.05

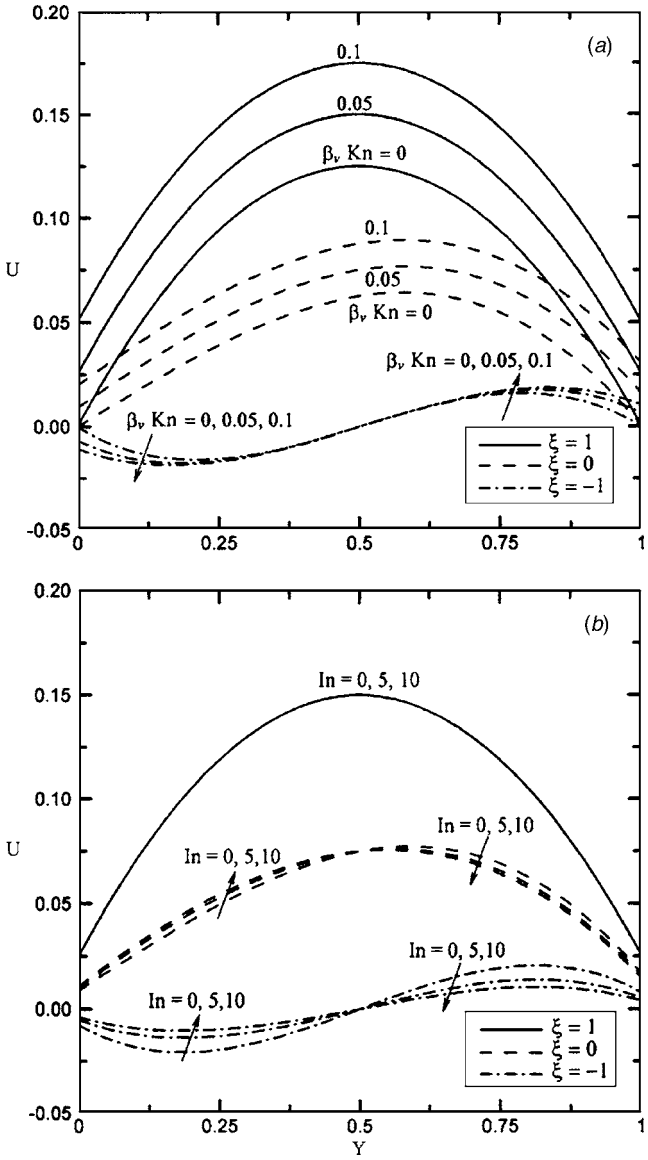

Fig. 3 Velocity distribution for (*a*) different values of β_vKn with *In*=1.667, (*b*) different values of *In* with β_vKn=0.05

Figure 2 shows that, except for the case of symmetric heating (ξ=1), the increase in β_vKn or in *In* leads to large temperature jump and small temperature variation with *Y*. All of the effects increase with the decrease of the wall-ambient temperature difference ratio. In Fig. 3, it is found that the increase in $\beta_v Kn$ leads to the increase in $|U|$. The parameter *In* also influences the flow excluding the case ξ=1. For ξ=0 and −1, the effect of fluid-wall interaction is to horizontally shift the velocity profile to the cooler-wall side and to reduce the fluid velocity, respectively. It is worth noting that as ξ increases, the slip induced by the rarefaction effect increases, but the slip induced by fluid-wall interaction effect decreases.

From Fig. 4(*a*), it is found that the volume flow rate *M* is a monotone increasing function of β_vKn excluding the case ξ=−1. Furthermore, such rarefaction effect increases with the increase of the value of ξ. It should be noted that as shown in Fig. 3(*b*), the value of $\int_0^1 UdY$ appears to keep a constant for an assigned value of *In*. The parameter *In*, therefore, exerts no influence on the volume flow rate *M*. We may recall that the physically impossible case *In*=0 only provides the comparative base for the effect of fluid-wall interaction. From Fig. 4(*b*), we may, therefore, conclude that, except for the case ξ=1, the heat transfer rate obviously decreases with the increases of the values of β_vKn and *In*. Moreover, the effects increase with the decrease of the wall-ambient temperature difference ratio.

Conclusions

An analytical study on the slip-flow natural convection in a parallel-plate microchannel with uniform but not necessarily symmetric wall temperature distributions has been made. Results of present study show that the effects of rarefaction and fluid-wall interaction are important and should be considered for micronatural convective flow and heat transfer problems. Such effects may result in the increase of the volume flow rate and the decrease of the heat transfer rate. As the wall-ambient temperature difference ratio decreases, the effects on the volume flow decreases and those on the heat transfer rate increase. The present analytical studies help the understanding of fluid transport and heat transfer behavior in microchannels and benefit the design of micropumps and microheat exchangers.

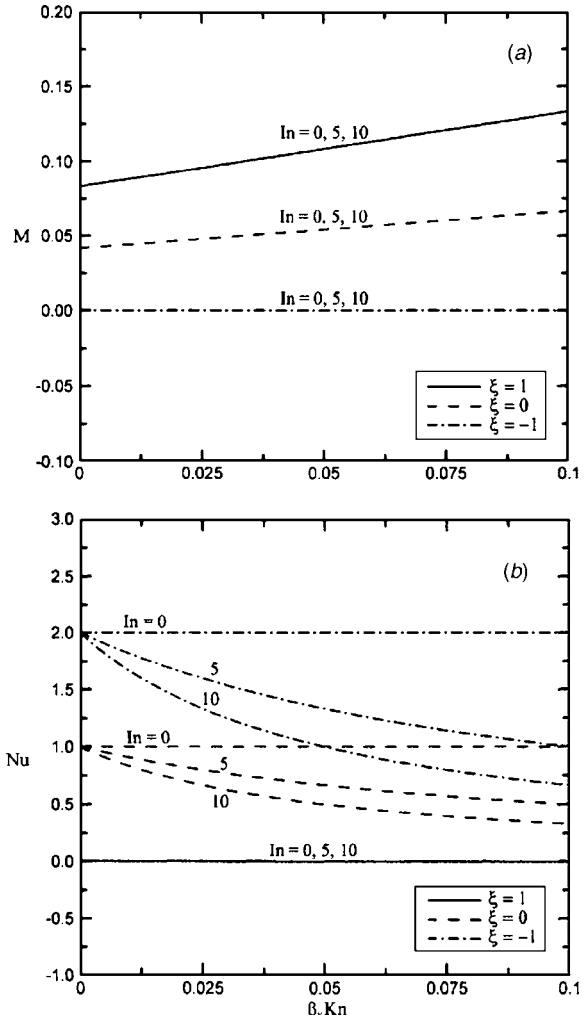

Fig. 4 (*a*) Volume flow rate, (*b*) heat transfer rate versus β_vKn for different values of *In*

Nomenclature

b = channel width
Br = Brinkman number, $\mu U_c^2/k(T_1-T_0)$
c, c_v = specific heats at constant pressure and constant volume, respectively
F_t, F_v = thermal and tangential momentum accommodation coefficients, respectively
g = gravitational acceleration
In = fluid-wall interaction parameter, β_t/β_v
k = thermal conductivity
Kn = Knudsen number, λ/b
ℓ = channel length
ℓ^* = entrance length (Fig. 1)
m = volume flow rate
M = dimensionless volume flow rate, Eq. (13)
Nu = dimensionless heat transfer rate (Nusselt number), Eq. (13)
p = pressure
$\hat{p}$ = pressure defect, $p-p_h$
p_h = hydrostatic pressure
Pr = Prandtl number, $\mu c/k$
q = heat transfer rate
Ra = Rayleigh number, $\rho_0 c U_c b/k$
T = temperature
u,v = velocity components in x,y directions
U = dimensionless velocity component in x direction, Eq. (6)
U_c = characteristic velocity, Eq. (6)
x,y = rectangular coordinate system
X,Y = dimensionless rectangular coordinate system, Eq. (6)

Greek Letters

β = thermal expansion coefficient
β_t, β_v = dimensionless variables, Eq. (9)
γ_s = ratio of specific heats, c/c_v
λ = molecular mean free path
μ = dynamic viscosity
Θ = dimensionless temperature, Eq. (6)
ξ = wall-ambient temperature difference ratio, Eq. (9)
ρ = density

Subscripts

1 = hotter-wall values
2 = cooler-wall values
0 = inlet properties of the fluid

References

[1] Schaaf, S. A., and Chambre, P. L., 1961, *Flow of Rarefied Gases*, Princeton University Press, Princeton.
[2] Arkilic, E. B., Breuer, K. S., and Schmidt, M. A., 1994, "Gaseous Flow in Microchannels, Application of Micro-Fabrication to Fluid Mechanics," ASME FED, **197**, pp. 57–66.
[3] Liu, J. Q., Tai, Y. C., and Ho, C. M., 1995, "MEMS for Presure Distribution Studies of Gaseous Flow in Microchannels," *Proceedings, IEEE Micro Electro Mechanical Systems*, pp. 209–215.
[4] Larrode, F. E., Housiadas, C., and Drossinos, Y., 2000, "Slip-Flow Heat Transfer in Circular Tubes," Int. J. Heat Mass Transfer, **43**, pp. 2669–2680.
[5] Yu, S., and Ameel, T. A., 2001, "Slip-Flow Heat Transfer in Rectangular Microchannels," Int. J. Heat Mass Transfer, **44**, pp. 4225–4234.
[6] Elenbaas, W., 1942, "Heat Dissipation of Parallel Plates by Free Convection," Physica (Amsterdam) **9**, pp. 1–28.
[7] Gebhart, B., Jaluria, Y., Mahajan, R. L., and Sammakia, B., 1988, *Buoyancy-Induced Flows and Transport*, Hemisphere, New York, Chap. 14.
[8] Aung, W., 1972, "Fully Developed Laminar Free Convection Between Vertical Plates," Int. J. Heat Mass Transfer, **15**, pp. 1577–1580.
[9] Kavehpour, H. P., Faghri, M., and Asako, Y., 1997, "Effects of Compressibility and Rarefaction on Gaseous Flows in Microchannels," Numer. Heat Transfer, Part A, **32**, pp. 677–696.
[10] Bejan, A., 1995, *Convection Heat Transfer*, Wiley, New York, Chap. 4.
[11] Eckert, E. R. G., and Drake, R. M., Jr., 1972, *Analysis of Heat and Mass Transfer*, McGraw–Hill, New York, Chap. 11.
[12] Rohsenow, W. M., and Hartnett, J. P., 1973, *Handbook of Heat Transfer*, McGraw–Hill, New York, Chap. 9.
[13] Goniak, R., and Duffa, G., 1995, "Corrective Term in Wall Slip Equations for Knudsen Layer," J. Thermophys. Heat Transfer **9**, pp. 383–384.

New Method to Determine the Velocities of Particles on a Solid Propellant Surface in a Solid Rocket Motor

Yumin Xiao

R. S. Amano
Fellow ASME
e-mail: amano@uwm.edu

Mechanical Engineering Department, University of Wisconsin-Milwaukee, Milwaukee, WI 53211

Timin Cai

Jiang Li

College of Astronautics, Northwestern Polytechnical University, Xi'an, Shaanxi Province, 710072 People's Republic of China

Use of aluminized composite solid propellants and submerged nozzles are common in solid rocket motors (SRM). Due to the generation of slag, which injects into a combusted gas flow, a two-phase flow pattern is one of the main flow characteristics that need to be investigated in SRM. Validation of two-phase flow modeling in a solid rocket motor combustion chamber is the focus of this research. The particles' boundary conditions constrain their trajectories, which affect both the two-phase flow calculations, and the evaluation of the slag accumulation. A harsh operation environment in the SRM with high temperatures and high pressure makes the measurement of the internal flow field quite difficult. The open literature includes only a few sets of experimental data that can be used to validate theoretical analyses and numerical calculations for the two-phase flow in a SRM. Therefore, mathematical models that calculate the trajectories of particles may reach different conclusions mainly because of the boundary conditions. A new method to determine the particle velocities on the solid propellant surface is developed in this study, which is based on the x-ray real-time radiography (RTR) technique, and is coupled with the two-phase flow numerical simulation. Other methods imitate the particle ejection from the propellant surface. The RTR high-speed motion analyzer measures the trajectory of the metal particles in a combustion chamber. An image processing software was developed for tracing a slug particle path with the RTR images in the combustion chamber, by which the trajectories of particles were successfully obtained.
[DOI: 10.1115/1.1999652]

Keywords: Solid Rocket Motor, X-Ray Real-Time Radiography Technology, Propulsion, Combustion

Introduction

Aluminized propellants and submerged nozzles have been used in most of the solid rocket motors (SRMs) to improve their performance. When these propellants burn, the aluminum powder melts and forms agglomerates on the propellant surface. These agglomerates move along the surface and frequently impinge onto the case wall, or may be ejected into the high-speed gas flow in the combustion chamber where they burn almost completely and result in the formation of liquid aluminum oxide (Al_2O_3) droplets. Slag is sometimes generated behind the submerged nozzle because the agglomerates flow along the case wall and enter the corner of the nozzle. The agglomerates may also be trapped in this region being pushed by the main stream in the combustion chamber. The entrapment depends on the droplet diameter, bulk density, velocity and radial distance from the motor centerline. In the space shuttle boosters and other larger-scale solid rocket motors the slag accumulation may reach 1000–1500 kg [1]. Thus, for SRM designers who wish to improve the motor's performance, it is important to predict a slag path by conducting a computer simulation analysis. Slag reduces the motor performance in the following cases:

(a) The slag is a material of neutral mass that reduces the motor's performance.
(b) The expulsion of the slag accumulated between the submerged portion of the nozzle and the motor aft dome may cause pressure perturbation in the combustion chamber, ejection-induced thrust, and side force, which may result in unstable motor operation or even a control failure.
(c) The slag accumulation forms a "melted pool" in the aft region of the motor, which may result in serious problems in the thermal protection of the insulator.

In the recent years, much research on slag accumulation was conducted because of the high cost of experiments and the harsh operation environmental condition. The research in this field focuses mostly on the development of a numerical simulation model for a slag motion. A numerical simulation for slag accumulation requires depth of the knowledge of particle size, particle dynamics through the combustion exhaust gas flows, surface tension of melted slag and adhesion to the motor walls, and coupled Lagrangian–Eulerian trajectory mechanisms.

Several researchers [2–6] conducted extensive research on slag accumulation and obtained some useful conclusions. As of today, a number of two-phase compressible viscous CFD codes have been developed to model internal flows in a SRM. Some examples are Thiokol's SHARP [7], SRA's CELMINT [8], and Aerospace's IS [9]. Several researchers [1,10,11] focused their research on slag behavior, including combustion, evaporation, and breakup. These studies have helped the aerodynamic engineers and designers better understand the mechanisms of a slag accumulation in a propellant combustion chamber. Because these researchers adopted different "capture rules," artificially chose the particles' ejection velocity, and selected different particle size distributions, their calculation results did not agree well with the experimental data.

Extensive literature exists on the distribution of Al_2O_3 particle size in the combustion products of aluminized composite propellants. Of all the reports, the experimental results by Braithwaite and Salita [12] cover a wide range, and the quenched propellant combustion bomb methodology provides a reasonable particle-size distribution. Their particle-size distribution function has been widely used.

In this study, two-phase flows are fully coupled in that the gas accelerates the droplets, expending momentum and energy to do so. Thus, the best two-phase flow modeling must be coupled to the gas phase and include the energy equation. Usually, calculations of particle-gas flow can be performed in two ways: (1) the Lagrangian method, in which particles are considered as a dispersed phase and each particle or particle group is followed in the Lagrangian coordinate system; and (2) the Eulerian method, in which both gas and particles are considered as continuous phases and can be treated in an integrated method.

The above discussion shows that numerical simulation is an

Contributed by the Heat Transfer Division for publication in the JOURNAL OF HEAT TRANSFER. Manuscript received by the Heat Transfer Division March 5, 2003; revision received April 19, 2005. Review conducted by: B. Farouk.

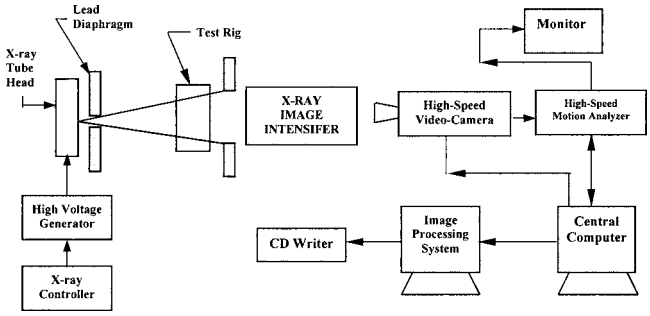

Fig. 1 Layout of the real-time x-ray radiography system

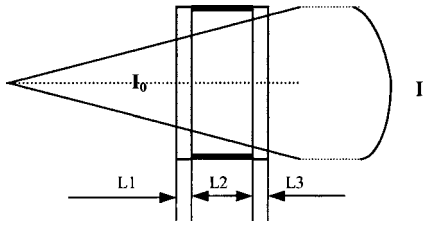

Fig. 2 Layout of x-ray imaging

efficient tool to study the particle-laden flow in a SRM. The key issue is to find an experimental method to provide data for the dependent parameters in the mathematical model to validate the simulation results. The x-ray real-time radiography (RTR), a relatively reliable technology developed in the 1980s, provides a possible way to improve this research. This paper presents a new method to determine a particle's initial velocity on the burning surface of a solid propellant, excluding the effects of size distribution, combustion, and breakup.

Radiography System

Char et al. [13] discussed the details of a real-time x-ray radiography system, and thus this section provides only a brief summary of the features that differ from those used by Char et al. Figure 1 shows a schematic diagram of the x-ray RTR system. The x-ray head produces a continuous stream of x rays. The x rays pass through an opening in the first of two lead diaphragms; attenuation occurs as the x rays encounter the test motor and the particles in the combustion chamber. The attenuated x rays pass through an opening in a second lead diaphragm on the other side of the test rig before reaching the image intensifier. The x ray signal causes fluorescence of cesium iodide on the receiving screen of the image intensifier. The image intensifier transforms the x ray image into a visible-light image with a time constant of less than 1 μs. A high-speed video camera (up to 600 fps) records this visible image, which is later analyzed with the image-processing system.

Since the attenuation coefficient of the gas for x rays is much less than that of metal particles, the attenuation of x rays by the gas is mostly ignored. The attenuation of a single particle to an x ray is limited and may not be identified by the x ray intensifier. Therefore, we can only observe those particles that are large enough to allow the x ray intensifier to identify attenuation to x rays. In addition, the x rays have to pass through the walls with a relatively low attenuation coefficient to x rays, but the motor's wall thickness is much larger than the particle size. The intensity variation caused by large particles with a high attenuation coefficient to x rays will, then, be weakened and the image may not be very clear. In this experimental system, the wall is made of an aluminum plate 10 mm thick and the tube voltage is 150 kV. The terms I_0, I_1, and I_2 are, respectively, the x-ray intensity from the x-ray tube head, the x-ray intensities before penetrating the aluminum plate in the combustion chamber, and after passing through the second aluminum plate.

Figure 2 shows the layout of x-ray imaging. From Beer's law [13] the following relation can be obtained:

$$I_1 = I_0 \exp(-\lambda_1 L_1) \tag{1}$$

$$I_2 = I_1 \exp(-\lambda_2 L_3) \tag{2}$$

where $L_1 = L_3 = 0.01$ m, $L_2 = 0.05$ m; λ is the attenuation coefficient, for aluminum $\lambda_1 = \lambda_2 = 0.15$.

Since the gray ranges for a digital image are 0 to 256, the smallest size of a particle to be identified on the image should satisfy the following relationship:

$$|\Delta I| \geqslant \frac{I_2}{256} \tag{3}$$

From Beer's law we have

$$dI = -I_0 \lambda \exp\left(-\sum_{i=1}^{n} \lambda_i L_i\right) dL$$

$$\Delta I = -I_0 \lambda \exp\left(-\sum_{i=1}^{n} \lambda_i L_i\right) \Delta L \tag{4}$$

and

$$\Delta L_{\min} = -\frac{\Delta I_{\min}}{I_0 \lambda \exp\left(-\sum_{i=1}^{n} \lambda_i L_i\right)} \tag{5}$$

Table 1 shows the smallest particle sizes, which can be resolved by image processing for some metal materials.

It is well known that electronic noise will result in shadows on the image; in such a case, the abovementioned smallest size to be identified is no longer valid. From Eq. (5) we can see that the smallest dimension is in proportion to $\Delta I_{\min}$, and if the noise signal changes the intensity by $n/256$ in the background, the actual smallest size to be identified will be n times that of the expected value. Moreover, the identification of particles by the RTR technique is also constrained by the resolution of the receiving screen. To obtain better resolution on RTR images for small particles, a two-dimensional combustion chamber and a propellant model were designed into the experiment (details are presented in the following sections). As the particles with a small size flow with the gas, the slag that accumulates in the aft domain of the chamber is mainly formed by larger particles. Our focus therefore is on this group of particles. An attempt was made to improve the propellant sample and ensure that more particles would be recorded on the trace of an x ray.

Experimental Method

Based on the feasibility analyses described in the preceding section, measurement of the particle trajectory in a firing SRM combustion chamber can provide important data to validate a compute code. However, in an actual case, the operation is very difficult, and thus several issues need to be resolved, which are summarized as follows:

Table 1 The smallest size to be identified by image processing with tube voltage of 150 kV (units: μm)

Fe	Al	Cu	W	Pb
12.6	26.1	11.2	5.50	8.17

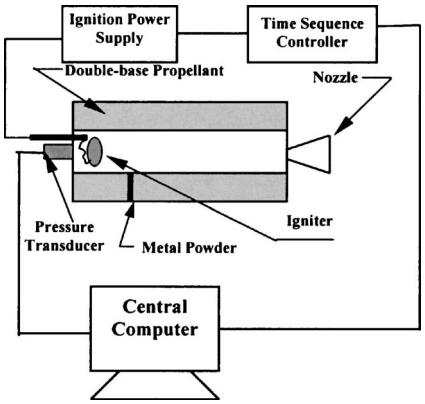

Fig. 3 Layout of test rig

(1) **Metal Power Injection System**: The injection of particles from a composite propellant burning surface should be imitated without scattering the particles throughout the entire chamber. If the particles are agitated, the position of a moving particle will be strongly affected by its neighbors. Therefore, aluminized composite propellant is not an appropriate candidate for the propellant model. For this reason, a double-base propellant was selected as the "driving force" of the metal powder. The imitation of power ejection can be accomplished by putting the metal powder into small holes or narrow slots.

Metal Particle Used for the Experiment: A material with a high attenuation coefficient to x rays should be selected as the test metal particles. Tungsten (W) powder is selected as the metal particle because of its high value of the attenuation coefficient.

Figure 3 shows the layout of the test rig. To control the ignition, a central computer sends signals to the time sequence controller, while the computer records the pressure signal. In order to enhance the identification of metal particles in RTR images, the following techniques are employed in the experiment:

(1) Particles are injected from a 0.5 mm slot created perpendicular to the main flow stream. In this way, the projections of particles at the same altitude can be located at the same pixel on the RTR image, and the attenuation to x rays at this position will be several times higher than that for a single particle, which can greatly enhance the image effect.
(2) The propellant sample injection path and the SRM combustion chamber can be assumed to be two-dimensional.
(3) A small focus should be used for the x ray generator to reduce the x ray intensity from the tube head, which will increase the ability to identify the details.

Figure 4 shows a sample model of propellant. To ensure two-dimensionality, all surfaces except the burning surface were insulated. Test conditions are listed as follows:

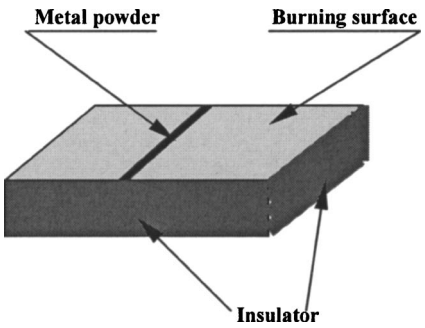

Fig. 4 Layout of propellant model

Combustion chamber:	$200\times60\times50$(mm)
Propellant sample model:	$150\times12\times50$(mm)
Slot:	0.5 mm
W powder:	75 μm in diameter
Designed operation pressure:	6×10^6 Pa
Tube voltage:	1.24×10^5 V
Recording speed:	250 frame/s
Tube current:	6 mA
Intensifier augment:	32
Combustion temperature:	2765 K
Burning rate of propellant:	8.3 mm/s
Propellant density:	2103 kg/m^3

The x rays were generated by a MG-421 x-ray tube head (product of Philips), and the dimensions of focus are 4.5×4.5 mm. The x-ray image intensifier was a PS93X intensifier that was produced by Precise Optics. The high-speed motion analyzer system includes a Hi-spec EM1012/2 motion analyzer and high-speed video camera with UVX high-augment lens (products of Kodak). Since the operation pressure is determined based on the dimensions of the chamber (the geometries of the chamber and the propellant are rectangular to ensure two-dimensional trajectory), only one operation condition was tested. Tungsten W powders with particle diameters of 75 and 5 μm were obtained commercially. Results from the 5 μm sample were not successful, and therefore, only results from the 75 μm powder are presented in this paper. As mentioned above, the time lag of the optic system is less than 1 μs; thus, the accuracy of measurement is determined by the resolution of RTR image to the spatial position. The measurement error in spatial position is ±1% (with calibration). The uncertainty of the system includes the time lag and spatial uncertainty. Time lag is a constant for the whole system and does not affect final data processing. While for the spatial uncertainty, a test was carried out determine the magnitude of vibration. With an operation pressure $(6\pm0.25)\times10^6$ Pa, the magnitude of vibration in the horizontal plane was less than 1 pixel. The position dispersion in RTR image is the main cause of the spatial uncertainty. Usually one position possesses 2–6 pixels in the horizontal and vertical directions, respectively. So the spatial uncertainties of the system are evaluated as ±1.45% and ±1.56% in the horizontal and vertical directions, respectively.

Image Processing

The x-ray image generation demonstrated that the image quality is mainly dominated by the x-ray intensity distribution on the receiver screen, but it is also affected by the following:

(1) The experimental system deviates from the ideal state. In an actual case, the x rays are not emitted from a single point, which may cause stripes or obscurity on the image. The Compton scattering induced by the motor walls and the propellant model will affect the intensity distribution seen on the screen. Environmental factors, such as the test rig vibration and voltage fluctuation, will also affect the image quality.
(2) The high-speed motion analyzer constrains the image resolution. For Hi-spec EM1012/2 motion analyzer, there are 239×192 pixels in one picture, and the memory of the processor and the high-speed data transportation constrain this index.

In view of the above factors, some processing of the initial images is necessary to improve the quality. Numerous kinds of commercial software are available for image processing; however, most of them focus on the artistic effects of a single picture and lack the capabilities to add images, to subtract background image,

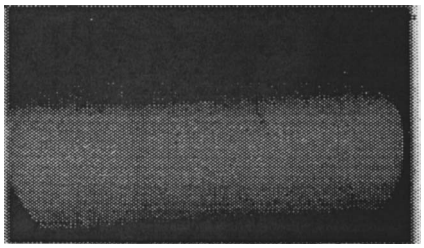

Fig. 5 Initial RTR image

or to filter time domain. As mentioned earlier, the particle trajectory is present in a series of motion pictures, so these x-ray images must be specially treated. Therefore, a RTR image processing code was developed with the following features: (1) background subtraction; (2) linear transformation of grays; (3) neighbor-domain averaging; (3) image enhancing; (4) time-domain filtering, and (5) image addition. Figure 5 shows an initial RTR image, and Fig. 6 shows the final particle trajectory after image processing.

Droplet Trajectory Modeling in SRM Combustion Chamber

In order to calculate the trajectory of a particle in the combustion chamber, the gas flow field must be simulated first. Because the mass fraction of particles in a two-phase flow is small, the effect of particles on the flow of gas phase is ignored. In the present calculation, the Navier–Stokes equations are solved by the AF method to calculate the flow field, and the Lagrangian method is used to model the particle trajectory. The motion equation of particle can be written as

$$m_p \frac{d\mathbf{V}_p}{dt} = \mathbf{F}_D + \mathbf{F}_w \tag{6}$$

and the position of the particle can be determined from

$$\mathbf{X}_p = \mathbf{X}_p^0 + \int_t^{t+\Delta t} \mathbf{V}_p dt \tag{7}$$

Assuming all particles are spherical, the drag force $\mathbf{F}_D$ is calculated from

$$\mathbf{F}_D = \frac{\pi}{8}\rho_g d_p^2 C_D |\mathbf{V}_g - \mathbf{V}_p|(\mathbf{V}_g - \mathbf{V}_p) \tag{8}$$

where C_D is determined by Wen and Yu [14]

$$C_D = \begin{cases} \dfrac{24}{\mathrm{Re}_d}[1 + 0.15\,\mathrm{Re}_d^{0.687}] & \mathrm{Re}_d \leqslant 1000 \\ 0.44 & \mathrm{Re}_d > 1000 \end{cases} \tag{9}$$

where the Reynolds Number Re_d is defined as

$$\mathrm{Re}_d = \frac{\rho_g |\mathbf{V}_g - \mathbf{V}_p| d_p}{\mu} \tag{10}$$

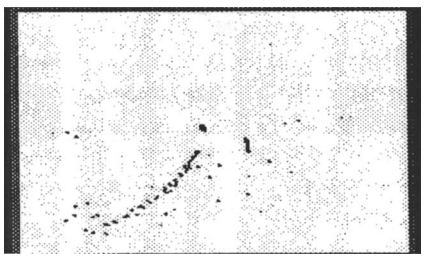

Fig. 6 Final RTR image after processing

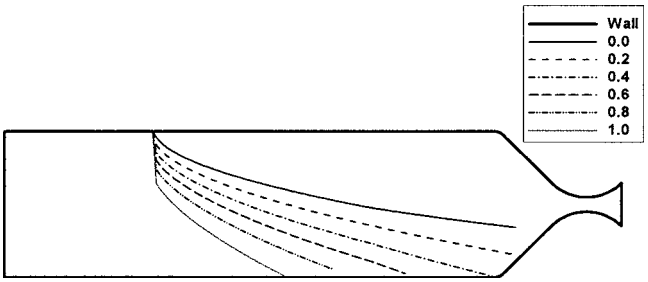

Fig. 7 Calculated trajectory with different ejection velocity

Upon integration of Eqs. (6) and (7), the trajectory of the particle can be obtained. However, when integrating Eq. (6), these initial conditions must be assigned: the ejection position and velocity of the particle. As there is no experimental data to provide any information to determine this velocity, two procedures were taken:

(a) The velocity was set to be zero, which means that the particles on the burning surface enter the gas under the force induced by the gas drag.
(b) The particle velocity is set equal to the surface gas velocity, which implies that there is no delay for velocity equilibrium between the gas and the particle.

As mentioned above, the initial particle velocity and its position are not known; this uncertainty procedure results in a different particle trajectory, and thus in a different slag accumulation. Actually, the initial condition lies between the two procedures mentioned above. The method used here is summarized as follows:

The initial velocity may be written as:

$$\mathbf{V}_p^0 = \beta \mathbf{V}_g|_{\mathrm{surface}}, \quad 0 \leqslant \beta \leqslant 1 \tag{11}$$

where $\mathbf{V}_g|_{\mathrm{surface}}$ is the injection velocity of gas on the propellant burning surface which can be obtained from

$$\mathbf{V}_g| = \dot{r}_p \times \frac{\rho_{pp}}{\rho_g}\mathbf{n} \tag{12}$$

where ρ_{pp} represents the density of propellant.

Next, a series of values for β are chosen, and the corresponding $\mathbf{V}_p^0$ obtained. From Eqs. (6), (7), and (11), a series of particle trajectories can be calculated. Figure 7 shows the calculated trajectories in one case with α=0., 0.2, 0.4, 0.6 0.8, and 1.0. By comparing the calculated trajectory with that obtained from the RTR measurement, an adequate value can be deduced. Let (x_i, y_i) be the particle position of the ith node in RTR image, and (x_i, y_i') be the particle position of the ith node on the calculated trajectory. The standard deviation between two trajectories is defined as

$$\sigma = \sqrt{\frac{\sum_{i=1}^{N}(y_i - y_i')^2}{N}} \tag{13}$$

Here the minimum value from a series of σ is obtained, and the corresponding α is computed, which is then used to determine the ejection velocity of the particles.

The present experiments found that when β=0.4 the corresponding σ reaches the minimum. Figure 8 shows the comparison between a calculated trajectory and a measured trajectory. With the present initial conditions, the calculated trajectory agrees well with the measured one.

Conclusions

Through this study an x-ray image processing program was developed. By applying this method moving trajectories of metal

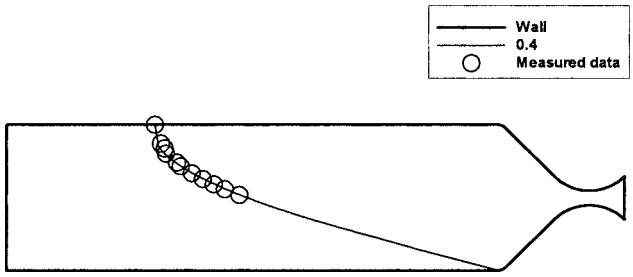

Fig. 8 Comparison between calculated trajectory and measured trajectory

particles in a firing combustion chamber were measured by using a RTR high-speed motion analyzer. Through this study the following conclusions emerge:

(1) From the experimental test of a SRM combustion chamber, the propellant-sample model and particle-injection model were successfully demonstrated to work properly.
(2) The metal particles whose injecting velocity ratio was estimated for particles of diameter 75 μm. And the results were determined using a Lagrangian trajectory approach. This, of course, does not imply that the coefficient obtained here is a universal constant for propellant flow cases, but the program developed in this study is capable of determining the proper coefficients for any other conditions.
(3) The developed image-processing computer code is suitable for processing RTR images of moving particles. Satisfactory results can be obtained for large-size particles (75 μm), but results for small particles (5 μm) need to be improved.
(4) The proposed method for determining the initial velocity of particles on the burning surface of a solid propellant has potential to be further used for other propulsion conditions.

Acknowledgments

The computations were conducted on ORIGIN 2000 at NCSA, Illinois. NSF provided funding under Grant Nos. NSF CTS970045N, CMS9821057 and CTS000003N.

Nomenclature

C_D = droplet drag coefficient
d = particle diameter
$\mathbf{F}$ = force
I = intensity of x-rays
L = distance
$\mathbf{n}$ = unit vector in normal direction
N = number of nodes
$\dot{r}$ = combustion rate
Re = reynolds number
t = time
$\mathbf{V}$ = velocity vector
x = x coordinate of pixel
$\mathbf{X}$ = position vector
y = y coordinate of pixel
y' = y coordinate of calculated position
β = velocity coefficient
λ = attenuation coefficient
ρ = density
σ = standard deviation
μ = viscosity

Subscripts

d = droplet
D = drag
g = gas
i = index
j = index
o = initial
p = particle
pp = propellant
w = weight

References

[1] Salita, M., 1995, "Deficiencies and Requirements in Modeling of Slag Generation in Solid Rocket Motors," J. Propul. Power, **11** (1), pp. 10–23.
[2] Boraas, S., 1984, "Modeling Slag Deposition in the Space Shuttle Solid Rocket Motor," J. Spacecr. Rockets, **21** (1), pp. 47–54.
[3] Haloulakos, V. E., 1991, "Slag Mass Accumulation in Spinning Solid Rocket Motors," J. Propul. Power, **7** (1), pp. 14–21.
[4] Hess, E., Chen, K., Acosta, P., Brent, D., and Fendell, F., 1992, "Effect of Aluminized-Grain Design on Slag Accumulation," J. Spacecr. Rockets, **29** (5), pp. 697–703.
[5] Meyer, R. X., 1992, "In-Flight Formation of Slag in Spinning Solid Propellant Rocket Motors," J. Propul. Power, **8** (1), pp. 45–50.
[6] Golafshani, M., and Loh, H.-T., 1989, "Computation of Two-Phase Viscous Flow in Solid Rocket Motor Using a Flux-Split Eulerian–Lagrangian Technique," AIAA Report No. 89-2785.
[7] Salita, M., Smith-Kent, R., Golafshani, M. T., Abel, R., and Pratt, D., 1990, "Prediction of Slag Accumulation in SICBM Static Flight Motors," *Thiokol TWR-10259*.
[8] Sabnis, J. S., De Jong, F. J., and Gibeling, H. J., 1992, "Calculation of Particle Trajectories in Solid Rocket Motors With Arbitrary Acceleration," J. Propul. Power, **8** (5), pp. 961–967.
[9] Chang, I. S., 1991, "An Efficient Intelligent Solution for Viscous Flows Inside Solid Rocket Motors," AIAA Report No. 91-2429.
[10] Chauvot, J. F., Dumas, L., and Schmeisser, K., 1995, "Modeling of Alumina Slag Formation in Solid Rocket Motors," AIAA Report No. 95-2729.
[11] Liaw, P., Shang, H. M., and Shih, M. H., 1995, "Numerical Investigation of Slag Behavior With Combustion/Evaporation/Breakup/VOF Models for Solid Rocket Motors," AIAA Report No. 95-2726.
[12] Braithwaite, P. C., Christensen, W. N., and Daugherty, V., 1988, "Quench Bomb Investigation of Aluminum Oxide Formation From Solid Rocket Propellants (Part I): Experimental Methodology," *Proceedings of the 25th JANNAF Combustion Meeting*, Vol. 1, pp. 178–184.
[13] Char, J. M., Kou, K. K., and Hsieh, K. C., 1987, "Observation of Breakup Process of Liquid Jets Using Real-Time X-Ray Radiography," AIAA Report No. 87-2137.
[14] Wen, C. Y., and Yu, Y. H., 1966, "Mechanics of Fluidization," Chem. Eng. Prog., Symp. Ser., **62**, pp. 100–111.

Forced Convection Past an Oblate Spheroid at Low to Moderate Reynolds Numbers

Rajai S. Alassar
Department of Mathematical Sciences, KFUPM Box # 1620, Dhahran 31261, Saudi Arabia
e-mail: alassar@kfupm.edu.sa

Forced convection past a heated oblate spheroid is studied in an attempt to investigate the effect of the axis ratio on the heat transfer rate. The time-dependent full Navier–Stokes and energy equations are solved using a series truncation method. The axis ratios considered range from 1/2 to 1 (a perfect sphere). The results for the flow and thermal fields are satisfactorily compared with relevant published research. The results are presented in the form of streamlines, isotherms, and the local and averaged Nusselt number distributions. [DOI: 10.1115/1.1999654]

Introduction

The problem of heat transfer from a sphere has been exhausted through many experimental and theoretical investigations. On natural convection, the reader is referred to the work of Potter and Riley [1], Geoola and Cornish [2,3], Riley [4], Brown and Simpson [5], Singh and Hasan [6], and Dudek et al. [7]. The classic references related to forced and mixed convection past a sphere are those by Dennis and Walker [8], Whitaker [9], Dennis et al. [10], Sayegh and Gauvin [11], Hieber and Gebhart [12], Acrivos [13], Wong et al. [14], and Nguyen et al. [15]. Studies related to heat or mass transfer from a sphere in an oscillating free stream are presented by Drummond and Lyman [16], and Ha and Yavuzkurt [17], Alassar et al. [18], and Leung and Baroth [19].

Research on axisymmetric flow over bodies of revolution other than spheres has been confined mainly to the low Reynolds number cases. In such cases (see, for example, the work by Lawrence and Weinbaum [20], Payne and Pell [21], and Breach [22]), the nonlinear inertia terms in the equations of motion are either neglected or linearized. Alassar and Badr, however, solved the full Navier–Stokes equations for the impulsively started flow [23] and the oscillating flow [24] over oblate spheroids and a detailed analysis of the flow field was given.

The studies related to heat transfer from oblate spheroids are scarce due to the complicated geometry. Alassar [25] investigated the conduction heat transfer problem by solving the steady version of the energy equation subject to the appropriate boundary conditions and showed that the solution for the sphere case can be obtained from his generalized results. The work of Alassar [25], however, deals with the conduction heat transfer and does not cover the complicated and the more general convective heat transfer in which the flow structure of a fluid dramatically influences the thermal field.

In this paper, heat convection past an oblate spheroid is investigated in an attempt to find the effect of the axis ratio on the heat transfer rate. The spheroid represents more realistic situations not observed in the idealization of particles through spheres. In fact, a sphere is a special case of the generalized spheroidal geometry.

Problem Statement. In this paper, a solid oblate spheroid of major and minor axes $2a$ and $2b$, respectively, suspended in an unbounded incompressible fluid which starts moving from rest with a uniform velocity U_o is considered. The spheroid is at temperature T_s which is hotter than the free stream whose temperature is maintained at T_∞ as sketched in Fig. 1. The oblate spheroid with focal distance $c'(c'=\sqrt{a^2-b^2})$ is generated by rotating an ellipse around its minor axis. The number ξ_o $[\xi_o=\tanh^{-1}(b/a)]$ defines the surface of the spheroid. The limiting case as ξ_o tends to infinity (or equivalently as $b/a\to 1$) is a sphere. On the other hand, as ξ_o tends to zero (or equivalently as $b/a\to 0$), the oblate spheroid becomes a flat circular disk.

The heat transfer process is governed by the conservation principles of momentum, mass, and energy. These laws can be written using the oblate spheroidal coordinates system (ξ,η,ϕ) as

$$\delta^3\cosh\xi\sin\eta(\sinh^2\xi+\cos^2\eta)\varsigma+\cosh\xi\frac{\partial}{\partial\xi}\left(\frac{1}{\cosh\xi}\frac{\partial\psi}{\partial\xi}\right)+\sin\eta\frac{\partial}{\partial\eta}\left(\frac{1}{\sin\eta}\frac{\partial\psi}{\partial\eta}\right)=0 \tag{1}$$

$$\delta^3(\sinh^2\xi+\cos^2\eta)\frac{\partial\varsigma}{\partial t}+\frac{\partial\psi}{\partial\eta}\frac{\partial}{\partial\xi}\left(\frac{\varsigma}{\cosh\xi\sin\eta}\right)-\frac{\partial\psi}{\partial\xi}\frac{\partial}{\partial\eta}\left(\frac{\varsigma}{\cosh\xi\sin\eta}\right)=\frac{2\delta}{\mathrm{Re}}\left\{\frac{\partial}{\partial\xi}\left[\frac{1}{\cosh\xi}\frac{\partial}{\partial\xi}(\cosh\xi\,\varsigma)\right]+\frac{\partial}{\partial\eta}\left[\frac{1}{\sin\eta}\frac{\partial}{\partial\eta}(\sin\eta\,\varsigma)\right]\right\} \tag{2}$$

$$\delta^3(\sinh^2\xi+\cos^2\eta)\frac{\partial\varphi}{\partial t}+\frac{1}{\cosh\xi\sin\eta}\left[\frac{\partial\psi}{\partial\eta}\frac{\partial\varphi}{\partial\xi}-\frac{\partial\psi}{\partial\xi}\frac{\partial\varphi}{\partial\eta}\right]=\frac{2\delta}{\mathrm{Re\,Pr}}\left\{\frac{1}{\cosh\xi}\frac{\partial}{\partial\xi}\left[\cosh\xi\frac{\partial\varphi}{\partial\xi}\right]+\frac{1}{\sin\eta}\frac{\partial}{\partial\eta}\left[\sin\eta\frac{\partial\varphi}{\partial\eta}\right]\right\} \tag{3}$$

where Re $(\mathrm{Re}=\rho U_o(2a)/\mu)$ is the Reynolds number, ρ is the fluid density, μ is the dynamic viscosity, Pr $(\mathrm{Pr}=\upsilon/\alpha)$ is Prandtle number, α is the thermal diffusivity, υ is the coefficient of kinematic viscosity, $\delta=\frac{c'}{a}=\sqrt{1-\left(\frac{b}{a}\right)^2}$, t is the dimensionless time, ψ is the dimensionless stream function, ς is the dimensionless vorticity, and φ is the dimensionless temperature.

The equations are made dimensionless by the variables:

$$\psi^*=\frac{\psi}{U_o a^2},\quad \zeta^*=\frac{\zeta a}{U_o},\quad t^*=\frac{tU_o}{a},\quad \text{and}\quad \varphi=(T-T_\infty)/(T_s-T_\infty) \tag{4}$$

where T is the temperature. The asterisks indicate dimensionless quantities and have been dropped in Eq. (1)–(3).

The boundary conditions to be satisfied are the no-slip and impermeability conditions on the surface of the spheroid and the free stream conditions away from it in addition to the thermal conditions. The boundary conditions can be expressed as

$$\psi=\frac{\partial\psi}{\partial\eta}=\frac{\partial\psi}{\partial\xi}=0\quad\text{and}\quad\varphi=1\quad\text{at}\quad\xi=\xi_o \tag{5}$$

$$\frac{\partial\psi}{\partial\xi}\to\frac{\delta^2}{2}\sinh 2\xi\sin^2\eta,\ \text{and}\ \frac{\partial\psi}{\partial\eta}\to\frac{\delta^2}{2}\cosh^2\xi\sin^2\eta\quad\text{as}\ \xi\to\infty \tag{6}$$

$$\varphi\to 0,\quad \zeta\to 0\ \text{as}\ \xi\to\infty \tag{7}$$

Method of Solution. The series truncation method of solution is based on expanding ψ, ζ, and φ using associated Legendre polynomials, Alassar et al. [18], as:

Contributed by the Heat Transfer Division for publication in the Journal of Heat Transfer. Manuscript received by the Heat Transfer Division January 22, 2004; revision received April 27, 2005. Review conducted by: N. K. Anand.

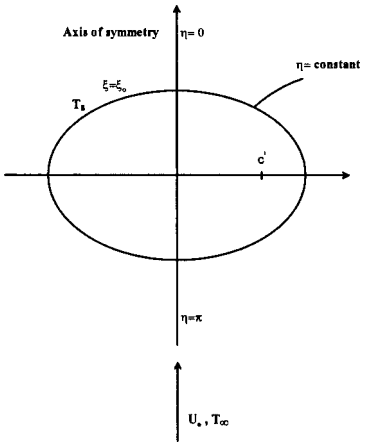

Fig. 1 The coordinate system

$$\{\psi,\zeta,\varphi\}=\left\{\sum_{n=1}^{\infty} f_n(\xi,t)\int_z^1 P_n(\Omega)d\Omega,\sum_{n=1}^{\infty} g_n(\xi,t)P_n^1(z),\ \sum_{n=0}^{\infty} h_n(\xi,t)P_n(z)\right\} \tag{8}$$

where $P_n(z)$ and $P_n^1(z)$ are the Legendre and first associated Legendre functions of order n, respectively, and $z=\cos\eta$.

The following equations on the modes of the series (8) can be obtained using the properties of Legendre functions. We leave out the details and refer the reader to the work of Alassar et al. [18].

$$\begin{aligned}&\frac{\partial^2 f_n}{\partial\xi^2}-\tanh\xi\frac{\partial f_n}{\partial\xi}-n(n+1)f_n\\&\quad=\delta^3\cosh\xi\, n(n+1)\left[\sinh^2\xi+\frac{2n^2+2n-3}{(2n-1)(2n+3)}\right]g_n\\&\qquad+\delta^3\cosh\xi\frac{n(n+1)(n+2)(n+3)}{(2n+3)(2n+5)}g_{n+2}\\&\qquad+\delta^3\cosh\xi\frac{n(n-1)(n-2)(n+1)}{(2n-1)(2n-3)}g_{n-2}\end{aligned} \tag{9}$$

$$\begin{aligned}&\delta^3\left[\sinh^2\xi+\frac{2n^2+2n-3}{(2n-1)(2n+3)}\right]\frac{\partial g_n}{\partial t}+\frac{(n+2)(n+3)\delta^3}{(2n+3)(2n+5)}\frac{\partial g_{n+2}}{\partial t}\\&\quad+\frac{(n-1)(n-2)\delta^3}{(2n-1)(2n-3)}\frac{\partial g_{n-2}}{\partial t}\\&\quad=\frac{2\delta}{\mathrm{Re}}\left[\frac{\partial^2 g_n}{\partial\xi^2}+\tanh\xi\frac{\partial g_n}{\partial\xi}+\left\{\frac{1}{\cosh^2\xi}-n(n+1)\right\}g_n\right]+S_n\end{aligned} \tag{10}$$

$$\begin{aligned}&\delta^3\left[\sinh^2\xi+\frac{2n^2+2n-1}{(2n-1)(2n+3)}\right]\frac{\partial h_n}{\partial t}+\frac{\delta^3(n+1)(n+2)}{(2n+3)(2n+5)}\frac{\partial h_{n+2}}{\partial t}\\&\quad+\frac{\delta^3 n(n-1)}{(2n-1)(2n-3)}\frac{\partial h_{n-2}}{\partial t}\\&\quad=\frac{2\delta}{\mathrm{Re}\ \mathrm{Pr}}\left[\frac{\partial^2 h_n}{\partial\xi^2}+\tanh\xi\frac{\partial h_n}{\partial\xi}-n(n+1)h_n\right]+H_n\end{aligned} \tag{11}$$

where

$$S_n=-\frac{1}{\cosh\xi}\left[\sum_{i=1}^{\infty}\sum_{j=1}^{\infty}\alpha_{ij}^n f_i\left(\frac{\partial g_j}{\partial\xi}-\tanh\xi\, g_j\right)+\sum_{i=1}^{\infty}\sum_{j=1}^{\infty}\beta_{ij}^n g_j\frac{\partial f_i}{\partial\xi}\right] \tag{12}$$

and

$$H_n=-\frac{1}{\cosh\xi}\left[\sum_{i=1}^{\infty}\sum_{j=0}^{\infty}\frac{2n+1}{2i+1}\alpha_{nj}^i h_j\frac{\partial f_i}{\partial\xi}+\sum_{i=1}^{\infty}\sum_{j=0}^{\infty}\gamma_{ij}^n f_i\frac{\partial h_j}{\partial\xi}\right] \tag{13}$$

The coefficients α, β, and γ are related to the 3-j symbols [18].

The solutions of the functions ψ, and ζ are advanced in time using a Crank–Nicolson finite-difference scheme. The process is well explained by Alassar and Badr [23] and need not be mentioned here again. The criterion used to determine the number of terms retained in the series and the effect of Reynolds number and the axis ratio are discussed by Alassar and Badr [26]. The treatment of the energy equation in the present paper is similar to the momentum equation.

Physical Quantities. The local amount of heat transferred from the spheroid is

$$q(\eta,t)=-\frac{K}{\mathrm{l}_\xi}\left(\frac{\partial\varphi}{\partial\xi}\right)_{\xi=\xi_o} \tag{14}$$

where K is the thermal conductivity, and l_ξ is a scale factor of the oblate spheroidal coordinate system. The local Nusselt number (N_u) is defined as

$$N_u(\eta,t)=\frac{2a\,q(\eta,t)}{\kappa}=-\frac{2\cosh\xi_o}{\sqrt{\sinh^2\xi_o+\cos^2\eta}}\sum_{n=0}^{\infty}\frac{\partial h_n}{\partial\xi}P_n(\cos\eta) \tag{15}$$

Averaging Nusselt number over the surface of the spheroid gives the averaged Nusselt number, $\overline{N_u}(t)$ as

$$\overline{N_u}(t)=-\frac{4}{1+\sinh\xi_o\tanh\xi_o\ln\left(\coth\frac{\xi_o}{2}\right)}\frac{\partial h_o}{\partial\xi} \tag{16}$$

The dimensionless drag coefficient C_D ($C_D=Da/\mu U_o A$, where D is the drag exerted by the fluid on the spheroid, and $A=\pi c'^2\cosh^2\xi$ is the spheroid's projected area) is the sum of two components, one due to friction and the other due to pressure

$$C_{\mathrm{DF}}=-2\tanh\xi_o\int_0^{\pi}\zeta(\xi_o,\eta)\sin^2/\eta\, d\eta \tag{17}$$

$$C_{\mathrm{DP}}=-\frac{\mathrm{Re}}{2\rho U_o^2}\int_0^{\pi}p'(\xi_o,\eta)\sin 2\eta\, d\eta \tag{18}$$

The pressure coefficient is defined as

$$p^*=p_\eta-p_\pi=\int_\pi^\eta\left(\frac{\partial\zeta}{\partial\xi}+\tanh\xi\zeta\right)_{\xi=\xi_o}d\eta \tag{19}$$

where p is the dimensionless pressure defined by $p=p'a/\mu U_o$, and p' is the dimensional pressure.

Results and Discussion. The problem under consideration is investigated by considering spheroids with axis ratios of 0.55, 0.60, 0.65, 0.70, 0.75, 0.80, 0.85, 0.90, 0.95, and 0.99 (almost a sphere) at three values of Reynolds numbers 10, 40, and 100. The effect of Reynolds number is investigated by considering a spheroid of axis ratio of 0.75 at Reynolds numbers of 10, 20, 30, 40, 50, 60, 70, 80, 90, 100, 200, 300, 400, and 500. This makes the total number of cases considered 41.

The series truncation method adopted here has been verified

Table 1 Comparisons at Re=20 for the sphere case

	Present	Dennis et al. [10]	Sayegh & Gauvin [11]	Chang & Maxey [28]	Wong et al. [14]	Dennis & Walker [8]	Jenson [29]	LeClair et al. [30]
$\overline{N}_u$	4.056	4.065	4.022		3.971	3.860		
C_{DF}	8.50	8.54	8.95	8.63	9.81			
C_{DP}	5.13	5.12	5.35	5.38				
C_D	13.63	13.65	14.20	14.00		13.20	14.73	13.56

several times by Alassar and Badr. [23,24] in the context of fluid motion alone. Comparisons have been made with the drag formula given by Payne and Pell [21], Breach [22], and Lai and Mockros [27].

The method of solution is further verified here by considering the problem of forced convection past a sphere for which the drag coefficient and Nusselt number are available in the literature. The problem was approximated using the present computational scheme by considering the case of a spheroid with axis ratio $b/a=0.99$ which corresponds to $\xi_o=2.647$. The unsteady flow solution following the sudden velocity increase continued until the final steady solution was reached. Tables 1 and 2 show comparisons between the drag coefficients, the Nusselt number, separation angle η_s, and the dimensionless wake length χ_s (the wake length divided by a) obtained from this study and those reported in the literature for the cases Re=20 and Re=40, respectively. In general, the tables show excellent agreements.

Flow Field. The unsteady flow continues until steady states are reached. Steady states are detected when no significant changes in the flow parameters are observed. At the start of the motion, no separation is observed (the separation point corresponds to where the surface vorticity ς_o is zero). As time progresses and due to the adverse pressure gradients, a bubble is formed at the rear stagnation point of the spheroid which rapidly increases in size. The separation point, then, migrates towards the front stagnation point. The depth and the breadth of the separation region is influenced by the axis ratio of the spheroid as well as the strength of the flow (Reynolds number). As the axis ratio increases, a stronger flow is required to set on separation.

The steady-states streamlines for Re=40 at all considered axis ratios are shown in Fig. 2. Figure 3 compares the streamlines for all Re values considered (10–500) when the axis ratio is fixed at 0.75. The sharp edge of the spheroid when the axis ratio is low promotes separation significantly. The strength of the flow for Re=10 is not sufficient to force a reversal in the direction of the motion near the wall of the spheroid at any of the axis ratios considered in the present study.

The surface vorticity is of extreme importance in the analysis of fluid motion because it represents the velocity gradients which in turn define all quantities such as the drag, whether separation occurs, and the heat transfer rate. In fact, separation occurs where the surface vorticity is identically zero. Figure 4 shows the surface vorticity for the case Re=40 at different axis ratios along with the corresponding dimensionless pressure distributions (Fig. 5). The surface vorticity figure shows the separation region as a region of positive vortictiy. The surface vorticity has a peak close to the edge of the spheroid near $\eta=90$. This peak gets closer to the edge as the axis ratio decreases. Observe also the higher pressure gradients as b/a decreases. These higher gradients are responsible for the separation of the flow which is not observed at low Reynolds numbers.

Thermal Field. At small times, the viscous effects are limited to the boundary layer region near the surface of the spheroid. The flow does not separate instantly. As time progresses, the boundary layer becomes thicker and a separation region gets formed. Similarly and due to the sudden rise of the spheroid's temperature, the thermal boundary layer thickness is initially very small. The high thermal gradients make the rate of heat transfer quite considerable. As time progresses, the heat transfer rate drops until it stabilizes indicating that steady states are reached. Figure 6, as an example of time developments, shows the isotherms at different times ($t=0.33$, 0.66, 3.31, 6.61, 9.92, 13.23, and 20.0) for the case Re=100 when $b/a=0.75$. The development of the boundary layer is quite obvious.

The time variations of the averaged Nusselt number $\overline{N}_u$, the standard way of presenting heat transfer rate, with b/a for the three cases of Re=10, 40, and 100 are shown in Figures 7–9,

Table 2 Comparisons at Re=40 for the sphere case

	Present	Dennis et al. [10]	Chang& Maxey [28]	Wong et al. [14]	Rimon & Cheng [31]	Jenson [29]	LeClair et al. [30]
$\overline{N}_u$	5.04			5.026			
C_{DF}	10.37	10.72	10.84	12.32			
C_{DP}	7.06	7.36	7.48				
C_D	17.44	18.08	18.32		18.6	18.6	18.6
η_s	35.78	35.00	35.18	31.26			
χ_s	0.533	0.600	0.534		0.660	0.480	

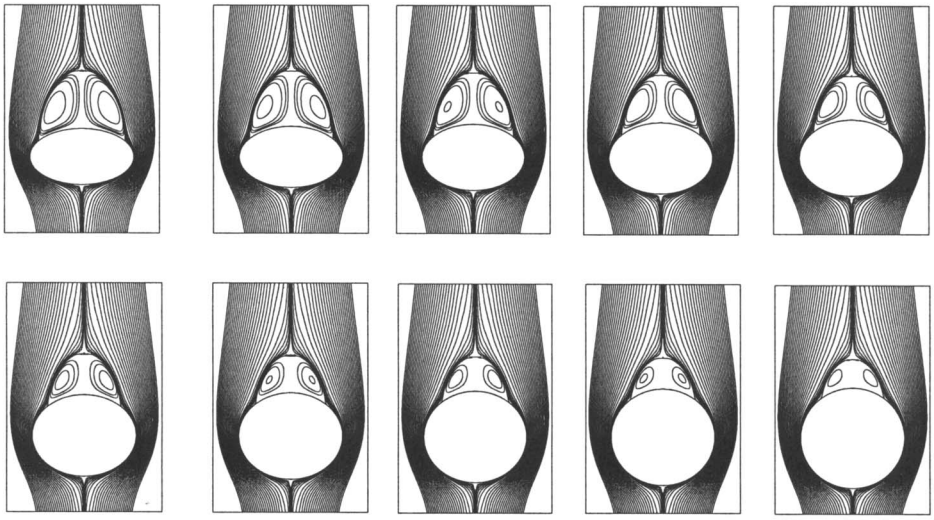

Fig. 2 The steady-state streamlines for Re=40 at different axis ratios (b/a=0.55–0.99)

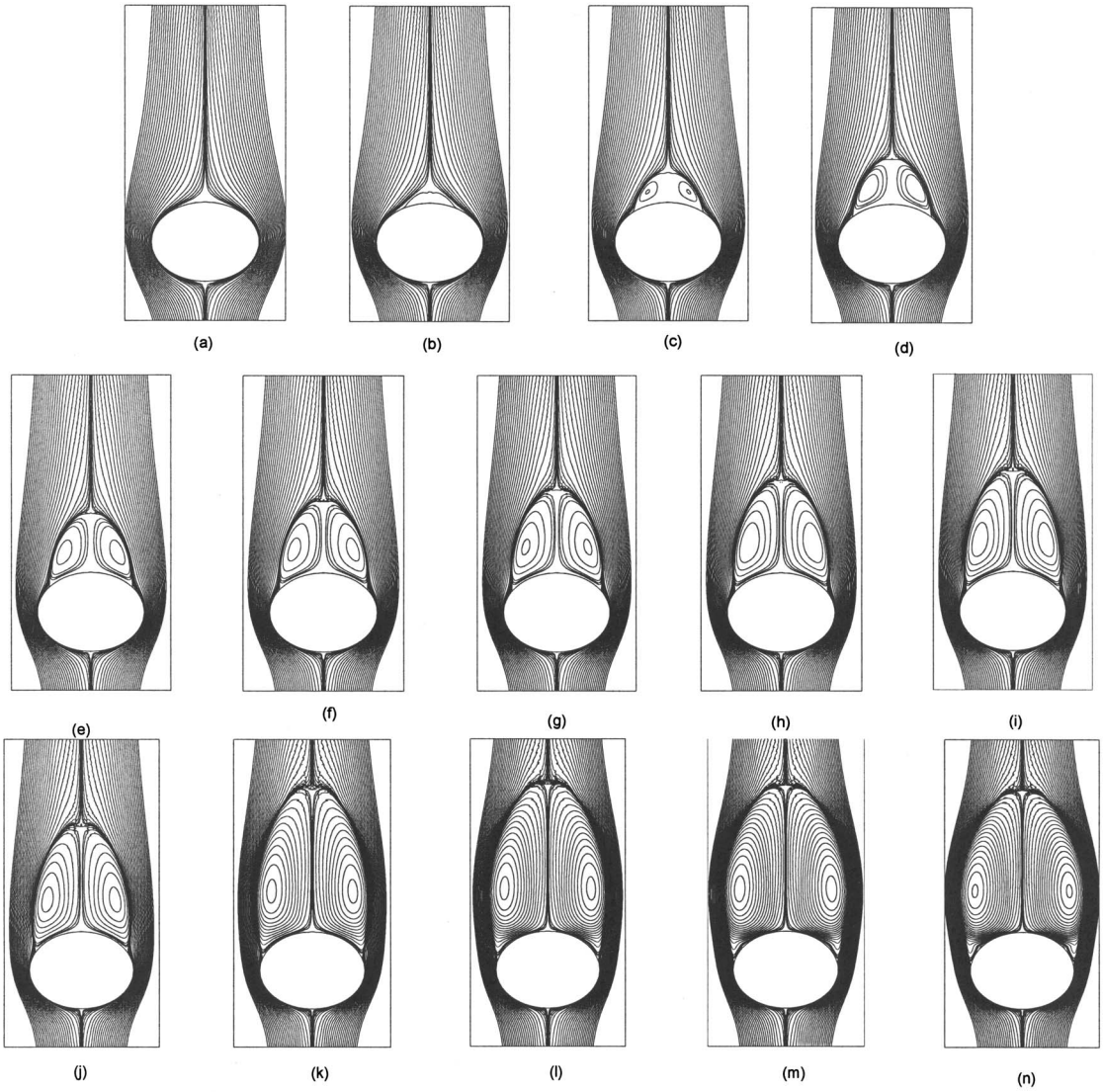

Fig. 3 The steady-state streamlines for b/a=0.75 at different Reynolds numbers. Re= (*a*) 10, (*b*) 20, (*c*) 30, (*d*) 40, (*e*) 50, (*f*) 60, (*g*) 70 (*h*) 80 (*i*) 90, (*j*) 100, (*k*) 200, (*l*) 300, (*m*) 400, (*n*) 500.

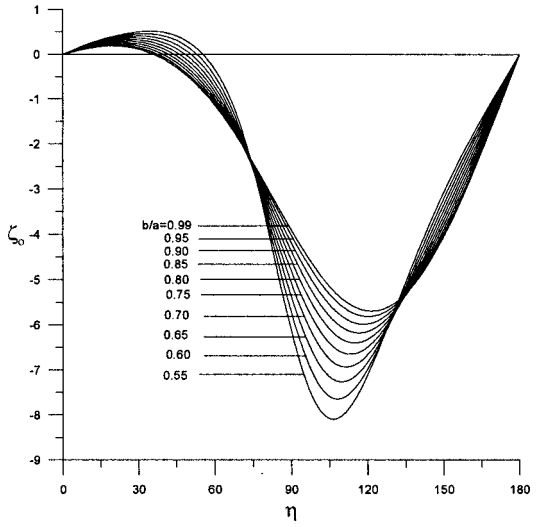

Fig. 4 Surface vorticity, Re=40

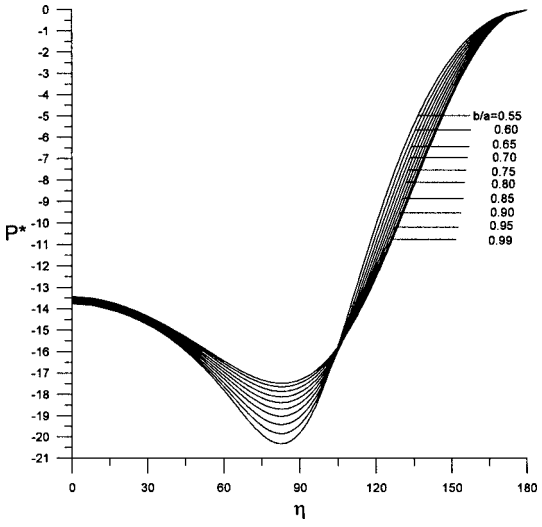

Fig. 5 Dimensionless pressure, Re=40

respectively. Figure 10 shows the variation of the averaged Nusselt number for all Re values considered but at the fixed axis ratio 0.75. One can observe that as the axis ratio decreases, the heat transfer rate or equivalently the averaged Nusselt number increases. This is due to the fact that the sharp edge of the spheroid gives rise to higher velocity gradients. These velocity gradients promote the heat transfer rate. The increase of the averaged Nusselt number with the increase of Re is not surprising and follows the known trend for the sphere case.

The heat transfer rate is not completely driven by convection. When the fluid around the spheroid is stagnant, convection ceases and the heat transfer process takes place only by conduction. The steady amount of heat transferred by conduction can be obtained by solving the steady version of the energy equation subject to the appropriate boundary conditions. It is not difficult to show, Alassar [25], that the conduction local Nusselt number is given by

$$N_u(\eta) = -\frac{2}{(2\tan^{-1} e^{\xi_o} - \pi)\sqrt{\sinh^2 \xi_o + \cos^2 \eta}} \tag{20}$$

The conduction averaged Nusselt number is given by

$$\overline{N_u} = -\frac{4}{\cosh \xi_o [2\tan^{-1} e^{\xi_o} - \pi]\left[1 + \sinh \xi_o \tanh \xi_o \ln\left(\coth\frac{\xi_o}{2}\right)\right]} \tag{21}$$

In the limit as $\xi_o \to \infty$, the oblate spheroid becomes a sphere and one can show that, in Eq. (20), $\lim_{\xi_o \to \infty} \overline{N_u} = 2$. This result is iden-

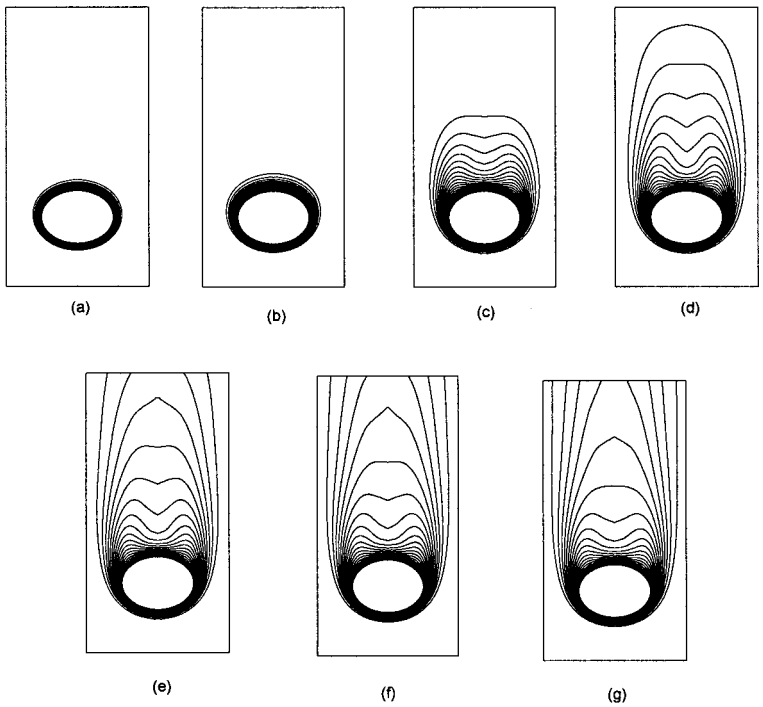

Fig. 6 The time development of isotherms for the case Re=100, *b*/*a* =0.75 *t*= (*a*) 0.33, (*b*) 0.66, (*c*) 3.31, (*d*) 6.61, (*e*) 9.92, (*f*) 13.23, (*g*) 20.0

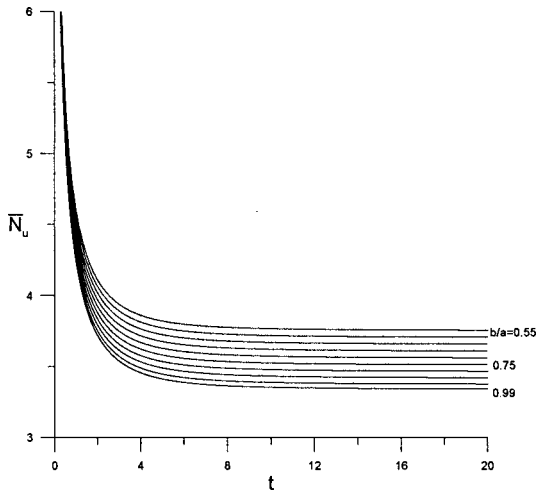

Fig. 7 The averaged Nusselt number, Re=10

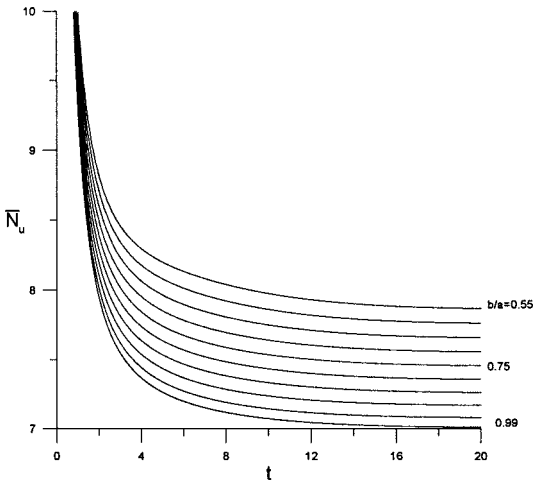

Fig. 9 The averaged Nusselt number, Re=100

tical to that obtained from the analysis of heat transfer from a sphere. Table 3 shows a summary of the averaged Nusselt number for the range of parameters considered in the present study. The values of the pure conduction averaged Nusselt number are also given. The effect of the free stream is isolated in the last column of the table by calculating the difference. One can observe that about 12% increase in the averaged Nusselt number is caused by the change in geometry from a sphere to a spheroid with axis ratio of 0.55 at all Re considered. It can be clearly observed from Fig. 11 that a linear relationship exists between $\overline{N_u}$ and b/a at a fixed Re. Moreover, the three curves have almost the same slope.

The local Nusselt number N_u gives the distribution of the heat transfer rate along the body of the spheroid. Figures 12–14 show N_u for the three cases of Re=10, 40, and 100, respectively, at b/a from 0.55 to 0.99. Figure 15 shows the variation of the averaged Nusselt number for all Re values considered but at the fixed axis ratio 0.75.

For the cases Re=10, 40, or even 100, the highest value of N_u at steady states is observed close to $\eta=180$ for the cases where the axis ratio b/a is close to unity. The highest value, however, takes place closer and closer to $\eta=90$ as the axis ratio departs from unity. As mentioned earlier, the higher velocity gradients close to the edge of the spheroid at $\eta=90$ promote the heat transfer rate. Figures 12–14 show a gradual increase in N_u from $\eta=0$ to $\eta=180$ for the case $b/a=0.99$ as opposed to the case $b/a=0.55$ where a sharp increase of N_u occurs until close to $\eta=90$ beyond which a decrease in the heat transfer rate is evident. A point worth noting here is the value of the local Nusselt number near the rear stagnation point at $\eta=0$. At low Reynolds number, for example Re=10 in Fig. 12, the local Nusselt number at $\eta=0$ for b/a near unity is close to the value of 2 which corresponds to the conduction heat transfer rate [simply the limit of Eq. (20) as $\xi_o \to \infty$]. As b/a decreases, this value of Nusselt number near $\eta=0$ changes. This change is mainly due to conduction. Equation (20) gives the values for conduction Nusselt number at $\eta=0$ as 1.99, 1.97, 1.93, 1.90, 1.86, 1.83, 1.80, 1.76, 1.73, and 1.69 for the cases of $b/a=0.99$, 0.95, 0.90, 0.85, 0.80, 0.75, 0.70, 0.65, 0.60, and 0.55, respectively. At low Reynolds numbers and except for conduction, little heat transfer is made by the flowing fluid near $\eta=0$. This is due to the fact that the region near $\eta=0$ is at stagnation. However, as Reynolds number increases, a recirculation region starts to develop near the rear stagnation point which naturally helps increase the heat transfer rate. This effect of the separation region is clear in Fig. 14 and 15. As this separation region grows due to the increase of Reynolds number (see, for example, the case Re=500 in Fig. 15) or the decrease of b/a, the Nusselt number near $\eta=0$ becomes quite significant.

Finally, we present steady-state isotherms for the case Re

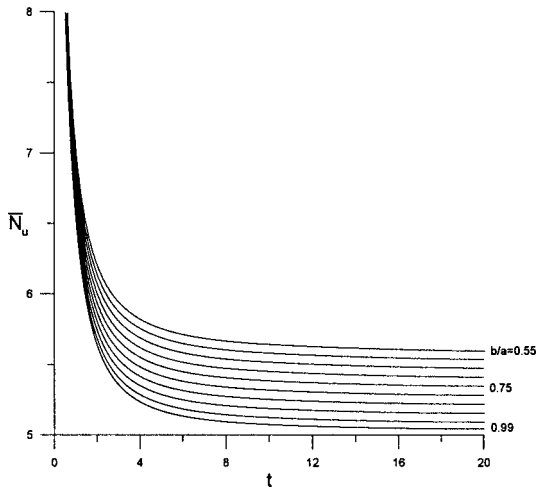

Fig. 8 The averaged Nusselt number, Re=40

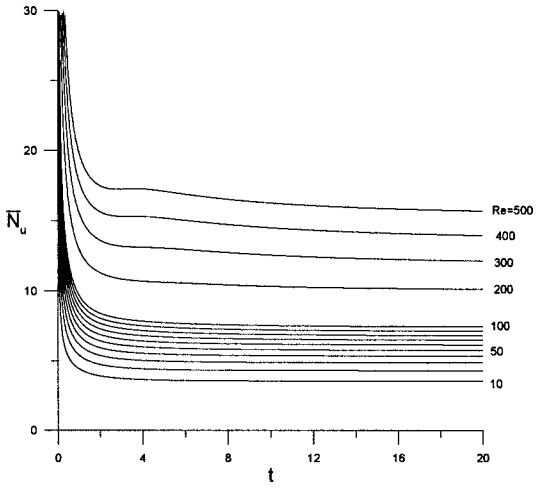

Fig. 10 The averaged Nusselt number, $b/a=0.75$

Table 3 Averaged Nusselt number

Re	b/a	$\overline{N}_u$	$\overline{N}_u$ Conduction	Difference
10	0.55	3.76	2.35	1.41
10	0.6	3.71	2.31	1.4
10	0.65	3.66	2.27	1.39
10	0.7	3.61	2.22	1.39
10	0.75	3.56	2.18	1.38
10	0.8	3.51	2.14	1.37
10	0.85	3.47	2.11	1.36
10	0.9	3.42	2.07	1.35
10	0.95	3.38	2.03	1.35
10	0.99	3.34	2.01	1.33
40	0.55	5.60	2.35	3.25
40	0.6	5.54	2.31	3.23
40	0.65	5.47	2.27	3.2
40	0.7	5.41	2.22	3.19
40	0.75	5.35	2.18	3.17
40	0.8	5.28	2.14	3.14
40	0.85	5.22	2.11	3.11
40	0.9	5.15	2.07	3.08
40	0.95	5.09	2.03	3.06
40	0.99	5.04	2.01	3.03

Re	b/a	$\overline{N}_u$	$\overline{N}_u$ Conduction	Difference
100	0.55	7.87	2.35	5.52
100	0.6	7.76	2.31	5.45
100	0.65	7.66	2.27	5.39
100	0.7	7.56	2.22	5.34
100	0.75	7.46	2.18	5.28
100	0.8	7.36	2.14	5.22
100	0.85	7.26	2.11	5.15
100	0.9	7.17	2.07	5.1
100	0.95	7.08	2.03	5.05
100	0.99	7.01	2.01	5
10	0.75	3.56	2.18	1.38
20	0.75	4.31	2.18	2.13
30	0.75	4.87	2.18	2.69
40	0.75	5.35	2.18	3.17
50	0.75	5.76	2.18	3.58
60	0.75	6.14	2.18	3.96
70	0.75	6.48	2.18	4.3
80	0.75	6.80	2.18	4.62
90	0.75	7.12	2.18	4.94
100	0.75	7.46	2.18	5.28
200	0.75	10.12	2.18	7.94
300	0.75	12.14	2.18	9.96
400	0.75	13.95	2.18	11.77
500	0.75	15.69	2.18	13.51

=100 (Fig. 16) at all considered axis ratios. The isotherms for all Reynolds numbers at the fixed $b/a=0.75$ are shown in Fig. 17.

Conclusion

The problem of forced convection past an oblate spheroid was solved in the range of Reynolds number of 10–500 for axis ratios ranging from 0.55 to 0.99 (almost a sphere). Verification of the model was carried out through comparing the results for the flow and thermal fields with the sphere case by considering a spheroid with axis ratio of 0.99.

Several important and interesting results related to the flow and thermal fields were found. The effect of geometry on the heat transfer rate was observed through the fact that the high velocity gradients close to the edge of the spheroid at $\eta=90$ promote the transfer rate. As the axis ratio decreases, the heat transfer rate or the averaged Nusselt number increases. It was observed that about 12% increase in the averaged Nusselt number is caused by the change in geometry from a sphere to a spheroid with axis ratio of 0.55 at all Reynolds numbers considered. A linear relationship was found to exist between the averaged Nusselt number and the

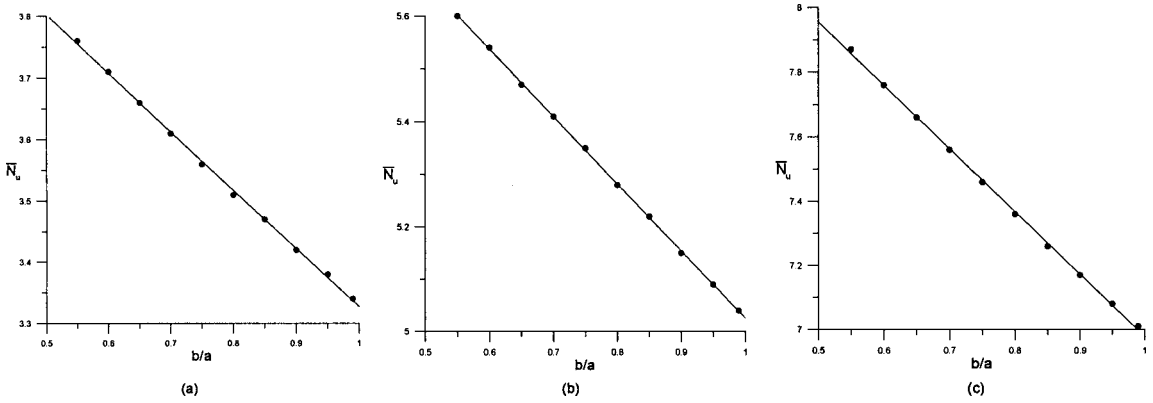

Fig. 11 $\overline{N}_u$ versus b/a, Re= (*a*) 10, (*b*) 40, (*c*) 100

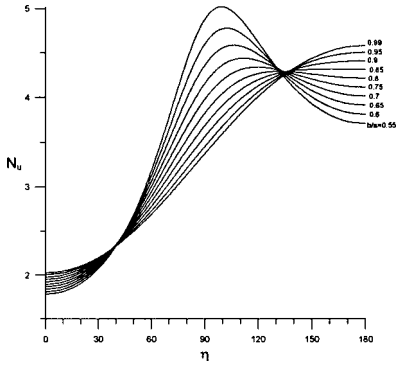

Fig. 12 N_u, Re=10

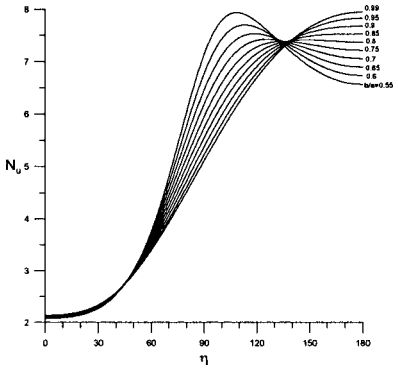

Fig. 13 N_u, Re=40

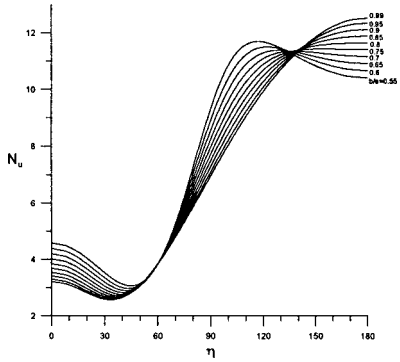

Fig. 14 N_u, Re=100

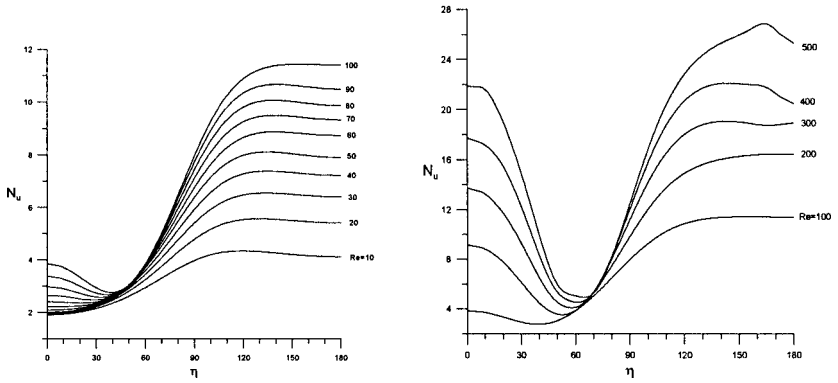

Fig. 15 N_u, b/a 0.75

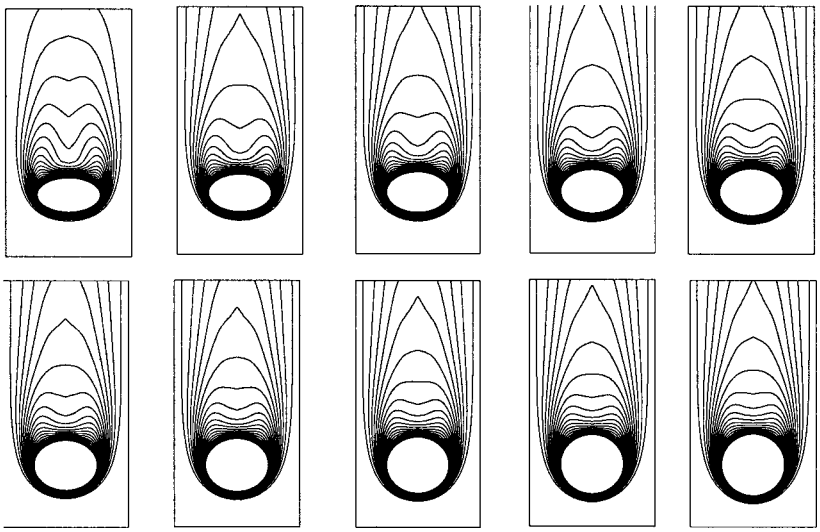

Fig. 16 The steady-state isotherms for Re=100 at different axis ratios (b/a =0.55–0.99)

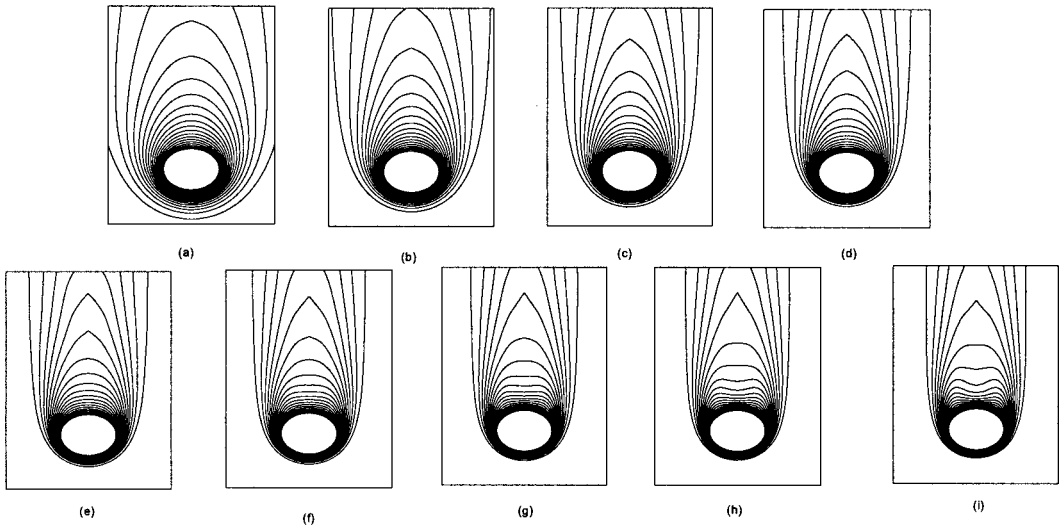

Fig. 17 The steady-state isotherms for $b/a=0.75$ at different Reynolds numbers. Re= (*a*) 10, (*b*) 20, (*c*) 30, (*d*) 40, (*e*) 50, (*f*) 60, (*g*) 70 (*h*) 80 (*i*) 90, (*j*) 100, (*k*) 200, (*l*) 300, (*m*) 400, (*n*) 500.

axis ratio of the spheroid. The recirculation region was found to induce convective heat transfer in the otherwise conduction-dominated rear stagnation region.

Acknowledgment

This research was generously supported by King Fahd University of Petroleum & Minerals (KFUPM) under Grant No. MS/SPHERICITY/225.

References

[1] Potter, J. M., and Riley, N., 1980, "Free Convection from a Heated Sphere at Large Grashof Number," J. Fluid Mech., **100**(4), pp. 769–783.
[2] Geoola, F. and Cornish, A. R. H., 1981, "Numerical Solution of Steady-State Free Convective Heat Transfer from a Solid Sphere," Int. J. Heat Mass Transfer, **24**(8), pp. 1369–1379.
[3] Geoola, F. and Cornish, A. R. H., 1982, "Numerical Simulation of Free Convective Heat Transfer from a Sphere," Int. J. Heat Mass Transfer, **25**(11), pp. 1677–1687.
[4] Riley, N., 1982, "The Heat Transfer from a Sphere in Free Convective Flow," Comput. Fluids, **14**(3), pp. 225–237.
[5] Brown, S. N., and Simpson, C. J., 1982, "Collision Phenomena in Free-Convective Flow over a Sphere," J. Fluid Mech., **124**, pp. 123–137.
[6] Singh, S. N., and Hasan, M. M., 1983, "Free Convection About a Sphere at Small Grashof Number," Int. J. Heat Mass Transfer, **26**(5), pp. 781–783.
[7] Dudek, D. R., Fletcher, T. H., Longwell, J. P., and Sarofim, A. F., 1988, "Natural Convection Induced Forces on Spheres at Low Grashof Numbers: Comparison of Theory with Experiment," Int. J. Heat Mass Transfer, **31**(4), pp. 863–873.
[8] Dennis, S. C. R. and Walker, M. S., 1964, "Forced Convection from Heated Spheres," Aeronautical Research Council No. 26, **105**.
[9] Whitaker, S., 1972, "Forced Convection Heat Transfer Correlations for Flow in Pipes, Past Flat Plates, Single Cylinders, Single Spheres, and for Flow in Packed Beds and Tube Bundles." AIChE J., **18**(21), 361.
[10] Dennis, S. C. R., Walker, D. A., and Hudson, J. D., 1977, "Heat Transfer from a Sphere at Low Reynolds Numbers." J. Fluid Mech., **60**(2), pp. 273–283.
[11] Sayegh, N. N., and Gauvin, W. H., 1979, "Numerical Analysis of Variable Property Heat Transfer to a Single Sphere in High Temperature Surroundings," AIChE J., **25**(3), pp. 522–534.
[12] Hieber, C. A., and Gebhart, B., 1969, "Mixed Convection from a Sphere at Small Reynolds and Grashof Numbers," J. Fluid Mech., **38**, pp. 137–159.
[13] Acrivos, A., 1966, "On the Combined Effect of Forced and Free Convection Heat Transfer in Laminar Boundary Layer Flows," Chem. Eng. Sci., **21**, pp. 343–352.
[14] Wong, K.-L., Lee, S-C., and Chen, C-K., 1986, "Finite Element Solution of Laminar Combined Convection from a Sphere," Trans. ASME, J. Appl. Mech., **108**, pp. 860–865.
[15] Nguyen, H. D., Paik, S., and Chung, J. N., 1993, "Unsteady Mixed Convection Heat Transfer from a Solid Sphere: The Conjugate Problem," Int. J. Heat Mass Transfer, **36**(18), pp. 4443–4453.
[16] Drummond, C. K., and Lyman, F. A., 1990, "Mass Transfer from a Sphere in an Oscillating Flow with Zero Mean Velocity," Comput. Mech. **6**, pp. 315–326.
[17] Ha, M. Y., and Yavuzkurt, S., 1993, "A Theoretical Investigation of Acoustic Enhancement of Heat and Mass Transfer 1. Pure oscillating flow," Int. J. Heat Mass Transfer, **36**(8), pp. 2183–2192.
[18] Alassar, R. S., Badr, H. M., and Mavromatis, H. A., 1999, "Heat Convection from a Sphere Placed in an Oscillating Free Stream," Int. J. Heat Mass Transfer, **42**, pp. 1289–1304.
[19] Leung, W. W., and Baroth, E. C., 1991, "An Experimental Study Using Flow Visualization on the Effect of an Acoustic field on Heat Transfer from Spheres," *Symposium on Microgravity Fluid Mechanics*, FED-Vol. **42**, The American Society of Mechanical Engineers.
[20] Lawrence, C. J., and Weinbaum, S., 1986, "The Force on an Axisymmetric Body in Lineraized, Time-Dependent Motion: A New Memory Term," J. Fluid Mech., **71**, pp. 209–218.
[21] Payne, L. E., and Pell, W. H., 1960, "The Stokes Flow Problem for a Class of Axially Symmetric bodies." J. Fluid Mech., **7**, pp. 529–549.
[22] Breach, D. R., 1961, "Slow Flow Past Ellipsoids of Revolution. J. Fluid Mech., **10**, pp. 306–314.
[23] Alassar, R. S., and Badr, H. M., 1999, "The Impulsively Started Flow Over Oblate Spheroids," ZAMP **50**, pp. 193–205.
[24] Alassar, R. S., and Badr, H. M., 1999, "Oscillating Flow over oblate spheroids," Acta Mech. **137**(3-4), pp. 237–254.
[25] Alassar, R. S., 1999, "Heat conduction from spheroids." ASME J. Heat Transfer, **121**, pp. 497–499.
[26] Alassar, R. S., and Badr, H. M., 1999, "Steady Flow Past an Oblate Spheroid at Small Reynolds Number," J. Eng. Math. **1**, pp. 1–11.
[27] Lai, R. Y. S., and Mockros, L. F., 1972, "The Stokes-Flow on Prolate and Oblate Spheroids During Axial Translatory Accelerations," J. Fluid Mech. **52**, 1–15.
[28] Chang, E. J., and Maxey, M. R., 1994, "Unsteady Flow About a Sphere at Low to Moderate Reynolds Number. Part 1. Oscillatory motion," J. Fluid Mech. **277**, 347–379.
[29] Jenson, V. G., 1959, "Viscous Flow Around a Sphere at Low Reynolds Numbers (<40)," Proc. R. Soc. London, Ser. A, **249**, 346.
[30] LeClair, B. P., Hamielec, A. E., and Pruppacher, H. R., 1970, "Numerical Study at the Drag on a Sphere at Low and Intermediate Reynolds Numbers," J. Atmos. Sci. **27**, pp. 308–315.
[31] Rimon, Y., and Cheng, S. I., 1969, "Numerical Solution of a Uniform Flow Over a Sphere at Intermediate Reynolds Numbers," Phys. Fluids, **12**, pp. 949–955.

Effectiveness-NTU Relationship for a Counterflow Heat Exchanger Subjected to an External Heat Transfer

Gregory F. Nellis
ASME Member
e-mail: gfnellis@engr.wisc.edu

John M. Pfotenhauer
ASME Member

University of Wisconsin, 1500 Engineering Drive, Madison WI 53706

This paper presents the analytical solution for the effectiveness of a counterflow heat exchanger subjected to a uniformly distributed, external heat flux. The solution is verified against conventional ε-NTU relations in the limit of zero external heat flux. This situation is of interest in applications such as cryogenic and process engineering, and the analytical solution provides a convenient method for treating differential elements of a heat exchanger in a numerical model. [DOI: 10.1115/1.2010496]

Introduction

The conventional ε-NTU relationships listed in most textbooks, e.g., [1], do not permit the application of a uniform heat flux to either fluid stream. The literature contains several examples of studies of the effect of parasitic heat transfer that is driven by a temperature difference from ambient. Chowdhury and Sarangi [2] present an analytical solution for the case where a heat leak is forced into the cold fluid; Barron [3] studied the case where a heat leak is imposed on either the hot or the cold fluids; and Ameel and Hewavitharana [4] derive the solution for the situation where a heat leak is imposed on both fluids. More complex numerical models, e.g., [5], are capable of applying an arbitrary heat flux.

Currently, there is no analytical solution for the performance of a counterflow heat exchanger subjected to a constant heat flux. Nevertheless, a convenient analytical solution for this situation in the form of an ε-NTU-type relation would be valuable. The primary utility of this solution is to facilitate a numerical solution that includes these and other second-order effects. The formulas presented here are particularly useful in this context—a typical heat exchanger cannot be predictively modeled in its entirety using an ε-NTU solution; instead it must be broken into a number of sub-heat exchangers, each of which can be treated more realistically using the constant property, constant heat transfer coefficient ε-NTU equations. The alternative solution presented here allows the impact of additional loadings to be rigorously considered within the framework of this type of numerical model. It has been useful to the authors in the study of recuperative heat exchangers that are integrated with current leads for superconducting electronics and therefore are subjected to dissipative heating [6] as well as for recuperative heat exchangers within cryosurgical probes that are subjected to external loading from the surrounding tissue [7] and for the high-effectiveness heat exchangers that are required for reverse-Brayton cryocoolers [8].

Contributed by the Heat Transfer Division for publication in the JOURNAL OF HEAT TRANSFER. Manuscript received: August 26, 2004. Final manuscript: received November 11, 2004. Review conducted by: Chang Oh.

Analytical Solution

Figure 1(*a*) illustrates a counterflow heat exchanger with uniform, external heat loads applied to the hot and cold streams ($\dot{g}_h$ and $\dot{g}_c$). The inlet temperatures and capacity rates of the hot and cold fluids are $T_{h,\text{in}}$, $T_{c,\text{in}}$, $\dot{C}_h$, and $\dot{C}_c$, respectively. Figure 1(*b*) illustrates a differential control volume within the heat exchanger.

The differential energy balances on the hot and cold streams are

$$d\dot{g}_h = \dot{C}_h dT_h + d\dot{q} \tag{1}$$

$$d\dot{q} + \dot{C}_c dT_c + d\dot{g}_c = 0 \tag{2}$$

The rate of heat transfer between the streams is related to the temperature difference according to

$$d\dot{q} = (T_h - T_c) dUA \tag{3}$$

where dUA is the differential amount of conductance in the control volume. The temperature difference between the streams (ΔT) is defined as

$$\Delta T = T_h - T_c \tag{4}$$

Differentiating Eq. (4) leads to

$$d\Delta T = dT_h - dT_c \tag{5}$$

Substituting Eqs. (1), (2), and (5) leads to

$$d\Delta T = \frac{d\dot{g}_h}{\dot{C}_h} - \frac{d\dot{q}}{\dot{C}_h} + \frac{d\dot{g}_c}{\dot{C}_c} + \frac{d\dot{q}}{\dot{C}_c} \tag{6}$$

The external heat inputs are assumed to be uniformly distributed along the heat exchanger

$$d\dot{g}_h = \dot{g}_h \frac{dUA}{UA} \tag{7}$$

$$d\dot{g}_c = \dot{g}_c \frac{dUA}{UA} \tag{8}$$

The rate equation is

$$d\dot{q} = dUA\Delta T \tag{9}$$

Substituting Eqs. (7)–(9) into Eq. (6) leads to

$$d\Delta T = \frac{\dot{g}_h}{\dot{C}_h}\frac{dUA}{UA} + \frac{\dot{g}_c}{\dot{C}_c}\frac{dUA}{UA} + \Delta T\left(\frac{1}{\dot{C}_c} - \frac{1}{\dot{C}_h}\right)dUA \tag{10}$$

Equation (10) can be rearranged to obtain

$$\frac{d\Delta T}{\dfrac{\dot{g}_h}{\dot{C}_h UA} + \dfrac{\dot{g}_c}{\dot{C}_c UA} + \Delta T\left(\dfrac{1}{\dot{C}_c} - \dfrac{1}{\dot{C}_h}\right)} = dUA \tag{11}$$

The quantities $\dot{g}_h/UA$ and $\dot{g}_c/UA$ are constants, and therefore Eq. (11) can be integrated from the hot end of the heat exchanger to any arbitrary position X within the heat exchanger, where X runs from 0 at the hot end to 1 at the cold end

$$\int_{\Delta T_{X=0}}^{\Delta T} \frac{d\Delta T}{\dfrac{\dot{g}_h}{\dot{C}_h UA} + \dfrac{\dot{g}_c}{\dot{C}_c UA} + \Delta T\left(\dfrac{1}{\dot{C}_c} - \dfrac{1}{\dot{C}_h}\right)} = UA\int_0^X dX \tag{12}$$

Carrying out the integration in Eq. (12) leads to

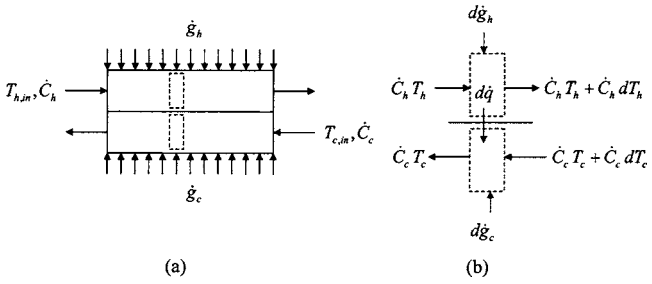

Fig. 1 (*a*) Counter-flow heat exchanger with a uniform external load applied to both streams and (*b*) a differential control volume for the heat exchanger

$$\frac{\Delta T\left(\frac{1}{\dot{C}_c}-\frac{1}{\dot{C}_h}\right)+\frac{\dot{g}_h}{\dot{C}_h UA}+\frac{\dot{g}_c}{\dot{C}_c UA}}{\Delta T_{X=0}\left(\frac{1}{\dot{C}_c}-\frac{1}{\dot{C}_h}\right)+\frac{\dot{g}_h}{\dot{C}_h UA}+\frac{\dot{g}_c}{\dot{C}_c UA}}=\exp\left[\left(\frac{1}{\dot{C}_c}-\frac{1}{\dot{C}_h}\right)UAX\right] \tag{13}$$

The hot-to-cold capacity ratio (Cr_h), the number of transfer units based on the hot-side capacity rate (NTU_h), the dimensionless external heat loads (χ_h and χ_c), and the dimensionless temperature difference Θ are defined as

$$Cr_h=\frac{\dot{C}_h}{\dot{C}_c} \tag{14}$$

$$\mathrm{NTU}_h=\frac{UA}{\dot{C}_h} \tag{15}$$

$$\chi_h=\frac{\dot{g}_h}{UA(T_{h,\mathrm{in}}-T_{c.\mathrm{in}})} \tag{16}$$

$$\chi_c=\frac{\dot{g}_c}{UA(T_{h,\mathrm{in}}-T_{c.\mathrm{in}})} \tag{17}$$

$$\Theta=\frac{\Delta T}{(T_{h,\mathrm{in}}-T_{c,\mathrm{in}})} \tag{18}$$

With these definitions, Eq. (13) becomes

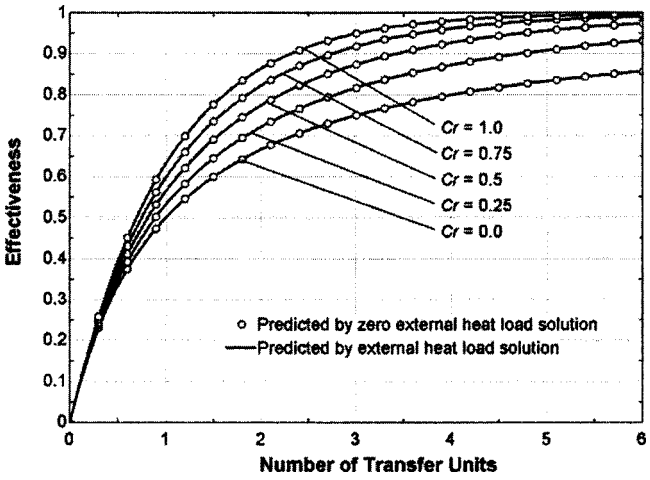

Fig. 2 Effectiveness as a function of NTU in the limit of no external heat load for various values of *Cr* using the zero external heat load solution, Eq. (30), and the solution derived here, Eq. (24)

$$\frac{\Theta(Cr_h-1)+\chi_h+Cr_h\chi_c}{\Theta_{X=0}(Cr_h-1)+\chi_h+Cr_h\chi_c}=\exp[(Cr_h-1)\mathrm{NTU}_h X] \tag{19}$$

An overall energy balance on the heat exchanger yields

$$\dot{g}_h+\dot{g}_c+\dot{C}_h(T_{h,\mathrm{in}}-T_{h,\mathrm{out}})=\dot{C}_c(T_{c,\mathrm{out}}-T_{c,\mathrm{in}}) \tag{20}$$

If Eq. (20) is divided by $UA\,(T_{h,\mathrm{in}}-T_{c,\mathrm{in}})$, then it becomes

$$\chi_h+\chi_c+\frac{(1-\Theta_{X=1})}{\mathrm{NTU}_h}=\frac{(1-\Theta_{X=0})}{Cr_h\mathrm{NTU}_h} \tag{21}$$

Evaluating Eq. (19) at $X=1$ (i.e., the cold end of the heat exchanger) leads to

$$\frac{\Theta_{X=1}(Cr_h-1)+\chi_h+Cr_h\chi_c}{\Theta_{X=0}(Cr_h-1)+\chi_h+Cr_h\chi_c}=\exp[(Cr_h-1)\mathrm{NTU}_h] \tag{22}$$

Combining Eqs. (21) and (22) leads to

$$\left(\mathrm{NTU}_h(\chi_c+\chi_h)+1+\frac{(\Theta_{X=0}-1)}{Cr_h}\right)(Cr_h-1)+\chi_h+Cr_h\chi_c$$
$$=[\Theta_{X=0}(Cr_h-1)+\chi_h+Cr_h\chi_c]\exp[(Cr_h-1)\mathrm{NTU}_h] \tag{23}$$

Equation (23) can be solved explicitly for the dimensionless temperature difference at either end of the heat exchanger

$$\Theta_{X=0}=\frac{\left(\mathrm{NTU}_h(\chi_h+\chi_c)+\frac{(Cr_h-1)}{Cr_h}\right)(Cr_h-1)+(\chi_h+Cr_h\chi_c)\{1-\exp[(Cr_h-1)\mathrm{NTU}_h]\}}{(Cr_h-1)\left\{\exp[(Cr_h-1)\mathrm{NTU}_h]-\frac{1}{Cr_h}\right\}} \tag{24}$$

with

$$\Theta_{X=1}=\mathrm{NTU}_h(\chi_c+\chi_h)+1+\frac{(\Theta_{X=0}-1)}{Cr_h} \tag{25}$$

which is the equivalent of an effectiveness-NTU relationship for this heat-exchanger configuration. In the limit of a balanced recuperator ($Cr_h=1$), Eq. (24) can be recast as

$$\Theta_{X=0}=\frac{1-\chi_c\mathrm{NTU}-\mathrm{NTU}^2\frac{(\chi_c+\chi_h)}{2}}{1+\mathrm{NTU}} \tag{26}$$

Because the heat transfer to and from the cold and hot streams is not the same due to the external heat transfer rates, it is necessary to define an effectiveness based on each of the two streams

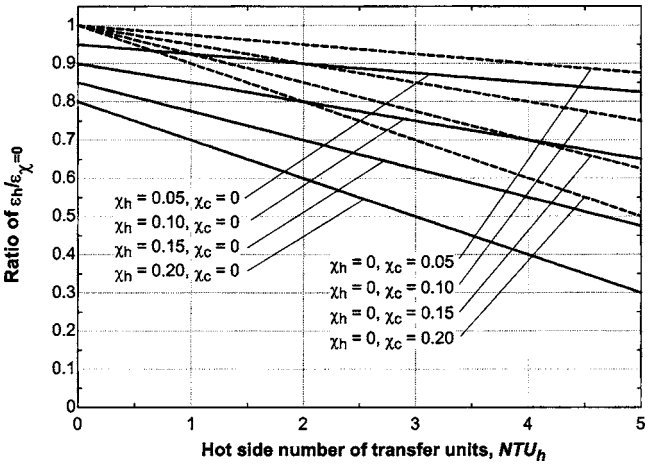

Fig. 3 Ratio of the hot-side effectiveness to the zero parasitic effectiveness as a function of NTU_h for various values of parasitic heat loads (with $Cr_h=1$).

$$\varepsilon_h = \frac{\dot{C}_h(T_{h,\text{in}} - T_{h,\text{out}})}{\dot{C}_{\min}(T_{h,\text{in}} - T_{c,\text{in}})} \tag{27}$$

$$\varepsilon_c = \frac{\dot{C}_c(T_{c,\text{out}} - T_{c,\text{in}})}{\dot{C}_{\min}(T_{h,\text{in}} - T_{c,\text{in}})} \tag{28}$$

The effectiveness equations can be written in terms of the dimensionless temperature differences

$$\varepsilon_h = \begin{cases} 1 - \Theta_{X=1} & Cr_h < 1 \\ Cr_h(1 - \Theta_{X=1}) & Cr_h > 1 \end{cases} \tag{29}$$

$$\varepsilon_c = \begin{cases} \dfrac{1 - \Theta_{X=0}}{Cr_h} & Cr_h < 1 \\ 1 - \Theta_{X=0} & Cr_h > 1 \end{cases} \tag{30}$$

In the limit of no external heat load, the above solution can be compared to the effectiveness-NTU relation for a counterflow heat exchanger reported in [1]. For unbalanced flow,

$$\varepsilon_{\chi=0} = \frac{1 - \exp[-\text{NTU}(1 - Cr)]}{1 - Cr\exp[-\text{NTU}(1 - Cr)]} \tag{31}$$

and for balanced flow

$$\varepsilon_{\chi=0,Cr=1} = \frac{\text{NTU}}{1 + \text{NTU}} \tag{32}$$

where ε is the effectiveness, NTU is the number of transfer units defined relative to the minimum capacity rate, and Cr is the ratio of the maximum to minimum capacity rate. Figure 2 illustrates the effectiveness as a function of the number of transfer units for different capacity ratios predicted by Eq. (24) and by Eqs. (31) and (32) in the limit of no external parasitic.

Figure 3 illustrates the ratio of the hot fluid effectiveness (ε_h) to the zero parasitic effectiveness ($\varepsilon_{\chi=0}$) as a function of the number of transfer units based on the hot side for a balanced recuperator ($Cr_h=1$) and various values of dimensionless external heat load on each side.

Note that the effectiveness associated with the hot side of the heat exchanger is, in general, less affected by a parasitic applied to the cold side, particularly at low NTU_h. In a similar manner, the effectiveness associated with the cold side of the heat exchanger is less affected by a parasitic applied to the hot side.

Summary

This paper presents the analytical solution for the performance of a counterflow heat exchanger in which a uniform, external heat load is applied to one or both sides. The solution is useful in many practical applications in order to estimate the impact of an applied parasitic on a particular device as it shows the appropriate dimensionless quantity that characterizes the heat load and allows a quantitative evaluation of its affect. Also, the analytical solution can be used to facilitate numerical analyses in which a heat exchanger exposed to an arbitrary external heat load is divided into differential segments, each of which may be evaluated using the expression derived here.

Acknowledgment

This work was funded by the Office of Naval Research under contract No. 0014-03-1-0175.

Nomenclature

$\dot{C}$ = capacity rate, W/K
Cr = minimum-to-maximum capacity ratio
Cr_h = hot-to-cold fluid capacity ratio
$\dot{g}$ = external heat load, W
NTU = number of transfer units based on minimum capacity rate
NTU_h = number of transfer units based on hot-side capacity rate
$\dot{q}$ = heat transfer rate, W
T = temperature, K
UA = total conductance, W/K
X = dimensionless position
χ = dimensionless external heat load
ΔT = temperature difference, K
ε = effectiveness
Θ = dimensionless temperature difference

Subscripts

c = cold side
h = hot side
in = inlet
min = minimum

References

[1] Incropera, F. P., and DeWitt, D. P., 2002, *Fundamentals of Heat and Mass Transfer*, 5th Edition, Wiley, New York.
[2] Chowdhury, K., and Sarangi, S., 1984, "Performance of Cryogenic Heat Exchangers With Heat Leak From the Surroundings," *Advances in Cryogenic Engineering*, 29, pp. 273–280.
[3] Barron, R. F., 1984, "Effect of Heat Transfer From Ambient on Cryogenic Heat Exchanger Performance," *Advances in Cryogenic Engineering*, 29, pp. 265–272.
[4] Ameel, T. A., and Hewavitharana, L., 1999, "Countercurrent Heat Exchangers With Both Fluids Subjected to External Heating," Heat Transfer Eng., **20**(3), pp. 37–44.
[5] Nellis, G. F., 2003, "A Heat Exchanger Model That Includes Axial Conduction, Parasitic Heat Load, and Property Variations," Cryogenics, **43**(9), pp. 523–538.
[6] Nellis, G. F., Pfotenhauer, J. M., and Klein, S. A., 2004, "Actively Cooled Current Leads for Superconducting Electronics Using Mixed-Gas Joule-Thomson Refrigeration," 2004 IMECE, ASME Paper No. IMECE2004-60284.
[7] Keppler, F., Nellis, G., and Klein, S. A., 2004, "Optimization of the Composition of a Gas Mixture in a Joule-Thomson Cycle," HVAC&R Res., **10**(2), pp. 213–230.
[8] Swift, W. L., Zagarola, M. V., Nellis, G. F., McCormick, J. A., Sixsmith, H., and Gibbon, J. A., 1999, "Developments in Turbo Brayton Technology for Low Temperature Applications," Cryogenics, **35**, pp. 989–995.